Nonequilibrium nanoparticle dynamics for the development of Magnetic Particle Imaging

Carolyn Shasha

A dissertation
submitted in partial fulfillment of the
requirements for the degree of

Doctor of Philosophy

University of Washington

2019

Reading Committee:

Kannan M. Krishnan, Chair

Anton Andreev

Jonathan T.C. Liu

Program Authorized to Offer Degree:
Physics

University of Washington

Abstract

Nonequilibrium nanoparticle dynamics for the development of Magnetic Particle Imaging

Carolyn Shasha

Chair of the Supervisory Committee:
Dr. Kannan M. Krishnan
Materials Science & Engineering, Physics

Magnetic Particle Imaging (MPI) is a promising new medical imaging platform currently in the preclinical stage. MPI uses iron oxide nanoparticles as tracers, and exploits their nonlinear magnetization response to external oscillating magnetic fields. The nanoparticle response is directly measured to create an image in MPI, and so optimizing nanoparticle properties as well as external magnetic field conditions in order to obtain improved image signal is crucial to the development of MPI as a clinical platform. A deep understanding of the physics of nanoparticle relaxation is fundamental to optimization and further development of MPI.

This work focuses on modeling the nonequilibrium dynamics of magnetic nanoparticles in order to optimize conditions for MPI and develop new therapeutic and diagnostic functionalities that can be integrated with MPI. A summary of theoretical models of nanoparticle dynamics is presented, and computational nonequilibrium models are outlined, which currently represent the most sophisticated methods for modeling nanoparticle dynamics. These models are verified and supported through experiment. Using these models, nanoparticle relaxation is explored in depth; the effect of applied field amplitude and frequency, as well as nanoparticle size, on the resulting relaxation mechanism and timescale is investigated in detail. These insights are then applied to the optimization of drive field conditions and nanoparticle size for MPI image resolution and sensitivity. A core size of 28 nm is found to

be optimal, with additional tuning required according to specific field conditions used.

Finally, a procedure for multicolor MPI, in which the signal from nanoparticles of different types or in different environments is separated, is developed. A multi-channel image reconstruction approach is outlined, and discrimination based on nanoparticle core size is demonstrated, resulting in successful generation of a multicolor MPI image of a 2D phantom. A procedure for quantitative temperature estimation with MPI is also proposed and verified experimentally. Overall, this work provides a theoretical foundation for nanoparticle relaxation physics in MPI, enabling further development towards the clinical stage.

TABLE OF CONTENTS

LIST OF FIGURES

LIST OF TABLES

GLOSSARY

AC: Alternating current

ACMS: Alternating current measurement system

ACS: Alternating current susceptibility

CT: Computed tomography

DC: Direct current

DLS: Dynamic light scattering

FFP: Field-free point

FMR: Ferromagnetic resonance

FOV: Field of view

FWHM: Full width at half maximum

LLG: Landau-Lifshitz-Gilbert

LRT: Linear response theory

MFH: Magnetic fluid hyperthermia

MNP: Magnetic nanoparticle

MPI: Magnetic particle imaging

MPS: Magnetic particle spectroscopy

MRI: Magnetic resonance imaging

MSB: Magnetic spectroscopy of nanoparticle Brownian motion

PEG: Polyethylene glycol

PET: Positron emission tomography

PPMS: Physical property measurement system

PSF: Point-spread function

ROI: Region of interest

SNR: Signal-to-noise ratio

SPION: Superparamagnetic iron oxide nanoparticle

TEM: Transmission electron microscopy

ACKNOWLEDGMENTS

Sincere thanks to Professor Kannan Krishnan for his mentorship, expertise, and guidance; his patience and genuine investment in his students' success have been invaluable throughout this process. Thank you as well to the current, past, and visiting members of the Krishnan group, for providing continuous support and discussion, and to the members of the Knopp group at the University Medical Center Hamburg-Eppendorf and the Farle group at the University of Duisburg-Essen for their collaborations. Special thanks to Dr. Dan Reeves and Dr. Jürgen Weizenecker for valuable guidance and discussion, and to Catherine Provost for ever-present support and reassurance.

Thank you to my science and math teachers, especially Thomas Maccarone, Chris Ratley, and Jonathan Shapiro, for always encouraging and inspiring me to study science, and to Profs. Derek Stein, Meni Wanunu, and Jens Gundlach for past mentorship and for providing an exciting introduction to research. Endless thanks and love to the many members of my family who have supported my education in countless ways, and to my wonderful friends, especially to Matt, for their constant love and support.

This work was was supported by NSF Grant No. DGE-1256082, and was facilitated through the use of advanced computational, storage, and networking infrastructure provided by the Hyak supercomputer system and funded by the STF at the University of Washington.

DEDICATION

For my grandfather Kazimierz and my father Mark.

Chapter 1

INTRODUCTION

The emerging field of biomedical nanomagnetics, which involves the application of nanoscale magnetic technologies to medical treatment and research, has enabled a wide range of new possibilities in the areas of medical imaging, diagnostics, and treatment. In particular, the use of biocompatible magnetic nanoparticles (MNPs) for a range of biomedical applications has been the focus of significant research in recent years. Due to their small size, MNPs are able to infiltrate biological systems and can bind to, or be internalized in, specifically targeted cells, provided they have appropriate functionalization or targeting ligands on their surface. Their magnetic properties allow these particles to be controlled and detected by an externally applied magnetic field, for specific functionality or guided delivery, allowing for a significant range of potential clinical uses [1,2]. These applications include targeted drug delivery [3–6], stem cell tracking [7–11], molecular detection through magnetic separation [12–17], contrast enhancement for magnetic resonance imaging [18–20], hyperthermia therapy in cancer treatment [21–25], and magnetic particle imaging [1,26], among others [1,2,27].

Magnetic particle imaging (MPI), in particular, is a promising new medical imaging technology which has the potential to incorporate other diagnostic and therapeutic functionalities, such as some of those listed above, and will be the primary focus of this thesis. In MPI, superparamagnetic iron oxide nanoparticles, a subcategory of MNPs, are used as tracers that can be detected in the body to generate an image. The fundamental physical principle and ultimate success of MPI relies on the unique magnetic properties of these nanoparticles.

1.1 Superparamagnetic nanoparticles

A nanoparticle, by definition, is a particle smaller than 100 nm in diameter. Magnetic nanoparticles are made up of ferromagnetic or ferrimagnetic materials, which have a permanent magnetic moment under zero applied magnetic field. Examples of such materials are iron, cobalt, nickel, and some of their oxides (although many of these oxides are antiferromagnetic). Magnetic materials on the nanoscale can be found in a wide array of modern technologies. Bulk magnetic materials form domain structures; when the size of a magnetic nanoparticle is reduced to below the single domain limit (e.g. around 30 nm for iron oxide), the MNP can become superparamagnetic at room temperature. In that case, the MNP is composed of a single magnetic domain, i.e. its internal magnetization is fully aligned, and will have a single magnetic moment which can spontaneously flip due to thermal excitations within a given time period (specifically, the time required to take a measurement of its magnetization). If the particle's magnetic moment can flip many times over the course of a measurement, its net magnetization will be measured to be zero. Under an applied field, the MNP will essentially behave as a paramagnet: it will align its magnetic moment to the external magnetic field, but will have zero remanent magnetization upon removal of the field. The magnitude of the magnetic moment, however, will be much larger (by as many as 4 orders of magnitude) than those in typical paramagnets. The lack of remanent magnetization is crucial for biomedical applications, as it enables the MNPs to avoid agglomeration and maintain colloidal stability. The large magnetic moment, however, allows superparamagnetic particles to be manipulated by external magnetic fields (specifically magnetic gradients) and remotely detected even when at extremely low concentrations. As a result, clinical applications using superparamagnetic nanoparticles would require only a small amount of total material to be introduced into the body, significantly reducing any potential concerns regarding toxicity.

Due to its biocompatibility, iron oxide is the typical material used for MNP tracers, particularly the magnetite phase (Fe_3O_4), which has the highest bulk saturation magnetization. Magnetite is ferrimagnetic, as is the maghemite phase ($\gamma-Fe_2O_3$), which has a slightly lower

saturation magnetization. While materials with larger magnetic moments, e.g. cobalt, would theoretically be preferred for these applications, cytotoxicity is a crucial issue for any material used for medical purposes. The United States Food and Drug Administration (FDA) and the European Medicines Agency (EMA) have already approved the medical use of magnetite and maghemite MNPs, and so iron oxides are a clear choice for *in vivo* biomedical applications, both for their magnetic properties as well as their low toxicity.

Superparamagnetic iron oxide nanoparticles (SPIONs) can now be chemically synthesized with a high degree of control over their physical properties, in particular their phase, size, and shape [28, 29]. The typical SPION fabrication procedure involves thermal decomposition of an organometallic precursor and stabilization with surfactants, which results in a hydrophobic magnetic core. In order to stabilize the particles in water, which is necessary for any biomedical application, the particles must undergo a phase transfer process and surface functionalization, typically involving coating with a polymer. A commonly used polymer for such a purpose is poly(ethylene glycol) (PEG), although coating materials can also include organic molecules, other polymers (e.g. dextran), and inorganic molecules (e.g. silica) [30–37]. The surface of the nanoparticle can then be further modified to incorporate additional functional groups or targeting molecules, depending on the specific desired application.

The functionalization of the nanoparticle surface is an important component for many practical applications; since SPIONs have sizes on the order of biomolecules, they can easily interact with biological molecules. For example, they can bind to proteins, genes, or viruses; interact with single cell-receptors; target cancerous tissue; or penetrate cells [2, 12, 13, 20, 38–40]. When we consider these functionalities in combination with their ability to be magnetically controlled and detected, the theranostic[1] power of SPIONs becomes evident.

In order to effectively manipulate and detect magnetic nanoparticles, their dynamics under an applied magnetic field must be fully understood. The magnetic moment of a super-

[1]Simultaneously therapeutic and diagnostic

paramagnetic particle will couple to the microscopic degrees of freedom of its environment (e.g. conducting electrons, phonons, nuclear spins, etc.), and so will undergo thermal fluctuations. The motion of the MNP magnetic moment under an applied field will therefore be a complex stochastic process. Additionally, the magnetic fields required for the applications discussed here are alternating current magnetic fields with frequencies on the order of tens of kilohertz. The short timescales involved give rise to nonequilibrium conditions and resulting nonlinear nanoparticle dynamics, which cannot be described with simple models.

While the scope of the discussion in this work is limited to the dynamics of magnetic nanoparticles in the context of biomedical applications, it should be mentioned that studying and modeling fast magnetization reversal is essential for a much wider range of technological applications, specifically in the realm of computer memory. Many hard drives are made with a pattern of nanomagnets, where each nanomagnet represents a bit of memory. Technological developments in this area, such as increasing the speed of reading and writing bits while maintaining data stability, require a deep understanding of the effects of thermal fluctuations and magnetic interactions on the dynamics of fast bit switching [41–43]. The nonequilibrium models that will be discussed in this thesis, then, have some applicability outside of the field of biomedical nanomagnetics.

1.2 Overview of magnetic particle imaging

In this work, we focus on one particular medical application of superparamagnetic nanoparticles: magnetic particle imaging, or MPI. As discussed above, due to their magnetic properties, SPIONs can generate a strong signal response to an applied magnetic field, enabling image reconstruction based on similar principles as in magnetic resonance imaging (MRI) or positron emission tomography (PET). Prior to an MPI scan, SPION tracers would be administered, likely intravenously, and if properly functionalized, allowed to circulate throughout the body. Using a combination of static gradient and alternating current magnetic fields, the concentration and distribution of magnetic nanoparticles can then be recorded, enabling reconstruction of a three-dimensional image [1, 26, 44]. The first clinical use for MPI would

be high-resolution, real-time cardiovascular imaging.

The concept of MPI relies on the nonlinearity of the magnetization curve for a superparamagnetic particle and the fact that its magnetization is eventually saturated for any applied magnetic field greater than the saturation field. If the MNPs are subject to an oscillating magnetic field, the magnetization response, $M(t)$, will vary with time. The time-varying magnetization will induce a voltage in the receive coil, which will be proportional to the rate of change of the magnetization, $M'(t)$. In this way, a signal from the nanoparticles is generated and subsequently detected. The spatial localization of the signal is achieved by superimposing a static magnetic field on top of the alternating field. The magnetization response saturates if this applied field is large, resulting in suppression of the recorded signal.

In practice, to implement this as a spatial encoding scheme for imaging, a strong static gradient field, generally called the selection field, is superimposed on the oscillating drive field. The selection field gradient generates a small well-defined region at its origin where the magnetic field is zero, referred to as the field-free point (FFP). Outside of the FFP, the static field increases in magnitude very rapidly, and therefore the magnetization of the particles is saturated in any region outside of the central point. The FFP can then be scanned across the sample. The resulting induced signal will be nonzero only when the FFP is at the location of the nanoparticle tracers. A tomographic image is formed as the FFP is scanned across the sample, causing any tracers in that voxel to reverse their magnetization and induce a signal in the detection coil. The shape of the differential susceptibility ($M'(t)$) determines the point-spread function (PSF) of the MPI imaging system. Understanding the factors that influence the shape of the PSF is key to optimizing the signal and the entire MPI system, and is a main focus of our present research.

SPIONs are already currently used as contrast agents to enhance signal in MRI [45], and so their safety and viability have already been well-tested. However, in MRI, SPIONs provide T2 (dark) contrast, whereas they provide positive (bright) contrast in MPI, which is favored by radiologists and clinicians. MPI on its own, then, is a promising technology that can theoretically provide better signal and spatial resolution than MRI, even when compared

to MRI that incorporates nanoparticle contrast agents [46]. Since MPI is a tracer-based imaging system, like PET, it produces a quantitative image signal (the signal is linear with tracer concentration) that is easy to interpret. This is not the case when nanoparticles are used as contrast agents in MRI, for example. The signal generated by contrast agents in MRI is substantially limited by the background signal from the surrounding biological tissue, and so resolution is not significantly improved with the addition of nanoparticles [47]. This problem is avoided with MPI. Biological tissue is weakly diamagnetic, which generates no MPI signal, so concerns of image noise arising from background signal are alleviated [1].

Because of the SPIONs' superparamagnetic properties, MPI has very high mass sensitivity, and therefore huge signal generating efficiency, many orders of magnitude greater per volume than protons detected with MRI, for example. The signal-to-noise ratio (SNR) with MPI is therefore much higher than MRI [44]. A large SNR is advantageous because it provides the ability to produce high-quality images even under suboptimal conditions, such as shorter scanning times. Faster image acquisition times are a huge improvement over other imaging techniques like MRI, which requires long acquisition times sometimes lasting as long as several hours, limiting the range of phenomena that can be accurately imaged. Real-time imaging with MPI over short timescales (on the order of tens of milliseconds) has already been demonstrated [44,48]. The high SNR also enables MPI to detect very low concentrations of MNPs, reducing the quantity needed for accurate imaging. MPI can obtain signals from less than one nanogram of optimized nanoparticles [46], whereas the minimum detectable concentration of MNPs in MRI ranges from micrograms to milligrams [49]. MPI also has the potential to provide high spatial image resolution, on the order of half a millimeter or less. This is similar to the spatial resolution possible with MRI, and better than PET, which has a resolution of 1-2 mm [50]. Although this level of resolution has not yet been fully realized experimentally (it has been demonstrated in phantom images but not yet *in vivo*), MPI is emerging as an imaging platform that can theoretically provide higher image quality than other current leading medical imaging techniques.

Furthermore, MPI is both safer and more cost efficient than other leading medical imaging

methods. MPI requires only a magnetic field gradient, rather than an expensive highly uniform superconducting magnet, as required for MRI. While PET uses radioactive tracers that require expensive cyclotron facilities and have a necessarily short half-life, MPI tracers can be stored for months and are cheaper to produce than radioactive tracers. MNPs are much safer than iodine and gadolinium contrast agents, which are commonly used in x-ray, CT, and MR imaging. As mentioned, iron oxide magnetic nanoparticles have been approved by the FDA and shown to have no adverse effects on the body, in contrast to iodine and gadolinium [51]. Again due to its high SNR, MPI only requires a very small amount of these tracers, compared to the concentration needed for contrast agents used in MRI. Unlike in MRI, the MPI signal is linear with tracer concentration, providing a quantitative image. Finally, the magnetic field strength used in MPI is much lower and therefore safer than those used in other magnetic imaging systems; MPI uses safe radio-frequency fields and does not require ionizing radiation like CT and PET.

1.3 Current challenges and possibilities in MPI research

MPI was first proposed by Bernhard Gleich and Jürgen Weizenecker in 2005 [26]. Since then, there has been significant progress in hardware, software, and tracer development. In collaboration with Philips Research, Bruker BioSpin has developed a preclinical small animal scanner, enabling 3D imaging of mice, rats, guinea pigs, and rabbits. The Bruker machine operates in frequency space, or f-space, which directly measures the frequency spectrum of the MNP response, and requires an initial calibration measurement. Concurrently, Magnetic Insight, founded by a research group from UC Berkeley, has developed the MOMENTUM™ Imager, also able to image small animals. The Magnetic Insight scanner operates in x-space, which enables faster image reconstruction [52].

With current MPI systems, nanomolar sensitivity and submillimeter resolution have been achieved [53–56]. However, in order to move beyond the preclinical stage and compete with other medical imaging modalities, these benchmarks need to be still improved, particularly the resolution (to below 0.5 mm). To push the limits of image SNR and resolution, nanopar-

ticle tracers need to be carefully optimized. An important challenge is the lack of a complete model of the magnetic relaxation behavior of SPIONs. In f-space MPI systems in particular, incorporating an accurate model of the MNP response would enable a model-based approach to image reconstruction, rather than a measurement-based approach, which requires a highly time-intensive calibration measurement.

The versatility of SPIONs allows for several exciting potential extensions of MPI, reaching into the categories of medical diagnostics and therapeutics. MNP dynamics are highly sensitive to their surrounding environment, which enables their use as sensors. For example, changes in viscosity can be detected using the technique of magnetization spectroscopy of nanoparticle Brownian motion (MSB), developed by John Weaver and Adam Rauwerdink [57]. It has also been indicated that other biologically relevant parameters, such as temperature, can be detected and even quantified using such a technique [58, 59]. With proper surface functionalization, sensing of specific biomolecules is also possible, due to changes in dynamics that result from differences in the binding state of MNPs, enabling a range of diagnostic applications [60–62]. These sensing techniques can in theory be combined with MPI to create multi-channel or multicolor images, in which color represents a parameter such as viscosity or temperature, potentially enabling simultaneous real-time imaging and diagnostics.

Another biomedical application of MNPs is magnetic fluid hyperthermia (MFH), in which high-frequency excitation fields are used to induce nonlinear MNP rotations in cancer cells, generating cytotoxic heat [22–24, 63–66]. In principle, MFH could be combined with MPI and temperature sensing to create a combined imaging and therapeutic platform, in which the MNPs and resulting heat generation could be quantitatively tracked. A related use could be targeted delivery of chemotherapy drugs, in which antitumor drugs are attached to the nanoparticle surface and then released via thermal activation from application of an external magnetic field. In a similar way, MPI combined with sensing of temperature or binding-state could enable a monitored targeted drug-delivery system. The above proposed applications all require a detailed understanding of MNP dynamics *in vivo*, including their dependence

on environmental and particle properties, under nonequilibrium conditions.

The Krishnan lab at the University of Washington has played an instrumental role in the development of MPI, particularly in the area of tracer development. The first synthesis and study of shape-controlled cobalt nanoparticles was outlined by Victor Puntes and Kannan Krishnan [67] and then continued by Yuping Bao [68]. Extending this work, the synthesis and cytotoxicity of iron oxide nanoparticles for magnetic fluid hyperthermia was investigated by Marcela Gonzales in her doctoral thesis [69]. Her work developed specific expertise regarding synthesis, functionalization, and optimization of SPIONs for biomedical applications. This work was continued by Matthew Ferguson, who focused on optimization of SPIONs for MPI, finding the first experimental results of an optimal size for nanoparticles for MPI, and developed hardware for measuring the MNP magnetization response [70]. Scott Kemp continued work on optimizing phase purity of MNP cores and scaling the synthesis procedure [29], resulting in a scalable procedure to synthesize phase- and size-optimized monodisperse MNP cores for MPI. Amit Khandhar continued work on surface functionalization of MNPs for biomedical applications, specifically for long-term circulation and uptake in cancer cells [71]. Surface conjugation for cancer targeting was studied by Asahi Tomitaka [72] and Hamed Arami [73], enabling various *in vivo* applications, and Eric Teeman has investigated the effect of cell internalization on the resulting MPI signal [74]. The product of these years of research from this group is the experimentally-driven development of optimized SPIONs for *in vivo* applications. My research aims to develop a theoretical foundation for the previous work, supported by computational simulations, by studying the fundamental physics of nanoparticle dynamics.

Modeling the nonequilibrium MNP dynamics, in order to further enable the above mentioned applications as well as to optimize conditions for MPI, will be the main focus of this thesis. An overview of the current understanding of nanoparticle relaxation dynamics, and the relevant connections to MPI image reconstruction, will be provided in §2. Computational nonlinear stochastic models will be developed in §3, which currently represent the most advanced methods for modeling nonequilibrium nanoparticle dynamics. These models will

be used extensively throughout the remainder of the thesis; in §4, nanoparticle relaxation timescales and mechanisms will be investigated in depth, which will allow us to optimize drive field frequency, amplitude, and nanoparticle size for MPI resolution and sensitivity in §5. Finally, in §6, these methods will be used to develop a platform for multicolor MPI based on core size discrimination and temperature estimation.

Chapter 2

THEORY OF NANOPARTICLE RELAXATION DYNAMICS IN MPI

The foundational basis of image acquisition in MPI is the response of superparamagnetic nanoparticles to oscillating magnetic fields. Magnetic relaxation effects play an important role in the resulting signal, particularly in the sensitivity and resolution of the final image. In this chapter, an overview of basic nanoparticle relaxation models in the equilibrium and linear regime is presented. It is intended to serve as the basis for a discussion of nonlinear dynamics, and to describe the connection between nanoparticle relaxation physics and image generation in MPI.

2.1 Equilibrium physics

A ferromagnetic particle smaller than a certain critical diameter (around 30 nm for magnetite at room temperature and 100 second measurement time) [75] will exhibit superparamagnetism. Superparamagnetic iron oxide nanoparticles fall under the single-domain limit, which means that they can be described as having one large magnetic moment. Superparamagnetism occurs when the energy barrier for a magnetic moment to reverse is less than the thermal energy of the system, and so the entire magnetic moment will spontaneously rotate within a particular time period, defined by the measurement time (typically assumed to be 100 s for DC measurements). For that measurement time, the average magnetization is then zero in the absence of an applied field, and will act as a paramagnet under an applied field, but with a much larger magnetic moment (up to 5 orders of magnitude greater than the Bohr magneton). There is also an implicit temperature scale when characterizing superparamagnetic particles; when any ferro- or ferrimagnetic material is heated above its Curie

temperature, it will lose its magnetic ordering and become a paramagnet. Superparamagnetism then requires the temperature to be below the Curie temperature of the material, but high enough that thermal energy is large enough for the magnetic moment to reverse within the defined measurement time.

Under an applied magnetic field, the particle's magnetic moment will rotate to align with the field. We define the equilibrium relaxation time constant τ, which refers to the time required for the particle moment to return to equilibrium after an external perturbation. When applying a field, we first consider the equilibrium case, where the timescale of the change in field is large enough that the particle can come to equilibrium at each step. Under an oscillating magnetic field, for example, this condition requires $1/f \gg \tau$. While this condition typically does not apply for MPI applications, it is still instructive to examine the equilibrium case before moving on to nonequilibrium scenarios.

2.1.1 The Langevin function

We model superparamagnetic nanoparticles as dipoles with magnetic moment magnitude $\mu = M_s V_c$, where M_s is the saturation magnetization of the material (~ 420 kA/m for magnetite), and V_c is the volume of the magnetic core. We distinguish this from the hydrodynamic volume, V_h, which includes the non-magnetic coatings that are applied to the surface of the core particle. In an ensemble of isotropic non-interacting magnetic nanoparticles, the equilibrium energy of an individual particle will be:

$$E = -\mu_0 \boldsymbol{\mu} \cdot \mathbf{H}. \tag{2.1}$$

Here, $\boldsymbol{\mu}$ is $\mu\hat{\mathbf{m}}$, with $\hat{\mathbf{m}}$ a unit vector pointing in the direction of the magnetic moment, and $\mathbf{H}$ is the applied field. Without loss of generality, from here on the field will be assumed to be applied in the z-direction. Considering a collection of such particles, the partition function of this ensemble is:

$$\mathcal{Z} = \sum_n e^{-E_n/k_BT}, \tag{2.2}$$

where T is the temperature and k_B is Boltzmann's constant. In the continuum limit, the average energy of the ensemble is:

$$\langle E \rangle = \frac{1}{\mathcal{Z}} \int E e^{-E/k_BT} dE. \tag{2.3}$$

At this point, we define $\boldsymbol{\xi} \equiv \mu_0 \mu \mathbf{H}/k_BT$, with magnitude $\xi = \mu_0 \mu H/k_BT$. Setting $\cos\theta = x$, the average energy can be written as:

$$\langle E \rangle = -\frac{\int_1^{-1} \xi e^{\xi x} dx}{\int_1^{-1} e^{\xi x} dx}. \tag{2.4}$$

We can then express the average particle magnetization in the z-direction as:

$$\langle m_z \rangle = \frac{\int_{-1}^{1} \mu x e^{\xi x} dx}{\int_{-1}^{1} e^{\xi x} dx}. \tag{2.5}$$

Evaluating this, we find that the average particle magnetization is proportional to the Langevin function:

$$\langle m_z \rangle = \mu \mathcal{L}(\xi), \tag{2.6}$$

where

$$\mathcal{L}(\xi) = \coth\xi - 1/\xi. \tag{2.7}$$

This well-known equation describes the magnetization of an ensemble of isotropic particles at equilibrium, i.e. when the particle dipole moments are allowed to fully relax at every step of the applied field. The Langevin function for three different particle core sizes is shown in Fig. 2.1. It should be emphasized that the Langevin function does not incorporate particle anisotropy, and so is only applicable as an approximation for small or nearly isotropic particles in a nonequilibrium case.

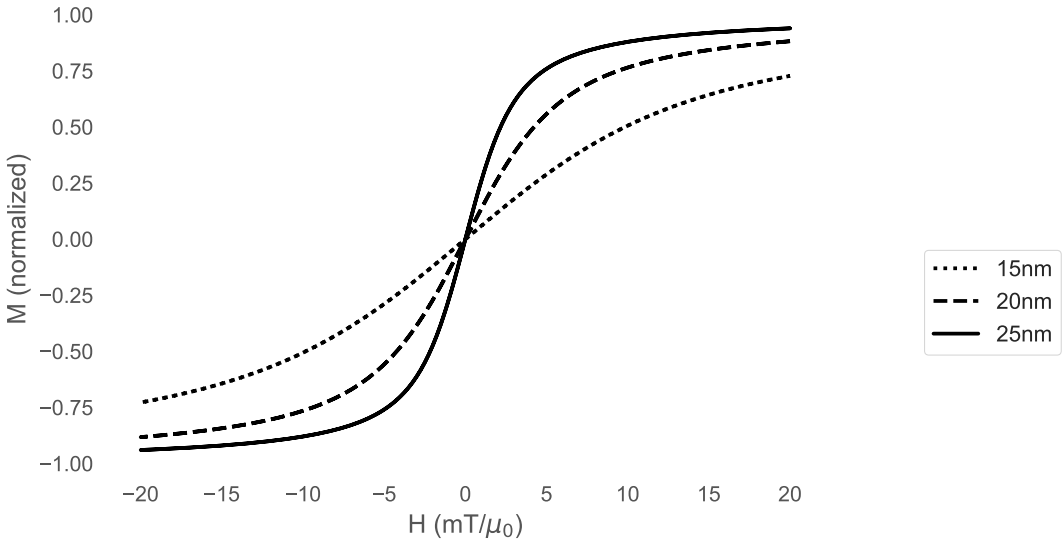

Figure 2.1: The Langevin function for three different particle core diameters, with $M_s = 420$ kA/m at 300 K.

2.1.2 Anisotropic partition function

In reality, superparamagnetic nanoparticles will have some degree of anisotropy, resulting from combined magnetocrystalline, shape, and surface anisotropies. Typically, uniaxial anisotropy is assumed, indicating that there is a single easy axis $\hat{\mathbf{n}}$ along which the magnetic moment prefers to align. In that case, the unitless anisotropic field is $\sigma = KV_c/k_BT$, where K is the effective anisotropy constant, incorporating all magnetocrystalline and shape anisotropy (the effective anisotropy will be discussed in further detail in the following chapter). We can then express the energy of a single particle as:

$$\frac{E}{k_BT} = -\sigma(\hat{\mathbf{n}} \cdot \hat{\mathbf{m}})^2 - \hat{\mathbf{m}} \cdot \boldsymbol{\xi}. \tag{2.8}$$

The partition function, in spherical coordinates, then becomes:

$$\mathcal{Z} = \int_0^{2\pi} \int_0^{\pi} \exp(\xi \cos\theta + \sigma \cos^2\beta) \sin\theta d\theta d\phi, \tag{2.9}$$

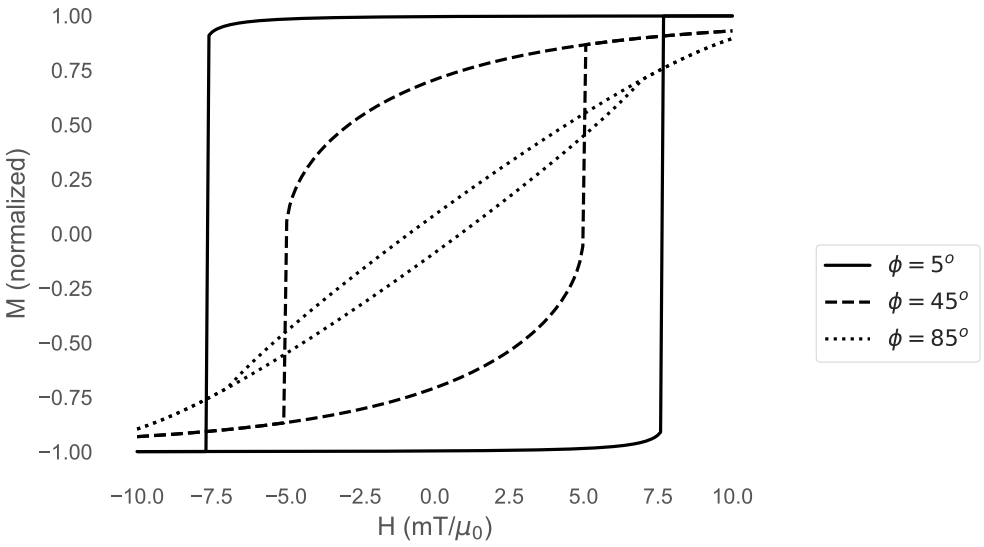

Figure 2.2: Hysteresis curves calculated from the Stoner-Wohlfarth model at different angles of the easy axis.

where β is the angle between $\hat{\mathbf{m}}$ and $\hat{\mathbf{n}}$. To simplify our calculations, from here on, we will assume that the easy axis $\hat{\mathbf{n}}$ is aligned with the magnetic field $\boldsymbol{\xi}$ in the z-direction. In this case, the partition function simplifies to:

$$\mathcal{Z} = \int_0^{2\pi} \int_0^{\pi} \exp(\xi \cos\theta + \sigma \cos^2\theta) \sin\theta d\theta d\phi, \tag{2.10}$$

and with $x = \cos\theta$:

$$\mathcal{Z} = 2\pi \int_1^{-1} e^{\xi x + \sigma x^2} dx. \tag{2.11}$$

Making a further assumption that the easy axis lies in the same plane as the magnetization (still assumed to be in the z-direction), following Stoner and Wolhfarth [76], the system becomes two-dimensional. Then, θ describes the angle between the moment and $\hat{z}$ and ϕ is the angle between the easy axis and $\hat{z}$. The energy, in unitless form, is then:

$$\frac{E}{k_B T} = -\sigma \sin^2(\theta - \phi) - \xi \cos\theta. \tag{2.12}$$

To find the equilibrium state of the particle, we take the derivative of the energy with respect to the moment direction θ:

$$0 = \frac{1}{k_B T}\frac{\partial E(\theta, \phi)}{\partial \theta} = \xi \sin\theta + 2\sigma \sin(\theta - \phi)\cos(\theta - \phi), \tag{2.13}$$

which simplifies to

$$\frac{\xi}{\sigma} = -\frac{\sin[2(\theta - \phi)]}{\sin\theta}. \tag{2.14}$$

To find a minimum we must also ensure $\frac{\partial^2 E(\theta,\phi)}{\partial \theta^2} > 0$. The Stoner-Wohlfarth hysteresis loop emerges from solving for the magnetization ($\cos\theta$) and plotting with respect to the field (see Fig. 2.2). The width of the hysteresis loop depends on the angle ϕ between the easy axis and the applied field. This model has an advantage over the simple Langevin function in that it accounts for particle anisotropy, but still assumes equilibrium conditions, and therefore does not account for particle relaxation.

2.1.3 Néel vs. Brownian relaxation mechanisms

There are two mechanisms by which a superparamagnetic nanoparticle can reverse its magnetic moment. Brownian relaxation refers to the physical rotation of the particle to align its magnetic moment with the applied magnetic field, and Néel relaxation refers to the reversal of the magnetic moment within the particle itself, assuming that the physical particle remains stationary (see Fig. 2.3). The particle will relax via either Brownian or Néel relaxation or some combination of both, although the faster mechanism will typically dominate. In MPI, nanoparticle dipole moments rotate under the influence of an external oscillating field, generating a measurable signal resulting from the changing magnetic field. The particle dynamics are typically discussed in terms of timescales of nanoparticle rotations, particularly the equilibrium relaxation time [77–79].

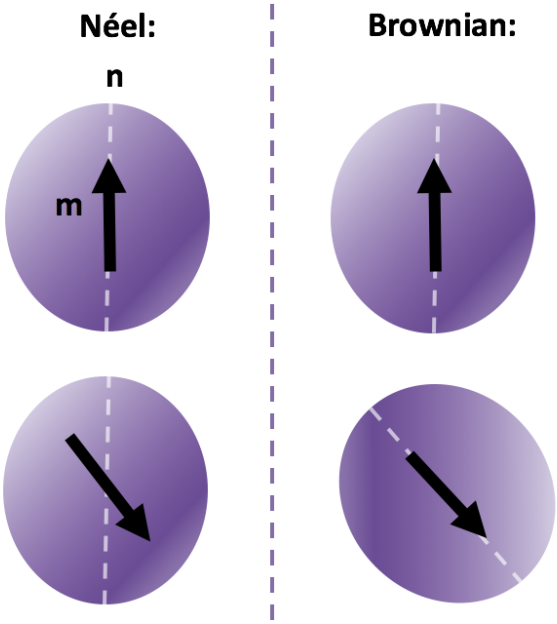

Figure 2.3: Néel vs. Brownian relaxation mechanisms. With Néel relaxation, the easy axis **n** stays stationary, while only the magnetic moment **m** rotates. Under Brownian relaxation, both the axis and the moment rotate.

Due to the magnetocrystalline anisotropy of MNPs, their magnetic moment will preferentially align with a particular crystallographic direction (the easy axis), a result of coupling between the atomic spin and orbital angular moments. This preferential alignment of the magnetic moment will also be influenced by shape asymmetry. The energy required to rotate the magnetization from the easy axis is denoted the anisotropy energy. As mentioned in the previous section, in the uniaxial case, the anisotropy energy can be expressed in terms of a single constant K, which incorporates all sources of anisotropy (magnetocrystalline, shape, etc.). The anisotropy energy has two minima, which correspond to alignment with the easy axis $\pm\hat{\mathbf{n}}$, separated by an energy barrier KV_c. When this energy barrier is smaller than the thermal energy k_BT, the particle magnetic moment is free to rotate between energy minima. Néel relaxation occurs when the particle orientation (the easy axis) remains fixed while the magnetic moment flips, and is characterized by the equilibrium Néel relaxation time [23, 80–82],

$$\tau_N = \frac{\sqrt{\pi}}{2}\tau_0 \frac{\exp(\sigma)}{\sigma^{1/2}}, \tag{2.15}$$

where the attempt time τ_0 is equal to $M_s/(2\alpha\gamma K)$. α is a dimensionless damping constant, assumed to be between 0.1 and 1, and γ is the gyromagnetic ratio.

When measuring MNP magnetization, the measurement time τ_M must be defined. In the case where $\tau_M \gg \tau_N$, the particle is in the superparamagnetic state, and the magnetization will flip multiple times over the course of the measurement resulting in zero net remanent magnetization. Alternatively, if $\tau_M \ll \tau_N$, then the magnetization will not reverse during the measurement; the particle will be in a blocked state. The blocking temperature is defined as the temperature at which $\tau_M = \tau_N$, when the transition between the blocked and the superparamagnetic state occurs [81]. If the particle is in the blocked state, the particle physically rotates along with the magnetic moment, and is then described by the Brownian relaxation mechanism. We can similarly quantify the characteristic equilibrium Brownian relaxation time [23, 24]:

$$\tau_B = \frac{3V_h\eta}{k_B T}, \tag{2.16}$$

where η is the viscosity of the surrounding medium and again V_h is the hydrodynamic volume including any surfactant. The mechanism by which the particle reverses its magnetic moment will be determined by the particle anisotropy and size (smaller particles exhibit only Néel relaxation, while larger particles exhibit primarily Brownian relaxation). The effective magnetic relaxation time is often expressed as [23, 24]:

$$\tau_{\text{eff}} = \frac{\tau_B \tau_N}{\tau_B + \tau_N}, \tag{2.17}$$

from which it can be seen that the mechanism with the lowest relaxation time for a given particle size and anisotropy will dominate. In reality, the two relaxation mechanisms are coupled in a non-trivial way, which is not fully described by this effective relaxation time [83, 84]. Furthermore, when a sufficiently large external driving field is applied ($\xi > 5$),

these equilibrium time constants can no longer completely describe the subsequent dynamics [79,84]. Under a strong applied field, particles' magnetic moments will align faster than in the equilibrium case, and so the true timescales of rotation will be shorter than the equilibrium relaxation times.

2.2 Linear response theory

One of the most common models of dynamic MNP magnetization is the Debye/Fannin model [85], which describes the linear response of a dipole to an oscillating field. In linear response theory (LRT), it is assumed that the applied field is low enough (or that the frequency is high enough) so that magnetic saturation, when all particle moments are fully aligned with the field, is not reached. We define χ to be the magnetic susceptibility, which will be constant with increasing applied field H (so $M = \chi H$, where M is the ensemble magnetization in the direction of the field). The equilibrium susceptibility, χ_0, of a system of non-interacting MNPs is defined to be [86]:

$$\chi_0 = \frac{M(H)}{H} = \frac{\mu}{H}\mathcal{L}(\xi), \tag{2.18}$$

where $\mathcal{L}(\xi)$ is the Langevin function (Eq. 2.7). In the Debye model [85,87], the magnetic susceptibility is broken down into real (in-phase) and imaginary (out-of-phase) components:

$$\chi = \chi' - i\chi'' = \chi_0 \left(\frac{1}{1+(\omega\tau)^2} - i\frac{\omega\tau}{1+(\omega\tau)^2} \right) \tag{2.19}$$

τ represents the effective magnetic relaxation time, from Eq. 2.17, and ω is the angular frequency of the applied field. The out-of-phase component will have a maximum at $\omega\tau = 1$, at which point the phase shift between the particle's magnetic moment and the applied field is maximum, resulting in energy loss. The magnetization in the direction of the field is then described by:

$$M(t) = \mu \int_0^\infty \left(\frac{1}{1+(\omega\tau)^2}\mathcal{L}(\xi\cos\omega t) - \frac{\omega\tau}{1+(\omega\tau)^2}\mathcal{L}(\xi\sin\omega t) \right) g(d)\mathrm{d}d. \tag{2.20}$$

Here we have included a size distribution $g(d)$ for the particles, where d is the particle diameter, typically considered to be a log-normal distribution [88]. This model for the magnetization is valid as long as linear response theory holds, i.e. for high frequencies or low fields (typically when ξ is less than 10). Although MPI measurements are often performed under conditions at which saturation is reached, outside of the validity regime for LRT, the Debye model is still a useful approximation that can be used to gain an understanding of the influence of nanoparticle relaxation and the resulting phase lag.

2.3 Relaxation theory in MPI

An ongoing challenge in MPI research is reaching theoretical detection limits and image resolution. To improve upon these, in addition to hardware advances, a complete understanding of nanoparticle relaxation dynamics is crucial. This section describes the influence of nanoparticle relaxation dynamics on the MPI signal. The discussion in this section will be limited to zero- and one-dimensional systems, but the principles apply generally to two- and three-dimensional systems as well.

2.3.1 Signal generation in MPI

Although there are different specific setups of current MPI systems, the main principle behind all is the same. A magnetic gradient field is applied across the section of the sample to be imaged, which is then scanned around the sample (in practice done by tuning the amplitude of an additional DC field), creating a single field-free point (FFP) or line. The magnetic gradient drives all MNPs into magnetic saturation except for the particles at the FFP, which experience a changing magnetic field. As the FFP passes over the particles, their magnetic moment flips, generating a signal current in a receive coil. As such, MPI is an inductive measurement, measuring the change in magnetic flux resulting from the changing particle magnetization $M'(H(t))$. The shape of $M'(H(t))$ is key to determining the resulting MPI signal, and is highly affected by nanoparticle tracer properties. The ideal shape for $M'(H(t))$ is a delta function, allowing perfect localization of the sample, which corresponds

to the derivative of a step function. In practice, $M(H)$ is often approximated to be the Langevin function.

There are two primary MPI system setups currently in development. The first is f-space (frequency-space) MPI, developed by Philips Hamburg, which first measures a harmonic spectrum system function for each sample and reconstructs the image in frequency space [26]. The second is x-space MPI, developed by Goodwill and Conolly at Berkeley, which measures $M'(H(t))$ directly as the point-spread function (PSF) [89, 90]. The resulting image is then a convolution of the tracer distribution and the PSF. In both methods, the image resolution is defined by the width of the PSF, often described by the full-width at half-maximum (FWHM), and the signal magnitude is defined by the height of the PSF. Resolution is also indicated by the harmonic spectrum (the Fourier transform of $M'(H(t))$); the wider the PSF, the faster the harmonic amplitudes will drop off (see Fig. 2.4). For this reason, ratios of the harmonic amplitudes (for example, the ratio of the 5th to the 3rd harmonic) can be used as a concentration-independent measurement of signal quality.

Magnetic particle spectroscopy (MPS) is functionally a zero-dimensional MPI system that applies an AC field uniformly across the sample and records the inductive signal in a receive coil. With MPS, the PSF of a given sample can be directly extracted. When the particle magnetization is approximated as the Langevin function, the derivative of the magnetization is given by:

$$M'(H(t)) = \frac{n\mu_0\mu^2}{k_B T}\mathcal{L}'(\xi), \tag{2.21}$$

with n as the particle concentration. As expected, the signal scales linearly with concentration. The derivative of the Langevin function is

$$\mathcal{L}'(\xi) = \left(\frac{1}{\xi^2} - \frac{1}{\sinh^2(\xi)}\right) \tag{2.22}$$

for $\xi > 0$, and equal to $1/3$ when $\xi = 0$. $M'(H(t))$ therefore has a maximum at $\xi = 0$, and decreases rapidly for increasing ξ, until it approaches zero in the saturation region. The

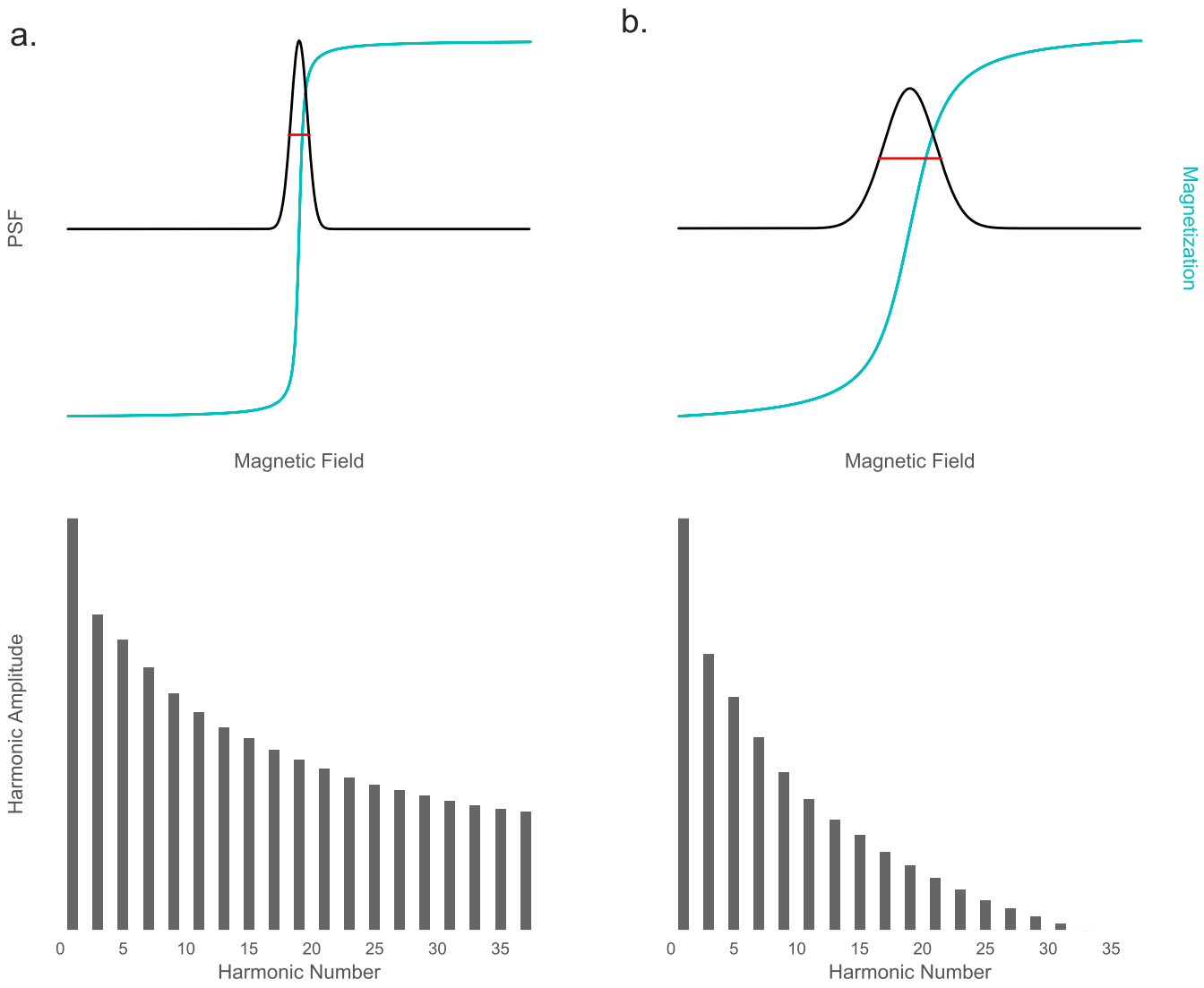

Figure 2.4: Nearly ideal (a.) and more realistic (b.) MPS measurements. Top: Particle magnetization (blue) and resulting PSF (black), with FWHM indicated in red. Bottom: Harmonic spectrum

FWHM here is

$$\Delta\xi^{\mathrm{FWHM}} \approx 4.16 \tag{2.23}$$

The FWHM of $M'(H(t))$, which indicates the image resolution that can be obtained by the sample, is then given by:

$$\Delta H^{\mathrm{FWHM}} = \frac{\Delta\xi^{\mathrm{FWHM}} k_B T}{\mu_0 \mu} = \frac{4.16 k_B T}{\mu_0 \mu}. \tag{2.24}$$

The signal-to-noise ratio (SNR) is indicated by the height of the PSF, which is proportional to the concentration and saturation magnetization, as well as the slope of the magnetization. In this idealized case, the peak of the PSF (where the slope of the magnetization is highest) will be given when the field strength is zero:

$$M'(0) = \frac{n\mu_0\mu^2}{3k_B T} \tag{2.25}$$

The width and height of the PSF (predicting resolution and SNR) are highly affected by properties of the sample itself, the sample environment, and the applied field. To optimize both, highly mondisperse particle sizes are required, as well as strong magnetic gradients.

For the remainder of the discussion, we will examine the one-dimensional case in the x-space formulation, following [52], although the principles apply equally to the Fourier space construction. In a 1D MPI system with linear gradient $-G$ and time-dependent field $H_0(t)$, the magnetic field at a position x will be:

$$H(x,t) = H_0(t) - Gx. \tag{2.26}$$

The location of the field-free point, $x_s(t)$, can be found by solving this equation for $(x,t) = 0$:

$$x_s(t) = G^{-1} H_0(t) \tag{2.27}$$

Or equivalently, the magnetic field at position x can be written in terms of the location of the FFP:

$$H(x,t) = G(x_s(t) - x) \tag{2.28}$$

If we assume a continuous distribution of nanoparticles $\rho(x)$ in the *adiabatic* limit (assuming that the particles' magnetization reaches equilibrium at every time step of the applied field), the sample magnetization follows the Langevin function:

$$M(x,t) = \mu\rho(x)\mathcal{L}\left[\frac{\mu_0\mu}{k_BT}G(x_s(t) - x)\right] \tag{2.29}$$

The magnetization flux can be obtained by integrating over x, which can be written as a convolution:

$$\Phi(t) = -\mu\rho(x) * \mathcal{L}\left[\frac{\mu_0\mu}{k_BT}G(x)\right]_{x=x_s(t)} \tag{2.30}$$

The changing magnetic flux will be recorded by an inductive detector that will have some sensitivity, σ. The received signal will then be:

$$s_{\text{adiab}} = \sigma\frac{d\Phi}{dt} = \sigma\mu\rho(x) * \dot{\mathcal{L}}\left[\frac{\mu_0\mu}{k_BT}Gx\right]_{x=x_s(t)}\frac{\mu_0\mu}{k_BT}G\dot{x}_f(t) \tag{2.31}$$

Defining $\gamma \equiv k_BT/\sigma\mu_0\mu^2G$ and the PSF $h(x) \equiv \dot{\mathcal{L}}(\mu_0\mu Gx/k_BT)$, the signal can be written as a simple spatial convolution (again emphasizing that this is the signal received in the adiabatic limit):

$$s_{\text{adiab}} = \gamma\dot{x}_s(t)\rho(x) * h(x)|_{x=x_s(t)}. \tag{2.32}$$

The velocity of the FFP, $\dot{x}_s(t)$, is simply the scanning rate of the system.

2.3.2 Relaxation effects in image reconstruction

For realistic MPI systems, the adiabatic approximation will not hold. The MNP moments will not align instantaneously with the field; instead, there will be some time required for

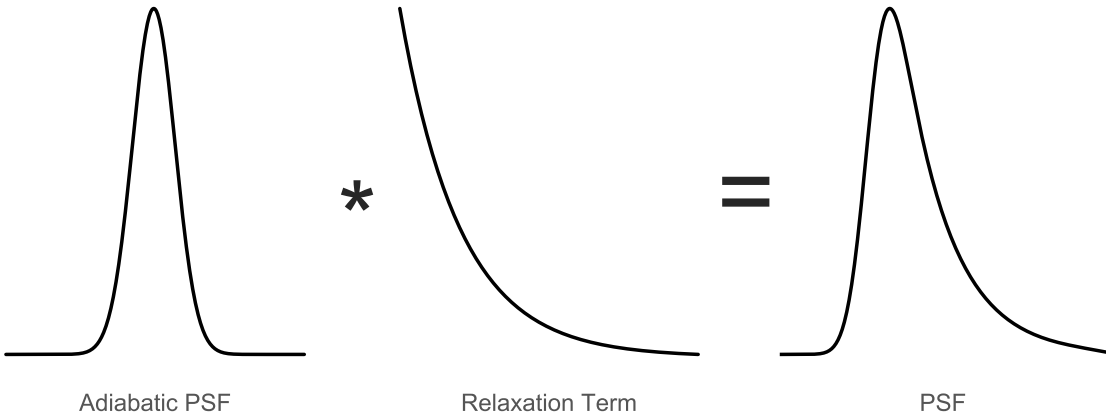

Figure 2.5: Non-adiabatic PSF shown as a convolution of the adiabatic PSF and a relaxation term. The effect is a widening of the PSF, resulting in lower image resolution.

alignment. This relaxation can be modeled using a Debye (exponential) relaxation kernel $r(t)$ [54]:

$$s(t) = s_{\text{adiab}} * r(t) \tag{2.33}$$

Plugging in Eq. 2.32, this becomes:

$$s(t) = \gamma \left(\dot{x}_s(t) \rho(x) * h(x)|_{x=x_s(t)} \right) * r(t). \tag{2.34}$$

This expression for the total signal now contains two convolutions; the inner convolution here is spatial, and the outer convolution is temporal.

The MPI image $\hat{\rho}$ can be generated by mapping the signal equation to the spatial location of the FFP. The resulting image will be a convolution of the adiabatic image with the relaxation kernel:

$$\hat{\rho}(x_s(t)) = \left(\rho(x) * h(x)|_{x=x_s(t)} \right) * r(t) \tag{2.35}$$

If we assume that the FFP is scanned linearly across the sample with a constant scanning rate v_s, then the location of the FFP can be expressed as $x_s(t) = v_s t$, and so $t = x_s(t)/v_s$.

When this is inserted into Eq. 2.35, the total MPI image equation, including relaxation, becomes:

$$\hat{\rho}(x_s(t)) = \left(\rho(x) * h(x)|_{x=x_s(t)}\right) * \left(\frac{1}{v_s}\right) r\left(\frac{x_s(t)}{v_s}\right) \tag{2.36}$$

The convolution is now purely spatial, with unit area $r(x_s(t)/v_s)/v_s$, which allows us to examine the effects of relaxation on the image. As seen in Fig. 2.5, the particle relaxation increases the width of the PSF, which decreases the image resolution, causing additional blur. The Debye exponential relaxation kernel is:

$$r(t) = \frac{1}{\tau} \exp\left[\frac{-t}{\tau}\right] u(t), \tag{2.37}$$

where $u(t)$ is the Heaviside step function (equal to 0 for $t < 0$, and 1 for $t > 0$), which serves the function of "turning on" the relaxation at $t = 0$. As before, τ is the effective relaxation time, which will be a function of particle characteristics as well as properties of the drive field. Again substituting $t = x_s(t)/v_s$, the relaxation kernel becomes:

$$r(t) = \frac{1}{v_s\tau} \exp\left[-\frac{x_s(t)}{v_s\tau}\right] u(x_s(t)) \tag{2.38}$$

Inserting this into Eq. 2.36 gives the MPI image:

$$\hat{\rho}(x_s(t)) = \hat{\rho}_{\text{adiab}}(x_s(t)) * \left(\frac{1}{v_s\tau}\right) \exp\left(-\frac{x_s(t)}{v_s\tau}\right) u(x_s(t)) \tag{2.39}$$

This important result gives an indication of the trade-offs encountered when attempting to optimize the MPI signal. While the adiabatic signal scales with MNP core size, indicating that increasing particle size should uniformly improve SNR and resolution, the relaxation time τ will monotonically increase with particle size, as indicated by Eqs. 2.15, 2.16 and 2.17. Consequently, increasing particle size will also contribute to increased relaxation effects, causing additional blur in the image. This suggests that there will be an optimal particle core size which maximizes signal and resolution; experimentally, the optimal size has been

found to be around 28 nm for magnetite particles [46]. Further theoretical exploration into the optimal nanoparticle size for MPI will be discussed in §5.

We can also look at the resulting signal in terms of the phase lag ϕ between the applied field and the particle response, which is often measured in place of the relaxation time:

$$\tan\phi = \omega\tau \tag{2.40}$$

For small angles, $\tan\phi \approx \phi$. The peak velocity of the FFP will be $v_s = \omega H/G$ [54], so $\tau = \phi H/Gv_s$. Using this, we can rewrite the relaxation kernel as a function of the phase lag:

$$r\left(\frac{x_s(t)}{v_s}\right) = \frac{Gv_s}{\phi H}\exp\left[-\frac{Gx_s(t)}{\phi H}\right]u(x_s(t)). \tag{2.41}$$

This results in the total image equation:

$$\hat{\rho}(x_s(t)) = \hat{\rho}_{\text{adiab}}(x_s(t)) * \frac{G}{\phi H}\exp\left[-\frac{Gx_s(t)}{\phi H}\right]u(x_s(t)) \tag{2.42}$$

Again, we can see the influence of the phase lag on the properties of the reconstructed image; this equation indicates how the phase lag and the drive field amplitude blurs the image. From Eq. 2.42 we can see that larger values of the phase lag or field amplitude will result in more image blur. Because of this, understanding the nature of the relaxation time and resulting phase lag is essential to predicting and improving MPI image resolution. The remainder of this work will focus on understanding and exploring the dynamics of MNPs outside of the adiabatic (equilibrium) regime.

Chapter 3

DEVELOPMENT OF A COMPUTATIONAL NONLINEAR MODEL OF NANOPARTICLE DYNAMICS

3.1 Nonlinear models

The equilibrium and linear models described in the previous chapter are seriously limited in their ability to describe the dynamics of nanoparticles under the fields employed in MPI. MPI relies on nanoparticles reaching magnetic saturation, which results in nonlinear behavior outside of the limits of the Debye model. The frequencies used (on the order of tens of kHz) are high enough that equilibrium conditions cannot be assumed. Furthermore, the AC field amplitudes used for MPI (on the order of tens of mT/μ_0) result in driven nanoparticle rotation rather than simple relaxation. In this chapter we proceed to the exploration of nonequilibrium, nonlinear models of nanoparticle dynamics.

3.1.1 Fokker-Planck equations

The first models we study are the Fokker-Planck equations, which describe the time evolution of the distribution of dipole-moment orientations $W(x,t)$, where $x \equiv \cos\theta$ represents the angle between the moment and the direction of the applied field. The Fokker-Planck equation was first developed by Brown in 1963 [80]. In this interpretation, a nanoparticle's magnetization is represented as an arrow pointing to a spot on the unit sphere. The function $W(\theta,\phi,t)$ describes the probability distribution of moments on the surface of the sphere, given the restriction that the total number of particles must be conserved. When the surface density of the magnetization changes, a surface current $J(\theta,\phi,t)$ will arise. The continuity equation will then be enforced:

$$\frac{\partial W(\theta,\phi,t)}{\partial t} = -\nabla \cdot J(\theta,\phi,t). \tag{3.1}$$

In the absence of thermal fluctuations, J will only depend on the velocity ($d\hat{\mathbf{m}}/dt$) of points. When thermal fluctuations are incorporated, the distribution function acquires a diffusion term, which is manifested as a term proportional to a diffusion constant D. This results in:

$$\frac{\partial W(\theta,\phi,t)}{\partial t} = -\nabla \cdot \left\{ \frac{d\hat{\mathbf{m}}}{dt} - D\nabla \right\} W(\theta,\phi,t). \tag{3.2}$$

The diffusion constant D is determined by the conditions at equilibrium, where there is no applied field and $\partial W/\partial t = 0$. If we first assume only Brownian relaxation, with relaxation time constant τ_B, the velocity of the magnetic moment can be written as a differential equation:

$$\frac{d\hat{\mathbf{m}}}{dt} = \frac{(\hat{\mathbf{m}} \times \boldsymbol{\xi}) \times \hat{\mathbf{m}}}{2\tau_B}. \tag{3.3}$$

Rewriting the numerator using vector identities and inserting the result into Eq. 3.2 results in:

$$\frac{\partial W}{\partial t} = \nabla \cdot \left[D\nabla - \frac{\boldsymbol{\xi} - \hat{\mathbf{m}}(\hat{\mathbf{m}} \cdot \boldsymbol{\xi})}{2\tau_B} \right] W. \tag{3.4}$$

This equation does not have an analytical solution for general directions of the applied field, but if we assume that the applied magnetic field is aligned with the polar axis ($\boldsymbol{\xi} = \xi\hat{\mathbf{z}}$), the dependence on the azimuthal angle will drop out, and Eq. 3.4 simplifies to:

$$\frac{\partial W}{\partial t} = \frac{1}{\sin\theta}\frac{\partial}{\partial\theta}\left[\sin\theta \left(D\frac{\partial W}{\partial\theta} - \frac{\xi}{2\tau_B}\sin\theta W \right) \right]. \tag{3.5}$$

Considering equilibrium conditions ($\partial W/\partial t \to 0$), we find $D = 1/2\tau_B$. We can then substitute $x = \cos\theta$, and so

$$\frac{\partial}{\partial x} = -\frac{1}{\sin\theta}\frac{\partial}{\partial\theta}. \tag{3.6}$$

Eq. 3.5 then becomes [91]:

$$2\tau_B \frac{\partial W}{\partial t} = \frac{\partial}{\partial x}\left[(1-x^2)\left(\frac{\partial W}{\partial x} - \alpha(t)W\right)\right], \tag{3.7}$$

where $\alpha(t) \equiv \mu_0 \mu H(t)/k_B T$. The average magnetization is found by integrating the probability distribution $W(x,t)$ over the unit sphere.

To solve this equation, $W(x,t)$ can be expanded in terms of Legendre polynomials:

$$W(x,t) = \sum_{n=0}^{\infty} a_n(t) P_n(x). \tag{3.8}$$

The coefficients $a_n(t)$ can then be solved recursively, with $a_0(t) = 1/2$:

$$\frac{2\tau_B}{n(n+1)}\frac{\mathrm{d}a_n}{\mathrm{d}t} = -a_n + \alpha(t)\left[\frac{a_{n-1}}{2n-1} - \frac{a_{n+1}}{2n+3}\right]. \tag{3.9}$$

Considering Néel relaxation only, the corresponding Fokker-Planck equation can be derived in a similar way including an anisotropy term [91]:

$$2\tau_N \frac{\partial W}{\partial t} = \frac{\partial}{\partial x}\left[(1-x^2)\left(\frac{\partial W}{\partial x} - \alpha(t)W - \alpha_K x W\right)\right], \tag{3.10}$$

where $\alpha_K = 2KV_c/k_B T$. This form again assumes azimuthal symmetry, with the easy axis aligned with the applied field in the z-direction. Solutions to this equation are again Legendre polynomials with coefficients $a_n(t)$:

$$\begin{aligned}\frac{2\tau_N}{n(n+1)}\frac{\mathrm{d}a_n}{\mathrm{d}t} = -a_n + \alpha(t)\left[\frac{a_{n-1}}{2n-1} - \frac{a_{n+1}}{2n+3}\right] + \alpha_K\left[\frac{(n-1)a_{n-2}}{(2n-3)(2n-1)}\right. \\ \left. + \frac{n a_n}{(2n-1)(2n+1)} - \frac{(n+1)a_n}{(2n+1)(2n+3)} - \frac{(n+2)a_{n+2}}{(2n+3)(2n+5)}\right].\end{aligned} \tag{3.11}$$

These solutions can be generated quickly, and provide some analytical information, which makes the Fokker-Planck formulation a useful tool for studying nonlinear nanoparticle dynamics. However, there are two major limitations to this method which must be emphasized. First, these equations are restricted to exclusively Néel or Brownian relaxation, rather than allowing for a combination of both. For nanoparticles with core diameter ∼25 nm, such as

those typically used for MPI, there is some indication that both mechanisms play an important role [92] and are coupled in a non-trivial way. Second, the Fokker-Planck equation for Néel relaxation assumes that the easy axes of the particles are aligned in the direction of the field. However, this approximation does not generally apply, and the relative angle between the easy axis and the field will significantly affect the nanoparticle dynamics.

Recently, Jürgen Weizenecker derived a Fokker-Planck equation for coupled Néel and Brownian rotation, allowing for full generalization of the direction of the easy axis, moment, and applied field [93]. The results will be presented here, but for the full derivation and additional details, refer to Ref. [93].

The average direction of the particle easy axis is here represented in spherical coordinates as $\hat{\mathbf{n}} = N_\rho \hat{\mathbf{e}}_\rho + N_\theta \hat{\mathbf{e}}_\theta + N_\phi \hat{\mathbf{e}}_\phi$, and the average direction of the particle moment is $\hat{\mathbf{m}} = E_r \hat{\mathbf{e}}_r + E_\vartheta \hat{\mathbf{e}}_\vartheta + E_\varphi \hat{\mathbf{e}}_\varphi$. Similarly, the direction of the magnetic field is $\mathbf{B} = B_\rho \hat{\mathbf{e}}_\rho + B_\theta \hat{\mathbf{e}}_\theta + B_\phi \hat{\mathbf{e}}_\phi$ in spherical coordinates, and $\mathbf{B} = B_1 \hat{\mathbf{e}}_1 + B_2 \hat{\mathbf{e}}_2 + B_3 \hat{\mathbf{e}}_3$ in Cartesian coordinates. It will also be useful to label the direction cosines:

$$u_1 = \cos(\varphi)\sin(\vartheta) \tag{3.12}$$

$$u_2 = \sin(\varphi)\sin(\vartheta) \tag{3.13}$$

$$u_3 = \cos(\vartheta) \tag{3.14}$$

$$p_1 = \cos(\phi)\sin(\theta) \tag{3.15}$$

$$p_2 = \sin(\phi)\sin(\theta) \tag{3.16}$$

$$p_3 = \cos(\theta) \tag{3.17}$$

This system will have only four degrees of freedom, represented by the four angles, since $\hat{\mathbf{m}}$ and $\hat{\mathbf{n}}$ are unit vectors and therefore have fixed unit radial length. The probability density can then be expressed as $W(\vartheta, \varphi, \theta, \phi)$. The fully generalized, coupled Fokker-Planck equation is presented here without derivation:

$$\frac{\partial W}{\partial t} = -\frac{1}{2\tau_B}\frac{1}{\sin(\vartheta)}\frac{\partial}{\partial \vartheta}\left[\frac{2KV_c}{k_BT}E_rE_\vartheta\sin(\vartheta)W - \sin(\vartheta)\frac{\partial W}{\partial \vartheta}\right] - \frac{1}{2\tau_B}\frac{1}{\sin(\vartheta)}\frac{\partial}{\partial \varphi}\left[\frac{2KV_c}{k_BT}E_rE_\varphi W\right]$$

$$- \frac{1}{2\tau_N}\frac{1}{\sin(\theta)}\frac{\partial}{\partial \theta}\left[\frac{M_sV_c}{\alpha k_BT}(\alpha B_\theta - B_\phi)\sin(\theta)W + \frac{2KV_c}{\alpha K_BT}N_\rho(\alpha N_\theta - N_\phi)\sin(\theta)W\right.$$

$$\left. - \sin(\theta)\frac{\partial W}{\partial \theta}\right] - \frac{1}{\tau_N}\frac{1}{\sin(\theta)}\frac{\partial}{\partial \phi}\left[\frac{M_sV_c}{\alpha k_BT}(\alpha B_\phi + B_\theta)W + \frac{2KV_c}{\alpha k_BT}N_\rho(\alpha N_\phi + N_\theta)W\right]$$

$$+ \frac{1}{2\tau_B}\frac{1}{\sin^2(\vartheta)}\frac{\partial^2 W}{\partial \varphi^2} + \frac{1}{2\tau_N}\frac{1}{\sin^2(\theta)}\frac{\partial^2 W}{\partial \phi^2}. \tag{3.18}$$

Here, α is the dimensionless damping constant which has appeared before. Since each component of $\hat{\mathbf{m}}$ and $\hat{\mathbf{n}}$ depends on all four angles, the above equation is fully coupled. To proceed, it will be convenient to introduce the normalized potentials, $\mathcal{N}_K$ and $\mathcal{N}_B$, which describe the internal anisotropy energy and the Zeeman interaction energy, respectively:

$$\mathcal{N}_K = \frac{KV_c}{k_BT}N_\rho^2 = \frac{KV_c}{k_BT}E_r^2 = \frac{KV_c}{k_BT}(p_1u_1 + p_2u_2 + p_3u_3)^2 \tag{3.19}$$

$$\mathcal{N}_B = \frac{M_sV_c}{k_BT}B_\rho = \frac{M_sV_c}{k_BT}(B_1p_1 + B_2p_2 + B_3p_3). \tag{3.20}$$

The coupled Fokker-Planck equation can now be rewritten as:

$$\begin{aligned}\frac{\partial W}{\partial t} = &\frac{1}{2\tau_B}\left[\frac{1}{\sin(\vartheta)}\frac{\partial}{\partial\vartheta}\left(\sin(\vartheta)\frac{\partial W}{\partial\vartheta}\right)+\frac{1}{\sin^2(\vartheta)}\frac{\partial^2 W}{\partial\varphi^2}\right]\\ &+\frac{1}{2\tau_N}\left[\frac{1}{\sin(\theta)}\frac{\partial}{\partial\theta}\left(\sin(\theta)\frac{\partial W}{\partial\theta}\right)+\frac{1}{\sin^2(\theta)}\frac{\partial^2 W}{\partial\phi^2}\right]\\ &-\frac{1}{2\tau_B}W\left[\frac{1}{\sin(\vartheta)}\frac{\partial}{\partial\vartheta}\left(\sin(\vartheta)\frac{\partial \mathcal{N}_K}{\partial\vartheta}\right)+\frac{1}{\sin^2(\vartheta)}\frac{\partial^2 \mathcal{N}_K}{\partial\varphi^2}\right]\\ &-\frac{1}{2\tau_N}W\left[\frac{1}{\sin(\theta)}\frac{\partial}{\partial\theta}\left(\sin(\theta)\frac{\partial \mathcal{N}_K}{\partial\theta}\right)+\frac{1}{\sin^2(\theta)}\frac{\partial^2 \mathcal{N}_K}{\partial\phi^2}\right]\\ &-\frac{1}{2\tau_N}W\left[\frac{1}{\sin(\theta)}\frac{\partial}{\partial\theta}\left(\sin(\theta)\frac{\partial \mathcal{N}_B}{\partial\theta}\right)+\frac{1}{\sin^2(\theta)}\frac{\partial^2 \mathcal{N}_B}{\partial\phi^2}\right]\\ &-\frac{1}{2\tau_N}\left[\frac{\partial \mathcal{N}_B}{\partial\theta}\frac{\partial W}{\partial\theta}+\frac{1}{\sin^2(\theta)}\frac{\partial \mathcal{N}_B}{\partial\phi}\frac{\partial W}{\partial\phi}\right]-\frac{1}{2\tau_B}\left[\frac{\partial \mathcal{N}_K}{\partial\vartheta}\frac{\partial W}{\partial\vartheta}+\frac{1}{\sin^2(\vartheta)}\frac{\partial \mathcal{N}_K}{\partial\varphi}\frac{\partial W}{\partial\varphi}\right]\\ &-\frac{1}{2\tau_N}\left[\frac{\partial \mathcal{N}_K}{\partial\theta}\frac{\partial W}{\partial\theta}+\frac{1}{\sin^2(\theta)}\frac{\partial \mathcal{N}_K}{\partial\phi}\frac{\partial W}{\partial\phi}\right]+\frac{1}{2\tau_N}\frac{1}{\alpha}\frac{1}{\sin(\theta)}\left[\frac{\partial \mathcal{N}_B}{\partial\phi}\frac{\partial W}{\partial\theta}-\frac{\partial \mathcal{N}_B}{\partial\theta}\frac{\partial W}{\partial\phi}\right]\\ &+\frac{1}{2\tau_N}\frac{1}{\alpha}\frac{1}{\sin(\theta)}\left[\frac{\partial \mathcal{N}_K}{\partial\phi}\frac{\partial W}{\partial\theta}-\frac{\partial \mathcal{N}_K}{\partial\theta}\frac{\partial W}{\partial\phi}\right].\end{aligned} \tag{3.21}$$

To find solutions to this equation, we can perform a series expansion into spherical harmonics:

$$W(\vartheta,\varphi,\theta,\phi)=\sum_{l=0}^{\infty}\sum_{m=-l}^{l}\sum_{r=0}^{\infty}\sum_{q=-r}^{r}D_{l,r}^{m,q}P_l^m(\vartheta)\mathrm{e}^{im\varphi}P_r^q(\theta)\mathrm{e}^{iq\phi}:=\sum_{l,m,r,q}D_{l,r}^{m,q}X_l^m(\vartheta,\varphi)Z_r^q(\theta,\phi). \tag{3.22}$$

Here, the expansion coefficients are represented by $D_{l,r}^{m,q}$, and P_l^m and P_r^q are the Legendre polynomials associated with the spherical harmonics X_l^m and Z_r^q. The variables l and m are associated with the angular momentum of the particle axis, while r and q describe the angular momentum of the particle moment. It will also be necessary to calculate the derivatives of the spherical harmonics, which will have the effect of raising and lowering the indices, represented by Δ (e.g., $l\to l+\Delta l$):

$$\sum_{l,m,r,q}\frac{\partial D_{l,r}^{m,q}}{\partial t}X_l^m Z_r^q=\sum_{l,m,r,q}D_{l,r}^{m,q}\sum_{\Delta l,\Delta m,\Delta r,\Delta q}g_{\Delta r,\Delta q}(r,q)f_{\Delta l,\Delta m}(l,m)X_{l+\Delta l}^{m+\Delta m}Z_{r+\Delta r}^{q+\Delta q}. \tag{3.23}$$

Since acting with an operator, such as taking the derivative, can only change the indices by one, our system will be simplified significantly; the operators in the Fokker-Planck equation act a maximum of two times. The full solution to the Fokker-Planck equation can then be written as a system of differential equations:

$$\frac{\mathrm{d}D_{L,R}^{M,Q}}{\mathrm{d}t} = \sum_{\Delta l=-2}^{2}\sum_{\Delta m=-2}^{2}\sum_{\Delta r=-2}^{2}\sum_{\Delta q=-2}^{2} f_{\Delta l,\Delta m}(L,M)g_{\Delta r,\Delta q}(R,Q)D_{L-\Delta l,R-\Delta r}^{M-\Delta m,Q-\Delta q}, \tag{3.24}$$

where $f_{\Delta l,\Delta m}(L,M)g_{\Delta r,\Delta q}(R,Q)$ represent matrix elements. In the fully general case, there will be 81 coefficients per row, with a total of 131 terms. Since we are only interested in systems where the magnetic field is applied along a single direction, here the z-direction, we can simplify this significantly by imposing azimuthal symmetry, which will send all $m, q = 0$. The system of differential equations then becomes:

$$\frac{\mathrm{d}D_{L,R}^{0,0}}{\mathrm{d}t} = \sum_{\Delta l=-2}^{2}\sum_{\Delta r=-2}^{2} f_{\Delta l,\Delta 0}(L,0)g_{\Delta r,\Delta 0}(R,0)D_{L-\Delta l,R-\Delta r}^{0,0}. \tag{3.25}$$

Now, the matrix elements $f_{\Delta l,\Delta 0}(L,0)g_{\Delta r,\Delta 0}(R,0)$ will contain only 11 coefficients with 28 total terms per row, and are listed in Appendix A. To generate solutions, the matrix must be truncated, which is done by setting a maximum value for L and R. For simplicity, we will choose the maximum value for both L and R to be represented by L_{max}. The matrix represented by $f_{\Delta l,\Delta 0}(L,0)g_{\Delta r,\Delta 0}(R,0)$ will have dimension $N \times N$, where $N = L_{max}^2$. In a case of $L_{max} = 25$, for example, we will have 625 coupled differential equations to solve.

The rows of the matrix correspond to elements of D_{LR}. With $L_{max} = 3$, the rows are labeled D_{00}, D_{01}, D_{02}, D_{10}, D_{11}, D_{12}, D_{20}, D_{21}, D_{22}, and so on. Element $D_{00} = 1/(4\pi)^2$, and the first row of the matrix will contain only zeros. Once the matrix is generated, then, we can eliminate the first row and multiply the first column by D_{00} to become a separate vector $\mathbf{a}$. Matrix $\mathbf{M}$ is then $(N-1)\times(N-1)$, starting with row D_{01}, and the equation can be written:

$$\frac{\mathrm{d}\mathbf{D}}{\mathrm{d}t} = \mathbf{M}\mathbf{D} + \mathbf{a}. \tag{3.26}$$

Solutions for **D** were generated using the *odeint* solver from the SciPy package in Python (code shown in Appendix B). The particles were initialized to have zero average magnetization, and convergence was observed with L_{max} above 25. Time steps were chosen to be 100 ns; decreasing the time step below 100 ns did not have a meaningful effect on the results. Once the elements of **D** are determined, we can extract the relevant physical properties, in particular, the average value of the particle magnetization in the z-direction:

$$\begin{aligned}
\langle M_z \rangle &= M_s \langle E_3 \rangle \\
&= M_s \langle \cos(\theta) \rangle \\
&= M_s \langle X_1^0 Z_0^0 \rangle \\
&= M_s \int\int\int\int X_1^0 Z_0^0 W(\vartheta, \varphi, \theta, \phi)\, \mathrm{d}\Omega\, \mathrm{d}\Omega' \\
&= M_s \sum_{l,m,r,q} D_{l,r}^{m,q} \int\int X_1^0 X_l^m \, \mathrm{d}\Omega \int\int Z_0^0 Z_r^q \, \mathrm{d}\Omega' \\
&= M_s \frac{(4\pi)^2}{3} D_{1,0}^{0,0}.
\end{aligned} \tag{3.27}$$

The time evolution of $D_{1,0}^{0,0}$ will therefore represent the average particle magnetization over time.

While the fully general coupled Fokker-Planck equation itself is quite complicated, once azimuthal symmetry is imposed and the required matrix is generated, solutions can be generated fairly easily and quickly, although the time required is highly dependent on L_{max}, as the number of coupled differential equations scales as L_{max}^2. Results will be presented and discussed in §3.4, where they will be compared to results from other computational methods developed later in the chapter.

3.1.2 Effective field model

For relatively low applied fields, another useful model, that we will mention briefly but not discuss in detail, comes from an approximation to the Fokker-Planck equation, and is called the effective field model. In this model, the frequency of oscillation is assumed to be low enough so the distribution remains in the Maxwell-Boltzmann (equilibrium) form, so that

$M(t) = M_s\mathcal{L}(\xi_e(t))$, where ξ_e is an effective field. This is able to produce nonlinear dynamics for the MNP magnetization [94]:

$$\frac{\mathrm{d}M(t)}{\mathrm{d}t} = -\frac{M(t)}{\tau}\left(1 - \frac{\xi(t)}{\xi_e(t)}\right), \tag{3.28}$$

where τ is again the effective relaxation time. Here, the effective field can be calculated at every time step using the inverse Langevin function, and will change in time but not necessarily be equal to the applied cosinusoidal field. This model is similarly limited in that it assumes that MNPs experience pure magnetic relaxation, rather than driven magnetic reversal. Consequently, this approximation, as well as the Debye model, diverges when the field applied is large (greater than $4K/3M_s$).

3.1.3 Stochastic Langevin equations

To investigate the dynamics of particles which experience both Néel and Brownian relaxation, we implement stochastic simulations of Langevin equations. Computational simulations are used to model the magnetic response of nanoparticles exposed to an external magnetic field. The nanoparticles are assumed to be spherical and single-domain, and so can be characterized by a single magnetic moment, as the sizes of particles that we typically consider for biosensing applications (5-30 nm in diameter) are well within the superparamagnetic limit [75]. The size of the nanoparticles as well as the anisotropy constants will vary according to a log-normal distribution, as is typically assumed [95]:

$$g(x) = \frac{1}{\sqrt{2\pi}\sigma x}\exp\left(-\frac{\ln(x/x_0)^2}{2\sigma^2}\right), \tag{3.29}$$

where x_0 is the median value and σ is the distribution shape parameter. Since some degree of particle agglomeration is common for nanoparticles in liquid suspensions, and particularly in biological environments [96], inclusion of these distributions is necessary to approximate potential agglomeration effects, as well as natural variation among particles from the fabrication process, as observed by TEM images [95,97]. As nanoparticles are typically coated with a non-magnetic coating as functionalization for specific biomedical purposes, we differentiate

between the magnetic core diameter and the hydrodynamic diameter. The particles are able to rotate via both Brownian and Néel rotation. The internal magnetization direction $\hat{\mathbf{m}}$ will rotate according to the Landau-Lifshitz-Gilbert equation. This differential equation will be coupled with the differential equation describing the general torque exerted on the easy axis $\hat{\mathbf{n}}$ of the particle [83, 98]. The coupled equations for a single particle are as follows:

$$\frac{\mathrm{d}\hat{\mathbf{m}}}{\mathrm{d}t} = \frac{\gamma}{1+\alpha^2}\left(\mathbf{H} + \alpha\hat{\mathbf{m}} \times \mathbf{H}\right) \times \hat{\mathbf{m}} \tag{3.30}$$

$$\frac{\mathrm{d}\hat{\mathbf{n}}}{\mathrm{d}t} = \frac{\boldsymbol{\theta}}{6\eta V_{\mathrm{h}}} \times \hat{\mathbf{n}}, \tag{3.31}$$

where γ is the electron gyromagnetic ratio in bulk iron [99], α is the damping coefficient, η is the viscosity of the surrounding medium, and V_{h} is the hydrodynamic volume. The effective magnetic field, $\mathbf{H}$, and the effective torque, $\boldsymbol{\theta}$, are determined from the total particle energy:

$$U = -\mu\mu_0\hat{\mathbf{m}} \cdot \mathbf{H}_{\mathrm{app}} - KV_{\mathrm{c}}(\hat{\mathbf{m}} \cdot \hat{\mathbf{n}})^2 - \sum_i \frac{\mu\mu_i\mu_0}{4\pi r_i^3}\left(3(\hat{\mathbf{m}} \cdot \hat{\mathbf{r}}_i)(\hat{\mathbf{m}}_i \cdot \hat{\mathbf{r}}_i) - \hat{\mathbf{m}} \cdot \hat{\mathbf{m}}_i\right), \tag{3.32}$$

where μ represents the magnitude of the particle's magnetic moment, equal to $M_{\mathrm{s}}V_{\mathrm{c}}$, where M_s is the saturation magnetization and V_c is the core volume. K is the effective anisotropy constant, which includes magnetocrystalline and shape anisotropy. Subscript i denotes particle number. The first term represents the Zeeman interaction with the applied field, $\mathbf{H}_{\mathrm{app}}$, the second term is the energy contribution from the effective particle anisotropy, and the third term represents the magnetic dipole-dipole interaction with all other particles i in the simulation. The vector $\mathbf{r}$ pointing to the center of each particle has magnitude r and direction $\hat{\mathbf{r}}$. For applications we are considering, the applied field is sinusoidal, with amplitude H_0 and angular frequency ω. We apply the field in the z-direction, and so:

$$\mathbf{H}_{\mathrm{app}} = H_0 \cos(\omega t)\hat{\mathbf{z}} \tag{3.33}$$

The effective magnetic field and torque can then be found by taking derivatives of the energy, and adding thermal fluctuations:

$$\mathbf{H} = -\frac{1}{\mu_0 \mu}\frac{\partial U}{\partial \hat{\mathbf{m}}} + \mathbf{H}_{\text{th}} = \mathbf{H}_{\text{app}} + \frac{2KV_{\text{c}}}{\mu}(\hat{\mathbf{m}}\cdot\hat{\mathbf{n}})\hat{\mathbf{n}} + \sum_i \frac{\mu_i \mu_0}{4\pi r_i^3}\left(3(\hat{\mathbf{m}}_i\cdot\hat{\mathbf{r}}_i)\hat{\mathbf{r}}_i - \hat{\mathbf{m}}_i\right) + \mathbf{H}_{\text{th}} \quad (3.34)$$

$$\boldsymbol{\theta} = \frac{\partial U}{\partial \hat{\mathbf{n}}} \times \hat{\mathbf{n}} + \boldsymbol{\theta}_{\text{th}} = -2KV_{\text{c}}(\hat{\mathbf{m}}\cdot\hat{\mathbf{n}})(\hat{\mathbf{m}}\times\hat{\mathbf{n}}) + \boldsymbol{\theta}_{\text{th}} \quad (3.35)$$

$\mathbf{H}_{\text{th}}$ represents the fluctuation field, which accounts for microscopic effects (interactions with nuclear spins, phonons, etc.) that cause fluctuations of the orientation of the magnetic moment. It is generally assumed [83, 100, 101] that this fluctuation field is a Gaussian stochastic process whose components have the following statistical properties:

$$\left\langle \mathbf{H}_{\text{th}}^i(t) \right\rangle = 0 \quad (3.36)$$

$$\left\langle \mathbf{H}_{\text{th}}^i(t)\mathbf{H}_{\text{th}}^j(t') \right\rangle = \frac{2k_B T}{\gamma\mu}\frac{1+\alpha^2}{\alpha}\delta_{ij}\delta(t-t'), \quad (3.37)$$

where k_B is Boltzmann's constant and T is the temperature. Similarly, $\boldsymbol{\theta}_{\text{th}}$ represents a thermally-generated torque with statistical properties:

$$\left\langle \boldsymbol{\theta}_{\text{th}}^i(t) \right\rangle = 0 \quad (3.38)$$

$$\left\langle \boldsymbol{\theta}_{\text{th}}^i(t)\boldsymbol{\theta}_{\text{th}}^j(t') \right\rangle = 12k_B T\eta V_{\text{h}}\delta_{ij}\delta(t-t'). \quad (3.39)$$

The presence of these fluctuation terms are the main reason why Monte Carlo methods are necessary to accurately predict the dynamics of nanoparticles, and why analytical methods typically have major limitations.

3.2 Integration of stochastic processes

Eqs. 3.30 and 3.31 are coupled stochastic Langevin equations which now must be integrated. Langevin equations are stochastic differential equations which describe the time evolution of physical variables, separated into macroscopic (slowly varying) variables and microscopic (fast) variables [102]. Here, the macroscopic variables include the magnetic

moment, axis, and applied field, and the microscopic variables are thermally generated random forces which must be calculated from a probability distribution. Langevin stochastic processes are assumed to be uncorrelated in time, based on a memoryless random walk (i.e. a Markov process). Solving equations with such a stochastic term is complicated, because the resulting trajectory is not differentiable.

A typical stochastic differential equation for a variable X_t in one dimension, with stochastic process λ_t, is written:

$$\frac{\mathrm{d}X_t}{\mathrm{d}t} = f(X_t, t) + g(X_t, t)\lambda_t \tag{3.40}$$

which has the solution:

$$X_t = \int f(X_t, t)dt + \int g(X_t, t)\lambda_t dt. \tag{3.41}$$

The function $f(X_t, t)$ is called the drift term, and the function $g(X_t, t)$ is the diffusion term. As the diffusion term depends on X_t, which is then multiplied by the stochastic term λ_t, the noise here is referred to as multiplicative (rather than additive). We assume that the mean of λ_t is zero (otherwise slow changes in λ_t could be absorbed into the deterministic function). The distribution of the noise term is assumed to be Markovian, with a flat power spectrum (i.e. white noise). This assumption is valid in our case because the timescale of molecular collisions are orders of magnitude smaller than the timescales of nanoparticle rotations. A 1D white noise process is defined by:

$$\langle \lambda_t \rangle = 0 \tag{3.42}$$

$$\langle \lambda_t \lambda_{t+\Delta t} \rangle = \delta(\Delta t) \tag{3.43}$$

The central limit theorem tells us that this noise distribution should converge to a Gaussian distribution. A Wiener process is defined as the integral of a Gaussian white noise process:

$$W_t = \int \lambda_t dt \tag{3.44}$$

We can then write the differential equation in terms of a Wiener process:

$$\mathrm{d}X_t = f(X_t, t)dt + g(X_t, t)\,\mathrm{d}W_t \tag{3.45}$$

A Weiner process is a continuous-time stochastic process (often simply called Brownian motion), defined as having beginning value W_0 at $t = 0$ equal to 0. The increments $\Delta W_t = W_t - W_{t+\Delta t}$ are Gaussian and independent, so:

$$\langle \Delta W_t \Delta W_s \rangle = 0 \tag{3.46}$$

The variance of each increment is equal to Δt, and the mean of each increment is zero:

$$\langle \Delta W_t \rangle = 0 \tag{3.47}$$

The standard deviation, then, is proportional to the square root of the measured time interval, $\sqrt{\Delta t}$.

There are two integration methods for stochastic calculus, both based on generalizations of the Riemann integral, where the integral is broken up into a series of rectangles and then summed. Itō calculus, where the integral is evaluated at the minimum value of each rectangle, is typically used in mathematics and in finance applications. Stratonovich calculus, where the integral is evaluated at the midpoint of each rectangle, is used when white noise can be approximated [103], which is the case here. Therefore, from here on we will exclusively use the Stratonovich interpretation, which is indicated by the circle notation:

$$\mathrm{d}X_t = f(X_t, t)\,\mathrm{d}t + g(X_t, t) \circ \mathrm{d}W_t \tag{3.48}$$

A general first-order solver for a stochastic differential equation is the Euler-Maruyama scheme:

$$X_{t+\Delta t} = X_t + f(X_t, t)\Delta t + g(X_t, t)\Delta W_t \tag{3.49}$$

The next higher order solver is the adapted Heun scheme:

$$X_{t+\Delta t} = X_t + \frac{1}{2}\left[f(X_t, t) + f(\bar{X}_{t+\Delta t}, t + \Delta t)\right]\Delta t + \frac{1}{2}\left[g(X_t, t) + g(\bar{X}_{t+\Delta t}, t + \Delta t)\right]\Delta W_t, \tag{3.50}$$

where here the predictor $\bar{X}_{t+\Delta t}$ is calculated with a first-order solver (such as the Euler-Maruyama scheme, Eq. 3.49). The midpoint of each rectangle is found by averaging the Euler-Maruyama solution with the initial conditions, and the final state is calculated by again evolving the midpoint value with the Euler-Maruyama solution.

We now have the necessary tools to integrate Eqs. 3.30 and 3.31, using the Stratanovitch-Heun scheme, following others [92, 100], which can properly account for the stochastic terms in the white-noise limit. The differential equations can then be written in the form:

$$\mathrm{d}\hat{\mathbf{m}} = f_m(\hat{\mathbf{m}}, \hat{\mathbf{n}}, t)\,\mathrm{d}t + g_m(\hat{\mathbf{m}}, \hat{\mathbf{n}}, t)\,\mathrm{d}\mathbf{W}_m \tag{3.51}$$

$$\mathrm{d}\hat{\mathbf{n}} = f_n(\hat{\mathbf{m}}, \hat{\mathbf{n}}, t)\,\mathrm{d}t + g_n(\hat{\mathbf{m}}, \hat{\mathbf{n}}, t)\,\mathrm{d}\mathbf{W}_n \tag{3.52}$$

This is really a set of six equations, as the relevant variables involved are three dimensional vectors. The stochastic fluctuations are assumed to be a Wiener process, represented by $\mathbf{W}$, with Cartesian components uncorrelated and independent. For numerical integrations, we choose a time step Δt which must be small enough to ensure convergence. The fluctuation term $\Delta\mathbf{W}$ then is a vector of normally distributed variables with mean zero, multiplied by $\sqrt{\Delta t}$ and the variance. The variance for $\mathbf{W}_m$ is $2kT(1+\alpha^2)/\gamma\mu\alpha$ from Eq. 3.37, and $12kT\eta V_{\mathrm{h}}$ for $\mathbf{W}_n$ from Eq. 3.39. The predictors for $\hat{\mathbf{m}}$ and $\hat{\mathbf{n}}$, calculated using the Euler-Maruyama scheme, are:

$$\bar{\mathbf{m}}(t + \Delta t) = \hat{\mathbf{m}}(t) + f_m(\hat{\mathbf{m}}, \hat{\mathbf{n}}, t)\Delta t + g_m(\hat{\mathbf{m}}, \hat{\mathbf{n}}, t)\Delta\mathbf{W}_m \tag{3.53}$$

$$\bar{\mathbf{n}}(t+\Delta t) = \hat{\mathbf{n}}(t) + f_n(\hat{\mathbf{m}}, \hat{\mathbf{n}}, t)\Delta t + g_n(\hat{\mathbf{m}}, \hat{\mathbf{n}}, t)\Delta \mathbf{W}_n. \tag{3.54}$$

We can then numerically integrate, following the Stratonovich-Heun scheme:

$$\mathbf{m}(t+\Delta t) = \hat{\mathbf{m}}(t) + \frac{f_m(\hat{\mathbf{m}}, \hat{\mathbf{n}}, t) + f_m(\bar{\mathbf{m}}, \bar{\mathbf{n}}, t+\Delta t)}{2}\Delta t + \frac{g_m(\hat{\mathbf{m}}, \hat{\mathbf{n}}, t) + g_m(\bar{\mathbf{m}}, \bar{\mathbf{n}}, t+\Delta t)}{2}\Delta \mathbf{W}_m \tag{3.55}$$

$$\mathbf{n}(t+\Delta t) = \hat{\mathbf{n}}(t) + \frac{f_n(\hat{\mathbf{m}}, \hat{\mathbf{n}}, t) + f_n(\bar{\mathbf{m}}, \bar{\mathbf{n}}, t+\Delta t)}{2}\Delta t + \frac{g_n(\hat{\mathbf{m}}, \hat{\mathbf{n}}, t) + g_n(\bar{\mathbf{m}}, \bar{\mathbf{n}}, t+\Delta t)}{2}\Delta \mathbf{W}_n. \tag{3.56}$$

The resulting vectors $\mathbf{m}$ and $\mathbf{n}$ do not necessarily have unit magnitude, so after each integration step they must be normalized. The components of $\mathbf{W}$ are randomly generated at each iteration, and so this can be called a Monte Carlo simulation. It should be noted that by ignoring the second equation and solving only for the first (the magnetic moment), immobilized particles can be simulated as well, which rotate only via Néel relaxation.

3.3 Simulation details

3.3.1 Simulation process

Nanoparticle dynamics are simulated according to Eqs. 3.55 and 3.56. The easy axis ($\hat{\mathbf{n}}$) and magnetic moment ($\hat{\mathbf{m}}$) of each particle are initialized separately to a random orientation. The particles are then allowed to thermalize for a certain number of time steps (one fifth of the total time steps used for the main simulation). This allows the magnetic moments to partially align with the easy axes at the natural energy minima. The oscillating field is then turned on, and the magnetic response recorded.

A number of parameters must be specified as inputs to the simulation. These include the total number of time steps for the simulation, N, the number of total particles to be simulated I, and the number of total repetitions of the simulation, X, to be averaged over. Properties

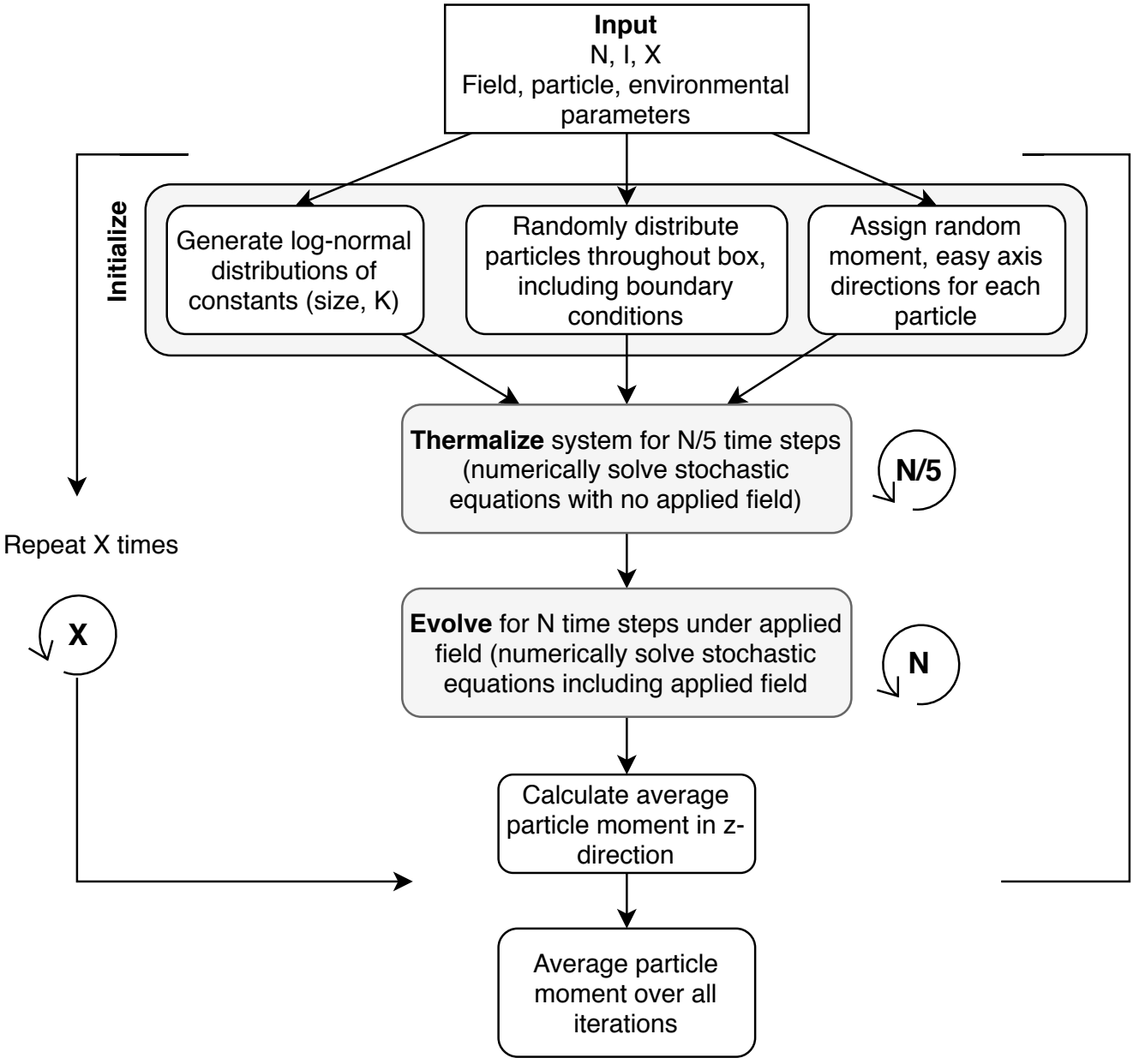

Figure 3.1: Simulation process.

of the applied AC field must be input, such as applied field amplitude H_0, frequency f, and the number of complete field cycles (an integer), n_{cycs}. Particle properties must be specified, such as core diameter d_C, hydrodynamic diameter d_H (or equivalently, coating size to be added to the core diameter), size distribution parameter σ, effective anisotropy K, anisotropy distribution parameter σ_K, and dimensionless damping constant α. The concentration, C, should also be specified, as number of particles per unit volume. Finally, environmental properties must be specified, such as temperature T and viscosity η. Several of these parameters will be discussed in detail later in this chapter.

The implementation of the numerical solver requires discretized time steps, of step size $\Delta t = \frac{1}{Nf}$, where N is the total number of time steps and f is the frequency of the applied field. After $t = N\Delta t$ one full cycle has been traced, i.e. the magnetic field has passed through one full period of oscillation. For convergent solutions, $\Delta t \leq 10^{-8}$ s must hold, implying $N \geq 10\ 000$ for fields on the order of 10 kHz.

The program records the average particle magnetization in the z-direction (the direction of the applied field) for each time step. The entire simulation is repeated X times, with new initializations each time. The output, then, is a vector $\langle m_z(t) \rangle$, related to the corresponding field values $H(t)$ (or equivalently, time steps n):

$$\langle m_z(t) \rangle = \frac{1}{X} \sum_{j=1}^{X} \left(\frac{1}{I} \sum_{i=1}^{I} m_{z,i}(H(t)) \right)_j \tag{3.57}$$

where again I is the total number of particles. For certain applications, it is also desirable to calculate the magnetic susceptibility as a function of particle frequency and field. This can be implemented in the program by performing the following calculation, where n is each time step and $\omega = 2\pi f$:

$$\chi'(\omega, T) = \frac{1}{H_0 N} \sum_{n=1}^{N} \langle m_{n,z} \rangle \cos(\omega n \Delta t) \tag{3.58}$$

$$\chi''(\omega, T) = \frac{1}{H_0 N} \sum_{n=1}^{N} \langle m_{n,z} \rangle \sin(\omega n \Delta t) \tag{3.59}$$

Since we have set the number of field cycles to be an integer, this ensures $N = 2\pi n_{\text{cyc}}/\omega\Delta t$. For susceptibility calculations, a range of temperatures and frequencies can be looped over in order to obtain a temperature- or frequency-dependent magnetic susceptibility profile.

The simulation process, outlined in Fig. 3.1, is:

1. From d_C and σ, an array of length I of particle core volumes V_c is constructed, calculated from generating individual particle diameters from a log-normal distribution. A similar array is generated corresponding to particle hydrodynamic volumes V_H, calculated from d_H. Similarly, an array of length I is generated from a log-normal distribution of anisotropy values K and σ_K.

2. Two $I \times 3 \times N$ matrices $\mathbf{M}_I$ and $\mathbf{N}_I$ are generated, one corresponding to particle moments $\hat{\mathbf{m}}$ and one corresponding to particle axes $\hat{\mathbf{n}}$. The first dimension represents each individual particle, and the second dimension corresponds to the three Cartesian coordinates. The first entry ($N = 0$) for each particle in each matrix is initialized to a random unit vector.

3. A cubic box of length $L = \sqrt[3]{I/C}$ is created, as well as an $I \times 3$ matrix, corresponding to the particle positions. Each particle is then randomly distributed within the box, achieved by generating a random number from $(0, L)$ for each of the three Cartesian coordinates for each particle. The average interparticle distance can be approximated by $r_{\text{avg}} = \sqrt{3}/\sqrt[3]{C}$. Periodic boundary conditions are enforced, so as to eliminate distorting boundary effects. To achieve this, any particles within $r_{\text{avg}}/3$ of each wall are duplicated and copied to the outside of the opposite wall. This process occurs first in the x-direction, then the y-direction (including the previously copied particles), and finally the z-direction, so that the boundaries are fully represented in three dimensional space.

4. Equations are numerically solved, repeating over $N/5$ iterations, with $H_{\text{app}} = 0$. Each iteration fills in a new entry to the particle moment and particle axis matrices, corre-

sponding to each time step. This allows the system to relax to an equilibrium state. After $N/5$ iterations, the $N/5$-th entry in both matrices is copied to $N = 0$, so that the new starting state is now the final state of the thermalization process.

5. The Langevin equations are numerically solved, iterating over N time steps, with H_{app} set to the desired AC field.

6. The z-component of $\mathbf{M}_I$ averaged over the first axis, resulting in the average particle moment in the z-direction for each time step. The result is saved in a new matrix.

7. Steps 2-5 are repeated X times to increase statistical precision.

8. The resulting matrices are averaged over all X, giving the average particle moment over all iterations at each time step.

9. Optional: Steps 2-8 are repeated for different temperatures or frequencies, and the magnetic susceptibility profile is calculated according to Eqs. 3.58 and 3.59.

The computer system memory required to run this simulation scales with N and I, and the run time scales with N and X. For non-interacting particles (if dipole interactions are turned off), increasing I is equivalent to increasing X. Consequently, to optimize run time, I should be maximized to utilize the maximum memory (this will be dependent on the computational capacity of the system), and then X should be further increased to reduce noise. In practice, these simulations are run on 20 parallel nodes on the UW HYAK supercomputing cluster, and typical parameters chosen are $N = 10\ 000$ per cycle, $I = 2000$, and $X = 10$. When the dipole interactions between particles are turned on, then the run time also scales with I^2, and so in that case a lower I and correspondingly higher X should be used.

3.3.2 Discussion of parameters

While certain parameters like the strength of the external magnetic field can be easily controlled and studied, the magnetocrystalline anisotropy of the particles is a feature that is

still not well understood, but which has a large impact on nanoparticle relaxation. The particle anisotropy establishes preferred orientations of the magnetic moment within the particle, which then determines the energy barrier between those orientations, influencing the relaxation dynamics of the particles [104]. Understanding and measuring the anisotropy is challenging. As a first order approximation, to study the underlying physics of reversal, we can assume that the particles have a uniaxial magnetocrystalline structure, with a single easy axis. We can also make the approximation that the particles are noninteracting, as the many-body effects of interparticle magnetic interaction can be complex. This provides us with a basic starting model. The anisotropy energy, per unit volume, of a uniaxial particle is:

$$E_{\text{ani}}^{\text{u}}/V_{\text{c}} = -K_{\text{eff}}(\hat{\mathbf{m}} \cdot \hat{\mathbf{n}})^2, \tag{3.60}$$

where K_{eff} is an effective anisotropy constant that includes shape, surface, and magnetocrystalline anisotropy. More explicitly, the effective anisotropy can be broken down into bulk magnetocrystalline anisotropy, K_B, which will be a property of the material, and surface anisotropy, K_S, incorporating a size dependence (where D is equal to the particle core diameter), as well as a shape parameter ϕ:

$$K_{\text{eff}} = K_B + \frac{6\phi K_S}{D} \tag{3.61}$$

For perfectly spherical particles ϕ is equal to 1. The best fit to data (e.g. Fig. 3.2) uses values of $K_B = 13$ kJ/m^3 and $K_S = 5.1 \times 10^{-5}$ kJ/m^3 , or equivalently $K_S = 3.9 \times 10^{-5}$ kJ/m^3 with $\phi = 1.3$, which is consistent with expected results [105].

As magnetite has an inverse cubic spinel crystal structure, the magnetocrystalline anisotropy should be inherently cubic. If surface or shape anisotropy dominates in any particular direction, the anisotropy can be assumed to be uniaxial. However, for approximately spherical particles, cubic anisotropy may be a more accurate description. Cubic anisotropy energy can be expressed as:

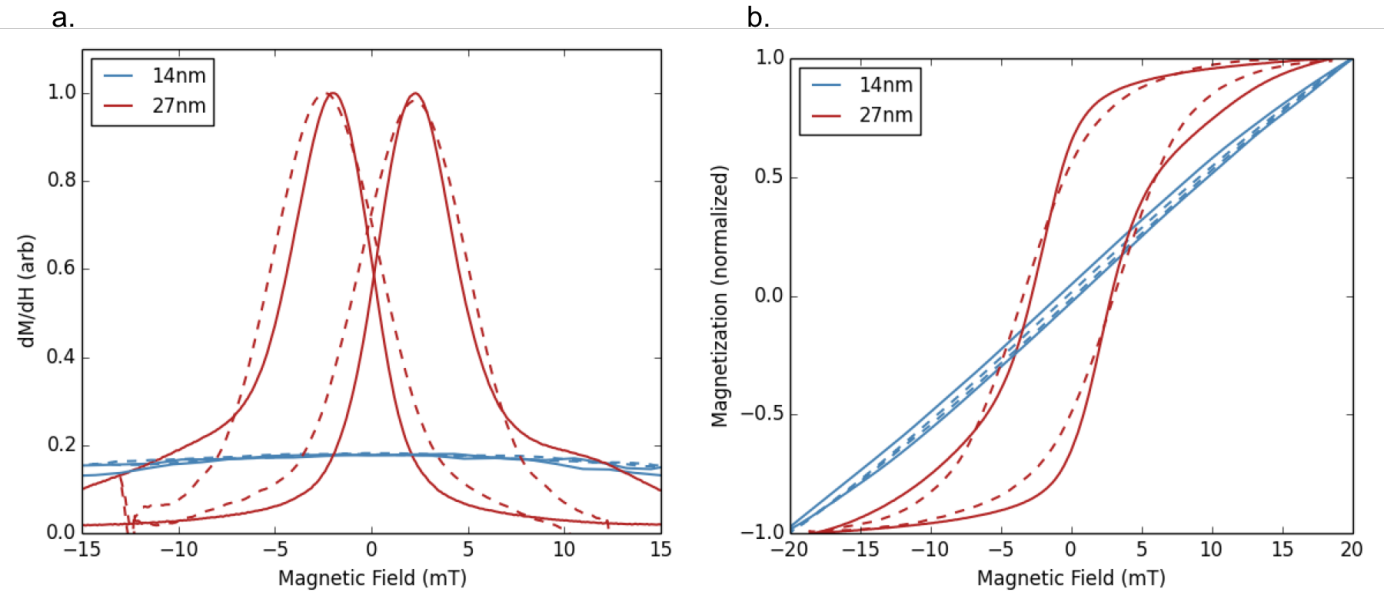

Figure 3.2: a. Experimental MPS data (solid lines) and simulated data (dashed lines) for two core sizes of nanoparticles. b. Integrated MPS data (solid lines) and simulated data (dashed lines) for two core sizes. Measurements were taken under an applied field of amplitude 20 mT/μ_0 and frequency 26 kHz. The magnetic moment has been normalized for better comparisons between simulated and measured data. The 14 nm particle shows essentially no MPS signal.

$$E_{\text{ani}}^{\text{c}}/V_{\text{c}} = K_1(\alpha_x^2\alpha_y^2 + \alpha_y^2\alpha_z^2 + \alpha_x^2\alpha_z^2) + K_2\alpha_x^2\alpha_y^2\alpha_z^2. \tag{3.62}$$

α_x, α_y, and α_z are the direction cosines of the magnetic moment. When cubic anisotropy is assumed, the values for K_1 which best fit the data range from -17 kJ/m^3 to -30 kJ/m^3 depending on particle size. Since the second term is typically orders of magnitude smaller than the first term, K_2 is fixed at -5 kJ/m^3, and changing it does not have any significant effect on the dynamics, as expected.

Another simulation parameter that requires some discussion is the resonance frequency γ, which appears in the Landau-Lifshitz-Gilbert equation (Eq. 3.30). This is typically set equal to the electron gyromagnetic ratio. However, as indicated by Song et al. [99], the natural resonance frequency of a sphere-shaped nanoparticle will be dependent on properties of the nanoparticle:

$$f_r = \frac{\gamma_e H_K}{2\pi} \tag{3.63}$$

where γ_e is the electron gyromagnetic ratio, and

$$H_K = \frac{4|K_1|}{3M_s} \tag{3.64}$$

for cubic anisotropy. Substituting this expression of f_r for γ in the LLG equation for simulation purposes has resulted in better fits to the data.

Apart from the anisotropy constant, the other main free parameter is the Gilbert damping parameter, α. The damping parameter is a phenomenological parameter, typically chosen to be between 0.1-1, but is difficult to measure directly. Simulations showing the effects of changing K and changing α are shown in Fig. 3.3. Decreasing the damping parameter narrows the width of the $M(H)$ loop (a.) and also decreases the height of the PSF (b.) as well as increasing its FWHM. Higher values of α, then, produce uniformly better PSFs, both in terms of signal strength and resolution. Decreasing the anisotropy constant narrows the $M(H)$ loop (a.), causing narrower and sharper peaks in the PSF (b.). For all simulation

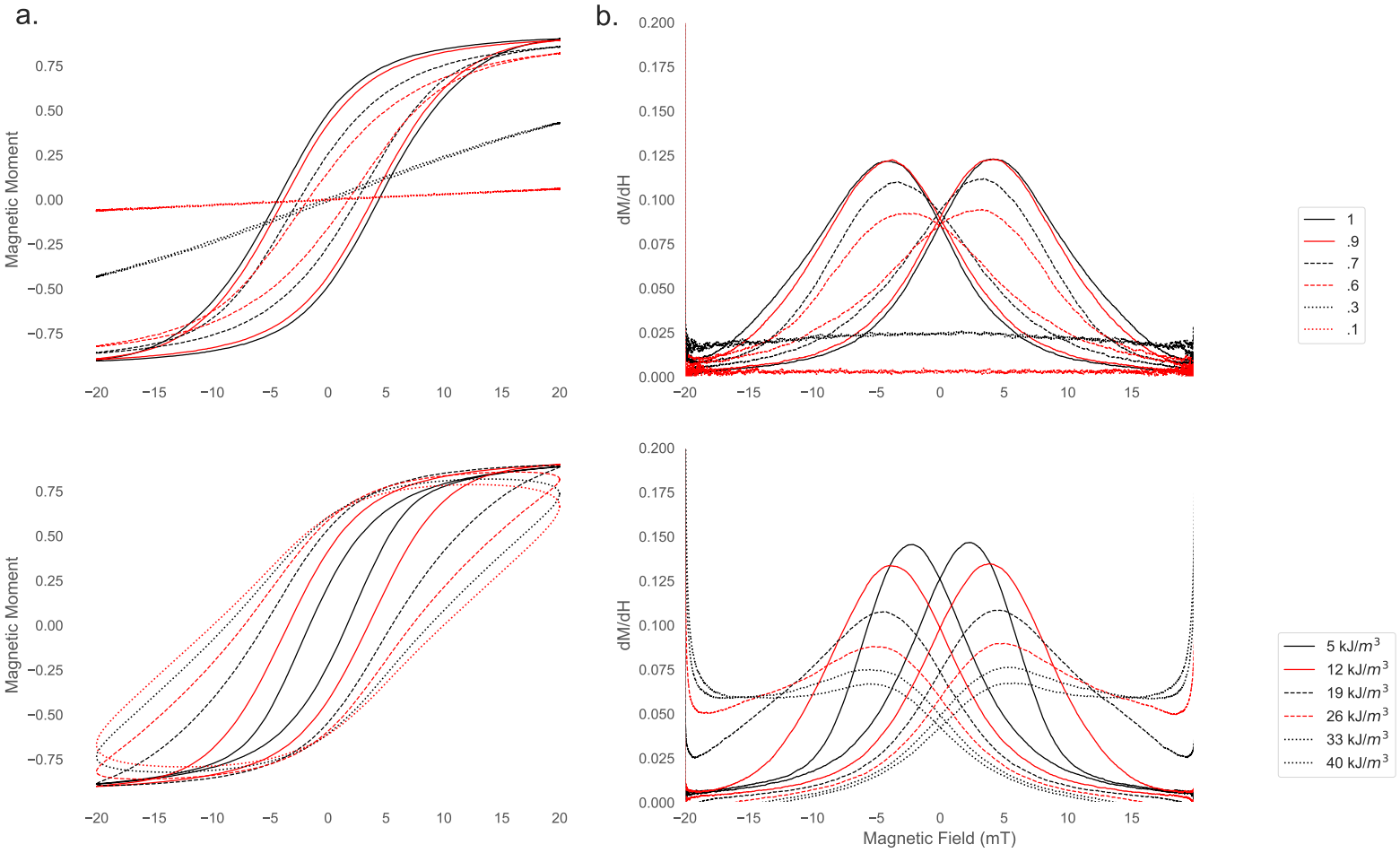

Figure 3.3: Top: Simulated M(H) (a.) and PSF (b.) for different values of the damping parameter. Bottom: Simulated M(H) (a.) and PSF (b.) for different values of the anisotropy constant. All simulations were run using 25 nm particles under a 20 mT/μ_0, 25 kHz field.

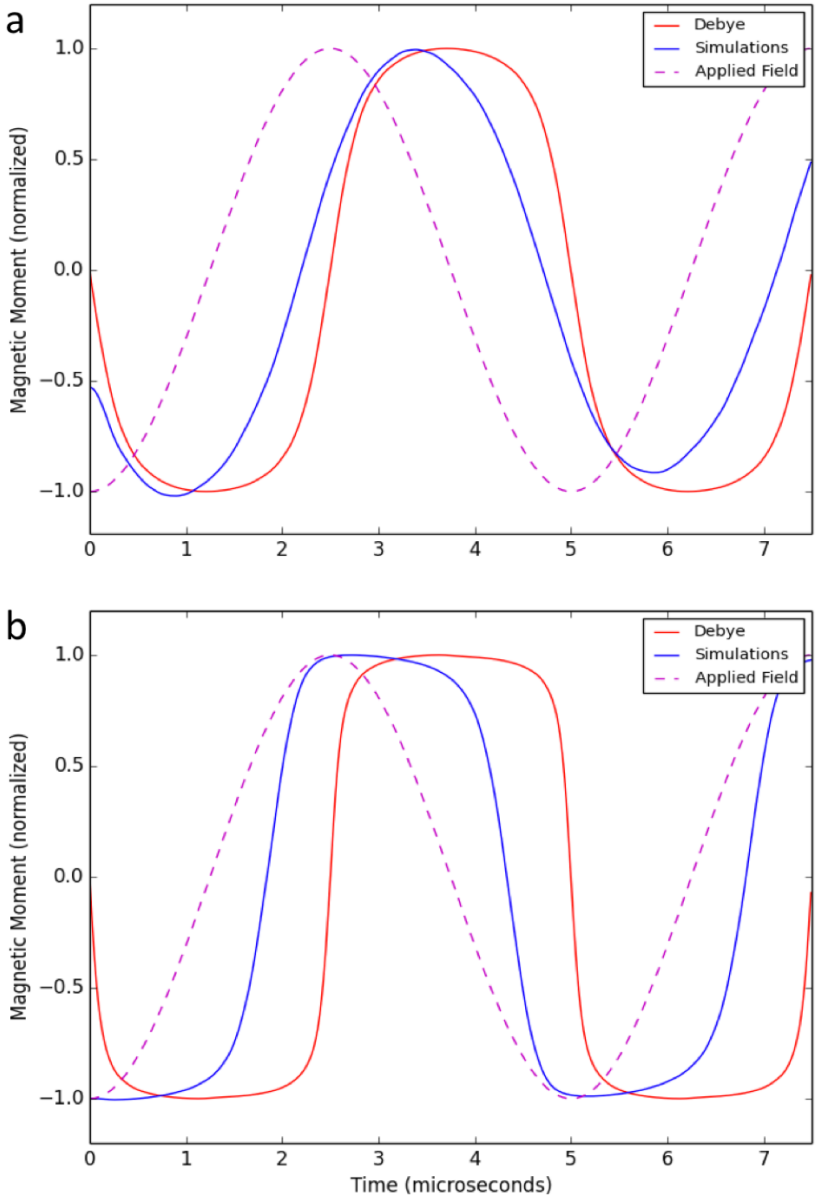

Figure 3.4: Simulations of the average normalized particle magnetic moment vs. theoretical Debye model under a 20 kHz, 10 mT/μ_0 field (a) and 30 mT/μ_0 field (b). The applied cosinusoidal field is also shown for reference.

results shown throughout this thesis, values of K and α are chosen based on best fits to data.

3.4 Model comparisons

We first compare experimental MPS data to stochastic Langevin simulations, shown in Fig. 3.2. Fig. 3.2a. shows the point-spread function, measured directly with MPS, and Fig. 3.2b. shows integrated MPS data (the particle magnetization as a function of the applied field) for two particle sizes. The corresponding stochastic Langevin simulations, with parameters chosen as best fits to data, are shown as well. For the small particle (14 nm), there is virtually no MPS response, and the integrated magnetization shows a linear response. For this particle size under these field conditions, then, linear response theory should hold, and the linear Debye model (Eq. 2.20) should be applicable. The linear behavior in the integrated magnetization curve is correctly reproduced by the simulations. The large particle (27 nm), as expected, displays nonlinear behavior and reaches magnetic saturation. Promisingly, the simulations reproduce this nonlinear behavior, indicating that they can be used to study nanoparticle dynamics outside of the linear regime.

To further investigate, Fig. 3.4 shows a comparison of these simulations with the linear Debye model (Eq. 2.20), tracking the normalized magnetic moment vs. time for a 22 nm particle under a 20 kHz oscillating field with amplitude 10 mT/μ_0 (a.) and 30 mT/μ_0 (b.). For particles larger than 22 nm, under these field conditions, the Debye model breaks down completely. When the applied field is increased, the simulations and theoretical Debye model diverge, and significant differences in shape can be seen. For lower fields, the phase lag appears to be accurately reproduced by the Debye model, although the shape of the magnetization response differs. As the field amplitude is increased, the phase lag is reduced significantly in the simulations, as expected (a stronger field should cause the magnetic moments to align faster with the field, decreasing phase lag). However, this behavior is not seen in the results from the Debye model.

In Fig. 3.5, the zero-field equilibrium relaxation times are plotted against calculations

of the effective relaxation time from simulations using the Debye model. To obtain the effective relaxation time, the $\chi''(\omega)$ spectrum was generated from simulations. According to the Debye model, at the peak frequency, $\omega\tau = 1$. Using this, we were able to obtain the effective relaxation time. At a lower field (5 mT/μ_0), the relaxation time corresponds well to τ_{eff} for small and large diameters; however, there is a discrepancy in the intermediate zone. When the field is increased to 20 mT/μ_0, this model gives a significantly smaller relaxation time than τ_{eff} for particles larger than ∼18 nm. The main conclusions that we can draw from this are that the Debye model only gives self-consistent results for low amplitude fields, and that τ_{eff} does not properly account for the coupling between relaxation mechanisms. The field dependence of Brownian and Néel relaxation times will be discussed in the next chapter.

Finally, we compare simulations from the coupled Fokker-Planck equation, Eq. 3.18, to results of simulations of the stochastic Langevin equations. Fig. 3.6 shows simulations of the magnetic moment of monodisperse uniaxial particles with identical characteristics, for two different core sizes, plotted against time and applied field. It can be seen that the simulations match very closely, especially for the smaller particles. Each method has distinct advantages; for a given desired number of particles to be simulated, solutions to the coupled Fokker-Planck equation can be generated relatively quickly. However, as formulated, it can only account for uniaxial anisotropy of nanoparticles, and does not incorporate interparticle interactions. Furthermore, polydispersity of nanoparticle core and hydrodynamic sizes, which is a key feature feature of realistic tracer samples, cannot be easily implemented in the Fokker-Planck formulation, unlike in the stochastic simulations. The stochastic simulations also allow for modeling of nanoparticle chains and clusters, which may be applicable for particles internalized into cell vesicles, for example. From a practical computational standpoint, the stochastic simulations can be easily parallelized, allowing them to take full advantage of multi-core processors or multiple compute nodes, whereas the code to solve the coupled Fokker-Planck equation is not easily parallelized. Consequently, the Fokker-Planck equations should be used when simple systems are considered and when low-noise results are required; for example, when studying small temperature or viscosity changes. When interparticle

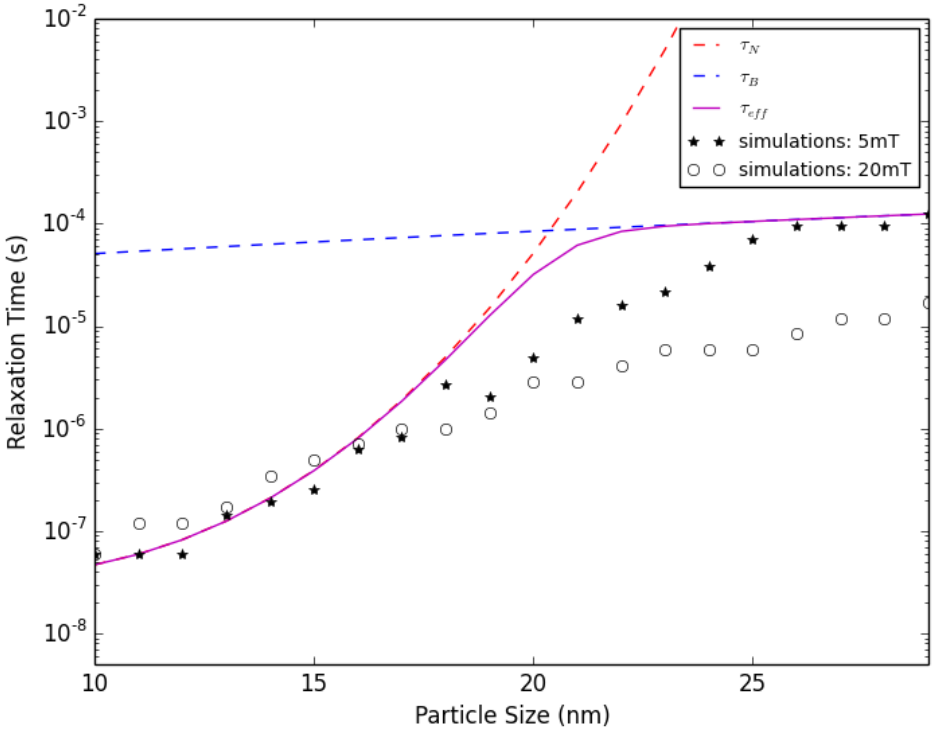

Figure 3.5: Effective relaxation times calculated from simulations using the Debye model for two applied amplitudes (5 mT/μ_0 and 20 mT/μ_0), plotted against particle diameter. Theoretical zero-field relaxation times (Brownian, Néel, and effective) are also shown.

interactions need to be considered, or when a large parameter space must be explored, stochastic Langevin simulations should be implemented instead.

To summarize, we have shown that nonequilibrium models are necessary in order to describe the dynamics of MNPs under fields applied in MPI. The Debye model breaks down for high (>5 mT/μ_0) fields, and for large particles (>20 nm). Both the coupled Fokker-Planck simulations and stochastic Langevin simulation methods are suitable for simulating the nonlinear MNP magnetic moment behavior, and generally agree with measured data, although each method has its own strengths and weaknesses. In the following chapter, we will use these methods to examine nanoparticle relaxation in detail.

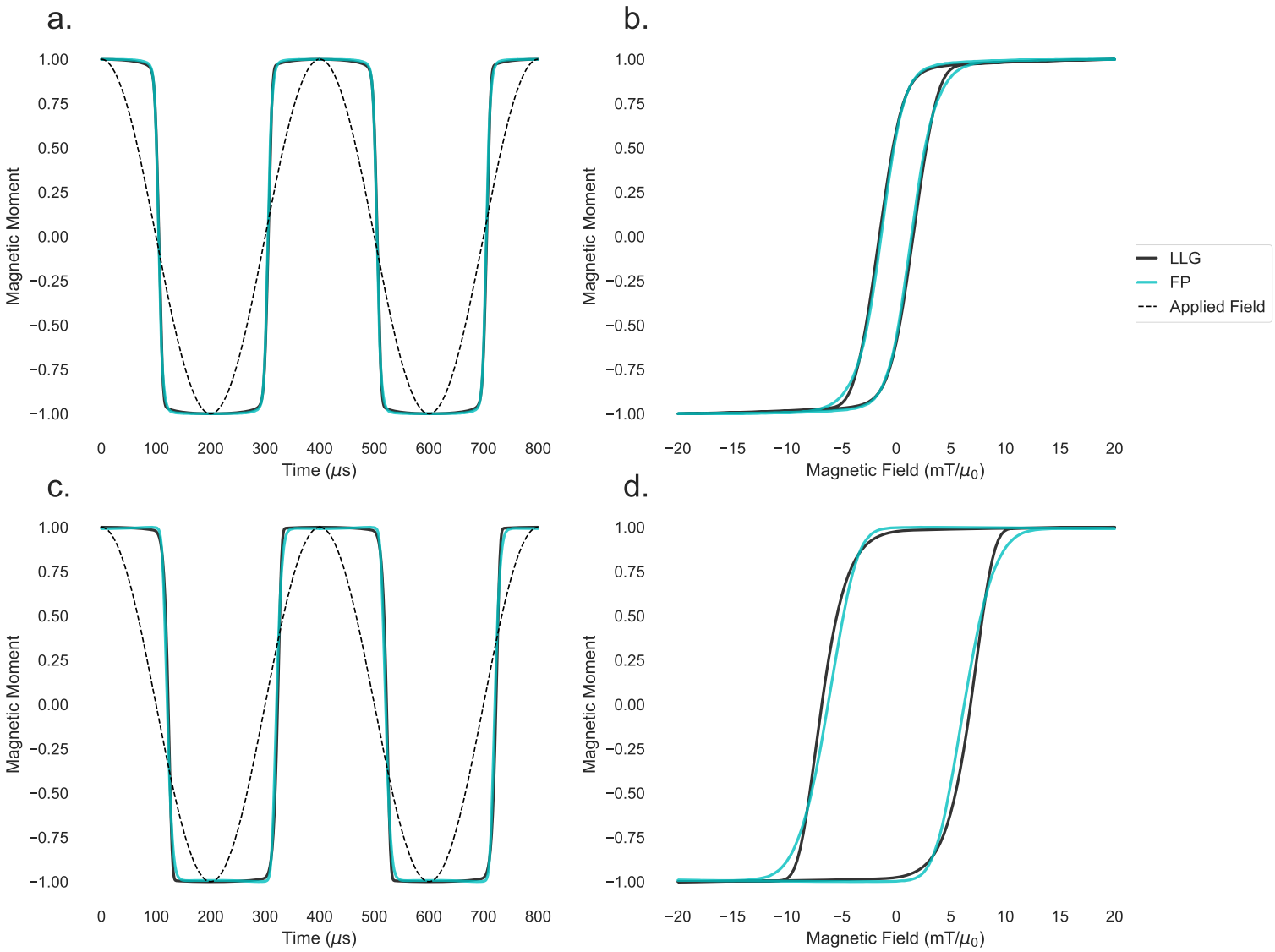

Figure 3.6: Top: simulations of the magnetic moment over time (a.) and plotted against magnetic field (b.) for a 22 nm particle. Bottom: simulations of the magnetic moment over time (c.) and plotted against magnetic field (d.) for a 29 nm particle. Simulations from the Langevin equations (labeled LLG and shown in black) agree well with simulations of the coupled Fokker-Planck equation (labeled FP and shown in cyan). In the left figures, the applied cosinusoidal field is also shown for reference.

Chapter 4

FIELD, SIZE, AND FREQUENCY DEPENDENCE OF NANOPARTICLE RELAXATION TIMESCALES

In this chapter, the methods developed in the previous chapter will be applied in order to study the relaxation timescales of nanoparticle dynamics under AC and DC fields. We will examine closely the effects of applied field and nanoparticle properties on relaxation time, and will use these insights in the following chapter to optimize field conditions and nanoparticle characteristics for MPI.

4.1 Importance of relaxation timescales in MPI

For the development of MPI, it is essential to quantify properties of the nanoparticle dynamics as a function of the applied field and characteristics of the nanoparticles and surrounding medium. Currently, there is no complete description for nanoparticle dynamics under the magnetic fields required for these applications. MNP dynamics are often described in terms of zero-field relaxation timescales; however, the effective relaxation times have been shown to be highly dependent on field strength (for both AC and DC fields) [79, 106]. Moreover, the physical regime where both Néel relaxation and Brownian relaxation may occur has yet to be described in any quantitative manner for the relevant field strengths and frequencies required for the above mentioned applications.

Brownian and Néel mechanisms are each characterized by respective timescales. The equilibrium relaxation time constant predicts the time required for thermal fluctuations to reorient the net magnetization to zero after an applied magnetic field is removed. In reality, the Brownian and Néel mechanisms are coupled, and the respective relaxation timescales are dependent on parameters like temperature, core and hydrodynamic size, and viscosity.

The equilibrium relaxation timescales, which are often used to describe MNP dynamics, ignore applied fields and so have limited applicability for MPI. The rotational time constant will change with field and frequency, and for high fields the external magnetic field may dominate over thermal terms. Understanding and modeling these physics is necessary for MPI, as the relaxation behavior will have major importance in the resulting MPI signal, as we will explore in later chapters. The relaxation timescale can be used to predict the MPI signal from different particles and under different field conditions, and we will ultimately use these insights to optimize field, frequency, and size of particles for MPI. Understanding these dynamics can also enable other sensing applications in combination with imaging, such as temperature sensing, viscosity quantification, and multi-color imaging, which will be investigated in §6.

4.2 Field dependence of relaxation timescales

In the small-field limit, the Debye model is often used to describe the AC susceptibility profiles of magnetic nanoparticles. The Debye model is a first-order approximation for small driving fields, which neglects non-linear behavior, and is limited to cases where the nanoparticle magnetization is not saturated. In linear response theory, as used in Debye's method, the AC susceptibility is written as $\chi = \chi' + i\chi''$, where the in-phase (χ') and out-of-phase (χ'') components of the susceptibility can be expressed as:

$$\chi'(\omega, T) = \frac{\chi_0}{1 + (\omega\tau_{\text{eff}})^2} \tag{4.1}$$

and

$$\chi''(\omega, T) = \chi_0 \frac{\omega\tau_{\text{eff}}}{1 + (\omega\tau_{\text{eff}})^2}, \tag{4.2}$$

where ω is the frequency of the applied field, T is the temperature, and τ_{eff} is the effective relaxation time of the nanoparticle. The static susceptibility, χ_0, is

$$\chi_0 = \frac{n\mu_0\mu^2}{3k_BT} \tag{4.3}$$

where μ_0 is the vacuum permeability, n is the number of particles, μ is the particle's magnetic moment, equal to M_sV_c, and k_B is Boltzmann's constant. The particle magnetization, along the direction of the applied field, can then be obtained by calculating:

$$M(t) = M_0(\chi' \cos(\omega t) + \chi'' \sin(\omega t)). \tag{4.4}$$

When the field is extremely low, M_0 can be approximated by $M_s\xi_0/3$, where $\xi_0 = \mu_0\mu H_0/k_BT$.[1] For reference, typical values for magnetite particles under MPI fields (diameter = 20 nm, M_s = 420 kA/m, H_0 = 20 mT/μ_0) yields $\xi_0 \approx 8.5$. For higher fields, setting $M_0 = M_s\mathcal{L}(\xi_0)$ improves the accuracy of the model [84], where $\mathcal{L}(\xi_0)$ is the Langevin function. In practice, there will be a non-zero distribution of particle core and hydrodynamic sizes, in which case Eq. 4.4 must be appropriately modified to an integral over particle sizes.

The Debye model indicates that the maximum of the out-of-phase ACS spectrum is given when $\omega\tau_{\text{eff}} = 1$, and so the effective relaxation time can be obtained from the ACS spectrum when the Debye model holds. The Debye model assumes symmetry in the ACS spectrum (when plotted vs. log frequency), which is often not seen experimentally. The Havriliak-Negami model [107] provides a phenomenological model for the susceptibility:

$$\chi = \chi_{\text{inf}} + \frac{\chi_{\text{amp}}}{(1 + (i\omega\tau)^{1-\alpha})^{\beta}}. \tag{4.5}$$

Here, χ_{inf} is the real susceptibility at high frequencies and χ_{amp} is the amplitude of the remainder of the frequency-dependent regime. The parameter α describes the width of the spectrum, and β incorporates the asymmetry. The model reduces to the Debye model in the limits of $\alpha = 0$ and $\beta = 1$. This model, in addition to incorporating particle size

[1] For clarity of notation, I will use H and ξ to refer to static fields, and H_0 and ξ_0 to refer to amplitudes of AC fields. AC fields will then be described as $H(t) = H_0\cos(\omega t)$ and $\xi(t) = \xi_0\cos(\omega t)$.

distributions, can be used for more accurate fitting of ACS spectra to obtain the effective relaxation time.

The effective relaxation time is often expressed as:

$$\tau_{\text{eff}} = \frac{\tau_N \tau_B}{\tau_N + \tau_B}, \tag{4.6}$$

which assumes that the relaxation mechanism with the lowest relaxation time will dominate. These relaxation mechanisms were described in detail in §2. It should be emphasized here that τ_N and τ_B refer to zero-field relaxation timescales. Once a magnetic field is applied, these equilibrium expressions will no longer hold.

4.2.1 DC magnetization timescales

We first consider the case of MNPs subjected to a static magnetic field. Brown developed an expression for a DC field-dependent Néel relaxation time [80]:

$$\tau_{N,H} = \frac{\tau_0 \sqrt{\pi}}{\sigma^{1/2}(1-h^2)} \left[(1+h)\exp(-\sigma(1+h)^2) + (1-h)\exp(-\sigma(1-h)^2) \right]^{-1} \tag{4.7}$$

with dimensionless parameter $h = H/H_k$, with H as the applied magnetic field, the unitless anisotropic field $\sigma = KV_c/k_BT$, and $H_k = 2K/\mu_0 M_s$. This expression holds as long as the magnetic field is not too large ($h < 0.4$), and only when the particles' easy axes are parallel to the field. When $\sigma \geq 2$, Eq. 4.7 can be approximated as:

$$\tau_{N,H} = \tau_0 \exp(\sigma(1-h)^2). \tag{4.8}$$

To properly generalize this expression, averaging over all directions of the easy axis would be necessary, assuming that easy axes in a realistic sample would be randomly oriented. Coffey *et al.* [108] showed that the Néel relaxation time under a DC field is highly dependent on the angle between the easy axis and the field. However, to date, no generalized expression has been derived. Furthermore, the above expressions for the Néel relaxation time are functions

of σ, which is expressed in terms of K, the effective uniaxial magnetocrystalline anisotropy constant. For spherical magnetite nanoparticles, the magnetocrystalline anisotropy is cubic rather than uniaxial, and uniaxial anisotropy may not necessarily be an accurate approximation, particularly when considering the relative orientations of the easy axis to the field [92].

Martsenyuk *et al.* [109] developed the following expressions for the Brownian relaxation time in a static magnetic field, with the field parallel and perpendicular to a small-amplitude probing field:

$$\tau_{\text{par}} = \frac{\mathrm{d}\ln\mathcal{L}(\xi)}{\mathrm{d}\ln\xi}\tau_B \tag{4.9}$$

$$\tau_{\text{perp}} = \frac{2\mathcal{L}(\xi)}{\xi - \mathcal{L}(\xi)}\tau_B \tag{4.10}$$

The above expressions are derived by treating the probing field as a small perturbation to the equilibrium field. From Eq. 4.10, we can find low-field ($\xi < 5$) and high-field ($\xi > 5$) approximations [109]:

$$\tau_{\text{low}} = \left(1 - \frac{1}{10}\xi^2\right)\tau_B \tag{4.11}$$

$$\tau_{\text{high}} = \frac{2}{\xi}\tau_B \tag{4.12}$$

The above expressions hold when $\xi \ll \sigma$ and $\sigma \geq 10$, i.e. when Brownian relaxation is clearly dominant and the field strength is still relatively small (compared to the anisotropy energy of the particle). It should be noted that DC magnetization timescales will have limited applicability to AC magnetic fields, except in the adiabatic limit of slowly varying magnetic fields (i.e. when the relaxation time is much smaller than the timescale of changes in the magnetic field).

4.2.2 AC magnetization

Yoshida and Enpuku [110] derived the following expression for the Brownian relaxation time under a large DC magnetic field, from fitting to the Fokker-Planck equation:

$$\tau_{B,H} = \frac{\tau_B}{\sqrt{1 + 0.21\xi^2}} \tag{4.13}$$

They further determined the following set of equations to describe the dynamics of thermally blocked MNPs under relatively large AC magnetic fields ($\xi_0 \geq 20$):

$$\chi'(\omega) = \frac{\chi_1}{1 + (\omega\tau_{B,H})^2} \tag{4.14}$$

and

$$\chi''(\omega) = k'' \frac{\chi_1 \omega\tau_{B,H}}{1 + (\omega\tau_{B,H})^2} \tag{4.15}$$

where

$$\chi_1 = \chi_0 \left[1 - \frac{0.0636\xi_0^2}{1 + 0.18\xi_0 + 0.0659\xi_0^2}\right] \tag{4.16}$$

and

$$k'' = 1 + \frac{0.024\xi_0^2}{1 + 0.18\xi_0 + 0.033\xi_0^2} \tag{4.17}$$

Using these expressions, the dynamics of purely Brownian particles under large AC fields can be described. For high DC fields, Eqs. 4.12 and 4.13 give similar results [84].

Dieckhoff *et al.* [106] developed an expression in the form of Eq. 4.13 for the effective Néel relaxation time under an AC field, based on fitting to experimental data:

$$\tau_{N,H} = \frac{\tau_N}{\sqrt{1 + 1.97\xi_0^{3.18}}}. \tag{4.18}$$

They did not provide analogous expressions for Eqs. 4.14-4.17, and only used field amplitudes up to 9 mT. The fit parameters (here 1.97 and 3.18) may be specific to the sample used,

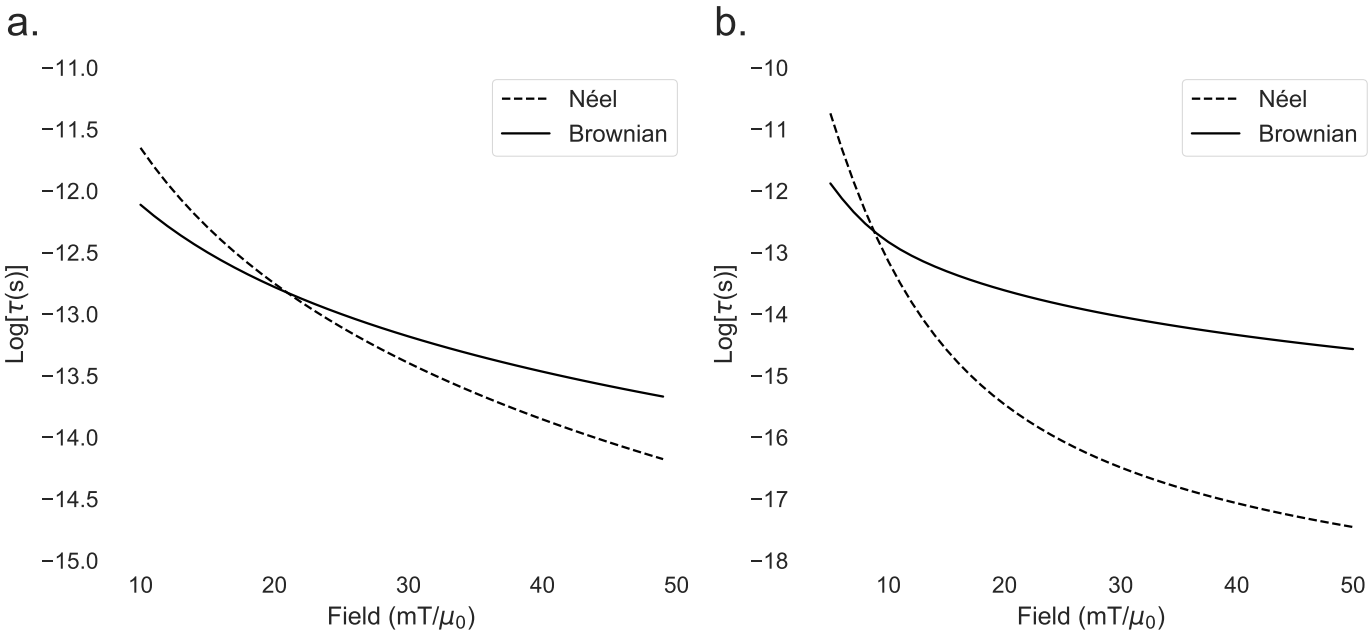

Figure 4.1: Brownian and Néel relaxation time as a function of applied field amplitude, for nanoparticles with 25 nm core diameter and 40 nm hydrodynamic diameter. a. $\tau_{N,H}$ and $\tau_{B,H}$ from Eqs. 4.18 and 4.13. b. Fokker-Planck results: $\tau_{N,F}$ and $\tau_{B,F}$ from Eqs. 4.29 and 4.28.

and so cannot necessarily be generalized, particularly for higher fields. However, for now we will use Eqs. 4.13 and 4.18 as a first model to examine the relaxation time dependence on magnetic field strength.

Fig. 4.1a. is a plot of the relaxation time calculated from Eqs. 4.13 and 4.18 as a function of applied field, with parameters $d_c = 25$ nm, $d_h = 40$ nm, $\alpha = 1$, $K = 5$ kJ/m^3, $M_s = 420$ kA/m, $T = 300$ K, and $\eta = 1$ cp. As can be seen from the figure, the Néel relaxation time has a much stronger dependence on field strength. Making the assumption that the relaxation mechanism with the shorter relaxation time will typically dominate, it can be inferred that for nanoparticles with these properties, for low fields, the Brownian mechanism will dominate, and for high fields, the Néel mechanism will dominate.

4.2.3 Nonlinear field dependence of relaxation timescales

Given that the above expressions have limited applicability to general fields, we turn to the nonlinear methods developed in the previous chapter to further examine the effects of field strength on relaxation time. Using the decoupled Fokker-Planck equations (Eq. 3.7 and Eq. 3.10) outlined in §3.1.1, we can extract the relaxation time separately for pure Brownian or pure Néel rotation. By truncating Eq. 3.9 or Eq. 3.11 after N terms, we can write the following matrix equation:

$$\tau_0 \frac{d\mathbf{y}}{dt} = \mathbf{A}\mathbf{y} + \mathbf{b}, \tag{4.19}$$

where $\mathbf{A}$ is an $N \times N$ matrix, and $\mathbf{b}$ and $\mathbf{y}$ are column vectors with N elements. The equilibrium timescales are represented by τ_0, so for Brownian relaxation $\tau_0 = \tau_B$, and for Néel relaxation $\tau_0 = \tau_N$. For pure Brownian rotation (Eq. 3.7), $\mathbf{A}$ will be a tridiagonal matrix with components [79]:

$$A_{n,n} = -\frac{n(n+1)}{2} \qquad n = 1, 2, 3, ..., N, \tag{4.20}$$

$$A_{n,n+1} = -\frac{n(n+1)}{2(2n+3)}\alpha \qquad n = 1, 2, 3, ..., N-1, \tag{4.21}$$

$$A_{n,n-1} = \frac{n(n+1)}{2(2n-3)}\alpha \qquad n = 2, 3, 4, ..., N. \tag{4.22}$$

The remaining components are zero. As before, $\alpha = \mu_0 \mu H / k_B T$. The first component of $\mathbf{b}$ will $b_1 = \alpha/2$, with remaining components equal to zero.

For Néel relaxation, the components of $\mathbf{b}$ are $b_1 = \alpha/2$ and $b_2 = \alpha_K/2$, where $\alpha_K = 2KV_c/k_BT$, and remaining components zero. In this case, $\mathbf{A}$ is a pentadiagonal matrix with matrix elements defined by [79]:

$$A_{n,n} = \frac{n(n+1)}{2}\left[-1 + \frac{n\alpha_K}{(2n-1)(2n+1)} - \frac{(n+1)\alpha_K}{(2n+1)(2n+3)}\right] \quad n = 1, 2, 3, ..., N, \tag{4.23}$$

$$A_{n,n+1} = -\frac{n(n+1)}{2(2n+3)}\alpha \qquad n = 1, 2, 3, ..., N-1, \tag{4.24}$$

$$A_{n,n-1} = \frac{n(n+1)}{2(2n-3)}\alpha \qquad n = 2, 3, 4, ..., N, \tag{4.25}$$

$$A_{n,n+2} = -\frac{n(n+1)(n+2)}{2(2n+3)(2n+5)}\alpha_K \qquad n = 1, 2, 3, ..., N-2, \tag{4.26}$$

$$A_{n,n-2} = \frac{n(n+1)(n-1)}{2(2n-3)(2n-1)}\alpha \qquad n = 3, 4, 5, ..., N. \tag{4.27}$$

Again, the remaining components are zero. For both of these cases, the solution to Eq. 4.19 will be dominated by the eigenvalue of $\mathbf{A}$ with the largest real part, λ^{max}. We can then find the effective relaxation time in terms of λ^{max} and the equilibrium relaxation time [79]. For Brownian relaxation, then:

$$\tau_{B,F} = -\frac{\tau_B}{\Re(\lambda_B^{max})}, \tag{4.28}$$

and for Néel relaxation,

$$\tau_{N,F} = -\frac{\tau_N}{\Re(\lambda_N^{max})}. \tag{4.29}$$

Using the above equations, relaxation timescales were calculated for a range of field values, with $N = 100$, and plotted in Fig. 4.1b. Parameters used in the computation were the same as in Fig. 4.1a., with $d_c = 25$ nm, $d_h = 40$ nm, $\alpha = 1$, $K = 5$ kJ/m^3, and $M_s = 420$ kA/m.

The overall trend is the same as in Fig. 4.1a., with Brownian relaxation dominating for low fields, and Néel relaxation dominating for high fields. However, the Fokker-Planck simulations indicate that this switch occurs at lower fields than suggested by Fig. 4.1a., and the Néel relaxation time decreases much more rapidly with field.

According to Fig. 4.1, the Néel process is much more strongly affected by an applied field, changing by many orders of magnitude as the field strength is increased from 5 mT/μ_0 to 50 mT/μ_0, whereas the Brownian process only changes by about one order of magnitude for the same range. Because of this, the Néel mechanism may be much faster under high applied

fields than the Brownian mechanism, even if the zero-field timescales are much higher. For example, with the parameters listed above, the zero-field relaxation timescales $\tau_N = 354$ μs, whereas $\tau_B = 21.6$ μs, a full order of magnitude lower.

To understand this, we can look at the internal energy density, when the field is along the z-axis:

$$U(\theta, \phi) = K \sin^2 \phi - \mu_0 M_s H \cos \theta \tag{4.30}$$

The angle θ is the angle between $\hat{\mathbf{m}}$ and $\mathbf{H}$, and ϕ is the angle between $\hat{\mathbf{m}}$ and $\hat{\mathbf{n}}$, equal to θ when the easy axis $\hat{\mathbf{n}}$ is aligned with the field. The energy is a function of the orientations of the magnetic dipole moment, the crystalline lattice, and the external field. Without an external field, the energy density is symmetric with two minima at the locations of the easy axes. The moment will flip when the thermal energy exceeds the energy barrier, KV_c, and in this case the zero-field relaxation time τ_N will define the magnetization dynamics. When an external field is applied, the energy density will no longer be symmetric. One minima will be lower, and the energy barrier will be reduced in that direction. For $0 < H < 2K/\mu_0 M_s$, there will be two unequal minima, and for $H \geq 2K/\mu_0 M_s$ there will be only one minimum, resulting in a lowered average time to transition. So, for example, there will be only one minimum in the energy density once the magnetic field strength reaches 25 mT/μ_0 for $M_s = 420$ kA/m and for $K = 5$ kJ/m^3, indicating that for fields above 25 mT/μ_0, the dynamics will be purely driven by the field, since spontaneous flipping of the magnetic moment is not possible.

The Fokker-Planck results here show only purely Brownian or purely Néel rotation, and the time constant calculated from the eigenvalue method only applies to DC fields (as the matrix $\mathbf{A}$ in Eq. 4.19 changes as a function of field). For that reason, we also look at stochastic Langevin simulations, using the methods described in §3.2 and §3.3, which incorporates both mechanisms simultaneously. With the stochastic simulations, it is possible to simulate purely Néel rotation as well by fixing the axes $\hat{\mathbf{n}}$ and simulating only Eq. 3.30. A limitation of the decoupled Fokker-Planck equations used here is that there is an assumption made that all particle axes are aligned with the field. The particle alignment can significantly

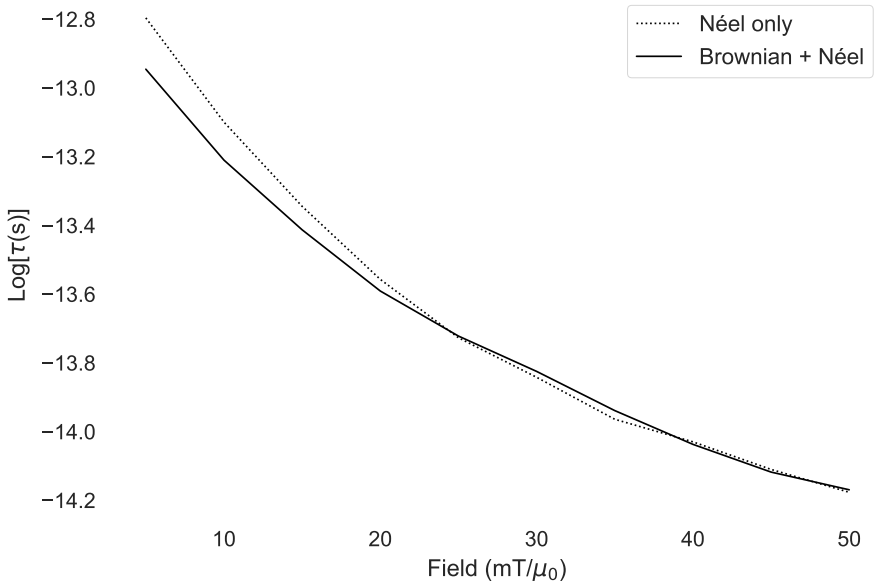

Figure 4.2: Relaxation time extracted from stochastic simulations. Results are shown for immobilized particles, where only Néel relaxation can occur, as well as particles dispersed in water where both Brownian and Néel relaxation may occur.

affect the dynamics [92], and so is an important factor to take into consideration. For realistic situations, it should typically be assumed that the nanoparticle axes have random orientations. However, since the coupled Fokker-Planck equation (Eq. 3.18), which does allow for generalized orientations of the easy axis, cannot be easily expressed in terms of a relaxation time, we will use stochastic Langevin simulations instead.

Stochastic Langevin simulations performed according to Eqs. 3.30 and 3.31 for similar conditions also indicate a decrease of relaxation time with field amplitude, shown in Fig. 4.2. Simulations were performed with parameters $d_c = 25$ nm, $d_h = 50$ nm, $f = 25$ kHz, $K = 5$ kJ/m^3 and otherwise identical parameters to Fig. 4.1. Simulations were run first allowing only Néel rotation (Eq. 3.30), and then with the full six coupled equations (Eq. 3.30 and 3.31), allowing for both Néel and Brownian relaxation. In the second case we can interpret the effective relaxation time as incorporating both the Néel and Brownian mechanisms. The relaxation time was extracted by taking the arctangent of the phase angle of the first har-

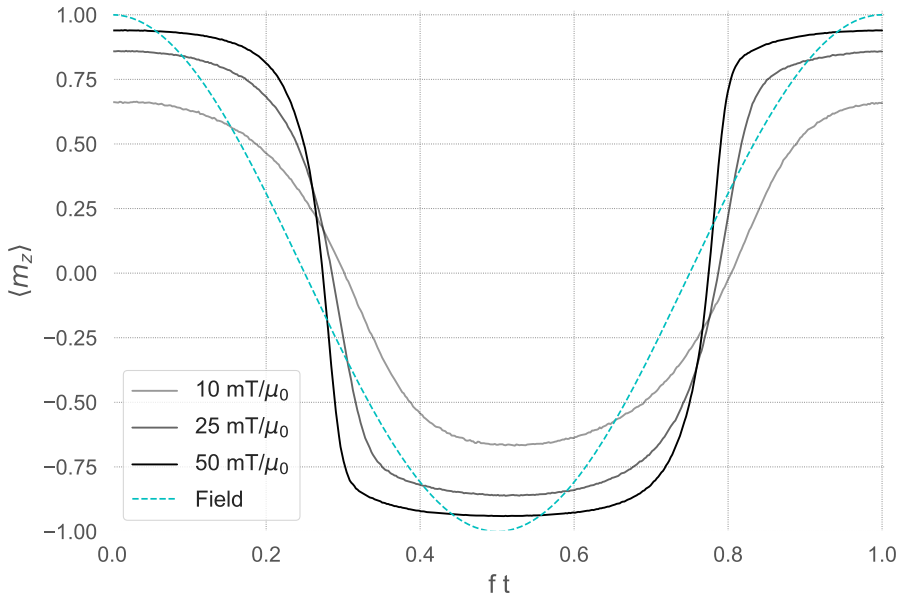

Figure 4.3: Simulation results of average particle magnetic moment over time. Results from three different applied field amplitudes are shown, as well as the normalized applied field.

monic of the magnetic moment, and dividing by the angular frequency (since $\tan\phi = \omega\tau$). For low fields, the Néel relaxation time is clearly higher, but then the relaxation times begin to overlap. The point at which the two lines overlap, starting at around 23 mT/μ_0, can be interpreted as the point where Néel relaxation starts to dominate when both mechanisms are allowed. It is clear that the effective relaxation time changes by a much less dramatic amount than predicted by the Fokker-Planck simulations in Fig. 4.1b. This is likely due to the fact that the Fokker-Planck calculations apply to only DC fields, compared to AC field amplitudes in the Langevin simulations, where the field changes according to a set frequency. Frequency dependence of the relaxation time will be discussed in a later section. For now, we can see that the relaxation time decreases with field strength, both for DC fields and AC field amplitudes.

We can see how AC field amplitude affects the magnetic moment dynamics in Fig. 4.3, which shows the magnetic moment over time for different applied AC field strengths. As

the field amplitude is increased, the moment shape becomes more like a square wave, and the phase lag is decreased. The phase lag is directly related to the relaxation time (again, as $\tan\phi = \omega\tau$), so for a fixed frequency as shown here, the relaxation time can be directly observed as the phase lag decrease.

4.2.4 Summary

In MPI, both static and alternating magnetic fields are employed. As shown above, expressions for field-dependent relaxation times have been derived for purely Brownian and purely Néel-dominated MNPs, with certain restrictions (particularly, for Néel relaxation times, that the field is applied parallel to the easy axis). However, as Diessler *et al.* [79] demonstrated, the Brownian and Néel relaxation mechanisms are coupled in a complex way that depends on applied field strength. With increasing field strength, both relaxation times decrease, but the Néel relaxation time decreases much more rapidly, as seen in Fig. 4.1.

Consequently, the zero-field relaxation timescales may indicate that particles are purely Brownian, but for stronger magnetic fields, Néel relaxation may dominate the dynamics. This will be especially relevant for high frequency fields, where the period of the AC field is smaller than either the zero-field Néel or Brownian timescales. In that case, the Brownian contribution may be very small, while the amplitude of the field may be strong enough to sufficiently decrease the effective Néel relaxation time so that a magnetic response is observed. Frequency dependence on relaxation timescales will be explored further in a later section.

4.3 Size dependence of relaxation timescales

When both relaxation mechanisms are considered, the relaxation time is often described by the reduced relaxation time, τ_{eff} (Eq. 4.6). The reduced time implies that the mechanism with the shortest equilibrium relaxation time will dominate. The magnetic core size and hydrodynamic size of the particle will affect which mechanism will dominate, in addition to the field amplitude, as shown in the previous section. The reduced relaxation time τ_{eff} is plotted as a function of particle core size in Fig. 4.4a.

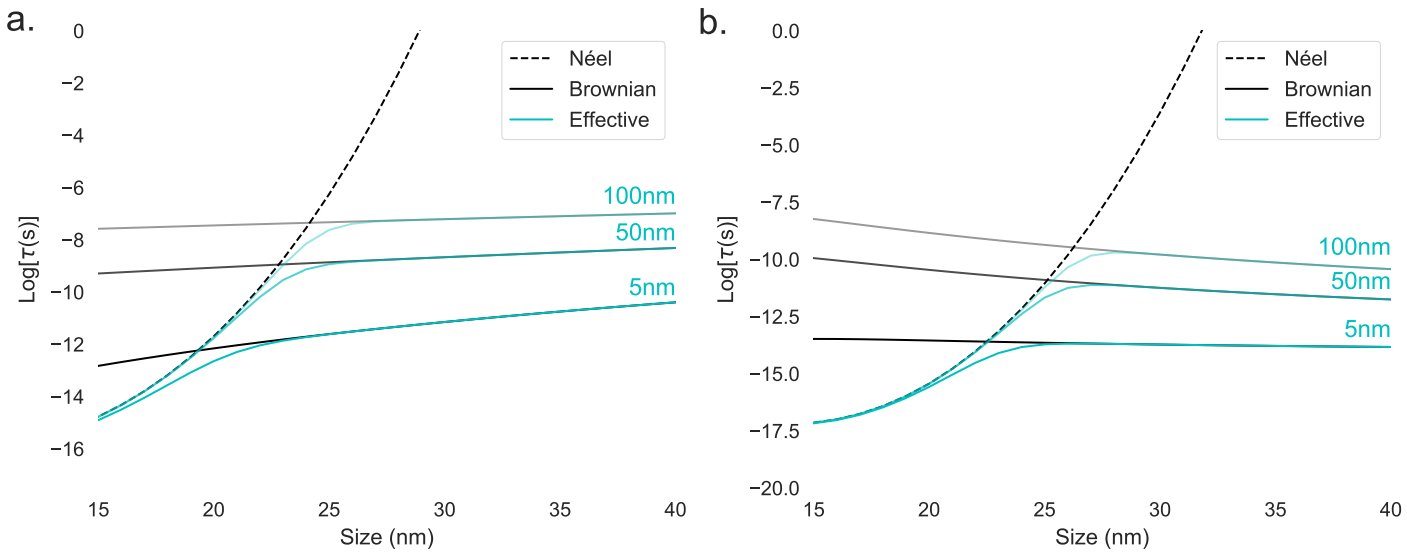

Figure 4.4: a. $\tau_{N,H}$ and $\tau_{B,H}$ from Eqs. 4.18 and 4.13 as a function of applied field with core diameter 25 nm and three different coating sizes, resulting in total hydrodynamic diameters (d_h) of 30 nm, 75 nm, and 125 nm. b. Fokker-Planck results: $\tau_{N,F}$ and $\tau_{B,F}$ from Eqs. 4.29 and 4.28 as a function of applied field with core diameter 25nm and three different coating sizes.

Since the timescale of the Brownian relaxation mechanism is highly dependent on the non-magnetic coating (τ_B scales as V_h), three different coatings have been plotted. The hydrodynamic diameter will be the sum of the core diameter and the non-magnetic coating, so for a core diameter of 25 nm and coating of 5 nm, the hydrodynamic diameter will be 30 nm. For MPI applications, where iron oxide nanoparticles must be dispersed in water, there will always be an additional non-magnetic coating, for hydrophilicity as well as functionalization for *in vivo* medical purposes, such as long-term blood circulation or cancer targeting. The increase in size due to the added coating is often ignored, and Brownian relaxation times are often compared to Néel relaxation times with $V_h = V_c$ [79], which is inaccurate for realistic MPI purposes. While the Néel mechanism is unaffected by added non-magnetic coatings, the Brownian mechanism is highly dependent on hydrodynamic size.

Using Eqs. 4.13 and 4.18, we can plot the field-dependent relaxation times as a function of size as well. From these, we can also calculate an effective reduced relaxation time, using the same formula as Eq. 4.6, but with $\tau_{B,H}$ and $\tau_{N,H}$ substituted for τ_B and τ_N. This is shown in Fig. 4.4b., also for three different coating sizes.

In the equilibrium (zero-field) case (Fig. 3.5), the relaxation time increases with size. In the field-dependent case (Fig. 4.4), the Néel relaxation time increases with size, but the Brownian relaxation time decreases with core size, in contrast to the zero-field case. In both cases, the coating size shifts the intersection point between Brownian and Néel relaxation. Larger coatings indicate that the Néel mechanism will dominate through larger sizes. With Eqs. 4.13 and 4.18, we can extract the core size at which the two timescales intersect, which indicates the size at which the Brownian mechanism starts to dominate, as a function of field amplitude and coating size, shown in Fig. 4.5. For very low field amplitudes (< 7 mT/μ_0) and small coatings (< 10 nm), Brownian relaxation starts to dominate when the core size is around 22 nm. As both the field amplitude increases and the coating size increases, Néel relaxation remains dominant for increasing core diameters. For high field amplitudes (> 50 mT/μ_0) and very large coatings (> 100 nm), Néel relaxation dominates up to particles that are larger than 27 nm. It should be emphasized again that these calculations are performed

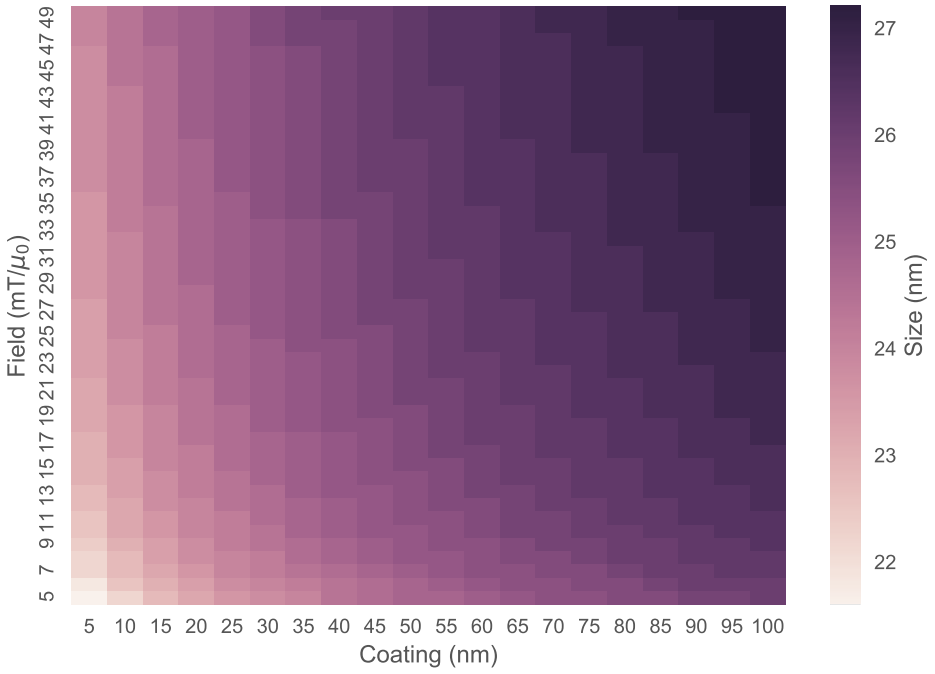

Figure 4.5: Heatmap showing the size at which the Brownian relaxation timescale becomes larger than the Néel relaxation timescale, according to Eqs. 4.13 and 4.18, as a function of applied field amplitude and coating size.

assuming DC fields, rather than AC fields, but Fig. 4.5 provides a general overview of how the field strength and coating size affect the relaxation mechanism and resulting relaxation time constant.

To further examine this behavior, we again turn to alternative methods. From eigenvalue calculations from the Fokker-Planck equations, we see similar behavior in Fig. 4.6 as in Fig. 4.4. Once again, it is clear that the theoretical models (Eqs. 4.13 and 4.18) underestimate the Néel contribution compared to the Fokker-Planck results. Again making the assumption that the mechanism with the shortest relaxation time will dominate, the Fokker-Planck calculations predict that Néel relaxation will be the dominant mechanism for particle sizes up through 40nm or greater, depending on the coating size. In Fig. 4.6, the effective relaxation time, $\tau_{E,F}$ shown in blue, has again been calculated according to Eq. 4.6, this

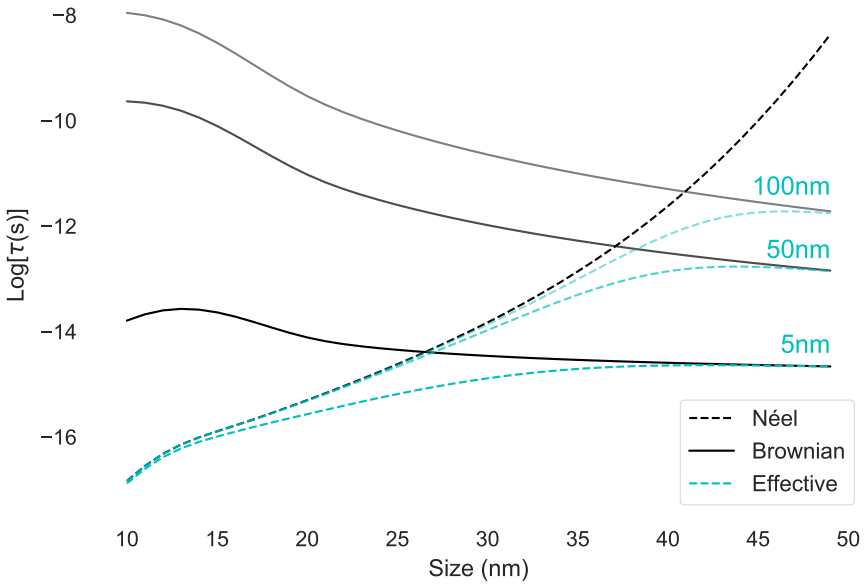

Figure 4.6: Fokker-Planck results: $\tau_{N,F}$ and $\tau_{B,F}$ from Eqs. 4.29 and 4.28 as a function of particle core size for three different coating sizes.

time with $\tau_{B,F}$ and $\tau_{N,F}$ substituted for τ_B and τ_N. As discussed previously, the eigenvalue calculations may have limited applicability to strong or high-frequency AC fields, but they should nevertheless be an improvement on the zero-field equilibrium timescales, τ_B and τ_N.

With the Fokker-Planck eigenvalue calculations, we can take a closer look at the dependence of Néel and Brownian relaxation times on particle size and field, in Fig. 4.7. As seen in the previous section, for all sizes and both relaxation mechanisms, the relaxation time decreases with applied field strength. The Néel relaxation time is clearly extremely dependent on field, and for low fields in particular, increases rapidly with particle size. Even for larger field strengths (20-30 mT/μ_0), the Néel relaxation time increases by several orders of magnitude. The Brownian relaxation time, just as in Fig. 4.4, does decrease with core size in general for most field strengths, in contrast to the trend predicted by the zero-field relaxation timescales.

The effective relaxation time, $\tau_{E,F}$, calculated from $\tau_{B,F}$ and $\tau_{N,F}$ in Fig. 4.7, is shown

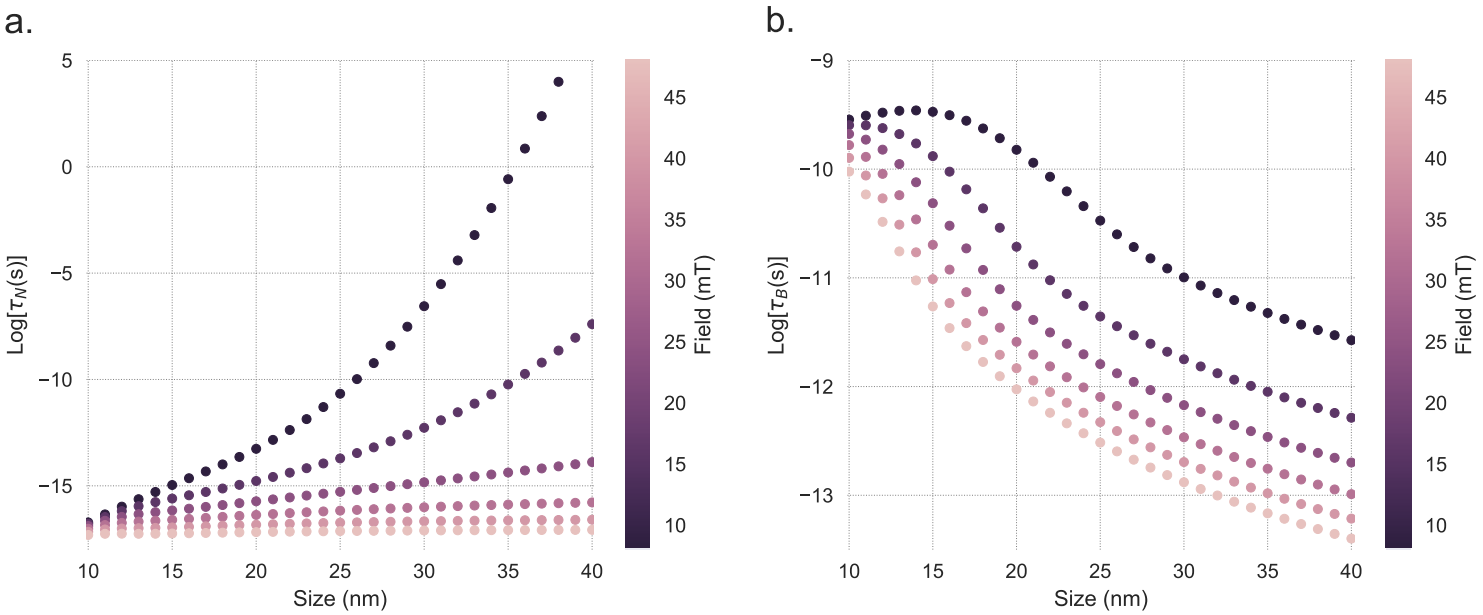

Figure 4.7: a. $\tau_{N,F}$ from Fokker-Planck results as a function of core size for different applied fields. b. $\tau_{B,F}$ from Fokker-Planck results as a function of core size for different applied fields. Coating size was fixed at 50nm.

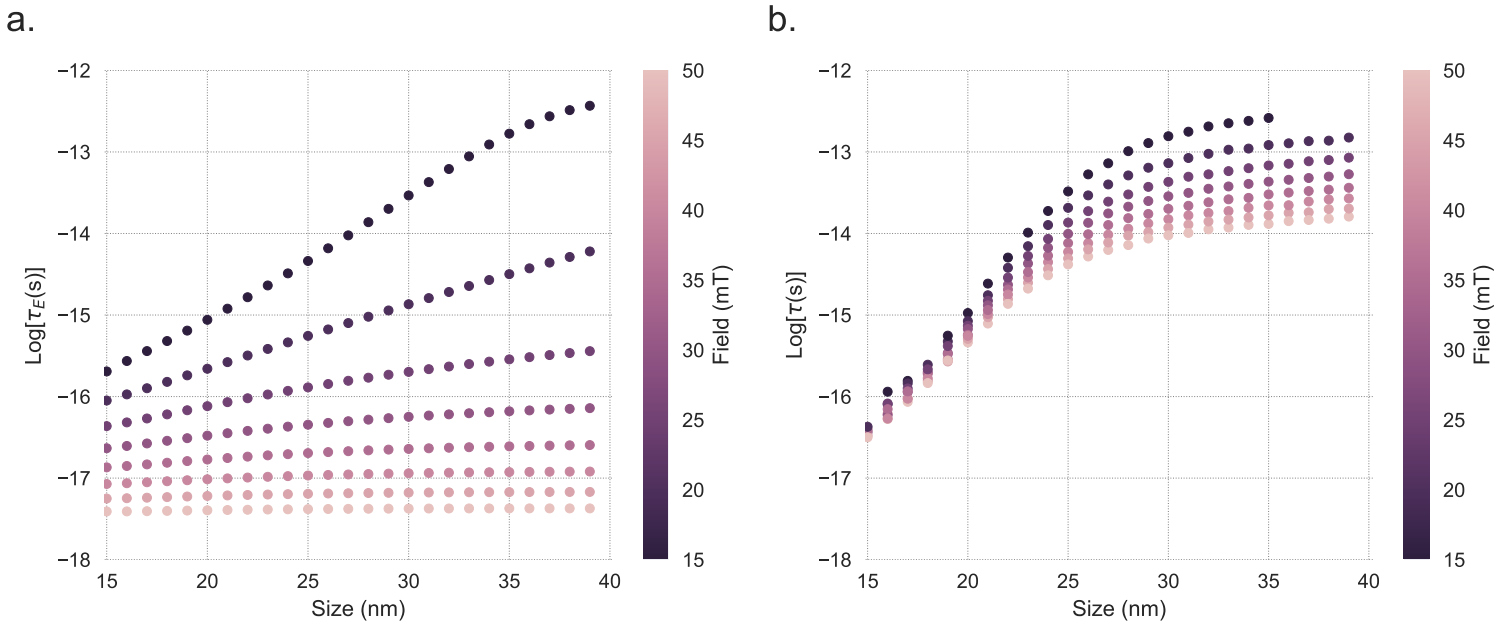

Figure 4.8: a. Néel relaxation time extracted from stochastic simulations of immobilized particles as a function of particle size for different applied fields. b. Effective relaxation time extracted from simulations of particles allowed to rotate via both Brownian and Néel mechanisms as a function of particle size for different applied fields. Coating size was fixed at 50 nm.

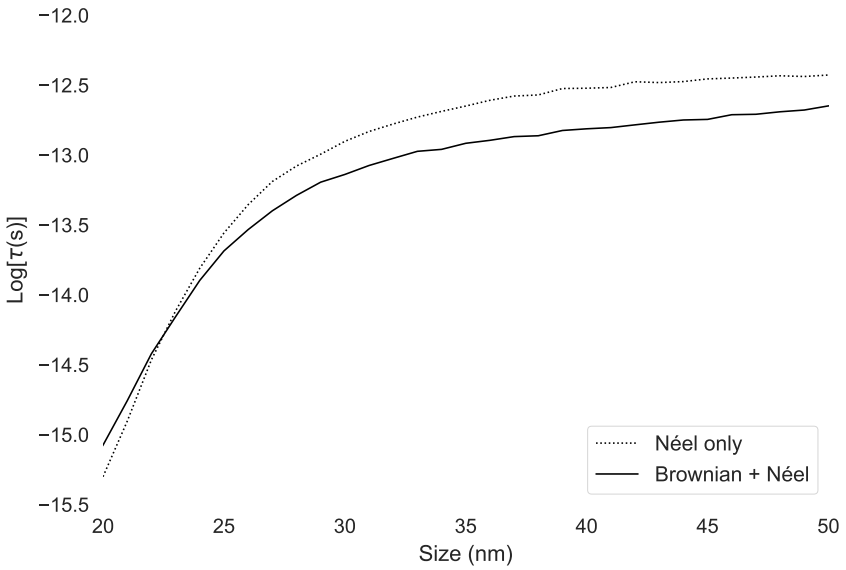

Figure 4.9: Relaxation time as a function of core size extracted from stochastic simulations with an applied field of 20 mT/μ_0 and 50 nm coating. Results are shown for immobilized particles, where only Néel relaxation can occur, as well as particles dispersed in water where both Brownian and Néel relaxation may occur.

in Fig. 4.8a. Stochastic Langevin simulation results are shown in Fig. 4.8b. The stochastic simulations deviate somewhat from the Fokker-Planck results; the simulations indicate a weaker dependence on field (as seen the previous section), but a stronger dependence on core size in the range $15 - 25$ nm. We can also look at the Néel relaxation time only from the simulations for a fixed field, shown in Fig. 4.9. Here, we see a strong deviation from the Fokker-Planck predictions: the Néel relaxation time increases sharply at first but then levels off, rather than growing exponentially as in Fig. 4.7a. While the Néel relaxation time is generally higher in the simulation results, as expected, the overall behavior is similar to the results when both mechanisms are in place.

To understand this behavior, we study the energy density, described by Eq. 4.30. The energy density is shown in Fig. 4.10 for a range of different AC field strengths at different points in the field cycle, when the axis is aligned with the field (so when $\phi = \theta$ in Eq. 4.30).

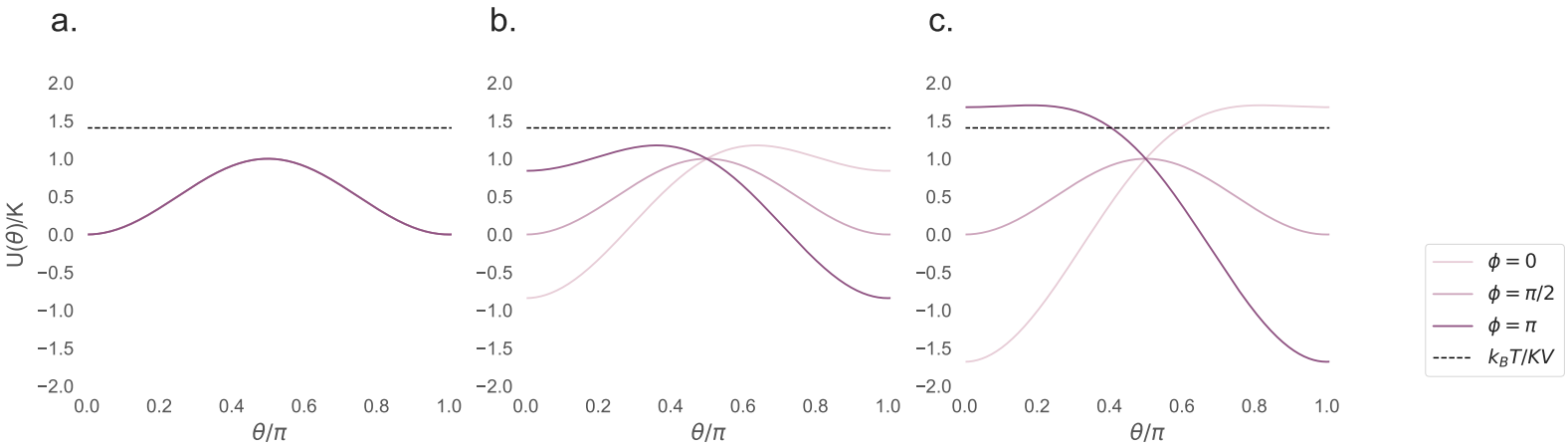

Figure 4.10: Energy density (Eq. 4.30) for a 10 nm particle as a function of θ, the angle between the particle magnetic moment and the applied field, for different values of ϕ, the angle between the particle magnetic moment and particle axis. The thermal energy density k_BT/KV is also shown a. No external applied field b. 10 mT/μ_0 applied field. c. 20 mT/μ_0 applied field.

For small applied fields, the energy density has two minima at all times, and so the particle has enough thermal energy to spontaneously flip. Increasing the particle size will lower the effective thermal energy k_BT/KV_c, which will increase the relaxation time. As the field is increased, asymmetry is introduced, lowering the effective energy barrier and shortening the relaxation time. For high fields, larger particles will no longer have enough thermal energy to spontaneously flip, and the rotation becomes purely driven by the field. The timescale of rotations will become highly dependent on applied field frequency, rather than the core volume.

So far, we have only examined the effect of increasing magnetic core volume, rather than total hydrodynamic volume. Unlike increasing core size, adding a non-magnetic coating does not necessarily have the effect of decreasing the relaxation time, as shown in Fig. 4.11. The zero-field Brownian relaxation timescale, τ_B, is dependent only on hydrodynamic volume, implying that for Brownian particles, increasing core diameter should have the same effect on the dynamics as increasing the coating size. However, Fokker-Planck eigenvalue calculations

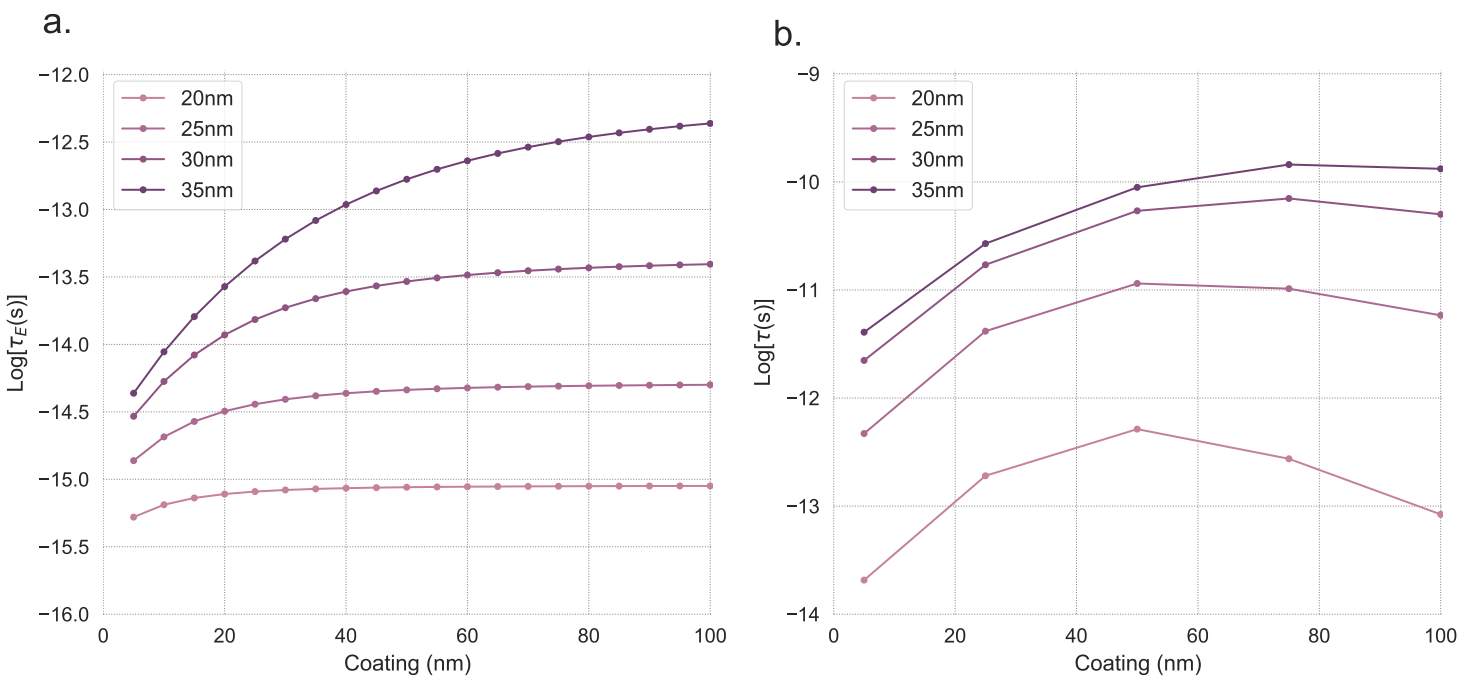

Figure 4.11: a. Effective relaxation time, extracted from Fokker-Planck equations, as a function of coating size, for four different core diameters, under a 20 mT/μ_0 applied field. a. Effective relaxation time, extracted from stochastic simulations, as a function of coating size, for four different core diameters, under a 20 mT/μ_0 and 1 kHz applied field.

(Fig. 4.11a.) indicate that this is not the case; increasing only the coating size results in an increase of $\tau_{E,F}$, in contrast to the decrease of $\tau_{E,F}$ seen when increasing the core size. This is intuitive; increasing the non-magnetic coating has the simple effect of increasing the particle inertia, which will always increase the Brownian relaxation time, while increasing the core volume will affect the coupling to the magnetic field.

From the stochastic Langevin simulations (Fig. 4.11b.), we see that increasing the coating size does increase the effective relaxation time up to a point, but then results in a decrease of the relaxation time. This may be because for small coating sizes, both Brownian and Néel mechanisms can occur, so adding additional non-magnetic volume increases the inertia and slows the Brownian mechanism, which increases the effective relaxation time. Eventually, though, if the coating size is large enough, the Brownian mechanism is suppressed, because the particle's inertia is too large to enable physical rotation. At that point, the particle dynamics are dominated by the Néel mechanism, which will result in a decrease of the effective relaxation time.

To validate this interpretation, we can look at the motion of the magnetic moment $\hat{\mathbf{m}}$ and easy axis $\hat{\mathbf{n}}$ over time from the simulations, shown in Fig. 4.12 for two different coating sizes. Immediately, we see that the two mechanisms are coupled in a non-trivial way: in most cases, both the axis and the moment are changing in time, but are never fully aligned. For a relatively small (25 nm) non-magnetic coating (top), both the axis and the moment rotate significantly. For a large (100 nm) coating (bottom), the motion of the axis is almost entirely suppressed, and Néel relaxation clearly dominates. For both coating sizes, however, increasing core volume increases the axis displacement (the Brownian component).

4.3.1 Coupling of the relaxation mechanisms

It is commonly assumed (e.g. from Eq. 4.6) that the relaxation mechanism with the lower relaxation time for a given field strength and nanoparticle size will dominate. However, as seen in Fig. 4.12, the mechanisms are coupled, and the orientation of the easy axis will affect the rotation dynamics of the magnetic moment. We can first look at two simple cases

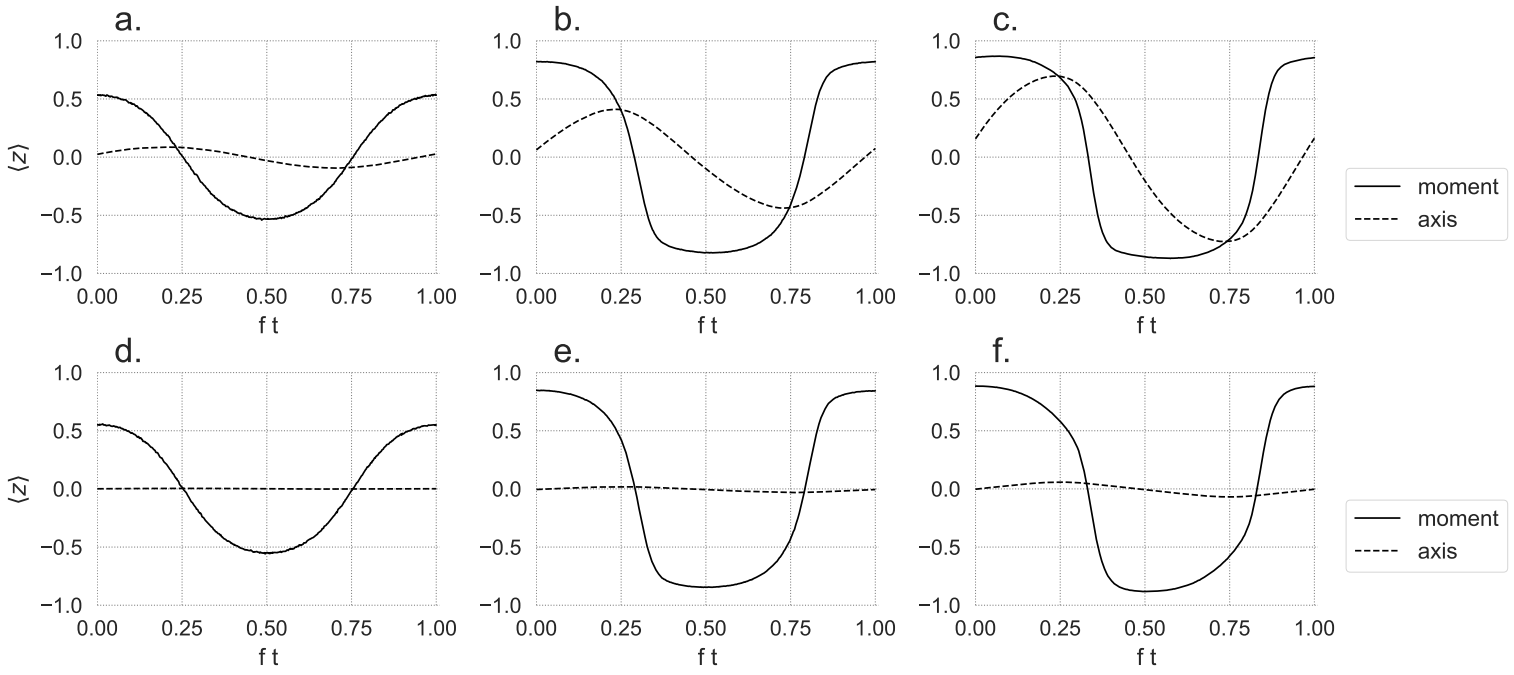

Figure 4.12: Stochastic simulations of average particle magnetic moment and average particle axis over time, under a 20 mT/μ_0 applied field. a. 15 nm core diameter, 25 nm coating. b. 25 nm core diameter, 25 nm coating. b 35 nm core diameter, 25 nm coating. d. 15 nm core diameter, 100 nm coating e. 25 nm core diameter, 100 nm coating. f. 35 nm core diameter, 100 nm coating.

where only Néel relaxation is allowed: first where the easy axes are oriented randomly, and second where the easy axes are aligned in the z-direction with the applied field (shown in red and blue, respectively, in Fig. 4.13a.). The dynamics of the magnetic moment are clearly significantly different in both cases; when the axes are aligned, the phase lag is increased, corresponding to an increase in the relaxation time. We can then look at the scenario where the axis is allowed to move as well, so both mechanisms are in place (shown in black). The relaxation time is clearly somewhere in between the first two cases; the axes align with the field, which increases the energy barrier, but since the axis can rotate once the field switches, the energy barrier is not as high as in the Néel-only case where the axes are aligned. A relatively low frequency (5 kHz) was used in the simulations shown in Fig. 4.13, so that the axes had enough time to fully rotate. Frequency dependence will be explored further in the following section.

We can further investigate the dynamics when both mechanisms are in place by looking at the applied field and internal energy, for example in Fig. 4.13b. The simulations indicate that the magnetic moment rotates first to align with the field. As the field flips from positive to negative, the energy begins to increase as the moment follows the field. The axis then rotates to minimize the internal energy. When the axis has rotated to align with the field, the moment now has a higher energy barrier to cross (compared to if the axis was randomly oriented, or perpendicular to the field). This indicates that depending on axis alignment, the Néel mechanism alone might be longer or shorter than when both mechanisms are in place. However, the energy minima are lower than they would be if the axis was unable to move (compare to the red line in Fig. 4.13a.). So allowing the axis to move results in a higher phase lag but lower minima, which means the steepness of the magnetization curve (which is the relevant characteristic for MPI signal) may increase.

The simulations indicate that even for different field strengths, the rotation of the axis is slower than the rotation of the moment (Fig. 4.14). So even under conditions where the Brownian mechanism should fully dominate (low frequency fields, large core sizes), the axis still lags behind the moment. It has been suggested that differences in Brownian vs.

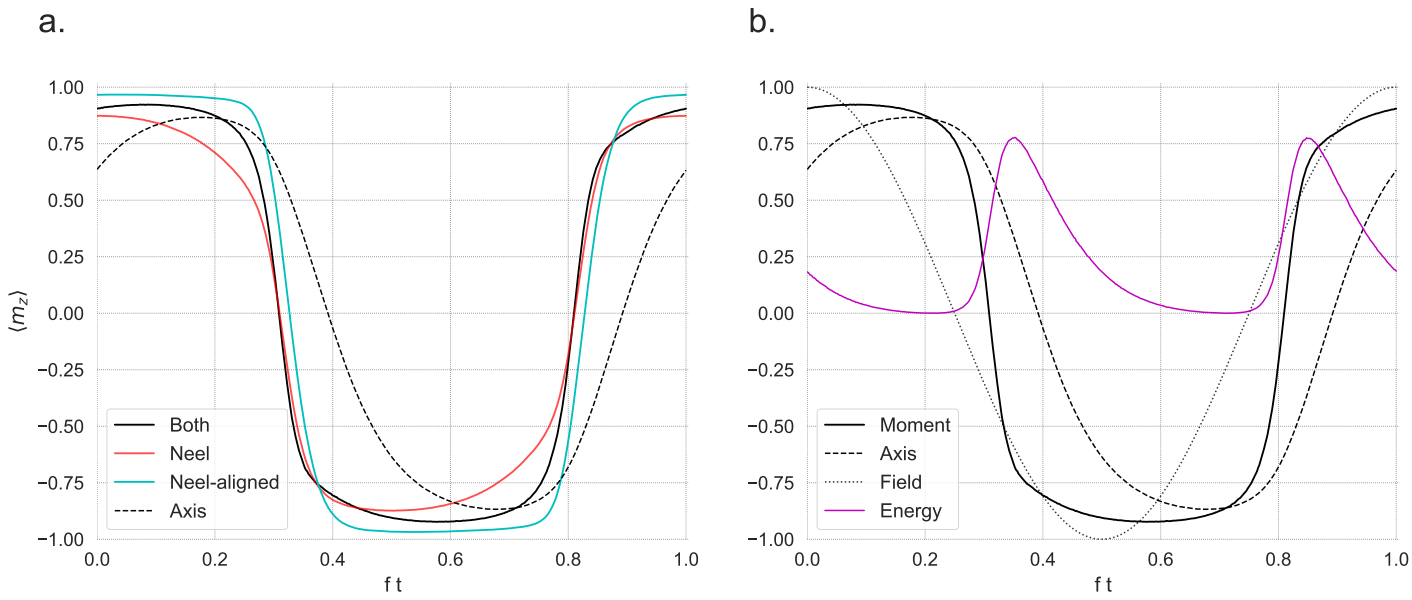

Figure 4.13: a. Stochastic simulations of the average magnetic moment (black) and axis (dashed) of a 35 nm particle with a 50 nm coating under a 20 mT/μ_0, 5 kHz applied field, undergoing both Brownian and Néel rotation. The simulated magnetic moment is also shown when the particle is immobilized and only able to rotate via Néel rotation, when the axes are randomly oriented (red) and aligned in the z-direction with the applied field (cyan). b. Stochastic simulations of the average magnetic moment (black) and axis (dashed) of a 35 nm particle with a 50 nm coating under a 20 mT/μ_0, 5 kHz applied field, undergoing both Brownian and Néel rotation. The normalized applied field (gray) and internal energy density (magenta) are also shown.

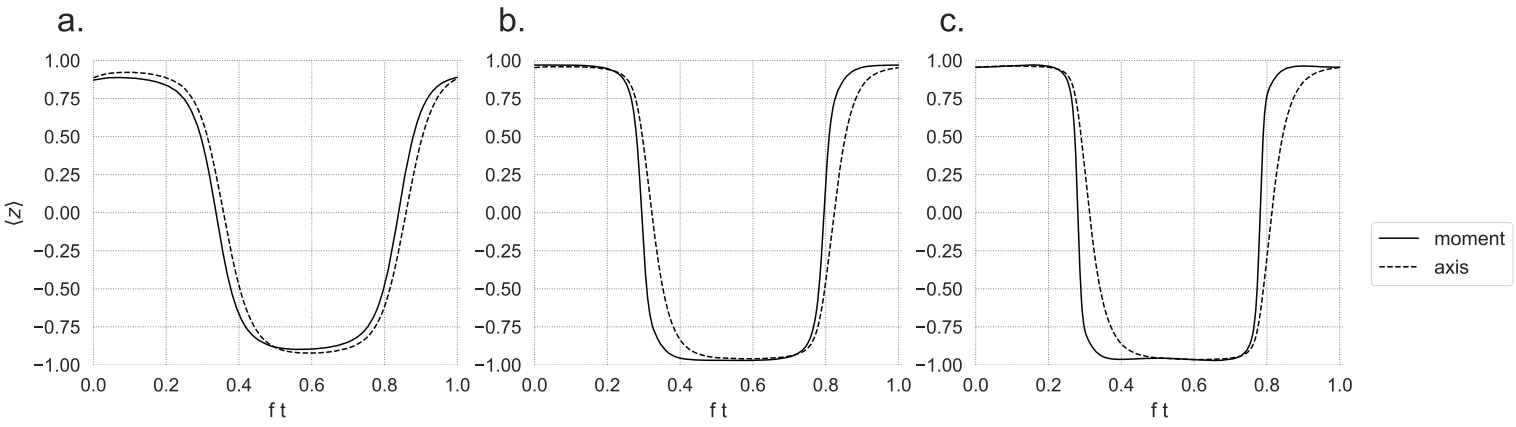

Figure 4.14: Stochastic simulations of average particle magnetic moment and axis over time for a 35 nm particle with 25 nm coating, under a 25 kHz ac field with amplitude 10 mT/μ_0 (a.), 20 mT/μ_0 (b.), and 30 mT/μ_0 (c.).

Néel dynamics occur because of the ramping of the AC field [79]. Since the Néel DC field relaxation timescales are longer than the Brownian timescales under low fields (e.g. Fig. 4.1), it has been predicted that the Brownian mechanism should dominate, even for high fields. To test that hypothesis, a step function field was simulated. For all the parameters tested (15 nm$< d_c <$50 nm, 1 kHz$\leq f \leq$100 kHz, 5nm$\leq$ coating $\leq$ 100 nm, 5 mT/$\mu_0 \leq H_0 \leq$ 50 mT/μ_0), both for the step function field and AC field, the axis lagged behind the moment (Fig. 4.15). This indicates that DC field relaxation timescales are inadequate when predicting AC dynamics.

4.4 Frequency dependence of relaxation timescales

A key feature of the AC particle dynamics, which will affect the phase lag and relaxation time, is the applied field frequency. When an AC magnetic field is applied, it is necessary to compare the effective relaxation time with $1/f$. If $\tau > 1/f$, rotation of the particle magnetic moment will not occur. If $\tau \ll 1/f$, then we can assume adiabatic conditions, and equilibrium behavior will occur. Calculating τ from Eqs. 4.13 and 4.18, however, would indicate that above 25 nm, $\tau > 1/f$ for frequencies above 25 kHz, and so particles of that

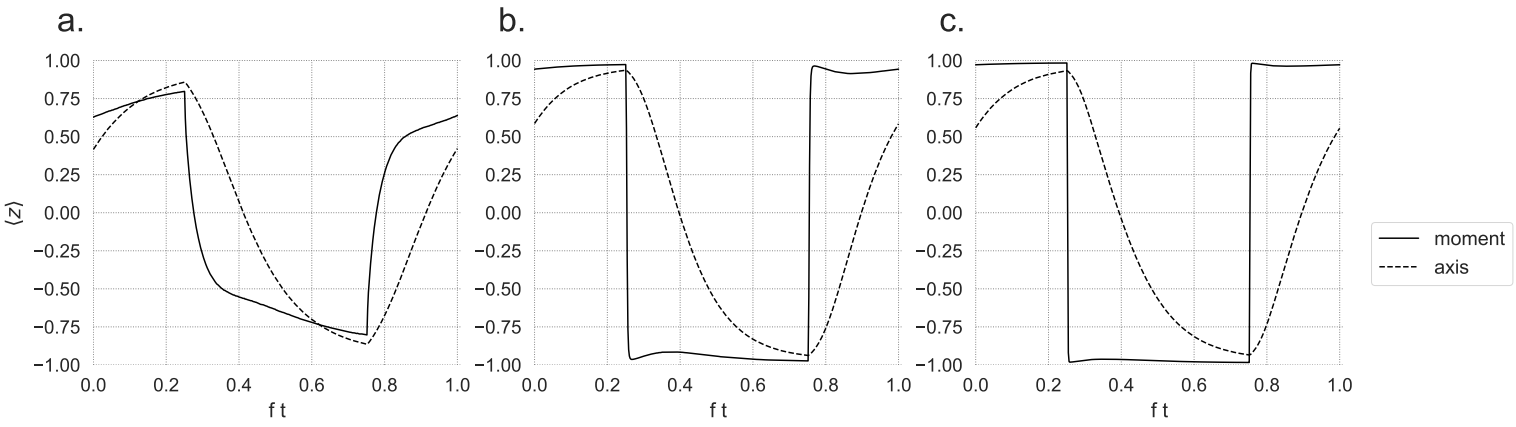

Figure 4.15: Stochastic simulations of average particle magnetic moment and axis over time for a 35 nm particle with 25 nm coating, under a 25 kHz step function field with amplitude 10 mT/μ_0 (a.), 20 mT/μ_0 (b.), and 30 mT/μ_0 (c.).

size would be unable to rotate. We see similar predictions from the Fokker-Planck eigenvalue calculations, for particles with 50nm or larger coatings. Clearly some aspect of the theory is incomplete, as evidenced by a large amount of MPS and MPI data.

The reason for the inconsistency is that the particle dynamics are directly affected by frequency. The phase lag is directly a function of frequency: $\tan\phi = \omega\tau$, where $\omega = 2\pi f$, so increasing the applied frequency will increase the phase lag. However, the applied frequency affects the relaxation time as well, as seen with simulations in Fig 4.16. The relaxation time decreases dramatically with frequency, particularly for frequencies < 20 kHz, for both cases (when only Néel relaxation occurs and when both mechanisms are possible). The phase lag, therefore, will be affected in a non-trivial way, since as ω increases, τ decreases.

Larger particles will be more strongly affected by frequency, as seen in Fig. 4.17. The magnitude of the phase lag generally increases with particle size as well as with frequency, but the dependence is much stronger for large particles. For 20 nm particles, increasing the frequency from 1 kHz to 100 kHz changes the phase lag by about 0.15 radians. For 35 nm particles, however, changing the frequency by the same amount results in an increase in the phase lag of around 0.45 radians, three times as large. A similar trend is seen with

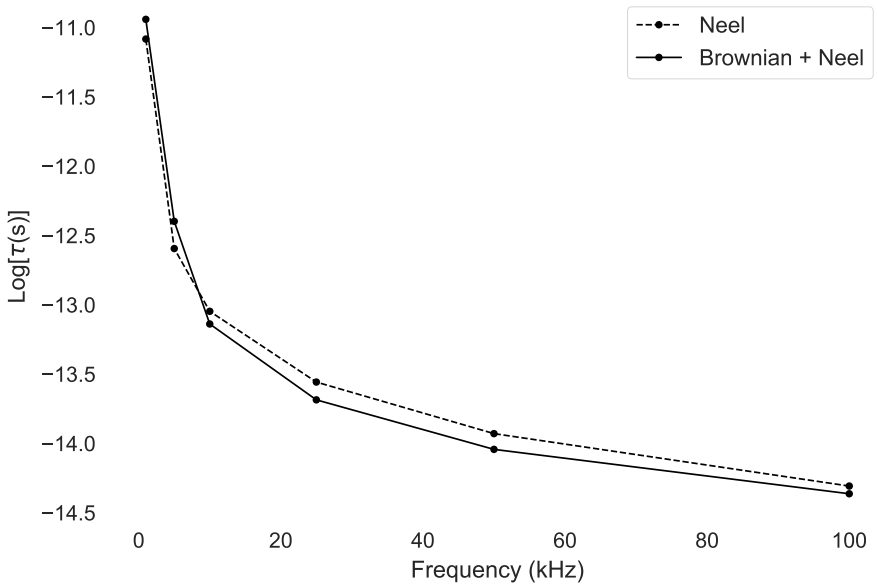

Figure 4.16: Relaxation time as a function of frequency extracted from stochastic simulations with an applied field of 20 mT/μ_0, 25 nm core size, and 50 nm coating. Results are shown for immobilized particles, where only Néel relaxation can occur, as well as particles dispersed in water where both Brownian and Néel relaxation may occur.

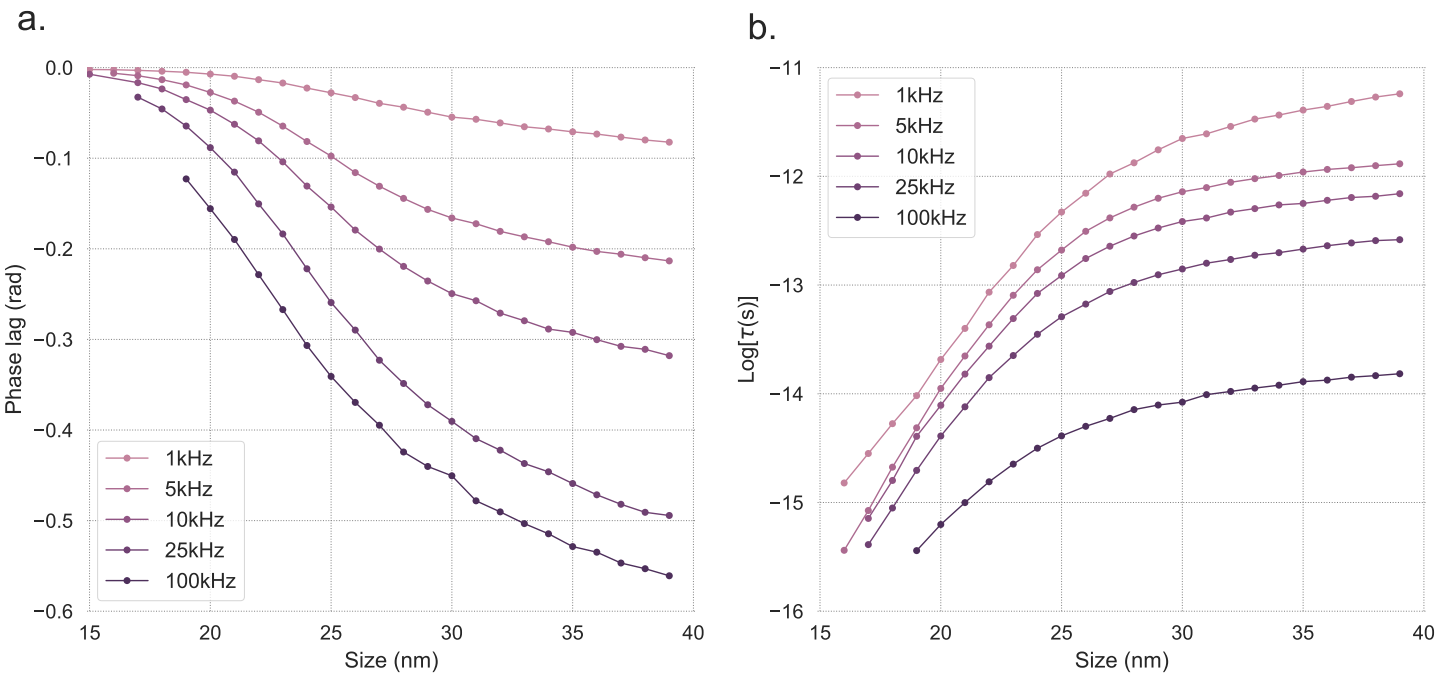

Figure 4.17: a. Phase lag as a function of core size extracted from stochastic simulations with an applied field of 20 mT/μ_0 and 5 nm coating for a range of frequencies. b. Relaxation time as a function of core size extracted from stochastic simulations with an applied field of 20 mT/μ_0 and 5 nm coating for a range of frequencies.

the relaxation time in Fig. 4.17b.: larger particles have a higher relaxation time overall, and experience a more dramatic decrease in relaxation time with increasing frequency.

We can look at the effect of changing frequency on relaxation mechanism by examining the motion of the axis and moment separately. Since the Brownian mechanism is slower and lags behind the Néel mechanism (as seen in the previous section), it will be more strongly affected by frequency. We can see this in Fig. 4.18, where increasing the frequency suppresses the axis motion. When the frequency is high enough, the axis cannot rotate quickly enough to align with the field. The magnetic moment, however, is still able to rotate and generate a signal. This helps explain why larger particles are more affected by frequency; larger particles will have a larger Brownian relaxation component, which is more strongly affected by frequency.

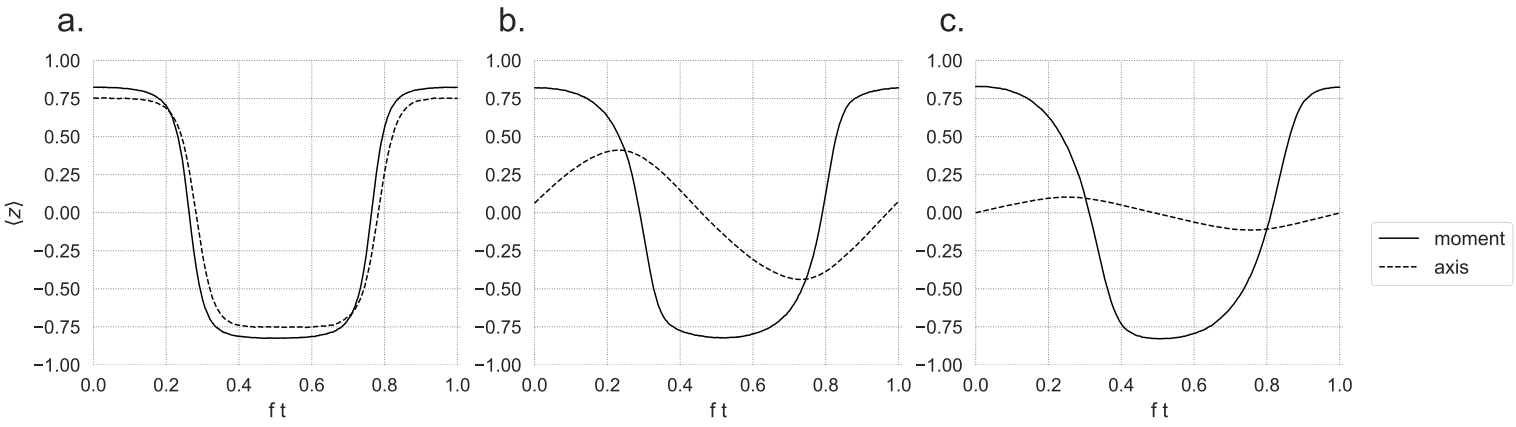

Figure 4.18: Stochastic simulations of average particle magnetic moment and axis over time for a 25 nm particle with 25 nm coating, under a 20 mT/μ_0 field with frequency 1 kHz (a.), 25 kHz (b.), and 100 kHz (c.).

4.4.1 Slew rate dependence of relaxation timescales

Several studies have demonstrated [54, 111] that rather than separating frequency and field strength, the magnetic slew rate (the product of the field amplitude and frequency, $H_0 f$) can be considered as a parameter as well. We can see this in Fig. 4.19, where the relaxation time from simulations is plotted against magnetic slew rate. We can fit a single curve:

$$\tau = \frac{A}{(H_0 f)^B}, \tag{4.31}$$

where the least squares best fit resulted in A = 2.0×10^{-4} and B = 0.8. The fit seems to overestimate τ for lower frequency values and underestimate for higher frequency values, but overall it does appear to provide a single fit to all slew rate values.

4.5 Conclusion

In this chapter, we have explored in depth the dependence of various factors on the relaxation time, which is a key component in describing the dynamics of MNPs for MPI. Several different methods were used, which each have benefits and require different approximations.

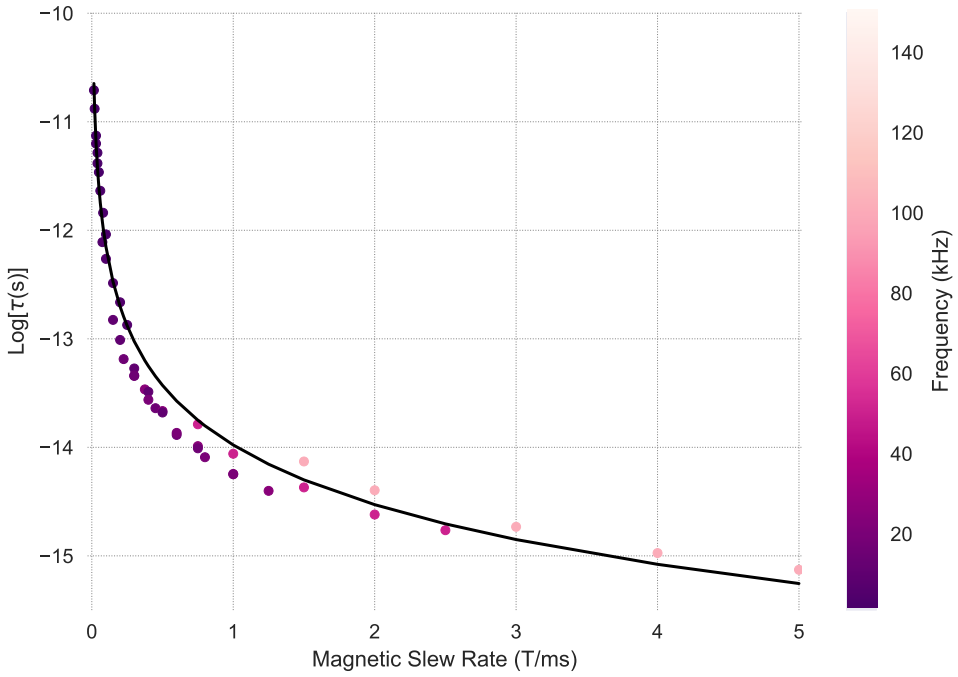

Figure 4.19: Relaxation time extracted from stochastic simulations as a function of magnetic slew rate for a 25 nm particle with 50 nm coating. Least squares fit is shown in black.

Theoretical models are useful to gain a basic understanding of the dependence of the relaxation time on certain parameters, but they are clearly incomplete. There is no fully complete theoretical model that describes the relaxation time of nanoparticles under AC fields including coupled Brownian and Néel rotation. Fokker-Planck equations are useful in that they require minimal computation time, and provide insight into the two different rotation mechanisms separately. However, the Brownian and Néel equations alone do not allow for consideration of coupled motion, and solutions to the Néel equation require the MNP easy axis to be aligned with the field, which will not necessarily result in realistic solutions. Stochastic Langevin simulations do allow for simulation of coupled motion, but are computationally expensive, and do not provide any analytic solutions.

Results from all methods indicate that the relaxation time decreases significantly with applied field amplitude. Clearly, the zero-field relaxation timescales are inadequate to accurately describe nanoparticle relaxation behavior. The two relaxation mechanisms are affected differently by the applied field strength: the Brownian mechanism is less sensitive to field strength. Because of this, the Néel mechanism may dominate even when the zero-field Néel timescale τ_N is much longer than τ_B. This means that there can be a strong magnetic response even if the particles are physically immobilized.

It is often assumed that particles used for MPI (25 nm and larger) are dominated by Brownian relaxation. The studies here indicate that this is not necessarily the case; the two mechanisms are coupled, and the moment rotates first, followed by the axis. The exact mechanism is highly dependent on coating and field, which are often ignored; the core size alone does not predict the relaxation mechanism. For large non-magnetic coatings, the motion of the axis is almost completely suppressed. Increasing the core size, in general, though, does increase the Brownian component, if coating size remains the same.

The frequency affects the relaxation time and mechanism as well: since the moment rotates faster than the axis, the Brownian mechanism will affected by frequency to a greater degree. For high frequencies, the motion of the axis may be completely suppressed. Increasing frequency and field amplitude appear to have a similar effect on the resulting dynamics, since

the relaxation time appears to follow a dependence on slew rate. Increasing slew rate, then, has the effect of suppressing the Brownian mechanism and reducing the overall effective relaxation time.

		coating size					
		25 nm		50 nm		100 nm	
		low $H_0 f$	high $H_0 f$	low $H_0 f$	high $H_0 f$	low $H_0 f$	high $H_0 f$
core size	20nm	B	C	C	N	N	N
	25 nm	B	N	B	N	N	N
	30 nm	B	N	B	N	C	N

Table 4.1: The dominant relaxation mechanism for different particle sizes and slew rates. The relaxation mechanism is indicated to be Néel-dominated (N), Brownian-dominated (B), or a combination (C).

Results are summarized generally in Table 4.1. For each set of conditions, the dominant relaxation mechanism is indicated. For cases where the axis motion was 40-60% of that of the moment motion, the relaxation mechanism is marked as "C", indicating that both relaxation mechanisms contributed significantly (see, as an example, Fig. 4.18b.). In this table, the low $H_0 f$ corresponds to a field amplitude $H_0 = 20$ mT$/\mu_0$ and frequency $f = 5$ kHz, and the high $H_0 f$ corresponds to a field amplitude $H_0 = 20$ mT$/\mu_0$ and frequency $f = 100$ kHz. As discussed previously, the Brownian mechanism is suppressed as coating size and slew rate increases. In the following chapter, we will use these insights directly to optimize field conditions and nanoparticle properties for MPI performance.

Chapter 5

OPTIMIZATION OF NANOPARTICLE SIZE AND DRIVE FIELD FOR MPI

5.1 Relevant parameters for signal generation in MPI

With developments in hardware, software, and tracer technology, there has been significant progress in recent years towards improving MPI image quality. However, in order for MPI to become a fully viable and competitive medical imaging platform, further progress in this area is required. The quality of an MPI image is defined by the signal amplitude, which determines the signal-to-noise ratio (SNR) and the sensitivity (the minimum detectable concentration of MNPs), and the spatial resolution. In particular, the spatial resolution of current prototype MPI scanners still lags behind that of MRI or CT, so improving MPI image resolution is a key focus of present investigation.

The spatial resolution of a given MPI image is dependent on hardware parameters, such as the gradient field and the strength of the saturation field. The resolution will be directly (inversely) proportional to the gradient field; current scanners use a gradient field of $1-7$ $(\mathrm{T/m})/\mu_0$ [54]. It is well known that increasing the gradient field will improve resolution, but current scanners are encountering hardware limits that make further increases difficult. The properties of the MNP tracers used for imaging will also directly affect the spatial resolution. Improving MNP saturation magnetization (by controlling phase/oxidation state) and controlling shape, crystallinity, and monodispersity of MNP tracers will improve both signal strength and resolution. Development of highly monodisperse single-phase spherical magnetite MNPs has so far resulted in significant improvement in MPI image quality [112].

According to Langevin theory, the image resolution should be inversely proportional to the MNP core volume, and signal strength should be proportional to the square of the

volume [52, 89]. In this model, then, increasing the nanoparticle core size should result in a dramatic effect on image quality, and so it is often assumed that increasing particle core size will have a unilaterally positive effect on image quality, as long as the particles stay small enough to fall under the superparamagnetic limit. However, once particle core size reaches a certain point, relaxation effects become more pronounced [112, 113]. Practical limits on performance improvement will therefore arise from increasing core size indefinitely. Previous results have indicated that large core sizes can result in image blurring [112,114–117] and reduced signal-to-noise ratio (SNR) [46, 115, 118]. Furthermore, in practice, as core size is increased, dispersing MNPs in water and maintaining their monodispersity becomes significantly more difficult due to increased interparticle magnetostatic interaction strength. It has been shown that by controlling drive field conditions (frequency and amplitude), substantial improvements to signal and resolution can be made [54]. Further improvements, to make MPI competitive with other medical imaging platforms, will therefore require a nuanced understanding of the relaxation physics.

To estimate the signal strength and resolution of the resulting image generated from a particular MNP tracer, we study the point-spread function (PSF), which is the derivative of the particle magnetization with respect to applied field (which for this application will be an AC sinusoidal field). The height of the PSF will define the sensitivity and indicate the signal-to-noise ratio (SNR) of the resulting image. The full-width-at-half-maximum (FWHM) of the PSF peak will give an indication of the spatial resolution. When defining resolution, we consider the minimum distance that two samples can be separated by while remaining separately identifiable. This requires the existence of a significant signal minimum between the two samples, such that the minimum value of the signal in between the samples is less than half of the maximum value at the sample positions. From that definition, we can then approximate resolution from a single sample by the FWHM of its PSF. In this chapter, we will measure the FWHM in mT/μ_0, but can easily convert this measurement to a spatial value, e.g. in millimeters, by dividing by the strength of the gradient field used in the MPI scanner. For a 1 $(\mathrm{T/m})/\mu_0$ gradient field, for example, a FWHM of 1 mT/μ_0 would

correspond to a predicted spatial resolution of 1 mm.

The strength of the signal, which will determine the sensitivity and SNR, will be proportional to the MNP concentration, as well as the MNP saturation magnetization and core volume. The signal strength will also be related to the sensitivity and noise resistance of the receive coil, as well as the total measurement time. Temporal resolution, therefore, will scale inversely with sensitivity and SNR.

To optimize MPI performance, we want to maximize signal strength and minimize the FWHM of the PSF. To model the PSF from a given MNP tracer, we refer to the image equation from §2.3:

$$\hat{\rho}(x_s(t)) = \hat{\rho}_{\text{adiab}}(x_s(t)) * \left(\frac{1}{v_s\tau}\right) \exp\left(-\frac{x_s(t)}{v_s\tau}\right) u(x_s(t)) \tag{5.1}$$

The PSF, $\hat{\rho}$, is expressed as a convolution of the adiabatic signal $\hat{\rho}_{\text{adiab}}$ (which we assume to be the derivative of the Langevin function), and a relaxation term. The PSF will be a function of the location of the field-free point, x_s, and the velocity of the scanner, v_s. Here, a Debye relaxation kernel has been assumed, which assumes that MNP relaxation is governed by a first-order differential equation, and is expressed as a product with the Heaviside step function, u. The relaxation time τ which defines this relaxation term was discussed extensively in the previous chapter, and will be dependent on the applied field frequency and amplitude, as well as the physical characteristics of the MNP tracer.

The peak of the adiabatic PSF, $\hat{\rho}_{\text{adiab}}$, again referencing §2.3, will be:

$$M'(0) = \frac{n\mu_0(M_sV_c)^2}{3k_BT}, \tag{5.2}$$

where n is the tracer concentration. Clearly, this predicts that the signal strength should scale as the square of the core volume, V_c; however, when convolved with the relaxation term, the PSF peak will decrease by some as yet undetermined degree.

The FWHM, Δx, of the PSF will also result from the convolution of the adiabatic PSF and the relaxation kernel. There is currently no closed analytical form of the solution to the

convolution. However, following others, we can reasonably approximate the nonadiabatic FWHM as a weighted sum of the adiabatic resolution Δx_{adiab} and the blur from relaxation Δx_{relax} [54]:

$$\Delta x \approx \alpha \Delta x_{\text{adiab}} + \beta \Delta x_{\text{relax}}. \tag{5.3}$$

The FWHM of an exponential decay function in the form $f(t) = \exp(-t/\tau)$ will be $\tau \ln(2)$. Using this, the FWHM of the relaxation term will be:

$$\Delta x_{\text{relax}}(H_0, f_0) = \ln(2) v_s \tau(H_0, f_0). \tag{5.4}$$

We can rewrite this in terms of the frequency and amplitude of the applied field, using the fact that $v_s = 2\pi f_0 H_0 / G$, where f_0 is the frequency of the applied field, H_0 is the amplitude of the applied field, v_s is the velocity of the scanner, and G is the magnetic field gradient:

$$\Delta x_{\text{relax}}(H_0, f_0) = \ln(2) \frac{2\pi f_0 H_0 \tau(H_0, f_0)}{G}. \tag{5.5}$$

The FWHM can also be expressed in terms of phase lag ϕ, equal to $2\pi f_0 \tau$ for small values of ϕ, which will be a function of the applied field (but is generally assumed to be independent of frequency) [54]:

$$\Delta x_{\text{relax}}(H_0) = \frac{\ln(2) \phi(H_0) H_0}{G} \tag{5.6}$$

Again referencing §2.3, the FWHM of the adiabatic PSF (the derivative of the Langevin function) is:

$$\Delta x_{\text{adiab}}(V_c) = \frac{4.16 k_B T}{\mu_0 M_s V_c}. \tag{5.7}$$

In reality, for frequency-space systems, the FWHM is not perfectly indicative of the spatial resolution. A more realistic estimate, taking into account additional hardware parameters, is [119]:

$$R = \frac{2\pi k_B T}{\log\left(\frac{2pH_0 f_0 n k_B T}{\sigma G}\right)\mu_0 M_s V_c G}, \tag{5.8}$$

where p is the receive coil sensitivity and σ is the noise level. While this expression may be more accurate, for our purposes, we will revert to the FWHM approximation, to avoid dependencies on scanner specifications like coil sensitivity. Also, due to the logarithm in the denominator, the $k_B T/M_s V_c$ term will dominate regardless, as in Eq. 5.7. For the remainder of this chapter, then, Δx will refer interchangeably to the FWHM of the PSF and the predicted image resolution.

The values for α and β in Eq. 5.3 have been experimentally determined from least-squares fitting [54], and are on the order of 1. Each term, then, will have a meaningful effect on the resulting resolution, so understanding their relative contributions will be key to optimization for resolution as well as sensitivity. Since the adiabatic term is proportional to MNP core volume but not the drive field, we can study the effects of relaxation by varying the field. As discussed in the previous chapter, the relaxation time decreases with field amplitude and frequency, but generally increases with size. In this chapter, we will explore the effects of relaxation behavior on the resulting MPI signal, and use that information to inform optimization of drive field and MNP size for MPI.

5.2 Drive field optimization

We begin by examining the effects of drive field amplitude and frequency on MPI image resolution and SNR, with the goal of identifying optimal field conditions for best resolution and maximal SNR. The effect of field amplitude, frequency, and magnetic slew rate on PSF is first examined using nonlinear stochastic simulations, and then supported by magnetic particle spectroscopy (MPS) measurements.

5.2.1 Stochastic simulation procedure and results

Using the stochastic simulation program developed in §3, the PSF was generated for a range of particle sizes, field amplitudes, and field frequencies, and the PSF peak and FWHM were extracted. Simulations were performed with $K = 5$ kJ/m^3 and $M_s = 420$ kA/m. As expected, increasing drive field amplitude increases the total signal, indicated by the maximum height of the PSF, shown in Fig. 5.1b.

However, the FWHM also increases with increasing applied field strength, as seen in Fig. 5.1a. This is an interesting result, because, as discussed in the previous chapter, nanoparticle relaxation time decreases significantly with applied field amplitude. Since the Langevin model is invariant to scanning parameters, the change in FWHM must be due to the relaxation term. We can see from Eq. 5.7 that the product $H_0\tau$ appears in the numerator, with all other parameters independent of field amplitude. So, even though the relaxation time decreases with field strength, it must not decrease quickly enough to compensate for the H_0 multiplicative term. For improved resolution, then, a lower drive field amplitude should be used; however, lowering the field amplitude will also result in lower SNR.

Changing drive field frequency has a similar effect to changing field amplitude: increasing frequency increases both FWHM and peak signal, indicated by Fig. 5.1c. and d. However, the exact dependence is subtly different; while Δx appears to increase fairly linearly with field, it appears to follow almost a logarithmic dependence with frequency, increasing sharply at first for low frequencies then leveling off at higher frequencies. The simulation results clearly indicate that image resolution is expected to improve with lower field amplitudes as well as lower drive field frequencies despite longer MNP relaxation time constants (the decrease of τ with increasing frequency was shown in §4.4). With everything else held constant, we see that Δx, in Eq. 5.5, will change as $f_0\tau$. This implies that, in an analogous manner to the field amplitude, the relaxation time drops more slowly than the frequency increases, so that the product of f_0 and τ increases with frequency.

The differences between changing field amplitude and frequency are investigated in Fig. 5.2.

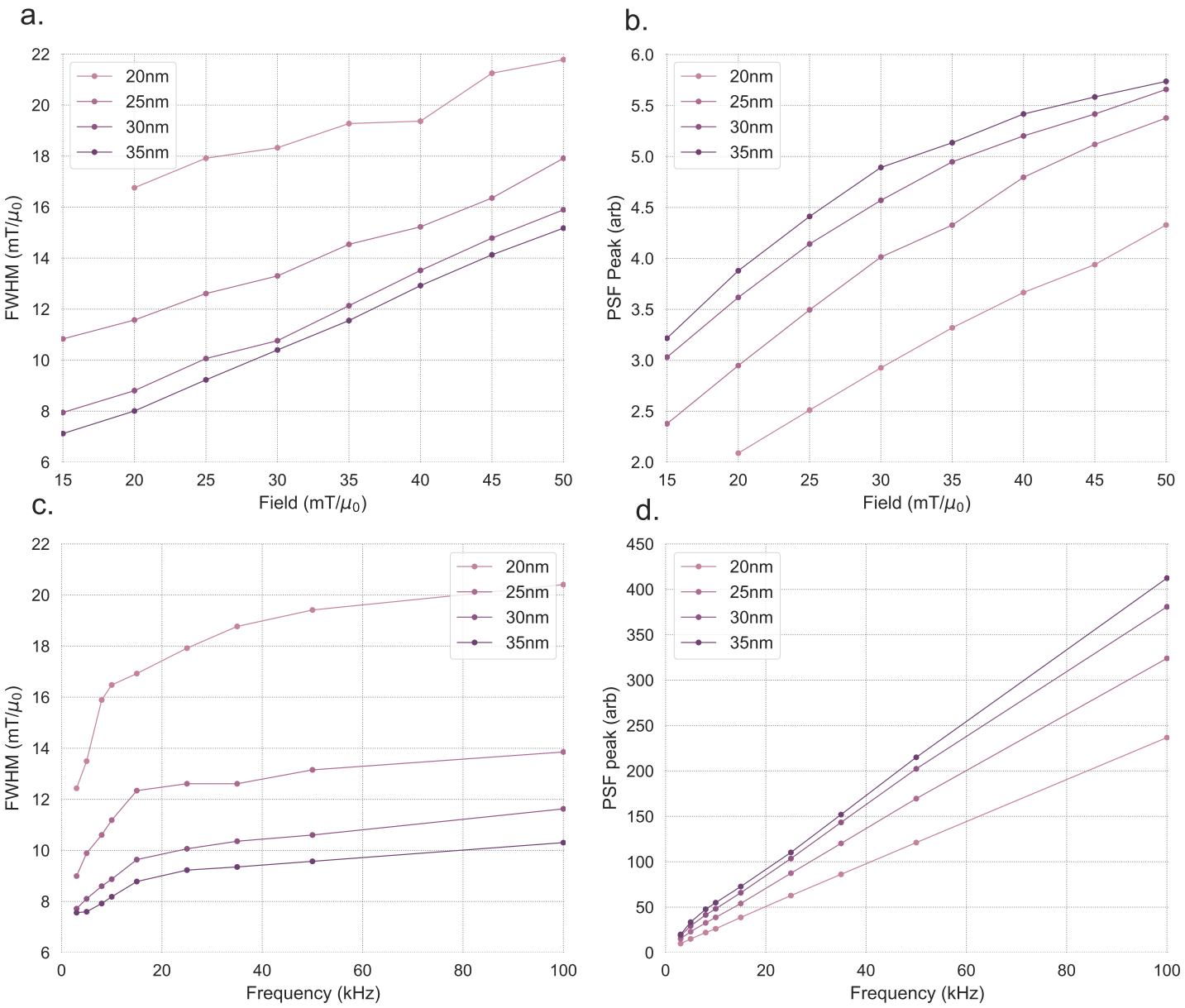

Figure 5.1: Results from stochastic simulations run with a 25 kHz drive field frequency (a. and b.) and 20 mT/μ_0 drive field amplitude (c. and d.) for four different core sizes. Resolution worsens with increasing field amplitude and frequency, while signal strength improves.

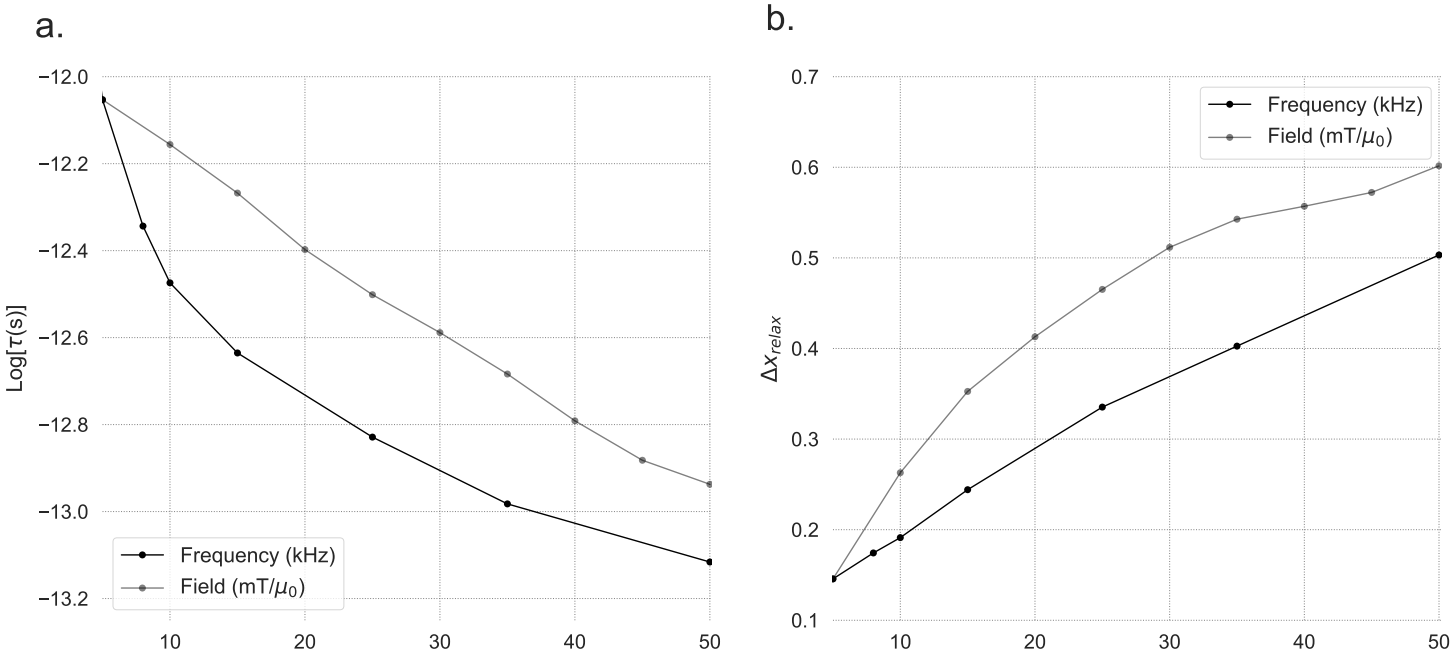

Figure 5.2: Relaxation time (a.) and FWHM (b.) as a function of applied field frequency and field for a 25 nm particle, generated from stochastic simulations. In the case of frequency (black), the horizontal axis has units of kHz, and in the case of field amplitude (grey), the horizontal axis has units of mT/μ_0.

When the field amplitude or frequency is increased by a factor of 10 (e.g. from 5 mT/μ_0 to 50 mT/μ_0 or from 5 kHz to 50 kHz), we can see that the relaxation time drops in both cases, but it drops faster with frequency than with field amplitude. Eq. 5.5 then indicates that Δx should increase more quickly with field amplitude than with frequency, which agrees with the simulation results shown in Fig. 5.2b.

For medical imaging purposes, scanning amplitude and frequency must be chosen to stay within the safety limits defined by limiting peripheral nerve stimulation (PNS) due to induced eddy currents in the body. This condition (the "Brezovich-Criterion") requires that the magnetic slew rate $H_0 \cdot f_0 \leq 615$ kHz·mT/μ_0 [120]. Previous results [54, 111] have indicated that magnetic performance is largely unchanged when the magnetic slew rate is held constant. This is examined in Fig. 5.3, where stochastic simulations indicate an approximately linear

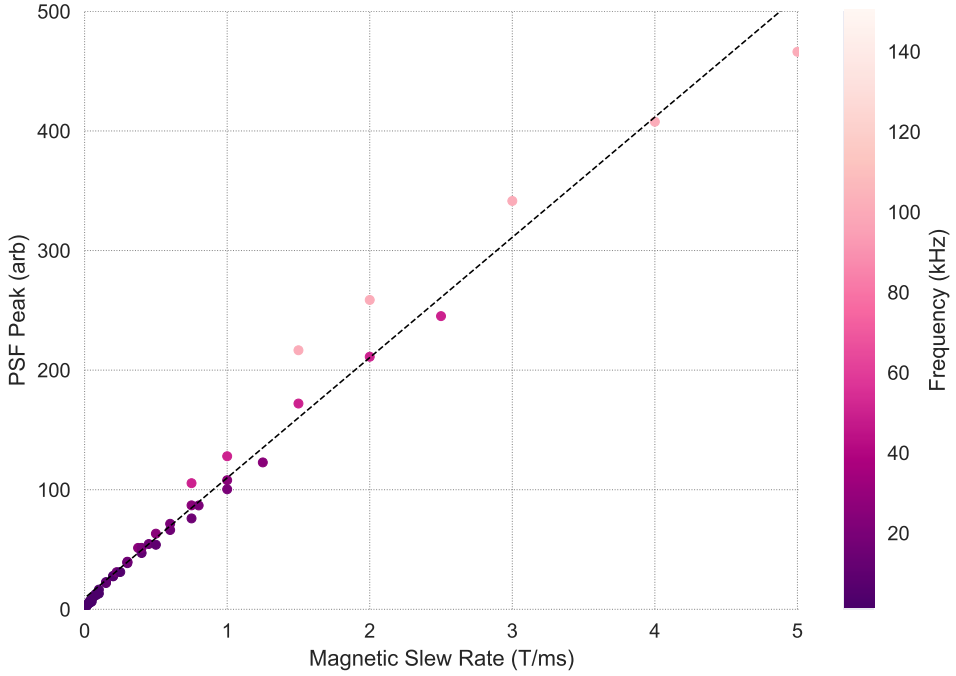

Figure 5.3: PSF peak as a function of magnetic slew rate for a 25 nm particle, generated from stochastic simulations.

increase in PSF peak with magnetic slew rate, despite some apparent subtle deviation with frequency. We can infer from this and from Fig. 5.1b. and d. that frequency and field amplitude both result in an approximately linear increase in signal strength as indicated by the PSF peak, and so can be seen as having an interchangeable effect on signal strength (in contrast to their effect on resolution).

These results indicate a potential avenue for field optimization: in order to minimize resolution, keep field amplitude low, and increase frequency to improve signal. Ultimately, for any applied field, there will be a trade-off between increased blurring due to relaxation and increased SNR. However, since field amplitude results in a greater increase in Δx compared to frequency, but has the same effect on SNR, frequency should be maximized rather than field amplitude, up to the medical safety criterion, to optimize for both image resolution and intensity. These conclusions, however, are so far primarily based on results from stochastic

simulations; next, we will test our results with magnetic particle spectroscopy (MPS).

5.2.2 Field dependence of the PSF from magnetic particle spectroscopy data

For MPS measurements, magnetite nanoparticles were synthesized according to a thermal decomposition process using an iron oleate precursor, as described in detail in [29]. Three particle sizes were used, with core diameters (size distribution parameters) of 21.9 nm (0.04), 25.3 nm (0.08), and 27.7 nm (0.07), assuming a log-normal distribution of core sizes. Size, size distribution, and crystallographic phase were determined with Transmission Electron Microscopy (TEM) images using ImageJ open source software. The nanoparticle cores were coated with a polyethylene glycol PEG-based amphiphilic polymer, resulting in respective hydrodynamic sizes (size distribution parameters) determined by Dynamic Light Scattering (DLS) of 94.3 nm (0.13), 77.1 nm (0.18), and 95.9 nm (0.15). Particles were dispersed in distilled water at a concentration of 0.9 gFe/l.

MPS measurements were performed on a home-built spectrometer, described in detail in [121]. The tracer magnetization response is recorded as the induced voltage in the receive coil. The system has a bandwidth of 1.04 MHz, allowing for detection of up to 40 harmonics after Fourier transform. Measurements of 150 μL aqueous solutions of particle samples were performed in triplicate and then averaged.

MPS results, shown in Fig. 5.4, generally agree with the generated simulation results. Due to the hardware limitations of the spectrometer, it was only possible to measure at three frequencies. However, the overall trends are still apparent; the FWHM and PSF peak both increase approximately linearly with both field and frequency, in agreement with Fig. 5.1. We can confirm our previous conclusion (also supported by Croft et. al [54]) that decreasing drive field amplitude, in particular, will improve image resolution, despite shorter relaxation timescales.

As is clear from Fig. 5.4, nanoparticle core size has a significant impact on the MPS signal as well. Once drive field has been controlled for optimal particle response, then, we can turn to the nanoparticle tracers themselves as an avenue for further MPI image improvement.

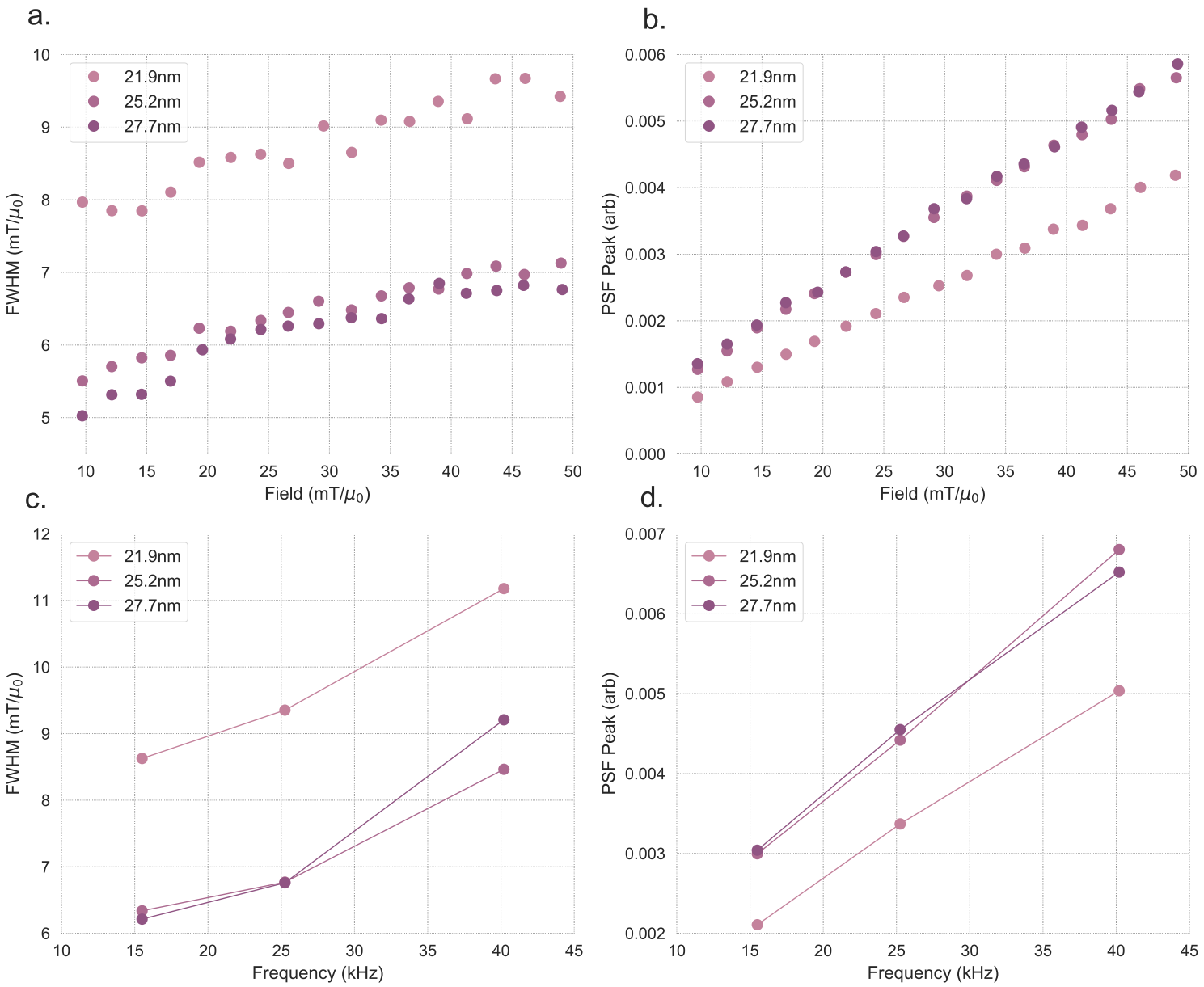

Figure 5.4: Results from MPS measurements run with a 15.5 kHz drive field frequency (a. and b.) and 25 mT/μ_0 field amplitude (c. and d.) for three different core sizes. Resolution worsens with increasing field amplitude and frequency, while signal strength improves with field amplitude and frequency.

5.3 Size optimization

We next investigate the effects of nanoparticle size on MPI signal. For a fixed MNP concentration and saturation magnetization (M_s), the signal strength (the peak of the PSF) will increase with magnetic core size, due to the increase in particle magnetic moment, $M_s V_c$. According to the Langevin model, Eq. 5.2 indicates that the PSF peak should scale as V_c^2, i.e. the sixth power of the core diameter, whereas the FWHM should scale as $1/V_c$, according to Eq. 5.7. Doubling the core diameter, then, would result in an eightfold improvement in the resolution, and a massive 64-fold improvement in the SNR. In reality, however, relaxation effects will somewhat diminish these theoretical improvements with nanoparticle size, and may even cause a decrease in MPI image quality with increasing core size. Defining and identifying whether there exists an optimal MNP core size for MPI will be the focus of this section.

5.3.1 Size dependence of the PSF from MPS data

We first investigate the effect of nanoparticle core size on the point-spread function with magnetic particle spectroscopy. MPS measurements of nanoparticles with three different core sizes and with three different field amplitudes were performed according to §5.2.2, with results shown in Fig. 5.5. Increasing particle size from 21.9 nm to 25.2 nm shows a significant improvement in signal, both in terms of resolution and signal strength. Further increasing the size from 25.2 nm to 27.7 nm, however, results in a much smaller improvement to both the FWHM and the PSF peak. In stark contrast to the predictions from Langevin theory, these results suggest that increasing the core size past ∼28 nm will not have a significant impact on the signal. It is clear that relaxation effects play a significant role for particles at these core sizes.

Both terms in Eq. 5.3 describing the FWHM of the PSF are dependent on size, unlike in the previous section where only the relaxation term was field-dependent. The adiabatic term (Δx_{adiab}) will decrease with MNP core size, while the relaxation term (Δx_{relax}) is

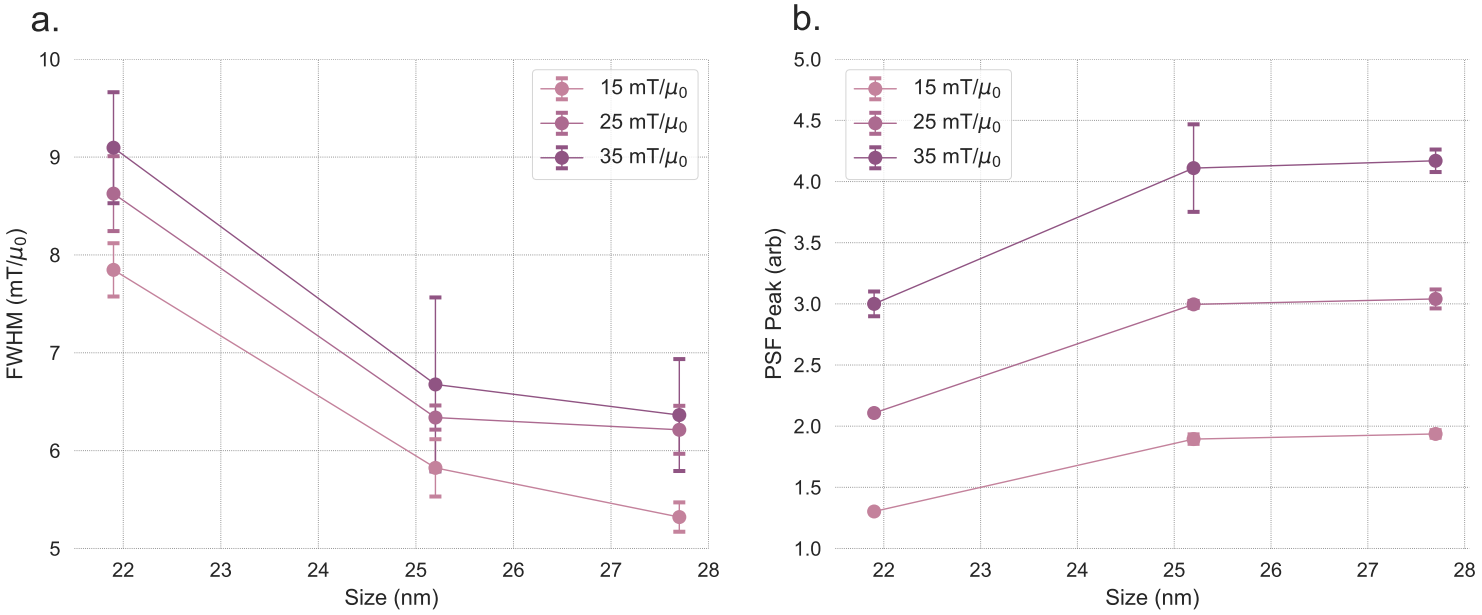

Figure 5.5: Results from MPS data taken with a drive field frequency of 15.5 kHz. Resolution and signal strength improve with increasing core size.

dependent on the MNP relaxation time τ. The relaxation time is a complex function of size, as was explored in the previous chapter, and there is no analytical expression to describe the dependence of core size on the effective relaxation time. To investigate further, we turn to stochastic simulations to study the behavior and effects of changing size.

5.3.2 Simulation and theoretical investigation of optimal core size

Simulations of Langevin equations were performed according to the parameters specified in §3 and §5.2.1. Examining simulation results in Fig. 5.6, we can see that the PSF peak does increase with core size, but not nearly as rapidly as predicted by the Langevin model. Once the size is increased past $\sim 25 - 30$ nm, the slope decreases significantly. These simulation results agree with the MPS data (e.g. Fig. 5.5b.), again indicating that the particle relaxation behavior has a significant effect on the signal, becoming more important with larger sizes, and lowering the PSF peak.

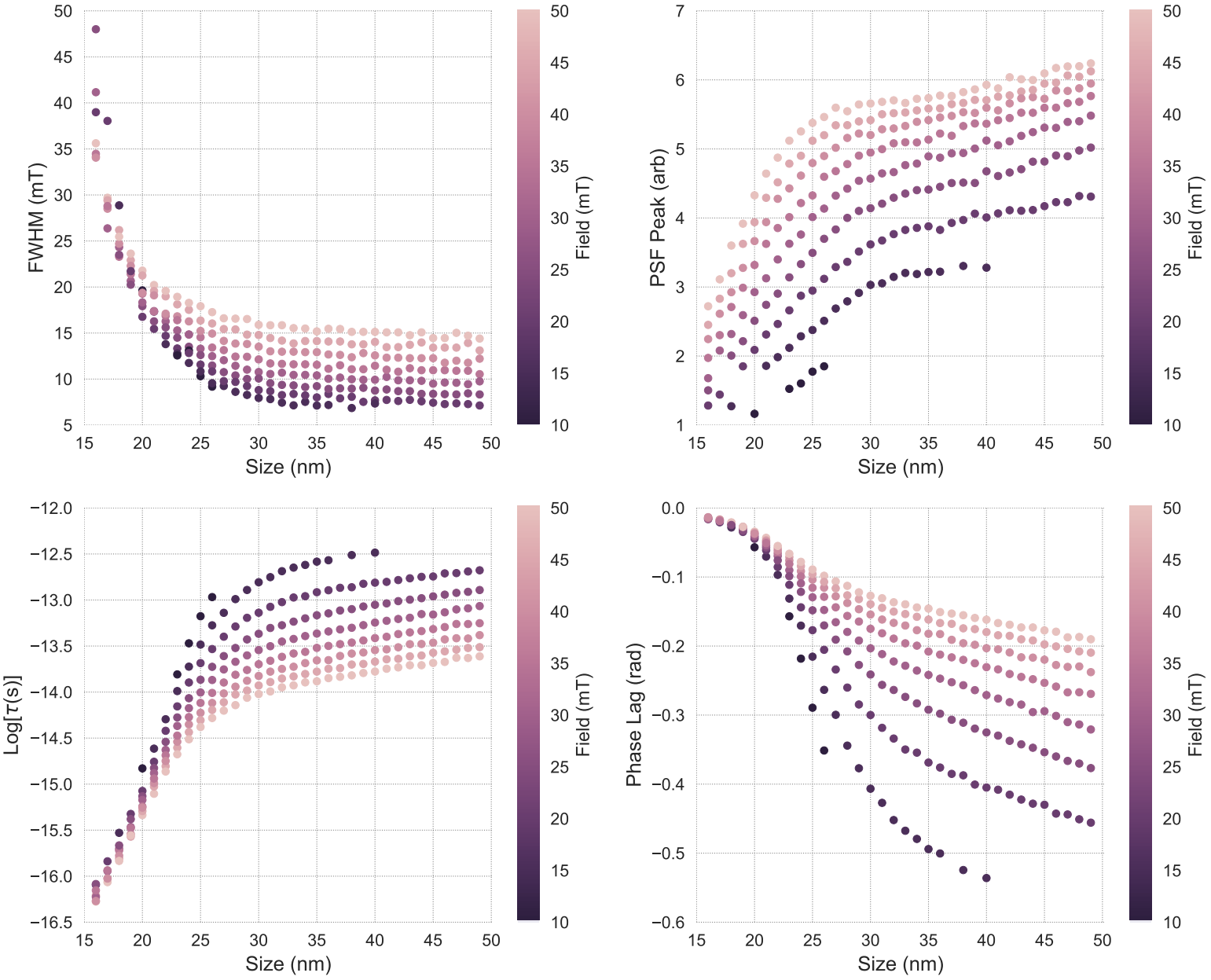

Figure 5.6: Results from stochastic simulations run with a 25 kHz drive field frequency and 50 nm non-magnetic coating for a range of field amplitudes. Resolution and signal strength improve with increasing core size, as relaxation time and phase lag increase.

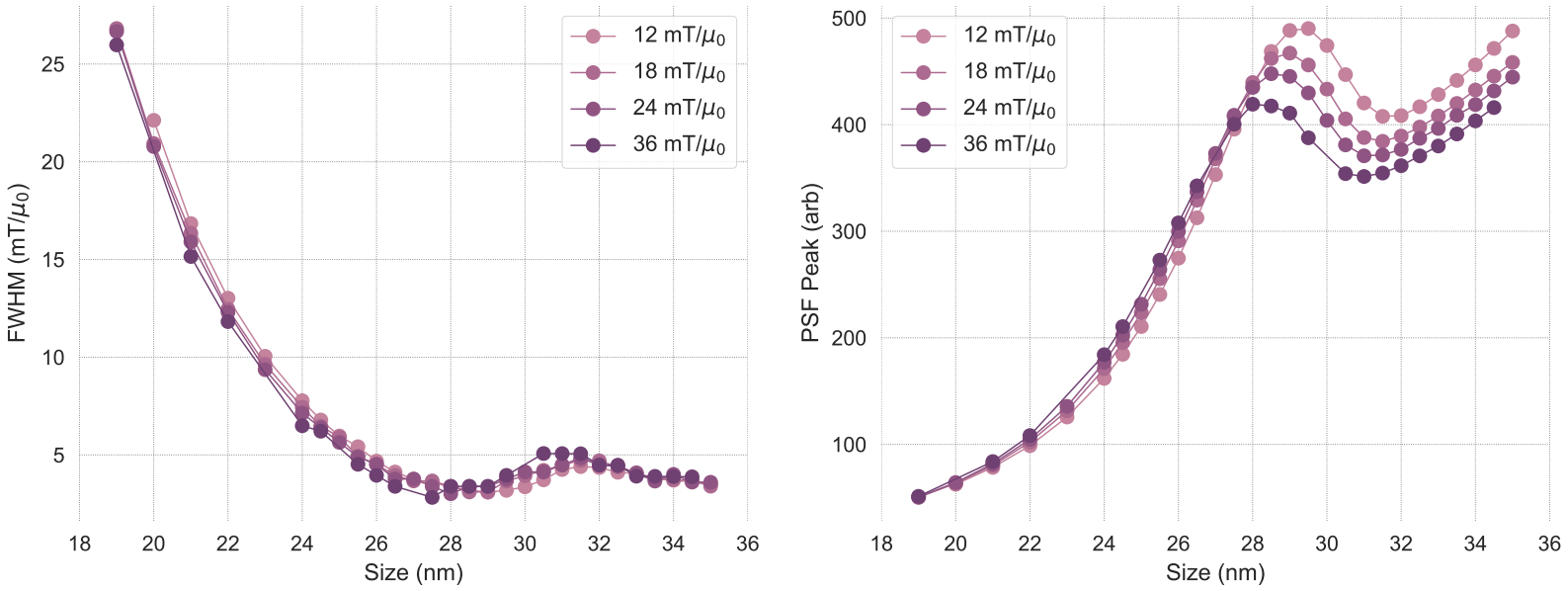

Figure 5.7: Results from simulations of the coupled Fokker-Planck equation. Resolution and signal strength generally improve with increasing core size.

From Fig. 5.6, we see that the FWHM generally decreases from small sizes, predicting better resolution with larger particles, but then levels off, again in agreement with the MPS results. After a certain point, again ∼30 nm, there is minimal gain in resolution when the size is increased further, in concurrence with MPS results in Fig. 5.5a. To gain further insight into this behavior, we can also extract the effective MNP relaxation time, shown in Fig. 5.6. From $\sim 15 - 25$ nm, τ increases by around 2 orders of magnitude, but increases by only 1 order of magnitude from $\sim 25 - 35$ nm. We can see that the magnitude of the phase lag ϕ also increases with relaxation time, as expected.

Simulations of the coupled Fokker-Planck equation, as described in §3.1.1, were performed with identical parameters. Results are shown in Fig. 5.7. The same general improvement with size is seen; however, interestingly, there is a temporary decrease in signal quality between $\sim 28 - 32$ nm. This indicates that there is a clear ideal size for particles below ~ 35 nm in diameter, at about $28 - 29$ nm, depending on applied field amplitude. Above ~ 35

nm, the FWHM appears to level out.

To determine whether the FWHM will decrease indefinitely with increasing size (or whether the PSF peak will increase indefinitely with increasing size), we can consider the end behavior of the relaxation time as $V_c \to \infty$. The adiabatic term (Δx_{adiab}) in Eq. 5.3 scales as $1/V_c$, so will tend to zero at large V_c. The relaxation term (Δx_{relax}) scales as τ. Therefore, if the relaxation time τ increases indefinitely with core volume, eventually, the total FWHM Δx will reach a minimum and begin to increase with increasing size. Otherwise, the FWHM will decrease indefinitely or asymptote to a constant value. Eigenvalue calculations from the Brownian Fokker-Planck equation, Eq. 3.7, predict that the relaxation time will decrease with with core volume, as discussed in detail in §4.3. If the Brownian Fokker-Planck model is accurate, then, we would predict that the FWHM will decrease indefinitely with core size. However, the stochastic simulations, which take into account both Brownian and Néel relaxation mechanisms, indicate a general increase of relaxation time with size, predicting that Δx will eventually hit a minimum and will begin to increase past a certain size, indicating that there will be an optimal core size for MPI image resolution.

By simulating immobile particles that relax purely via the Néel mechanism, we can look at the effect of increasing the relaxation time on resolution, since the Néel relaxation time will be higher and increase faster than the effective relaxation time when both mechanisms are active (as discussed in §5.3). In this case (shown in cyan in Fig. 5.8a.), we can see that the FWHM does reach a minimum and starts to gradually increase at large core sizes. The PSF peak also reaches a maximum and begins to slowly decrease with increasing core size (Fig. 5.8b.). We can conclude, then, that for immobile particles, there will be a clear optimal size for best resolution and signal strength in MPI, around 32 nm for these particular field conditions and particle properties. In the case of mobile particles, e.g. when dispersed in water, where both relaxation mechanisms may occur, we do not necessarily see a clear turnaround point, but there is a distinct change in slope both in the FWHM and the PSF peak as a function of core size, at which point the improvement to the predicted image quality significantly slows.

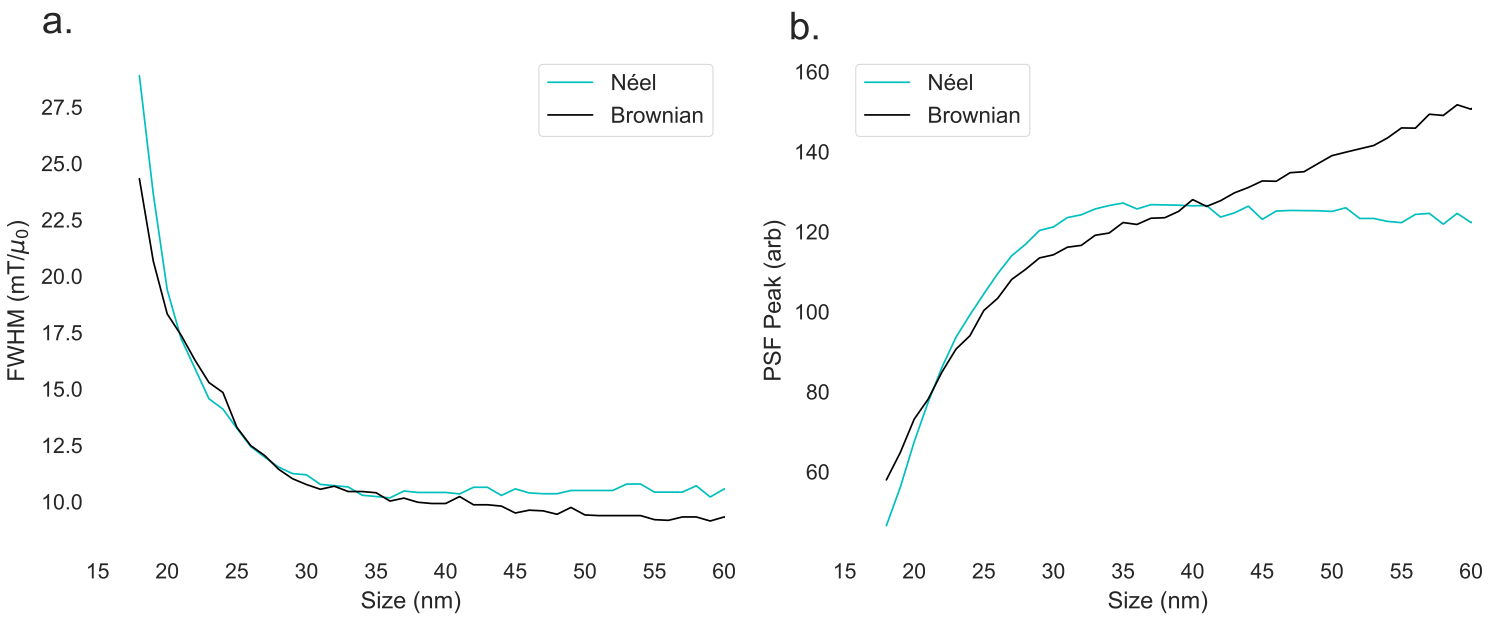

Figure 5.8: Stochastic simulations with a 25 kHz, 30 mT/μ_0 drive field and 50 nm non-magnetic coating, for Néel-only relaxation (cyan) as well as Néel plus Brownian relaxation (black).

We can assume that this turnaround point occurs when relaxation behavior starts to dominate. At that point, then, the adiabatic term in Eq. 5.3 would be approximately equal to the relaxation term. We can set the two terms equal, assuming that $\alpha \approx \beta \approx 1$, and set $\Delta x_{\text{adiab}} = \Delta x_{\text{relax}}$, which occurs at a particular relaxation time τ':

$$\ln(2)\frac{2\pi f_0 H_0 \tau'}{G} = \frac{4.16 k_B T}{\mu_0 M_s V_c}. \tag{5.9}$$

From here, we can solve for τ':

$$\tau' = \frac{4.16 k_B T G}{\ln(2) 2\pi f_0 H_0 \mu_0 M_s V_c}. \tag{5.10}$$

When $\tau > \tau'$, relaxation behavior will dominate. We can plot τ' as a function of core size and compare that to the effective relaxation time extracted from simulations, which is shown in Fig. 5.9. It is clear that the slope of τ changes around the intersection point where $\tau = \tau'$. By identifying the particle core size d_c' at that intersection point, we can identify the size at which relaxation behavior begins to dominate. Fig. 5.10 shows simulation data of the FWHM and PSF peak as a function of particle size, with d_c' indicated. It is clear that d_c' occurs near a critical change in the slope in each case, indicating a shift in the size-dependent behavior. For $d_c < d_c'$, the rate of change of Δx and the PSF peak is larger than when $d_c > d_c'$. Increasing the size past d_c', then, will result in minimal improvements to the signal.

Due to practical difficulties in fabricating large monodisperse particles, as well as increased likelihood for particle agglomeration for large particles, which will be discussed in the following sections, identifying this critical size, d_c', will be dependent on applied field amplitude, frequency, and non-magnetic coating size. d_c' for a range of applied field strengths and frequencies is shown in Fig. 5.11. The field amplitudes and frequencies that fall outside of the Brezovich-Criterion lie to the right of the red line. For fields that lie within the medical safety limits (to the left of the red line), d_c' is between $27-29$ nm. d_c' generally decreases with increasing field strength, which indicates that particles on

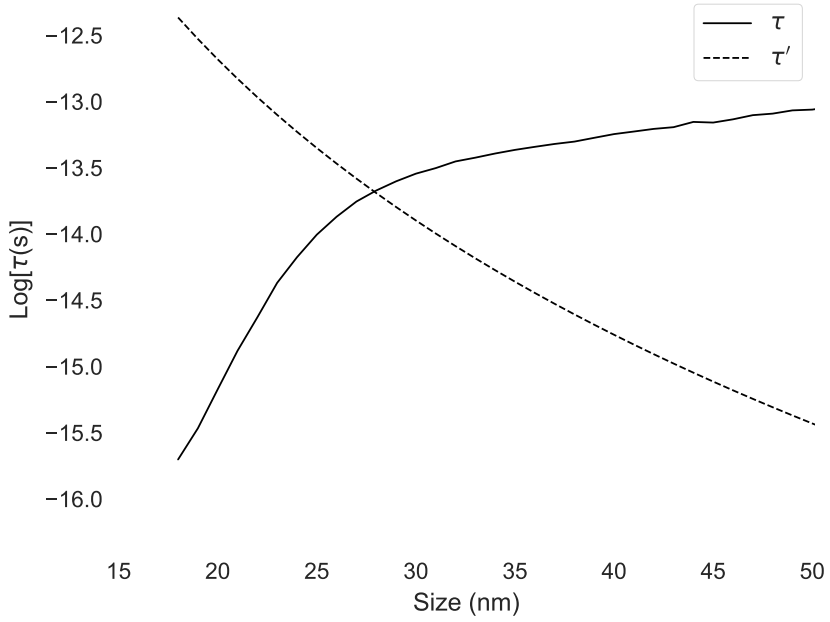

Figure 5.9: Relaxation time (solid) extracted from stochastic simulations with a 25 kHz, 30 mT/μ_0 drive field and 50 nm non-magnetic coating, for Néel plus Brownian relaxation, as well as τ' from Eq. 5.10 as a function of size. The intersection point, which occurs at d_c', indicates the crossover point where relaxation behavior begins to dominate.

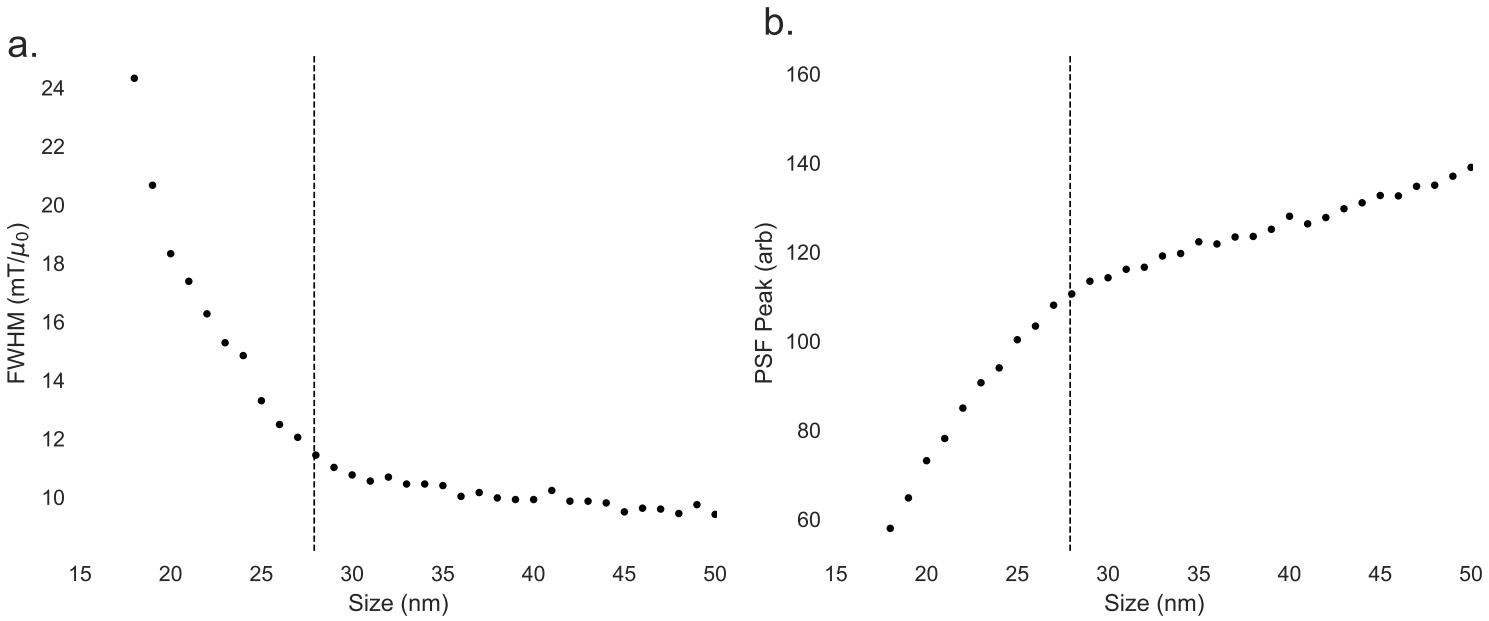

Figure 5.10: Stochastic simulations with a 25 kHz, 30 mT/μ_0 drive field and 50 nm non-magnetic coating, for Néel plus Brownian relaxation (black). d_c' is identified (dashed).

the small end of this range would result in a better MPI signal when the field amplitude is stronger, i.e. when relaxation effects become more prominent. d_c' also generally decreases with increasing field frequency, again implying that smaller particles would result in better MPI image quality for high-frequency fields, due to the larger relaxation effects that arise at high frequencies.

Assuming that particles are able to freely rotate, e.g. if they are dispersed in an aqueous solution, as is the case for typical MPI applications, the hydrodynamic size of the particles will have an effect on the relaxation dynamics as well. Fig. 5.11 shows d_c' for two different non-magnetic coating sizes, which approximate the common 5 kDa and 20 kDa polyethelyene-glycol (PEG) coatings, which have respective approximate lengths of 32 nm and 127 nm. 10 kDa PEG is not shown but is also commonly used, which has an approximate length of 64nm. While the overall trends with field amplitude and frequency remain the same, d_c' changes by a few tenths of a nanometer when the coating is changed. Due to the complex relationship

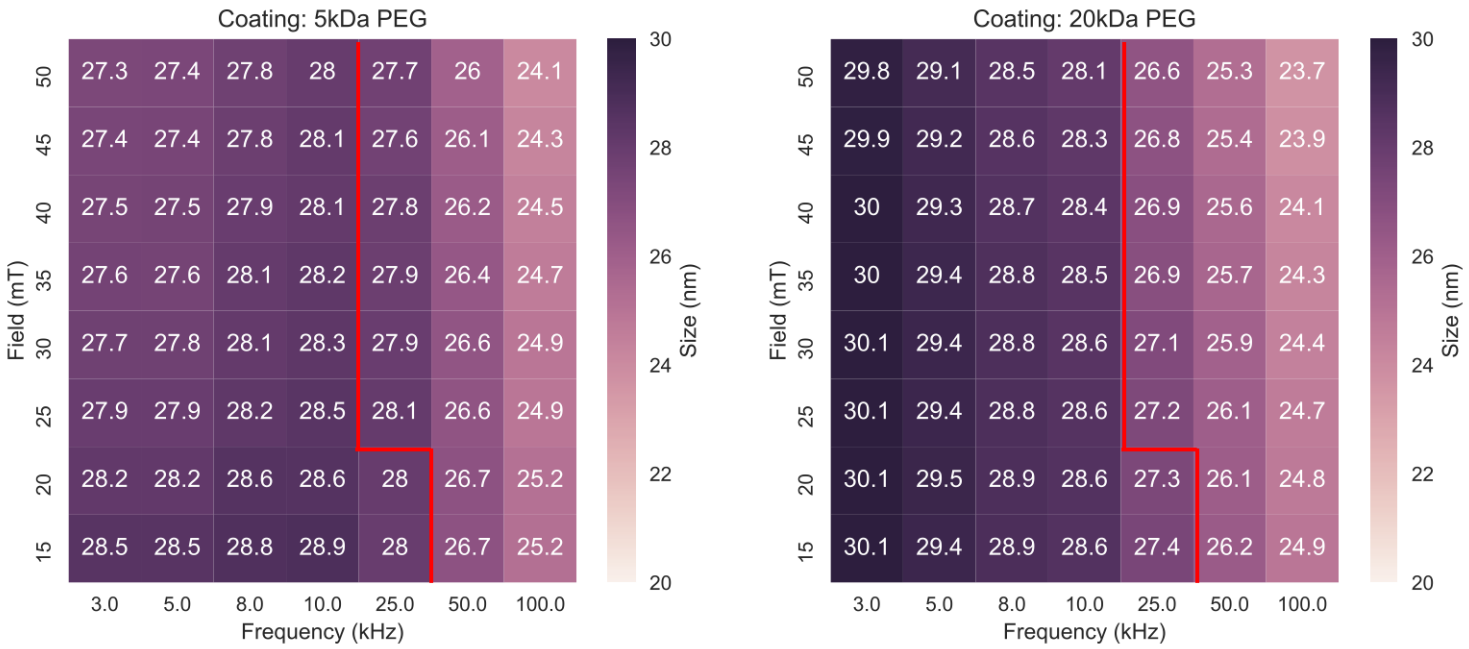

Figure 5.11: d_c' for a range of applied field amplitudes and frequencies, extracted from stochastic simulations. Two coating sizes are shown. The red line denotes medical safety limits.

between Brownian and Néel relaxation with field, as was explored in the previous chapter, there is no simple trend of d_c' with coating size that can be identified.

So far, we have shown that for a given field amplitude, frequency, and coating, there is a specific size d_c' at which relaxation effects will begin to arise which will limit MPI signal improvement. It is not yet necessarily clear, though, that d_c' corresponds to an *optimal* core diameter for MPI, since in the case of Brownian particles, the signal quality may still improve with increasing size. However, there are practical limitations to further increasing the size beyond d_c', which will be explored in the following sections.

5.3.3 Effects of dipolar interactions

According to the results in Fig. 5.6, increasing the core size should keep incrementally improving the MPI signal quality, at least up to core diameters of 50 nm. However, from a practical standpoint, once nanoparticles reach a certain core size, agglomeration effects will begin to arise due to dipole-dipole interactions. Since we assume that the MNPs used for MPI are single-domain and superparamagnetic, we can approximate each nanoparticle as a single magnetic dipole with moment $\mu = M_s V_c$. The interaction energy between two magnetic dipoles is:

$$U_{int} = -\frac{\mu_1 \mu_2 \mu_0}{4\pi r^3} \left(3(\hat{\mathbf{m}}_1 \cdot \hat{\mathbf{r}})(\hat{\mathbf{m}}_2 \cdot \hat{\mathbf{r}}) - \hat{\mathbf{m}}_1 \cdot \hat{\mathbf{m}}_2\right). \tag{5.11}$$

If we assume that the minimum distance that two particles can be separated is equal to their hydrodynamic diameters, we can calculate the maximum dipole interaction energy per particle for a collection of monosized particles. We can then compare that value to the thermal energy $k_B T$. If $k_B T$ is smaller than the maximum interaction energy, there is a high likelihood that the particles may agglomerate in solution, which will result in a substantial decrease in MPI signal.

By calculating the interaction energy as a function of MNP core size (Fig. 5.12a.), we can extract the maximum core size for which the interaction energy is less than the thermal

energy (at room temperature) for a given coating size, which we will label d_c^*, shown in Fig. 5.12b. For particles $27 - 29$ nm in diameter, the coating would have to be a minimum of 80nm to prevent agglomeration. For larger particles with core sizes greater than 30 nm, the coating would need to be a minimum of 100 nm, and so would preclude the use of 5 kDa or 10 kDa PEG. However, there is also a disadvantage to simply increasing the coating size (or PEG chain length) indefinitely; increasing the hydrodynamic size indefinitely will eventually suppress the particles' Brownian relaxation (as discussed in §4.3), which will in turn decrease the resulting signal.

We can examine the effect of including dipolar interactions on d_c'. The left side of Fig. 5.13 shows d_c' for a range of field amplitudes and coating sizes, while the right side shows the smaller of d_c' and d_c^*. For larger coatings (> 50 nm), d_c' is not affected. However, when the coating size is decreased below 75 nm, dipole interactions significantly limit the maximum core size that should be used. This indicates that when small coatings (e.g. 5 kDa PEG) are used, the core size should be appropriately reduced as well, otherwise increased agglomeration will become a challenge in the phase transfer process. If core sizes larger than d_c^* are used, the MPI signal will be reduced due to increased interparticle interactions.

5.3.4 Polydispersity of nanoparticle core size

One final point that should be considered is that MPI signal will improve with monodispersity of MNP size and shape. If we assume, as is typical, that nanoparticle sizes follow a log-normal distribution, we can characterize the polydispersity of any given sample with the size distribution parameter σ. Fig. 5.14 shows the results of simulations of collections of particles with different size distribution parameters, demonstrating that both MPI resolution and signal strength worsen with increasing polydispersity. Therefore, when optimizing nanoparticle size for MPI, nanoparticles should be as monodisperse as possible.

In practice, however, when the average core size of a sample of nanoparticles is increased, the polydispersity of the sample will typically increase as well. During the nucleation and growth step of typical IONP fabrication processes, the longer the growth phase, the larger

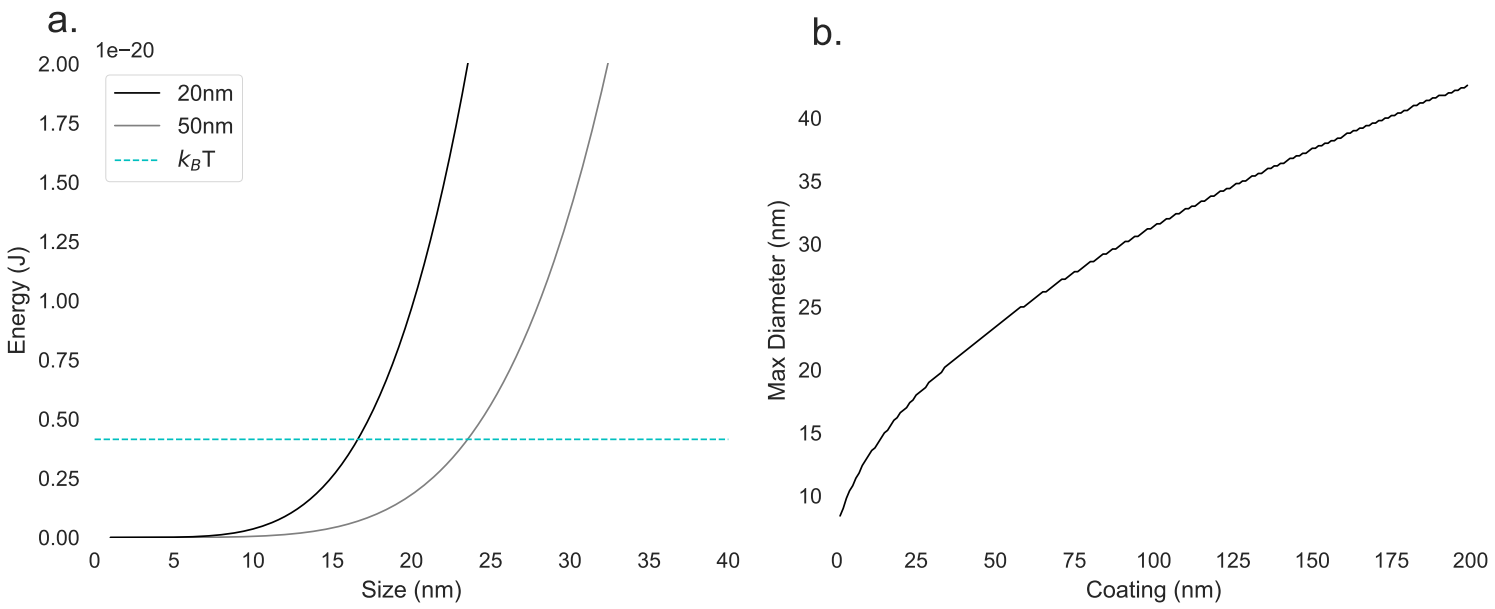

Figure 5.12: a. Interaction energy vs. particle core size for two different coating sizes (20 nm in black and 50 nm in grey). Thermal energy k_BT is also indicated. The interaction energy increases with core volume, and eventually becomes larger than the thermal energy. b. The maximum particle diameter (d_c^*) at which the interaction energy is lower than the thermal energy, as a function of coating size. This assumes that the minimum particle separation is equal to the total particle hydrodynamic diameter.

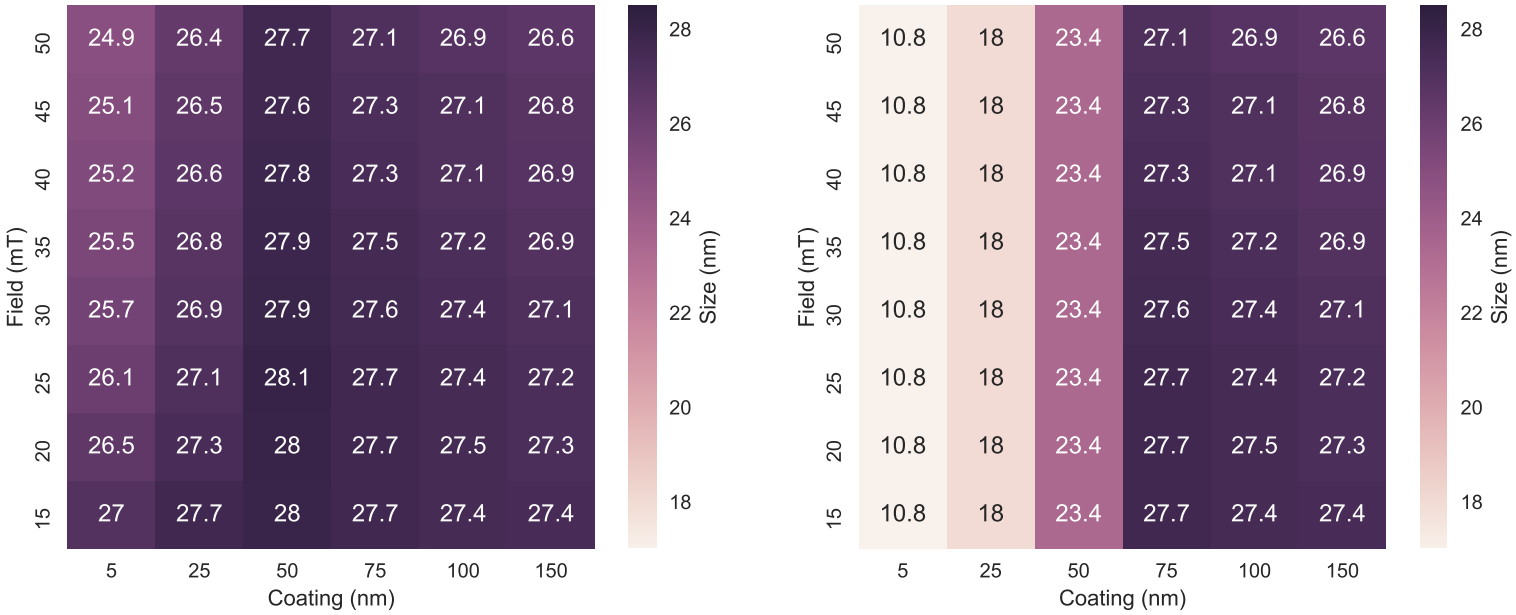

Figure 5.13: Left: d_c' for a range of applied field amplitudes and coating sizes, with a 25 kHz field, extracted from stochastic simulations. Right: The smaller of d_c' and d_c^* for a range of applied field amplitudes and coating sizes, extracted from stochastic simulations. Particles with large coatings are generally unaffected by interparticle interactions, while particles with small coatings will experience agglomeration at smaller sizes.

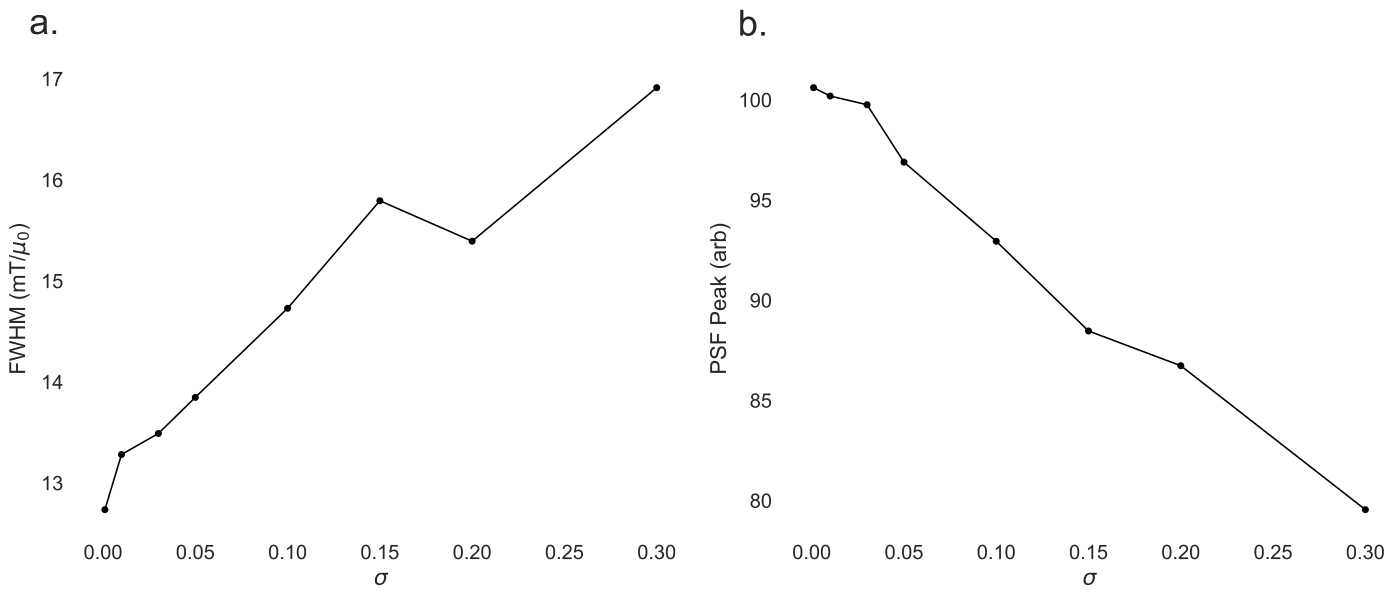

Figure 5.14: FWHM and PSF peak extracted from stochastic simulations as a function of polysdispersity of nanoparticle size, under an applied 20 mT/μ_0 and 25 kHz field. Resolution and signal strength both worsen with polydispersity.

the average size will be, but also the larger the variance of core sizes will be. Using these fabrication procedures [122], it is technically quite difficult to fabricate particles with core size greater than 27 nm and $\sigma \leq 0.05$, for example. Consequently, in practice there will be trade-offs to increasing core size, as increasing core size typically increases polydispersity as well. We conclude, then, that the smaller of d_c' and d_c^* will correspond to the "optimal" core size for MPI purposes, from a practical standpoint, since further increasing the core size will result in higher polydispersity and increased chance of agglomeration, both of which will ultimately decrease the MPI signal quality.

5.4 Conclusion

In this chapter, we have examined ways to optimize MPI signal with drive field and nanoparticle core and coating size. Table 5.4 summarizes the optimal core size, based on simulation results described in the previous section, for typical MPI fields that fall within the medical

safety limits, taking into account interparticle interactions as well as polydispersity. For typical MPI field conditions and coatings of at least 10 kDa PEG, increasing core size to ∼28 nm will result in significant signal improvements; however, when core size is increased beyond 28 nm, relaxation effects dominate and improvements to the MPI signal are minimal. Furthermore, beyond 28 nm, interparticle interaction effects will begin to dominate for typical MPI field conditions and coating sizes, decreasing the resulting signal. From a practical point of view, this results in decreased particle stability, where particles will tend to precipitate out of solution. Polydispersity will also necessarily increase as the average core size increases. We conclude, then, that 28 nm is the optimal core diameter for typical MPI measurements, taking into account both fundamental physical relaxation effects as well as practical limitations.

	5 kDa			**10 kDa**			**20 kDa**		
	5 kHz	**10 kHz**	**25 kHz**	**5 kHz**	**10 kHz**	**25 kHz**	**5 kHz**	**10 kHz**	**25 kHz**
15 mT/μ_0	23.1±0.1	23.1±0.2	23.1±0.3	29.6±0.1	29.1±0.2	27.7±0.3	29.4±0.1	28.6±0.2	27.4±0.3
20 mT/μ_0	23.1±0.1	23.1±0.1	23.1±0.2	29.4±0.1	29.1±0.1	27.7±0.2	29.5±0.1	28.6±0.1	27.3±0.2
30 mT/μ_0	23.1±0.1	23.1±0.1	23.1±0.1	29.1±0.1	29.1±0.1	27.6±0.1	29.4±0.1	28.6±0.1	27.1±0.1

Table 5.1: The smaller of d_c' and d_c^* for typical MPI field conditions and nanoparticle coatings, incorporating uncertainty from polydispersity of nanoparticle size distribution, assuming a typical $\sigma = 0.1$. Polydispersity has a larger effect when the field amplitude is low and the frequency is high.

Chapter 6

DEVELOPMENT OF MULTICOLOR MPI

6.1 Motivation

In conventional MPI, the signal from the nanoparticle tracer response creates a single contrast image, in which the strength of the tracer signal at each spatial location is translated to image intensity of the corresponding pixel during the image reconstruction process. The result of this is a grayscale (or equivalent) image. Recently, there has been exploration into the possibility of multicolor (also referred to as "multi-contrast" or "multi-channel") MPI, in which the signal generated from different tracer types or different tracer environments is separated [123]. If the signal from different particle types can be separately reconstructed on individual channels, a multicolor image can be generated, in which each channel corresponds to one color, enabling a new range of therapeutic and diagnostic applications that could function in combination with MPI.

When considering potential theranostic applications of multicolor MPI, a major enabling factor is the wide potential for functionalization of the nanoparticle surface. Iron oxide nanoparticles are particularly versatile in this way. When synthesized via thermolysis of organometallic precursors, superparamagnetic iron oxide nanoparticles (SPIONs) need to be coated with a capping ligand, e.g. oleic acid, which renders them hydrophobic. In order to be dispersed in water for use in biomedical applications, they must undergo a phase transfer process, typically either by ligand exchange [124–126] or with the addition of a polymer coating, for example, poly(maleic anhydride alt-1-octadecene) (PMAO), which interacts hydrophobically with the capping ligand [127]. Once SPIONs are coated with a polymer, additional molecules can be attached to the surface.

When SPIONs are delivered into the bloodstream, extracellular serum proteins adsorb

onto the nanoparticle surface, forming a protein corona [128, 129], which may decrease nanoparticle stability and facilitate nanoparticle removal from the bloodstream and body [130]. To reduce protein adsorption and improve biocompatibility and stability, SPIONs can be coated with poly(ethylene glycol) (PEG) containing co-polymer [29] in addition to PMAO, which enables long term circulation of particles in the blood [131, 132], necessary for applications like cardiovascular imaging. Alternatively, SPIONs can be coated with silica [36, 37], on top of which ligands can be attached, such as ligands for cancer targeting [39, 40, 72, 133, 134]. Cancer targeting ligands include antibodies, oligosaccharides, oligopeptides, and folic acid [135, 136].

In addition to functionalization for long-term blood circulation and cancer targeting, SPIONs can be coated on medical devices; for example, on diagnostic catheters and guide wires used for cardiovascular interventions [137–139]. A possible application of multicolor MPI, then, would involve distinguishing between particles coated on a catheter and guide wire (used for inserting stents in the heart or diagnosing heart disease) and particles flowing in the blood, on which preliminary studies have been done [139]. This technique could, in theory, replace coronary catheter angiography. Coronary catheter angiograms, which require threading a catheter through the femoral artery, are performed at a rate of approximately 1 million per year in the United States [140]. The catheters are used to inject iodine into the heart, which is then used as a contrast agent in order to allow diagnosis with x-ray imaging or CT. However, iodine can have serious health consequences, particularly for elderly patients or patients with chronic kidney disease. For these patients, the injection of iodine can result in renal failure, and the insertion of the catheter through the femoral artery itself carries a finite risk [140]. Multicolor MPI could therefore provide a significantly safer alternative to coronary angiography.

To create a multi-channel image with MPI, the signal from MNPs of different sizes or in varying chemical, thermal, or viscous environments must be distinguished, in contrast to single-channel MPI which produces a monochromatic image. This is possible due to the sensitivity of the relaxation behavior of MNP tracers. MNP properties and properties of the

local environment that influence the MNP relaxation behavior, and therefore resulting MPI signal, include temperature, viscosity, mobility state, material, degree of interparticle interactions, and core or hydrodynamic size. There has been recent investigation into several of these with magnetic particle spectroscopy (MPS) and 1D and 2D MPI [57,123,141–146], most notably quantitative viscosity imaging in [147], qualitative temperature mapping in [148] and quantitative temperature mapping in [59]. These studies show that the MPI signal is highly sensitive to particle properties and environment, which can enable discrimination based on particle type, and in some cases quantification of environmental properties.

Because of this, multicolor MPI could be used to combine medical imaging with disease diagnostics and treatment. For example, quantifying the viscosity of the MNP environment can provide information about nanoparticle binding to or internalization in cells, which would be useful for applications like targeted cancer treatment. Blood viscosity could also be detected as an indication of disease [149], such as a brain hemorrhage, during which blood coagulation occurs [150]. Temperature can be another significant marker of disease; malignant cells have a higher temperature than normal cells, by possibly up to 1 degree Celsius, and general inflammation results in temperature changes [151–154]. Detecting local temperature changes during an imaging scan could therefore provide information for disease diagnostics, and detection sensitivity of $< 1^{\circ}$C should be possible with MPI [59]. Magnetic fluid hyperthermia (MFH), in which magnetic nanoparticles are used to locally heat cancer cells [22–24,63–66] could also be combined with active monitoring of temperature with MPI, allowing for a thermally-controlled cancer treatment system. Additionally, cancer detection via protease sensing with MPI could be achieved by detecting changes in interparticle interaction strength using linker peptides that are cleaved in the presence of proteases expressed by malignant cells [60].

In order to realize the above applications clinically, a very sensitive signal separation technique is required. In this chapter, we build on previous work to develop new avenues for multicolor MPI, as well as explore the theoretical basis and underlying physics which enable spectral discrimination. The signal harmonics, obtained by taking a simple Fourier

transform of the magnetic response signal, provide a strong potential basis for multicolor imaging because of their high sensitivity to particle conditions. Here, we use the methods and insights developed in the previous chapters to study the changes in the magnetization harmonics of nanoparticles based on changes in particle properties or environments, and use that to demonstrate and explore new possibilities of multicolor MPI.

6.2 MPI signal in frequency space

In this chapter, we will study the measured MPI signal in frequency-space (or f-space) MPI, in which the harmonic frequencies of the nanoparticle response are directly recorded, in contrast to x-space MPI, which was discussed in §2.3.1. In principle, all measurements can be converted to the time domain via Fourier transform, which would correspond to x-space reconstruction. Here, we discuss image reconstruction in f-space because it will allow us to directly consider the harmonics of the magnetization response, which will be fundamental for discriminating between nanoparticle samples. This will also allow us to directly build on certain techniques, for example magnetic spectroscopy of nanoparticle Brownian motion (MSB), which is the technique of using the signal harmonics to determine the microscopic environment of mobile nanoparticles [141].

6.2.1 Single channel image reconstruction in f-space MPI

When reconstructing an image in MPI, it is of course crucial that the relationship between the spatial particle distribution and the resulting induced signal be known. In f-space MPI, this relationship is determined by first measuring a *system function*, or system matrix, which will characterize the frequency response of a given nanoparticle sample at a known location. The system function is generated by moving the sample around the entire field-of-view (FoV) of the scanner and recording the response. The result will be a matrix containing frequency components for all values of the offset field resulting from the static gradient field. Once the system function is known, an MPI scan can be performed where the nanoparticle distribution is unknown, and the image can be reconstructed from the system function. The

reconstruction process will be described in this section, following Ref. [155].

The induced voltage from a spatial particle distribution ρ in frequency space will be:

$$u_k = \int_V s_k(\mathbf{r})\rho(\mathbf{r})\,\mathrm{d}^3 r, \tag{6.1}$$

where s_k is the system function, with index k denoting frequency components. Since the induced voltage must be real, we can ignore the negative frequency components, as they will not provide any additional information. The induced voltage u_k is then a vector containing K frequency components, where K is the total number of harmonics measured, as determined by the bandwidth of the receive circuit system. The integral here is performed over the total volume of the object, which can be considered to be the FoV of the scanner. The system function is:

$$s_k(\mathbf{r}) = -\frac{\mu_0}{T_R}\int_0^{T_R} \boldsymbol{\sigma}(\mathbf{r}) \cdot \frac{\partial \bar{\mathbf{m}}(\mathbf{r},t)}{\partial t} \mathrm{e}^{-2\pi i k t/T_R}\,\mathrm{d}t, \tag{6.2}$$

where T_R is the total period of the scanning field in all dimensions. For 2- and 3-dimensional systems, the frequencies of the drive field in each direction are slightly different, resulting in a Lissajous trajectory; T_R refers to the total time required for one complete scan. As in §2.3.1, $\boldsymbol{\sigma}$ is the receive coil sensitivity, here represented more accurately as a spatially dependent vector. This allows for incorporation of all geometrical parameters of the receive coil, as well as differences in the sensitivity of the receive coils along each dimension. The average individual particle magnetization is represented by $\bar{\mathbf{m}}$, so that the total magnetization of the entire MNP sample is:

$$\mathbf{M}(\mathbf{r},t) = \rho(\mathbf{r})\bar{\mathbf{m}}(\mathbf{r},t). \tag{6.3}$$

The system function is measured with a calibration MNP sample with known concentration ρ_0 and known shape ΔV_{cal}. A small cubical volume is often used. If the size of the calibration sample is infinitely small and located at a known point $\mathbf{r}'$, then the particle distribution can be expressed by the Dirac delta function:

$$\rho^D_{\mathbf{r}'}(\mathbf{r}) = \rho_0 \delta(\mathbf{r} - \mathbf{r}'). \tag{6.4}$$

The signal induced by this calibration sample, obtained by inserting Eq. 6.4 into Eq. 6.1, will be:

$$\begin{aligned} u_k^{\mathbf{r}'} &= \int_V s_k(\mathbf{r}) \rho^D_{\mathbf{r}'}(\mathbf{r}) \, \mathrm{d}^3 r \\ &= \int_V s_k(\mathbf{r}) \rho_0 \delta(\mathbf{r} - \mathbf{r}') \, \mathrm{d}^3 r \\ &= \rho_0 s_k(\mathbf{r}'). \end{aligned} \tag{6.5}$$

This now allows us to easily solve for the system function:

$$s_k(\mathbf{r}') = \frac{u_k^{\mathbf{r}'}}{\rho_0}. \tag{6.6}$$

So, by measuring the induced signal u_k when the calibration sample is positioned at $\mathbf{r}'$, the system function can be easily obtained.

In reality, the calibration sample will have a finite size with volume ΔV_{cal}. However, as long as the voxel size of the reconstruction grid ΔV is larger than ΔV_{cal}, then the following approximation will be valid (and would be exact if it is assumed that the system function remains constant within a particular voxel) [155]:

$$s_k(\mathbf{r}') \approx \frac{u_k^{\mathbf{r}'}}{\rho_0 \Delta V}. \tag{6.7}$$

This allows us to determine the system function from the measurement vector $u_k^{\mathbf{r}'}$, as long as the calibration sample size is smaller than the voxel size. The voxel size of the reconstruction grid will determine the limiting image resolution, so when optimizing for resolution, the calibration sample size should be as small as possible. However, for a given sample concentration, the signal-to-noise ratio (SNR) of the system function will be directly related to the size of the calibration sample, since the signal strength will scale linearly with total MNP mass, assuming that the particles are non-interacting. When choosing a size for

the calibration sample, then, there will be a necessary trade-off between desired resolution and SNR.

The total system matrix must then be generated from measurements performed with the sample at all locations in the FoV. So, if there are N total voxels within the reconstruction grid, the calibration sample must be shifted to all N positions and measured at each point. The sample is typically moved using a robot arm, so this is a relatively time-intensive process. At each position, a full measurement of all K frequency components is performed on each detecter, so the resulting system function s_k will have dimension $K \times N \times 2$ for 2D measurements, or $K \times N \times 3$ for 3D measurements.

When the FoV is discretized into individual voxels, the integral in Eq. 6.1 becomes a sum, with each $\mathbf{r}_n$ representing the location of each voxel:

$$\tilde{u}_k = \Delta V \sum_{n=1}^{N} s_k(\mathbf{r}_n)\rho(\mathbf{r}_n). \tag{6.8}$$

Writing $\tilde{u}_k$ and $\rho(\mathbf{r}_n)$ as vectors $\mathbf{u}$ and $\boldsymbol{\rho}$ which have K and N components, respectively, Eq. 6.8 can be written as a matrix equation:

$$\mathbf{u} = \mathbf{S}\boldsymbol{\rho}, \tag{6.9}$$

where $\mathbf{S}$ is the complex-valued $K \times N \times 2$ or $K \times N \times 3$ system matrix. Once $\mathbf{S}$ has been determined, a measurement can be performed on an unknown distribution. In that case, $\boldsymbol{\rho}$ is the vector which contains the unknown particle distribution, which we want to solve for, and $\mathbf{u}$ is the measurement vector which consists of the complex-valued Fourier coefficients of the induced signal. In reality, the measurement vector $\mathbf{u}$ will be distorted by noise, such as thermal noise in the receive coils and noise induced by eddy currents in biological tissue. Eq. 6.9 will therefore not necessarily have an exact solution. We will label the measurement vector, including noise distortions, as $\tilde{\mathbf{u}}$, and so Eq. 6.9 becomes:

$$\tilde{\mathbf{u}} \approx \mathbf{S}\boldsymbol{\rho}. \tag{6.10}$$

To solve this for $\boldsymbol{\rho}$, we can use a least-squares approach, in which the Euclidean norm of the residual vector is minimized:

$$||\mathbf{S}\boldsymbol{\rho} - \tilde{\mathbf{u}}||_2^2 \rightarrow \min \tag{6.11}$$

When SNR is low, however, the least-squares approach can lead to an ill-posed problem, which results in unusable solutions. To address this issue, Tikhonov regularization is often used, in which the Tikhonov regularization parameter $\tilde{\lambda}$ is introduced:

$$||\mathbf{S}\boldsymbol{\rho} - \tilde{\mathbf{u}}||_2^2 + \tilde{\lambda}||\boldsymbol{\rho}||_2^2 \rightarrow \min. \tag{6.12}$$

Since here we are using a scalar $\tilde{\lambda}$ rather than a matrix, this particular method is also called L_2 regularization. The additional regularization term is used to penalize solutions for $\boldsymbol{\rho}$ that have a large Euclidean norm, which helps avoid overfitting to noise, effectively smoothing the solution. The regularization term $\tilde{\lambda}$ must be chosen carefully so that the resulting solution is neither too smooth (resulting in loss of spatial resolution) nor too noisy.

There are many computational methods that can be used to solve the above regularized least-squares problem; however, for the work in this chapter, we will use the Kaczmarz method, which is widely used for image reconstruction in MPI. The Kaczmarz method is an iterative solver which operates on a single row of the matrix at a time. Each equation of the system (each row) is interpreted to be a hyperplane in the D-dimensional solution space. At each sub-iteration i, the orthogonal projection of the current estimate of the solution onto the hyperplane is computed. This is expressed mathematically as:

$$\boldsymbol{\rho}^{i+1} = \boldsymbol{\rho}^i + \frac{\tilde{u}_j - \mathbf{S}_j^* \cdot \boldsymbol{\rho}^i}{||\mathbf{S}_j||_2^2}\mathbf{S}_j^*, \tag{6.13}$$

where $\tilde{u}_j$ is the j-th component of $\tilde{\mathbf{u}}$ and $\mathbf{S}_j$ is the j-th row of $\mathbf{S}$. The Kaczmarz method is typically initialized with a zero start vector, and the convergence speed will be dependent

on the orthogonality of the system matrix rows. Further details about this process can be found in Ref. [155].

6.2.2 Properties of the system function

Now that the image reconstruction procedure has been outlined and the system function has been introduced, we can closely examine the system function, which contains the harmonics of the MNP magnetization response under a static and AC field. Eventually, we will be interested in the dependence of these harmonics on particle properties. To help develop that understanding, in this subsection, we will examine the positional dependence of the magnetization harmonics when the particles are exposed to a static gradient field in addition to the AC field. To simplify the discussion here, we will consider scans along only one dimension.

In an MPI scanner, the time-dependent AC field is generated by the drive field:

$$H_D(t) = H_0 \cos(\omega_0 t), \tag{6.14}$$

where ω_0 and H_0 are the angular frequency and amplitude, respectively, of the AC field. At every voxel in the FoV, there will be a spatially-dependent bias field, which is generated by the selection (gradient) field $H_S(x)$, equal to Gx where G is the strength of the gradient. The total field will be:

$$H(x,t) = H_S(x) - H_D(t). \tag{6.15}$$

The period of the applied AC field, T_R, is now equal to $2\pi/\omega_0$ since the field is only applied along one direction. The one-dimensional system function is:

$$s_k(x) = -\frac{\mu_0 \sigma}{T_R} \int_{-T_R/2}^{T_R/2} \frac{\mathrm{d}\bar{m}(x,t)}{\mathrm{d}t} \mathrm{e}^{-ik\omega_0 t}\, \mathrm{d}t. \tag{6.16}$$

The time derivative of the particle magnetization can be written in terms of the derivative of the magnetization with respect to the applied field:

$$\frac{\mathrm{d}\bar{m}(x,t)}{\mathrm{d}t} = \bar{m}'(H)\frac{\mathrm{d}H(x,t)}{\mathrm{d}t}. \tag{6.17}$$

Inserting Eq. 6.17 into Eq. 6.16 produces:

$$s_k(x) = -\frac{\mu_0\sigma}{T_R}\int_{-T_R/2}^{T_R/2}\bar{m}'(H)\frac{\mathrm{d}H(x,t)}{\mathrm{d}t}\mathrm{e}^{-ik\omega_0 t}\,\mathrm{d}t. \tag{6.18}$$

To further evaluate this, we follow the steps outlined in Ref. [89]. We can express t as a function of H_D, which will turn the integral over time into an integral over the drive field. Since H_S is independent of time, $\mathrm{d}H/\mathrm{d}t = \mathrm{d}H_D/\mathrm{d}t$. The system function then becomes:

$$s_k(x) = -\frac{\mu_0\sigma}{T_R}\int_{H_D(-T_R/2)}^{H_D(T_R/2)}\bar{m}'(H_S - H_D)\mathrm{e}^{-ik\omega_0 t(H_D)}\,\mathrm{d}H_D. \tag{6.19}$$

Rearranging Eq. 6.14 gives:

$$t(H_D) = \pm\frac{1}{\omega_0}\arccos\left(\frac{H_D}{H_0}\right). \tag{6.20}$$

When this is inserted into Eq. 6.19, to evaluate the integral, each half of one period of the drive field needs to be integrated separately:

$$\begin{aligned} s_k(x) &= -\frac{\mu_0\sigma}{T_R}\left[\int_{-H_0}^{H_0}\bar{m}'(H_S - H_D)\mathrm{e}^{ik\arccos(H_D/H_0)}\,\mathrm{d}H_D \right.\\ &\qquad\left. + \int_{H_0}^{-H_0}\bar{m}'(H_S - H_D)\mathrm{e}^{-ik\arccos(H_D/H_0)}\,\mathrm{d}H_D\right] \\ &= -\frac{\mu_0\sigma}{T_R}\int_{-H_0}^{H_0}\bar{m}'(H_S - H_D)\left(\mathrm{e}^{ik\arccos(H_D/H_0)} - \mathrm{e}^{-ik\arccos(H_D/H_0)}\right)\mathrm{d}H_D \\ &= -\frac{2i\mu_0\sigma}{T_R}\int_{-H_0}^{H_0}\bar{m}'(H_S - H_D)\sin(k\arccos(H_D/H_0))\,\mathrm{d}H_D. \end{aligned} \tag{6.21}$$

At this point, we notice that the integrand can be written in terms of Chebyshev polynomials of the second kind:

$$U_k(x) = \frac{\sin((k+1)\arccos x)}{\sin(\arccos x)}. \tag{6.22}$$

Using this, plus the identity:

$$\sin(\arccos x) = \sqrt{1-x^2}, \tag{6.23}$$

we can write the system function as:

$$s_k(x) = -\frac{2i\mu_0\sigma}{T_R}\int_{-H_0}^{H_0} \bar{m}'(H_S - H_D)U_{k-1}(H_D/H_0)\sqrt{1-(H_D/H_0)^2}\,\mathrm{d}H_D. \tag{6.24}$$

This expression is only applicable over the range $[-H_0, H_0]$, as the real part of the expression

$$U_{k-1}(x)\sqrt{1-x^2} = \sin(k\arccos(x)) \tag{6.25}$$

is equal to zero for $|x|> 1$. Finally, recalling that $H_S(x) = Gx$, we can write the system function as the convolution of the spatial derivative of the particle magnetization and Chebyshev polynomials:

$$s_k(x) = -\frac{2i\mu_0\sigma}{T_R}\bar{m}'(Gx) * \left(U_{k-1}(Gx/H_0)\sqrt{1-(Gx/H_0)^2}\right). \tag{6.26}$$

Writing the system function in this way will help us predict the spatial behavior of the harmonic amplitudes under a gradient field, as used in MPI. Noting that Chebyshev polynomials have exactly $k-1$ zero-crossings between the range $[-x, x]$ for polynomials of order k, since $\bar{m}'(H)$ should be strictly positive over the range $[-H_0, H_0]$, the harmonic amplitudes should have $k-1$ zero-crossings, where k represents the harmonic number.

As discussed previously, if particles are assumed to be isotropic, non-interacting, and identical, the average particle magnetization as a function of applied field is proportional to the Langevin function under low frequency fields [86]:

$$L(\xi) = M(\xi)/M_s = \coth\xi - 1/\xi, \tag{6.27}$$

where again $\xi = \mu_0\mu H/k_BT$. Using this as a first approximation of the average particle magnetization, we can plot the magnitude of various harmonic amplitudes as a function of

bias field based on Eq. 6.26 for different sized particles, shown in Fig. 6.1. Also shown is the ideal case, where the particle magnetization is a step function. For realistic particle sizes, the higher harmonic amplitudes drop off, particularly at high values of the bias field.

While the even harmonic amplitudes are typically zero due to symmetry of the magnetization response, we notice here that under the application of a bias field, the even harmonics become non-zero and can even surpass the odd harmonics, adding to the total signal strength when the gradient field is not centered directly over the sample.

Again using the Langevin function as an example model of $\bar{m}(H)$, we can calculate the resulting expected harmonic amplitudes and see that they agree with Eq. 6.26. In Fig. 6.2, the Fourier transform of $L'(\xi)$ was taken directly, with $\xi = \mu_0\mu(H_0\cos(\omega_0 t) + H_{\text{bias}})/k_BT$.

In reality, $\bar{m}(H)$ cannot be completely described by the Langevin function. For the applied frequencies and particle sizes used in MPI, there will be a phase lag between the particle magnetization and applied field due to relaxation behavior, as was discussed extensively in the previous chapters. Because of that, we expect that additional particle and environmental properties, other than those incorporated in the Langevin model, will affect the resulting signal. The sensitivity of the system function, as described above, should allow us to determine subtle differences in signal when properties are changed.

6.2.3 Multi-channel f-space image reconstruction

We now consider multi-channel image reconstruction. In standard frequency-space MPI, the image is reconstructed from the induced voltage signal using a single system function, which is the kernel to the integral imaging equation, as was discussed in detail previously. For multi-contrast MPI, multiple system functions are used for image reconstruction, with each system function corresponding to a single channel. The multi-channel reconstruction process is described below.

The general multi-channel image reconstruction procedure for continuous variables was first outlined in Ref. [147]. An additional parameter $\boldsymbol{\nu}$ can be defined, which describes one or multiple nanoparticle state variables. In this way, continuous variables can be incorpo-

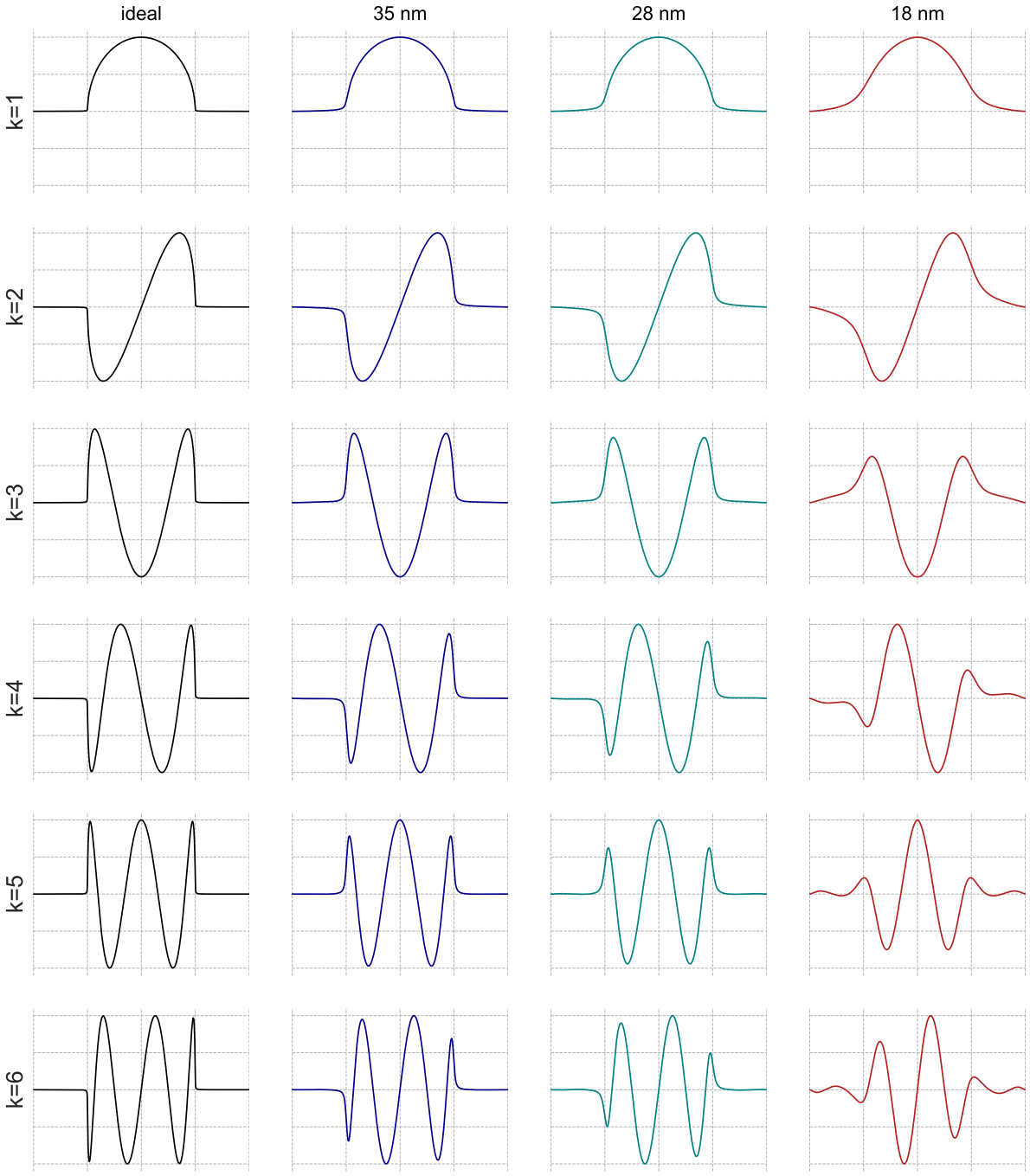

Figure 6.1: Simulated normalized 1D system functions for different sized particles, assuming their magnetization follows the Langevin function. In the ideal case, the frequency components are Chebyshev polynomials of the second kind.

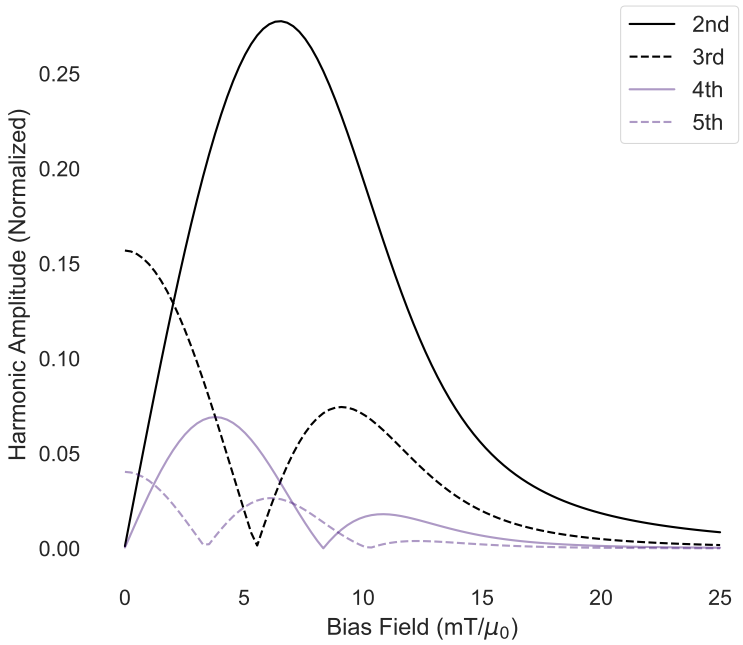

Figure 6.2: Second, third, fourth, and fifth harmonic amplitudes of signal produced by a 21 nm Langevin nanoparticle under an AC field with amplitude 10 mT/μ_0 and frequency 1 kHz, normalized to the maximum amplitude of the first harmonic. Dashed lines indicated odd harmonics, and solid lines indicate even harmonics.

rated into the system function. For example, $\boldsymbol{\nu}$ might directly represent the temperature or viscosity of a nanoparticle environment. However, it is not restricted to a single property; any combination of physical properties can be described by $\boldsymbol{\nu}$, as long as there is a one-to-one correspondence to a particular nanoparticle state. The number of physical properties described by $\boldsymbol{\nu}$, which we label l, will determine its dimension.

The particle distribution will then be a function of both position and state, i.e. $\rho = \rho(\mathbf{r}, \boldsymbol{\nu})$. The corresponding system function will also be a function of $\boldsymbol{\nu}$. The generalized signal equation will then be a double integral over the total volume of the FoV and the parameter space of $\boldsymbol{\nu}$, which we will label Ω:

$$u_k = \int_V \int_\Omega s_k(\mathbf{r}, \boldsymbol{\nu}) \rho(\mathbf{r}, \boldsymbol{\nu}) \, \mathrm{d}^l \nu \, \mathrm{d}^3 r. \tag{6.28}$$

This equation is fully generalized, allowing for spatial dependence of $\boldsymbol{\nu}$. However, in some cases, for example when $\boldsymbol{\nu}$ is describing a property of the nanoparticle itself, such as core or hydrodynamic size, it should not be dependent on the spatial location of the nanoparticles. In that case, the variables can be separated:

$$\rho(\mathbf{r}, \boldsymbol{\nu}) = \varrho(\mathbf{r}) c(\boldsymbol{\nu}), \tag{6.29}$$

where c now represents the state density, with $\int_\Omega c(\boldsymbol{\nu}) \, \mathrm{d}^l \nu = 1$. The variable ϱ now purely represents the spatial particle distribution. This will allow us to identify a system function $\hat{s}_k(\mathbf{r}) \equiv \int_\Omega s_k(\mathbf{r}, \boldsymbol{\nu}) c(\boldsymbol{\nu}) \, \mathrm{d}^l \nu$ which incorporates all parameters of the system. This system function $\hat{s}_k$ and Eq. 6.29 can be inserted into Eq. 6.28, which will reduce to the single-channel reconstruction model, Eq. 6.1:

$$\begin{aligned} u_k &= \int_V \int_\Omega s_k(\mathbf{r}, \boldsymbol{\nu}) \varrho(\mathbf{r}) c(\boldsymbol{\nu}) \, \mathrm{d}^l \nu \, \mathrm{d}^3 r \\ &= \int_V \hat{s}_k(\mathbf{r}) \varrho(\mathbf{r}) \, \mathrm{d}^3 r. \end{aligned} \tag{6.30}$$

This model is particularly useful when considering that nanoparticle tracers used for MPI have polydisperse size distributions, for example. However, while certain parameters such

as particle size are typically independent of spatial location, there are some state variables that may take specific values at different locations, e.g. temperature or viscosity. In that case, the state parameter $\boldsymbol{\nu}$ will be coupled to the spatial position. In such a system, the state parameter can be expressed in terms of position using a vector-valued function φ, so that $\boldsymbol{\nu} = \varphi(\mathbf{r})$. The total distribution can then be described by:

$$\rho(\mathbf{r}, \boldsymbol{\nu}) = \varrho(\mathbf{r})\delta(\boldsymbol{\nu} - \varphi(\mathbf{r})). \tag{6.31}$$

This indicates that ρ is equal to the particle spatial distribution ϱ when $\boldsymbol{\nu} = \varphi(\mathbf{r})$, and equal to zero otherwise. If φ is constant in time, the signal generated will then be:

$$\begin{aligned} u_k &= \int_V \int_\Omega s_k(\mathbf{r}, \boldsymbol{\nu})\varrho(\mathbf{r})\delta(\boldsymbol{\nu} - \varphi(\mathbf{r}))\,\mathrm{d}^l\nu\,\mathrm{d}^3 r \\ &= \int_V \hat{s}_k(\mathbf{r}, \varphi(\boldsymbol{\nu}))\varrho(\mathbf{r})\,\mathrm{d}^3 r, \end{aligned} \tag{6.32}$$

where $\hat{s}_k(\mathbf{r}, \varphi(\boldsymbol{\nu}))$ is a variation of a typical single-channel system matrix.

So far, we have only discussed continuous variables. However, we may have a discrete parameter space; for example, samples with different mean core sizes, or immobilized and mobile particles. In the case of a discrete parameter space, we can assign an index to the parameter state variable, $\boldsymbol{\nu}_i$, where i represents the individual discrete particle states, up to n total states. We can then write the total particle distribution as:

$$\rho(\mathbf{r}, \boldsymbol{\nu}) = \sum_{i=1}^{n} \varrho_{\nu_i}(\mathbf{r})\delta(\boldsymbol{\nu} - \boldsymbol{\nu}_i), \tag{6.33}$$

where $\varrho_{\nu_i}(\mathbf{r})$ is the spatial distribution of all particles in state $\boldsymbol{\nu}_i$. A corresponding system function $\hat{s}_{k,\nu_i} = s_k(\mathbf{r}, \boldsymbol{\nu}_i)$ can then be defined for each $\boldsymbol{\nu}_i$. Using these expressions, the signal equation becomes:

$$\begin{aligned} \hat{u}_k &= \sum_{i=1}^{n} \int_V \int_\Omega s_k(\mathbf{r}, \boldsymbol{\nu})\varrho_{\nu_i}(\mathbf{r})\delta(\boldsymbol{\nu} - \boldsymbol{\nu}_i)\,\mathrm{d}^l\nu\,\mathrm{d}^3 r \\ &= \sum_{i=1}^{n} \int_V \hat{s}_{k,\nu_i}(\mathbf{r})\varrho_{\nu_i}(\mathbf{r})\,\mathrm{d}^3 r. \end{aligned} \tag{6.34}$$

Here, the total measured signal $\hat{u}_k$ is the superposition of the individual signals generated by particles of type ν_i, i.e. $\hat{u}_k = \sum_i u_{k,\nu_i}$.

Now that we have identified the system functions for each respective case, we can move on to image reconstruction from an unknown particle distribution. With single contrast image reconstruction, outlined in §6.2.1, the signal equation Eq. 6.1 can be reformulated as a regularized least-squares minimization problem. When all particles are in a single state ν_i, for example, the least-squares minimization can be expressed as:

$$\rho_{\nu_i} = \text{argmin}_{\tilde{\rho}_{\nu_i}} \sum_{k=1}^{K} |u_k - \int_V \hat{s}_{k,\nu_i}(\mathbf{r}) \tilde{\rho}(\mathbf{r}) \, \mathrm{d}^3 r|^2. \tag{6.35}$$

This expression can be generalized to the case of a discrete state parameter space, where the total measurement signal is simply a superposition of the individual signals, as described above:

$$\rho_{\nu_1}, \ldots, \rho_{\nu_n} = \text{argmin}_{\tilde{\rho}_{\nu_1}, \ldots, \tilde{\rho}_{\nu_n}} \sum_{k=1}^{K} |u_k - \sum_{i=1}^{n} \int_V \hat{s}_{k,\nu_i}(\mathbf{r}) \tilde{\rho}_{\nu_i}(\mathbf{r}) \, \mathrm{d}^3 r|^2. \tag{6.36}$$

This reconstruction requires calibration measurements of each system function $\hat{s}_{k,\nu_i}(\mathbf{r})$ for each particle state $\boldsymbol{\nu}_i$, which appears in Eq. 6.34.

For continuous and spatially dependent parameter spaces, described by the signal equation in Eq. 6.32, the optimization problem becomes:

$$\rho, \varphi = \text{argmin}_{\tilde{\rho}, \tilde{\varphi}} \sum_{k=1}^{K} |u_k - \int_V \hat{s}_k(\mathbf{r}, \tilde{\varphi}(\mathbf{r})) \tilde{\rho}(\mathbf{r}) \, \mathrm{d}^3 r|^2. \tag{6.37}$$

Both the spatial distribution and the vector-valued function φ need to be determined. Here, the main challenge lies in determining the full system function $\hat{s}_k$. Since measuring the system for a single parameter ν_i is already quite time consuming, a measurement-based approach for this may be impractical. An alternative would be to simulate the system function using a model, for example as was done in the previous subsection using the Langevin function as a model. However, depending on the relevant parameters, simulations and theoretical models are often either too time consuming or inaccurate.

In a fully general case, such as in Eq. 6.1, the reconstruction requires:

$$\rho = \operatorname{argmin} \sum_{k=1}^{K} |u_k - \int_V \int_\Omega \hat{s}_k(\mathbf{r}, \boldsymbol{\nu}) \tilde{\rho}(\mathbf{r}, \boldsymbol{\nu}) \, \mathrm{d}\nu \, \mathrm{d}^3 r|^2. \tag{6.38}$$

Again, obtaining the generalized system function $\hat{s}_k$ is the main difficulty here. It is possible to avoid this problem by discretizing the parameter space, for example by setting $\varrho_{\nu_i}(\mathbf{r}) = w_i \rho(\mathbf{r}, \boldsymbol{\nu}_i)$ with discretization weights w_i. This will reduce the problem to multi-channel reconstruction.

In Ref. [147], this multi-channel reconstruction procedure was shown to be able to quantify nanoparticle viscous environments by measuring system functions for two viscosity states and using the discrete multi-channel reconstruction procedure. In the following section, we apply the multi-channel reconstruction procedure to a new application: core size discrimination.

6.3 Core size discrimination with MPI

In this section, we investigate the potential for multi-contrast MPI using MNP core size classification and differentiation. An advantage to this technique is that particle cores can be functionalized separately, but can otherwise be characterized independently of the tracer environment. Several specific approaches to multicolor spectroscopy based on size or nanoparticle type differentiation have been proposed [143,144,156]; however, they all have significant limitations. Previous techniques have so far only demonstrated potential for differentiation between particles of substantially different sizes (differences in particle core diameters of at least 10-15 nm, leading to reduced or no signal from at least one of the partcles). Also, past demonstrations of multicolor MPI based on tracer, rather than environment, discrimination involved nanoparticle tracers that did not display optimized MPI performance, primarily due to high polydispersity and non-optimal sizes. However, for a strong MPI signal, particles must be restricted to a relatively narrow range of sizes tailored to the applied field, otherwise signal will be dramatically lowered, as was explored in the previous chapter. Consequently, realistic high-quality multicolor imaging requires differentiation between particles whose diameters are only a few nanometers apart. The optimal size for MPI performance

of phase-pure magnetite tracers was discussed in the previous chapter, and is around 28 nm in core diameter. Due to this size restriction, a size-based differentiation approach requires highly monodisperse particles with carefully controlled size, as well as a highly sensitive signal separation technique.

With highly tailored single-core MNPs specifically designed for optimal MPI performance, as defined by image resolution and signal intensity, MNP cores of different sizes could be separately functionalized for specific purposes, e.g. long-term circulation [157], cancer targeting [133], or coating of devices for cardiovascular interventions [158, 159], allowing for reconstruction of high resolution images with high sensitivity on each channel. Each channel, corresponding to a different core size, can be assigned to a different color, resulting in a multicolor image. In this section, we adapt the multi-channel reconstruction procedure outlined in the previous section to demonstrate particle size discrimination and combine it with sample localization in 2D MPI using highly monodisperse optimized MNPs.

6.3.1 Initial simulation and MPS study

In total, four nanoparticle core sizes were fabricated within a range of $21 - 28$ nm; for most experiments presented in this section, three samples were used at a time. The core diameters of each sample were 21.9 nm, 23.8 nm, 25.3 nm, and 27.7 nm with respective size distribution parameters of 0.04, 0.05, 0.08, and 0.07, assuming a log-normal distribution of core sizes. For particles in this size range under an applied AC field, a combination of Néel rotation (flipping of the magnetic moment within the particle) and Brownian rotation (rotation of the entire particle to align with the field) will occur, as discussed in §4.

The samples were first measured using zero-dimensional MPS, using a custom-built spectrometer [160] with a drive frequency of 26 kHz and a drive-field amplitude of 20 mT/μ_0. MPS measurements are used to predict the MPI performance of each sample. The MNP tracer response $\mathrm{d}m/\mathrm{d}H$ plotted against the applied field defines the point-spread function (PSF). As discussed in §5.1, the height of the PSF indicates the signal intensity of the MPI signal, and the full-width at half-maximum (FWHM) determines the potential image resolu-

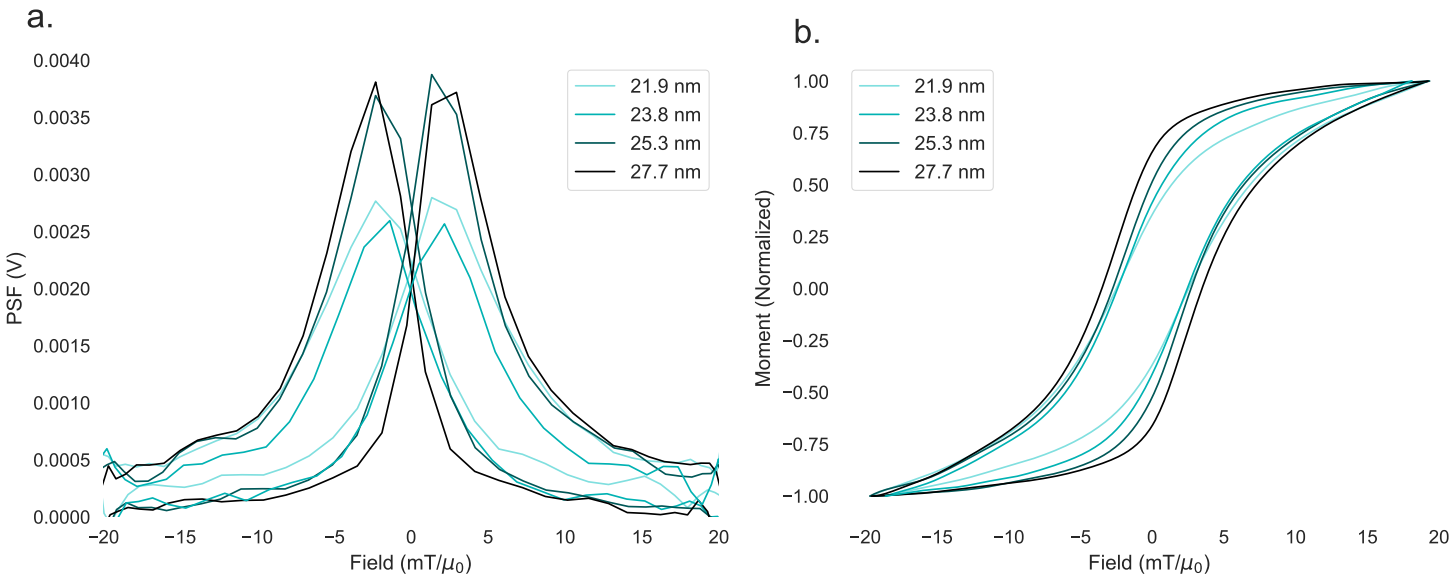

Figure 6.3: a. The point-spread function for four nanoparticle samples as measured by MPS. The smaller samples show decreased peak height and broader FWHM compared to the larger samples. b. The integrated $m(H)$ magnetization curves.

tion, at least for 1D MPI sequences along the direction of excitation [54]. Fig. 6.3 shows that the smaller two samples, 21.9 nm and 23.8 nm, indicate significantly worse performance, both in terms of signal intensity and resolution, than the larger two samples, which are comparable in terms of indicated performance. We therefore expect a lower signal-to-noise ratio (SNR) from images generated from the two smaller samples than from the two larger samples. It can also be seen that the FWHM decreases with increasing core size. Hysteresis loops ($m(H)$), generated by integrating the time-domain MPS data, show the differences in magnetization response among the four samples: once the field is reversed, the larger particles take longer to reverse their magnetic moment, indicated by the increasing width of the hysteresis loop with size (this reflects the phase lag increase with size). While the PSF for the two smaller samples and two larger samples each look similar, the $m(H)$ curve clearly shows that there is a continuous progression with size, indicated by the increasing steepness of the curve and width of the loop.

During an MPI scan, all particles outside the dynamic region are magnetically saturated. As the field-free point is scanned over the sample, the particles' magnetic moment will rotate in a manner that can be characterized in part by the effective relaxation timescale. The equilibrium relaxation time, whether Brownian (τ_B), or Néel (τ_N) increases with particle size. While in reality, the rotation mechanism and effective relaxation time will be dependent on field conditions, we can nevertheless see that the relaxation dynamics are highly sensitive to particle size. In general, larger particles will have a longer relaxation time, and will therefore take longer to begin magnetic reversal once the field is switched. This effect can be seen in Fig. 6.3, where the integrated $m(H)$ loop widens with increasing core size. Due to these differences in the reversal dynamics, differences will arise in the frequency spectra, as measured in each sample system matrix.

Our goal here is to meaningfully differentiate between the signals induced by each core size; from the zero-dimensional MPS measurements, it is difficult to identify significant differences between the two small samples, and especially between the two larger particle samples. Also, since the height of the PSF is concentration-dependent, after normalizing the signal for concentration, differences will become even smaller. Therefore, we move on to one-dimensional MPS, where a gradient field is applied along a single direction. We can then examine the spatial dependence of the harmonic spectrum of the recorded MPI signal, which should be highly sensitive to particle characteristics, including size.

Recalling the derivations from §6.2.2, we can begin by looking at the size dependence of harmonic amplitudes in one dimension from the Langevin function. In Fig. 6.4, the harmonic amplitudes, generated by taking the Fourier transform of the Langevin function, are plotted as a function of bias field, where the total field inserted into the Langevin function is $H = H_0 \cos(\omega_0 t) + H_{\text{bias}}$. There are clear peaks in the second and third harmonics, which we expect, since they should have the same form as Chebyschev polynomials of the second kind (Fig. 6.1). Importantly, the location and shape of these peaks are size-dependent; it's clear that the location of these peaks shifts based on particle core size. This is a promising indication that the system functions of each nanoparticle sample will show meaningful

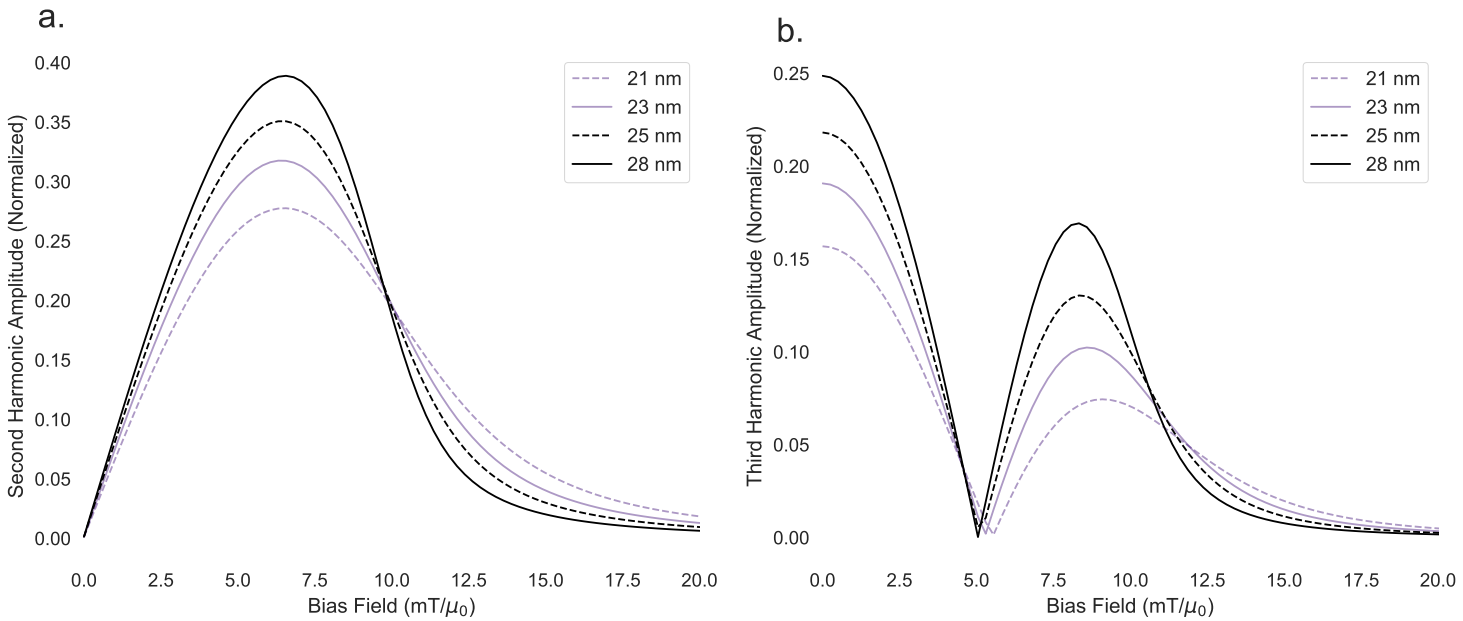

Figure 6.4: a. Amplitude of the second harmonic for four particle sizes b. 3rd. normalized to first harmonic

differences.

However, the Langevin function model ignores relaxation behavior and so cannot accurately describe nanoparticle dynamics in MPI, especially for high frequency fields. For a more sophisticated model, we use stochastic Langevin simulations, as described in §3. After simulating the particle response to the applied magnetic field (again $H = H_0 \cos(\omega_0 t) + H_{\text{bias}}$), the harmonic amplitudes can be extracted by taking the Fourier transform of the average particle magnetization at each value of the bias field, which corresponds to spatial location under a constant gradient field. Simulations for a range of bias field strengths for particles under a 25 kHz applied field, with AC field amplitude equal to 20 mT/μ_0, are shown in the top row of Fig. 6.5. The same characteristic peaks are observed, with an increasing number of zero-crossings with harmonic number, as expected. Again, while the even harmonics would typically not be expected to contribute to the signal, the application of a bias field introduces non-zero values of even harmonics.

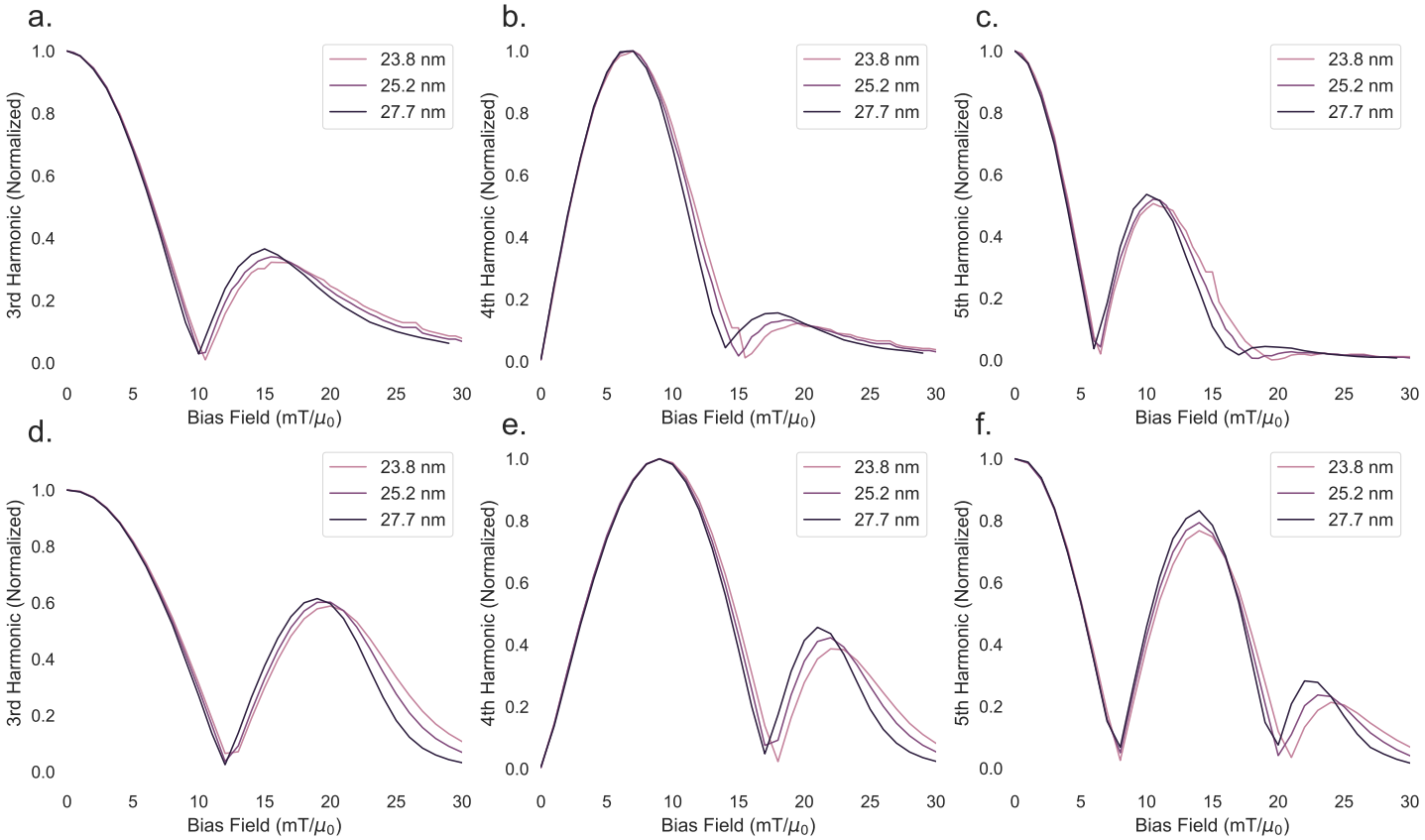

Figure 6.5: Top row: Measurements of the 3rd (a), 4th (b), and 5th (c) harmonic amplitudes as a function of offset field for three particle sizes. Bottom row: Simulations of the 3rd (d), 4th (e), and 5th (f) harmonic amplitudes as a function of offset field for three particle sizes.

Finally, 1D MPS measurements were performed under the same conditions as the simulations; results are shown in the bottom row of Fig. 6.5. The qualitative behavior of the harmonic amplitudes in the MPS measurements matches the simulations, and it can again be shown, as predicted from the analysis in §6.2.2, that there are $k-1$ zero-crossings for each harmonic amplitude with number k. As particle core size increases, the location of these zero-crossings, and corresponding peaks, shift to the left (to lower values of the bias field).

The important observation here is that size-dependent differences in AC nanoparticle

dynamics emerge under a gradient field that may not be visible in zero-dimensional MPS. This indicates that there will be a size-dependent spectral response (here recorded as a 1D system function) that can be used to separate the signal from different particle types and reconstruct a multi-channel image.

6.3.2 MPI experimental setup and reconstruction procedure

We now proceed to two-dimensional MPI scans. The particle core sizes are discriminated in a multi-step process. The first step involves measuring a calibration system function for each sample. Then, a collection of measurement scans of each sample is made, with the samples at a number of different locations within the field of view (FoV). Discrete multi-channel image reconstruction is then performed, as described in §6.2.3. The images are then processed, and weight vectors for each channel, corresponding to each nanoparticle sample, are generated. Each image is then classified based on core size. Finally, a measurement scan will be performed of all three samples within the FoV, and a single multicolor image will be reconstructed.

Multi-contrast MPI was performed using a Philips preclinical MPI package with a Bruker preclinical MPI system [161]. The FoV was 24×24 mm^2 in the xy-plane, with a voxel size of 1×1 mm^2. The drive field frequency was 24.5 kHz in the x-direction and 26 kHz in the y-direction. The drive field amplitude was 12 mT/μ_0 in both directions. With these parameters, a single scan of the 2D FoV takes 652.8 μs. The applied gradient field was 1.2 (T/m)/μ_0 in the x- and y-direction, and 2.4 (T/m)/μ_0 in the z-direction.[1] The three signals were filtered and digitized with a bandwidth of 2.5 MHz. The measurement is performed in frequency space, so the final measurement vector consists of the Fourier transformed time signals.

The three samples used for the initial 2D MPI scans had diameters 21.9 nm, labeled

[1]Gauss's law for magnetism states that the divergence of a magnetic field must be equal to zero. Since this scanner is built with a positive gradient field in the x- and y-directions, a gradient in the z-direction is required in order to satisfy Gauss's law, even though no measurements are made along the z-direction.

S, 25.2 nm, labeled M, and 27.7 nm, labeled L. The three calibration measurements were performed by averaging 10 000 individual measurements at each grid position for each sample, and the system matrix was constructed by concatenating the Fourier transformed time signal at each grid position. The system matrices are labeled $\mathbf{S}_{\mathrm{S}}$, $\mathbf{S}_{\mathrm{M}}$, and $\mathbf{S}_{\mathrm{L}}$ corresponding to the samples S, M, and L respectively.

For the image scans, each sample was attached to the arm of a three axis robot (Isel Automation GmbH) and moved to the center position of the scanner, as well as 20 additional random positions within the FoV. 10 000 measurements were taken at each position. The random positions were the same for each of the three experiments and are listed in Table 6.1 and shown in Fig. 6.6.

position	0	1	2	3	4	5	6	7	8	9	10
x (mm)	0.00	-3.87	-5.54	0.84	3.03	7.32	8.34	0.71	-6.33	1.58	2.45
y (mm)	0.00	-8.32	-3.12	-5.46	1.19	8.68	-7.49	-3.37	0.93	-7.35	-2.62
position	11	12	13	14	15	16	17	18	19	20	
x (mm)	-7.23	5.57	-1.54	7.65	2.95	-1.03	5.15	-3.16	-8.21	2.62	
y (mm)	1.58	-0.05	-3.78	7.6	3.93	4.36	3.31	0.2	7.47	6.31	

Table 6.1: A table with all sample positions.

The measurements and system matrices were first frequency filtered; only frequencies above 80 kHz and with a signal to noise ratio above 3.5 were used for reconstruction. To analyze the influence of noise, the measurements obtained at each position were block averaged with a block length M_{avg} of 10 000, 1000, and 100, yielding 1, 10, and 100 final multi-channel images per sample and position, respectively.

Using the system matrices $\mathbf{S}_{\mathrm{S}}$, $\mathbf{S}_{\mathrm{M}}$, and $\mathbf{S}_{\mathrm{L}}$, multi-channel image reconstruction was performed by solving the Tikhonov regularized optimization problem, as outlined in §6.2.3:

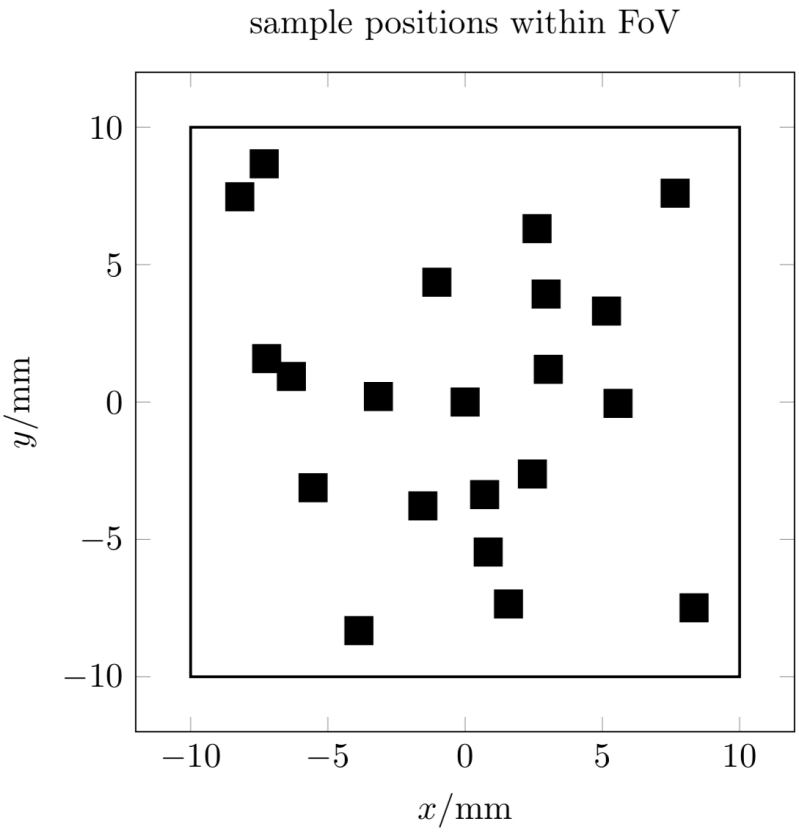

Figure 6.6: Distribution of the 21 positions listed in Table 6.1 within the FoV (thick rectangle). The size of the markers matches the size of the samples up to a global scaling of the figure.

$$\mathbf{c}_S, \mathbf{c}_M, \mathbf{c}_L = \text{argmin} \left\| \begin{pmatrix} \mathbf{S}_S & \mathbf{S}_M & \mathbf{S}_L \end{pmatrix} \begin{pmatrix} \tilde{\mathbf{c}}_S \\ \tilde{\mathbf{c}}_M \\ \tilde{\mathbf{c}}_L \end{pmatrix} - \hat{\mathbf{u}} \right\|_2^2 + \tilde{\lambda} \left\| \begin{pmatrix} \tilde{\mathbf{c}}_S \\ \tilde{\mathbf{c}}_M \\ \tilde{\mathbf{c}}_L \end{pmatrix} \right\|_2^2 . \tag{6.39}$$

The unknown particle distributions for each channel, labeled $\mathbf{c}_\mathrm{S}$, $\mathbf{c}_\mathrm{M}$, and $\mathbf{c}_\mathrm{L}$, were determined for each measurement vector $\hat{\mathbf{u}}$, and obtained with 10 000 iterations of the Kaczmarz solver. The Tikhonov regularization parameter $\tilde{\lambda}$ was chosen to be 0.01, 0.05, and 0.1 for M_avg of 10 000, 1000, and 100 respectively. Since noise will be higher for lower values of M_avg, $\tilde{\lambda}$ should increase accordingly.

As shown in Fig. 6.7, each reconstructed image contains the channels $\mathbf{c}_\mathrm{S}$, $\mathbf{c}_\mathrm{M}$, and $\mathbf{c}_\mathrm{L}$. The signal generated by the samples within the different channels is collected by summing over a circular region of interest (ROI) for each channel individually, shown in Fig. 6.8. The ROI is centered at the corresponding sample position and has a radius of 4 voxels clipped against the edges of the reconstructed images. The summation results in a weights vector $w = (\sigma_\mathrm{S}, \sigma_\mathrm{M}, \sigma_\mathrm{L})$ containing the summed signal for the channels $\mathbf{c}_\mathrm{S}$, $\mathbf{c}_\mathrm{M}$, and $\mathbf{c}_\mathrm{L}$ respectively. Explicitly, the signal weights, as well as the relative weights α, are calculated as follows.

For a single image, generated from one of the three samples at a single position, the channel S weight will be

$$\sigma_S = \sum_{j \in \mathrm{ROI}} \mathbf{c}_{S,j}, \tag{6.40}$$

and the relative weight is

$$\alpha_S = \frac{\sigma_S}{\sigma_S + \sigma_M + \sigma_L}. \tag{6.41}$$

Similarly, the channel M signal weight and relative weight will be

$$\sigma_M = \sum_{j \in \mathrm{ROI}} \mathbf{c}_{M,j} \tag{6.42}$$

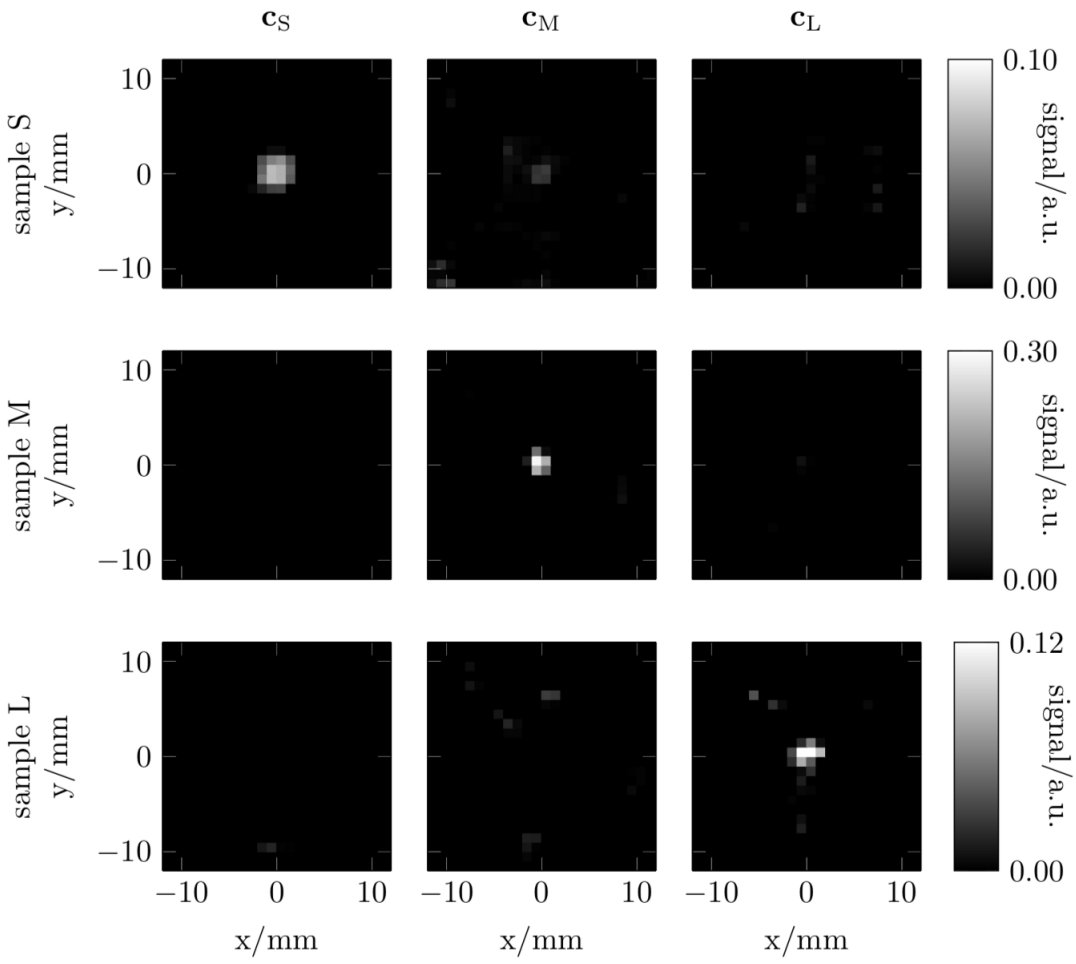

Figure 6.7: Multi-channel reconstruction $M_{\text{avg}} = 10\ 000$ of sample S (top row), sample M (middle row), and sample L (bottom row) located at the center (position 0) of the field of view. The signal strength and distribution throughout the channels $\mathbf{c}_S$ (left column), $\mathbf{c}_M$ (middle column), and $\mathbf{c}_L$ (right column) is characteristic for each sample and changes very little with the sample location.

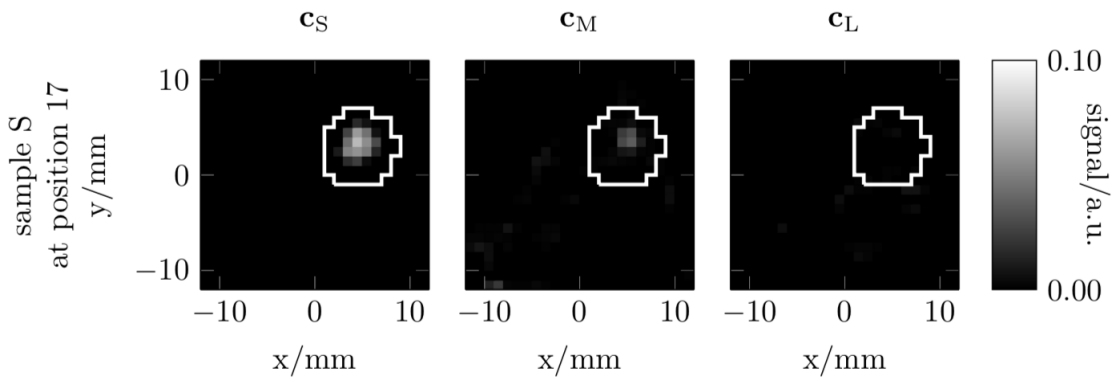

Figure 6.8: Multi-channel reconstruction $M_\mathrm{avg} = 10\,000$ of sample S at position 17. The ROI is indicated by the white line. Summation of the ROI for each channel yields the weights vector w = (0.72, 0.11, 0.02).

$$\alpha_M = \frac{\sigma_M}{\sigma_S + \sigma_M + \sigma_L}, \tag{6.43}$$

and the channel L signal weight and relative weight will be

$$\sigma_L = \sum_{j \in \mathrm{ROI}} \mathbf{c}_{L,j} \tag{6.44}$$

$$\alpha_L = \frac{\sigma_L}{\sigma_S + \sigma_M + \sigma_L}. \tag{6.45}$$

The core size discrimination algorithm described here will be applied to each set of images. Weight vectors $w_{s,p,i}$ are calculated for all samples $s \in \{\mathrm{S}, \mathrm{M}, \mathrm{L}\}$, positions $p \in \{0, 1, \ldots, 20\}$ and each image i. Taking the weight vectors $w_{s,p,i}$ and relative weight vectors $\alpha_{s,p,i}$ as observations, the task of core size discrimination can be formulated as a classification problem, where we have to identify a suitable core size label, i.e. S, M, or L, for each observation. We use the nearest centroid classification algorithm for this task. This algorithm is split into two parts: a learning phase and a classification phase. In the learning phase we use the weight vectors $w_{s,p=0,i}$ and class labels s as training data to calculate the three centroids

$$\mu_s = \frac{1}{N}\sum_{i=1}^{N} w_{s,p=0,i}, \tag{6.46}$$

where N is the total number of reconstructed images at position 0. In the classification phase a class label C is assigned to each of the remaining observations $w_{s,p,i}$, $p \neq 0$, by finding the nearest centroid

$$C = \arg \min_{s\in\{\mathrm{S,M,L}\}} \|\mu_s - w_{s,p,i}\|_2. \tag{6.47}$$

6.3.3 Core size classification

An example set of reconstructed images on each channel, in this case with samples at position 0, is shown in Fig. 6.7. Although the full set of reconstructed images for all positions is not shown here, the reconstructions shown in Fig. 6.7 are qualitatively representative for most of the multi-channel reconstructions. There is a strong signal contribution at the location of the sample in at least one of the channels, typically corresponding to the "correct" channel (i.e. channel $\mathbf{c}_\mathrm{S}$ for sample S, channel $\mathbf{c}_\mathrm{M}$ for sample M, and channel $\mathbf{c}_\mathrm{L}$ for sample L). While there is some signal detected at the sample location in other channels (in Fig. 6.7, e.g., there is clearly some signal from sample S reconstructed in channel M), the signal is much weaker than in the correct corresponding channel. There are only a few cases observed where image noise creates "hot" pixels that are brighter than the sample signal.

The reconstructions shown in Fig. 6.7 were generated by averaging over all 10 000 images. As the block averaging length M_avg decreases, the signal from sample S shifts from primarily channel $\mathbf{c}_\mathrm{S}$ to $\mathbf{c}_\mathrm{M}$. Signal from sample S within channel $\mathbf{c}_\mathrm{L}$ occurs rarely and therefore seems to be coincidental noise. With the medium sized cores (sample M) and large cores (sample L), we find essentially all of the signal in channels $\mathbf{c}_\mathrm{M}$ and $\mathbf{c}_\mathrm{L}$, respectively, regardless of block averaging length. Signal within the other channels occurs rarely and is mostly caused by noise. While this behavior was typical for reconstructions generated at most sample positions, when the sample was located close to the corners of the FoV, specifically positions

5, 6, 14, and 19, there was significantly more signal leakage into other channels, especially leakage into channel $\mathbf{c}_{\mathrm{M}}$ for samples S and L. This corresponded with an overall drop in the signal intensity for all samples.

		true core size								
		$M_{\mathrm{avg}} = 10000$			$M_{\mathrm{avg}} = 1000$			$M_{\mathrm{avg}} = 100$		
		S	M	L	S	M	L	S	M	L
class label	S	20	0	2	200	12	38	1950	247	400
	M	0	20	0	0	188	0	43	1753	0
	L	0	0	18	0	0	162	7	0	1600

Table 6.2: A confusion matrix for each averaging block length M_{avg} shows the number of correct assignments in the diagonal of each matrix. The number of false assignments is listed in the off-diagonal elements.

Classification of core size using signal weight vectors was performed for each image and block averaging length, as described in §6.3.2. The results are summarized in Table 6.2, which shows the confusion matrices for each block averaging length. Each row of the matrix represents the predicted sample core size, while each column represents the true core size. Correct predictions are found on the diagonal of each matrix, and misclassifications are represented in the off-diagonal elements. For block averaging lengths M_{avg} of 10 000, 1000, and 100, the core size is predicted successfully in 96.7%, 92.1%, and 88.9% of the cases respectively.

If we analyze the spatial distribution of the misclassified observations, there is a strong accumulation of misclassifications at positions 5, 6, 14, and 19, which represent the corners of the FoV, as shown in Fig. 6.9. For samples located in those four positions close to the corners of the FoV, prediction rates are as low as 33-66%, which is a direct consequence of the increased signal leakage and reduced signal intensity in the corresponding multi-channel images. We hypothesize that the local excitation trajectory at these positions is the

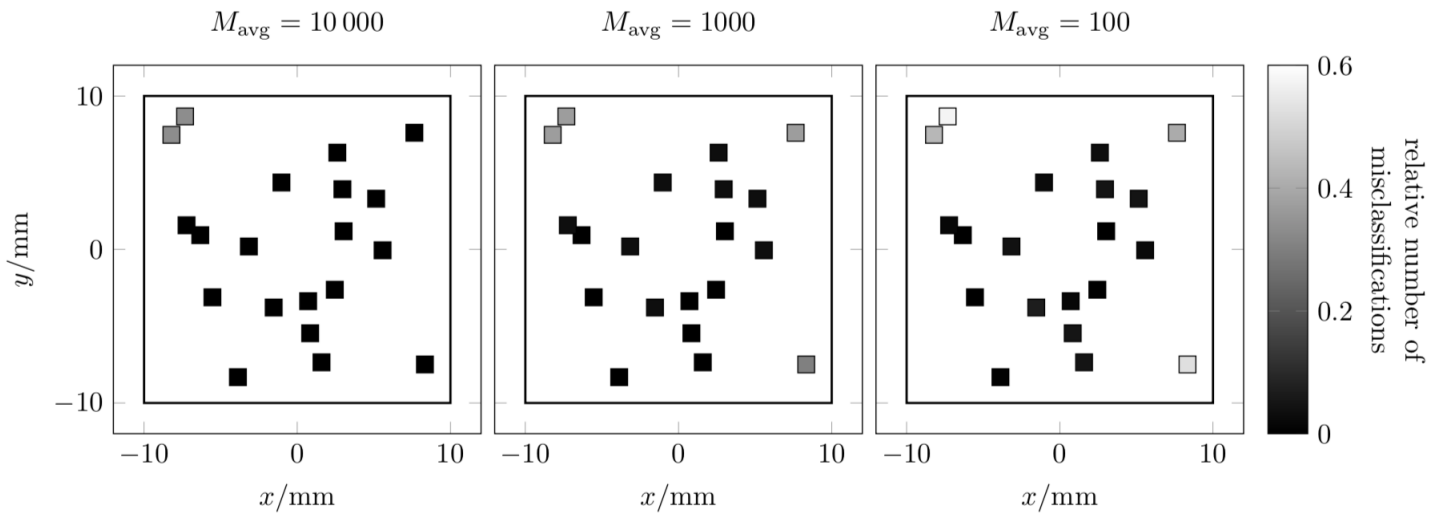

Figure 6.9: The relative number of misclassifications is shown for all averaging block lengths M_{avg} as a dependence on the position of the sample. Most misclassifications occur with the sample close to the corner of the FoV. There is also an increase of the relative number of misclassifications with decreasing block averaging length.

underlying cause for these anomalies. The drive field follows a Lissajous trajectory (example shown in Fig. 6.10), and so in the corners of the FoV, it lacks a strong field reversal as with, for example, the excitation trajectory at the central position. If those four positions are excluded from the analysis, the prediction rates improve significantly, to 100%, 98.3%, and 97.5%.

To assess the image quality, the signal-to-noise ratio (SNR) of the multi-channel images is calculated for each block averaging length. Following the same notation as before, the resulting 2D image reconstructions are referred to as $\mathbf{c}_{s,p,i}$. The image signal $a_{s,p,i}$ is given by the respective maximal voxel value found in the circular region of interest (ROI) around the corresponding sample position. The image noise $n_{s,p}$ is quantified by the standard deviation of all remaining voxel values outside the ROI in all images with equal sample s and location p. The SNR of image i is then simply given by the quotient $a_{s,p,i}/n_{s,p}$ of signal and noise. The SNR mainly depends on the sample used and the block averaging length. Results are

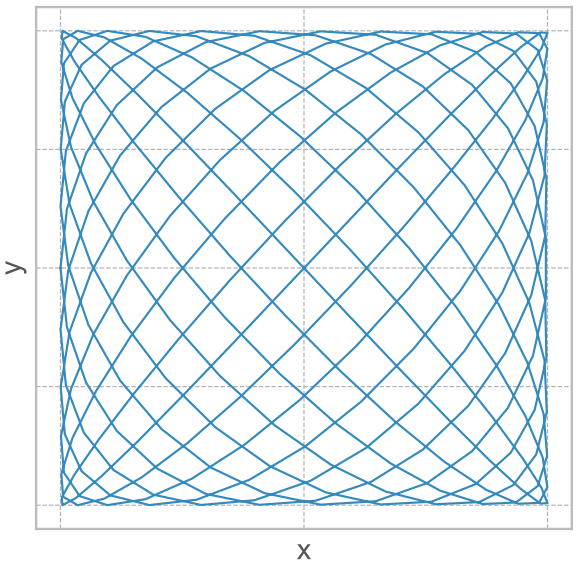

Figure 6.10: A 2D Lissajous trajectory when the ratio of frequencies is 11/12.

shown in Table 6.3.

The sample size, which corresponds to the image resolution, is also estimated by evaluation of the projected images $\mathbf{c}_{s,p,i}$, and is given by the number of voxels $v_{s,p,i}$ inside the ROI with voxel values above half of the image signal $a_{s,p,i}$. The estimated sample size also depends on the sample used and the block averaging length. The estimated sample sizes are also shown in Table 6.3.

We found that the height and FWHM of the PSF extracted from MPS for each nanoparticle sample were able to correctly qualitatively predict their imaging performance. While the height and FWHM of the zero-dimensional MPS peak are known to predict 1D MPI SNR and resolution along the scanning direction, it was unclear if those results could be generalized to 2D excitation sequences. The SNR of sample S in the 2D images is worse than that of samples M and L by at least a factor of 3, while the SNR of samples M and L are comparable, differing by 60% or less. This is consistent with our predictions from MPS, where we found that the peak of the PSF generated from sample S was significantly lower

		$M_{\text{avg}} = 10000$		$M_{\text{avg}} = 1000$		$M_{\text{avg}} = 100$	
		SNR	ESS	SNR	ESS	SNR	ESS
core size	S	40	8	30	12	20	10
	M	260	3	100	5	60	6
	L	150	4	160	6	90	6

Table 6.3: Median signal-to-noise ratio (SNR) and estimated sample size (ESS), in voxels, for each block averaging length M_{avg}.

than those of samples M and L, which are about the same height. Similarly, the FWHM from the PSF of sample S was 42-44% greater than those of the samples M and L, which is consistent with our results that the estimated sample size of sample S is approximately double those of M and L. The FWHM of samples M and L differed by less than 2%, which is reflected by the fact that the estimated sample size of samples M and L is approximately the same in the 2D scans.

The polydispersity of the nanoparticle core sizes naturally limits the maximum accuracy that can be acheived. There will be significant overlap in core size among samples, even with low size distribution parameters (< 0.1), as seen in Fig. 6.11. As a result, there will be some unavoidable signal leakage into other channels, as we have observed. Improving monodispersity of samples will be a key component to improving prediction accuracy in the future. This can potentially be achieved either during the synthesis process or with an additional filtering step, although in the latter case, maintaining signal strength is quite challenging.

The above results indicate that it is possible to distinguish between particles that differ in core diameter by as little as 2.5 nm with a high degree of accuracy. The two main factors influencing the core size prediction rates are the block averaging length and the spatial position of the sample within the FoV. Raising the block averaging length, which directly

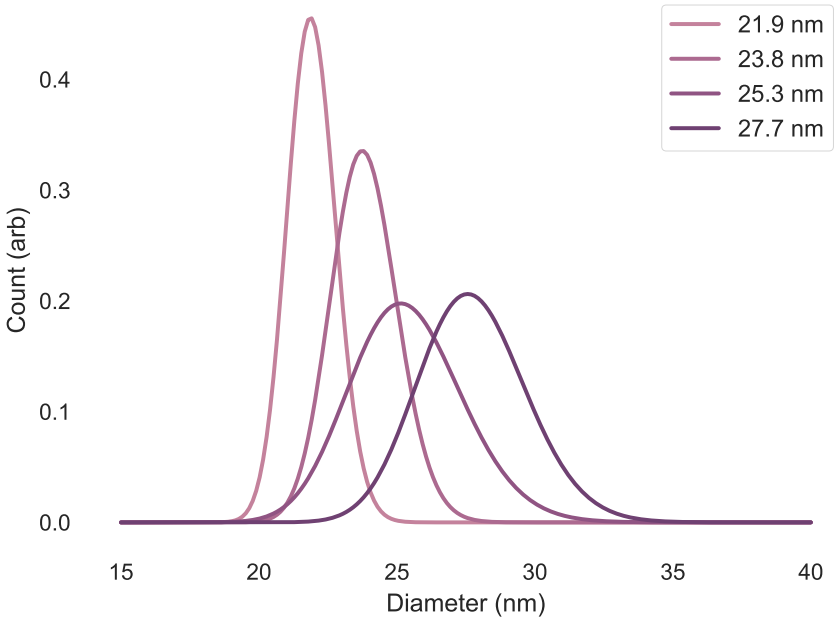

Figure 6.11: Distribution of nanoparticle sizes, assuming that they follow a log-normal distribution.

relates to the SNR of the MPI measurement, increases the visual quality of the multi-channel images as well as the core size prediction rates.

6.3.4 MPI final image reconstruction

The final step here is to test this reconstruction procedure for a measurement with multiple sample types. In this test, system functions were first obtained for three different particle sizes. Then, a single measurement scan was performed on a holder containing all three samples. The final measurement was then reconstructed on three separate channels, with each channel corresponding to a particular sample and an assigned color. Each region of the FoV was then classified based on size, and a final colorized image was generated.

To perform these measurements, a sample holder was constructed, consisting of three wells separated by 9.3 mm. Liquid samples of three particle sizes were inserted into each well, as shown in Fig. 6.12. A color was chosen for each particle core size: the smallest

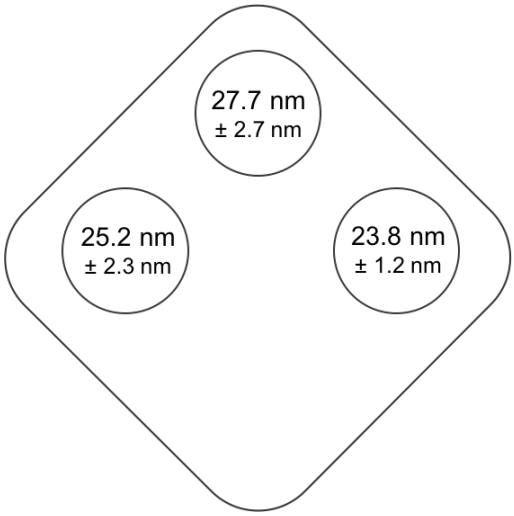

Figure 6.12: Diagram of sample holder for phantom measurements. Three wells contain particle samples of three sizes.

core size, 23.8 nm, was chosen to be green; the 25.2 nm sample was chosen to be blue; and the largest, 27.7 nm, was red. MPI measurements were again performed on the preclinical Bruker MPI system at the University Medical Center Hamburg-Eppendorf, using the same field conditions as in §6.3.3.

First, a calibration system matrix measuring the response of each sample individually under varying offset fields was acquired. The system matrix was obtained using a 30×30 mm^2 Cartesian grid with a pixel size of 3×3 mm^2. To generate the system matrix, 4000 measurements for each grid position were averaged. For each 2D measurement scan, a total of 5000 frames were measured. Each measurement was first reduced by block averaging groups of 200 frames, and a low-pass filter was applied to remove selected frequencies of the measured data. The system matrix-based approach, described in detail in the previous sections, was used for multi-channel image reconstruction. For each measurement, between 200-300 iterations of the Kaczmarz algorithm were used to obtain images for each channel.

A 2D measurement scan of the entire sample holder was performed. In total, three channels were obtained from reconstruction, each corresponding to a system matrix of a specific

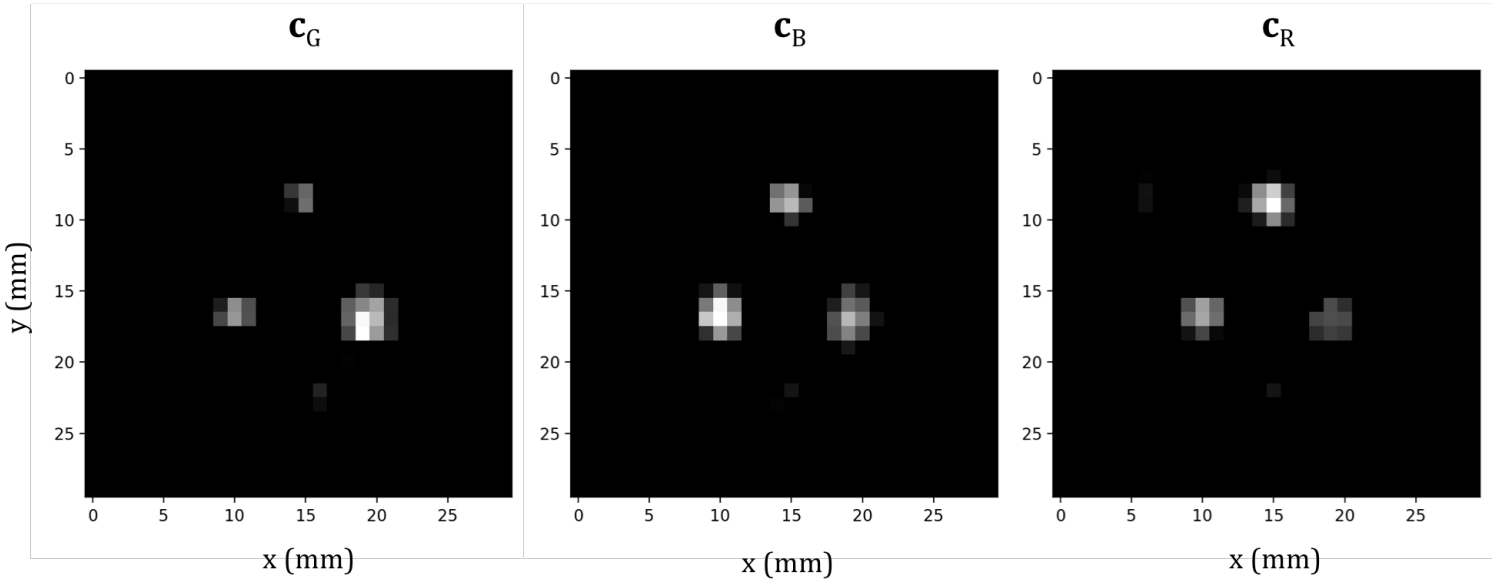

Figure 6.13: Final image reconstruction on each channel (green, blue, and red).

particle core size, shown in Fig. 6.13. In all reconstructed images, the strongest signal contribution is found in the channel matching the sample. However, there is also significant overlap in the signal from different channels, corresponding to non-matching system matrices, and consequently non-ideal signal separation. Signal overlap can be attributable to the nonzero size distributions of the nanoparticle samples, as discussed in §6.3.3 and shown in Fig. 6.11 which predicts some overlap in particle size among samples. The overall signal strength in each channel is lower compared to data obtained with a mono-spectral reconstruction.

Next, classification based on core size was performed, again using the nearest centroid classification procedure developed in the previous section. However, in this case, each image contained three ROIs, which were defined based on location of the sample (which corresponded to the voxel containing the maximal signal in that region). Each ROI was then classified and labeled based on core size and corresponding color. Finally, a multicolor image was constructed, with each pixel colorized based on its classified core size. The intensity was mapped directly to the corresponding channel for that pixel. The result is a multicolor

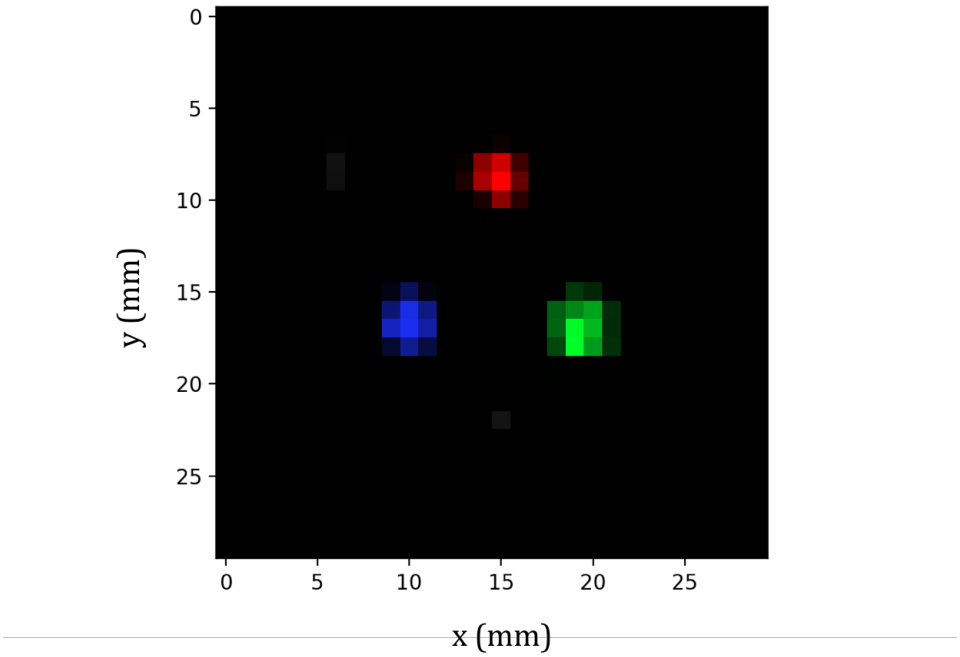

Figure 6.14: Final reconstructed multicolor image of three nanoparticle samples.

image (Fig. 6.14).

6.3.5 Conclusion

In this section, we were successfully able to generate a 2D multicolor MPI image with three sample types. This is the first study indicating that optimized MNP tracers, separated by only a few nanometers in core diameter, can be spectrally distinguished. These results could enable a range of new medical imaging applications, wherein optimized MNP cores would be functionalized separately for different purposes, including cancer targeting, circulation in the blood, or coating of devices such as catheters and guide-wires. These separately functionalized particles could then be distinguished in high resolution multi-channel images using this multi-contrast imaging technique.

6.4 Temperature estimation with AC measurements

Now that we have looked at cases of discrete multi-channel reconstruction, we now turn to the case of a continuous parameter: temperature. Temperature measurement has the potential to be enormously beneficial when used in conjunction with biomedical applications of magnetic nanoparticles, particularly those that involve particle heating, such as hyperthermia and heat-triggered release of chemotherapy drugs [162–166]. The magnetization response of magnetic nanoparticles is sensitive to small changes in temperature [58], and so it should be possible to use MPI measurements to determine the temperature of the nanoparticle environment.

Temperature plays an important role in biological and physiological processes. Changes in internal body temperature can be indicative of infection [154] or of hyper- or hypothyroidism [167–169]. Temperature is also closely related to the metabolic rate of mammalian cells and bodies [167, 170]. Furthermore, tissue containing malignant cancer cells can have a higher temperature than normal cell tissue [152, 153]; thermography is often used for diagnosis and imaging of breast cancer [151, 152].

A separate application of MNPs is magnetic fluid hyperthermia (MFH), in which nanoparticles are rotated with an applied radio-frequency magnetic field, resulting in cytotoxic heat generation [22–24]. Difficulties in monitoring the distribution of heat in the surrounding tissue and resulting rate and spread of temperature increase are one of the major impediments towards translating this application clinically [171, 172]. Using the nanoparticles themselves to monitor real-time temperature *in vivo* would introduce a novel and non-invasive temperature imaging method for this and other biomedical applications.

6.4.1 Theoretical basis for temperature estimation

As we have now discussed several times, in a first approximation, the magnetization of magnetic nanoparticles under an applied alternating magnetic field is proportional to the

Langevin function:

$$M(\xi) \propto \coth \xi - 1/\xi, \tag{6.48}$$

where $\xi = \frac{\mu_0 M_s V_c H}{k_B T}$. Until this point, we have made the approximation that the saturation magetization M_s is constant. However, in reality the bulk saturation magnetization is temperature dependent and follows an approximate Bloch's law relationship of the form [173]

$$M_s(T) = M_0(1 - bT^a), \tag{6.49}$$

where $b = 2.8 \times 10^{-5}$ has been experimentally determined for iron oxide [58], and M_0 is the magnetization at 0 K. Some results have shown a to be in the range of 1.5-1.65 [58]. For an alternating applied magnetic field, $H(t) = H_0 \cos \omega t$. We can perform a Fourier expansion on the magnetization to obtain the harmonics. By taking the ratios of various harmonics, the proportionality constants from the magnetization will cancel, allowing for a pure temperature-dependent measurement. The ratio of the 5th to the 3rd harmonics, for example, will be a monotonic function of H_0/T, shown in Fig. 6.15.

According to the Langevin model, then, by measuring the ratios of harmonics at a set drive field amplitude, the temperature can in theory be determined. Notice that since the drive field amplitude appears in the argument of the function as well, varying amplitude can be used to create a calibration curve.

Of course, relaxation effects will become prominent when the frequency and particle size are increased. If the particles remain immobilized, their relaxation will be purely Néel, and characterized by the field-dependent Néel relaxation time, which to first approximation can be represented by Eq. 4.18, reproduced here, with the expression for the equilibrium Néel relaxation time inserted:

$$\tau_{N,H} = \frac{\sqrt{\pi}\tau_0 \exp(\sigma)}{2\sigma^{1/2}\sqrt{1 + 1.97\xi_0^{3.18}}}. \tag{6.50}$$

Unfortunately, the temperature dependence no longer appears only with the field amplitude, as the attempt time τ_0 is equal to $M_s/(2\alpha\gamma K)$, where we are now considering M_s to be temperature dependent, and $\sigma = KV_c/k_B T$.

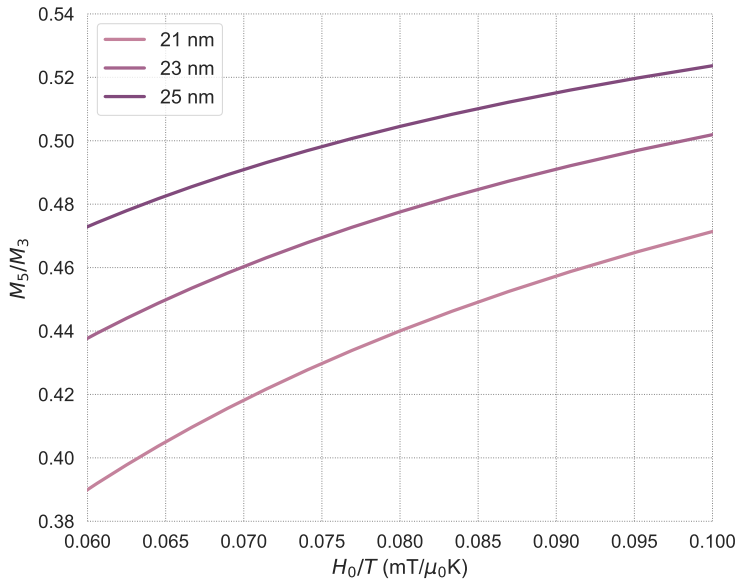

Figure 6.15: Ratio of 5th to 3rd harmonics of the Langevin function for three different particle sizes. The ratio of the harmonics is a monotonic function of the ratio of the applied field amplitude to the temperature.

In the event of mobilized particles, where Brownian rotation is possible as well, there will instead be a dependence on the Brownian relaxation time, Eq. 4.13:

$$\tau_{B,H} = \frac{3\eta V_h}{k_B T\sqrt{1+0.21\xi_0^2}} \tag{6.51}$$

It should be noted that viscosity (η) is temperature-dependent as well, and can be described by Vogel's equation [174]:

$$\eta = \exp\left(A + \frac{B}{C+T}\right). \tag{6.52}$$

For water, $A = -3.7188$, $B = 578.919$, and $C = -137.546$. Consequently, for realistic particle motion, there will be a complex dependence of the dynamics on temperature, and the exact dependence will be difficult to extract.

One possible solution was proposed by Zhong *et al.* [175], who showed that the ratio of

MNP harmonics can be expressed in the following way:

$$\frac{M_3}{M_1} = \frac{M_{3L}}{M_{1L}} f(\tan\phi, H_0/T), \tag{6.53}$$

where M_{3L} and M_{1L} are the harmonics of the Langevin function, and ϕ is the phase lag. This expression should apply for any of the harmonic ratios, e.g. the 5th/3rd harmonic. Using the ratios of harmonic amplitudes is advantageous because, as mentioned, several constants, such as the particle concentration, will cancel, allowing for easier extraction of the field or temperature dependence. The parameter f represents the necessary compensation from the phase lag due to relaxation effects. In the case of a very low frequency applied field, for example, $\tan\phi = 0$, and so $f = 1$, reducing to the Langevin harmonics. The parameter f can be fit using:

$$f(\tan\phi, H_0/T) = \frac{1}{1 + \alpha(H_0/T)(\tan\phi)^\beta}, \tag{6.54}$$

where $\alpha(H_0/T)$ can be fit to a function $\alpha = A(H_0/T)^B$. This implies that relaxation effects can be separated from temperature dependence, as long as the phase lag ϕ can be measured. In Ref. [175], only low frequencies (< 2 kHz) and low amplitudes (≤ 4 mT/μ_0) were studied. Here, we will apply this approach to look at temperature estimation with realistic MPI fields and frequencies (on the order of tens of kHz and tens of mT/μ_0).

6.4.2 Predicting temperature with AC measurements

To estimate temperature using AC measurements, we will adapt Eq. 6.53 to instead incorporate the 5th and 3rd harmonic amplitudes, as the fundamental harmonic is often inaccurate when measured experimentally due to feedthrough from the excitation signal. We will assume:

$$\frac{M_5}{M_3} = \frac{M_{5L}}{M_{3L}} f(\tan\phi, H_0/T), \tag{6.55}$$

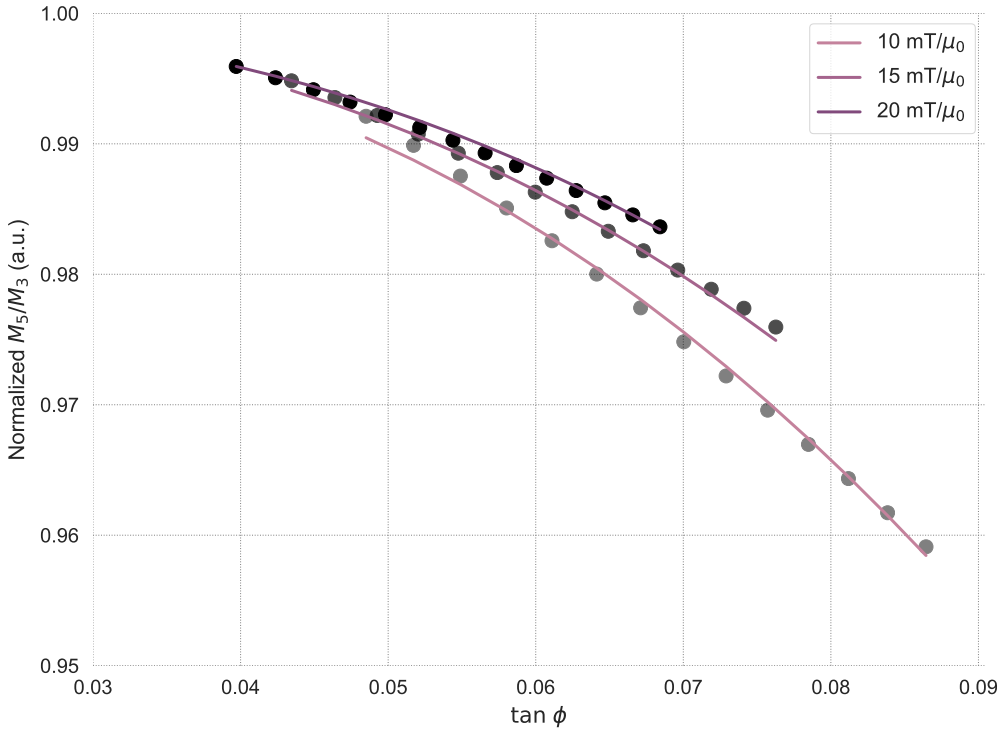

Figure 6.16: Best fits (solid lines) to simulated data (points) to Eq. 6.54, using a least-squares approach, at constant temperature, varying applied field frequency and amplitude. The ratio of the 5th and 3rd harmonics is normalized to the corresponding Langevin function harmonic ratio.

where the function $f(\tan\phi, H_0/T)$ is the same as defined in Eq. 6.54. To test this approach, simulations of the coupled Fokker-Planck equation, as outlined in §3.1.1, were performed. Due to the high level of sensitivity required for temperature estimation measurements, simulations of the Fokker-Planck equation were chosen over stochastic Langevin equations due to their ability to generate simulations of an effectively large number of particles in significantly less time. A 25 nm particle was simulated, with hydrodynamic diameter 50 nm and anisotropy constant K of 5 kJ/m^3. The average time-dependent magnetic moment was generated, and then the harmonic amplitudes and phase were extracted through Fourier transform. The temperature dependence of M_s and η were incorporated into the simulations.

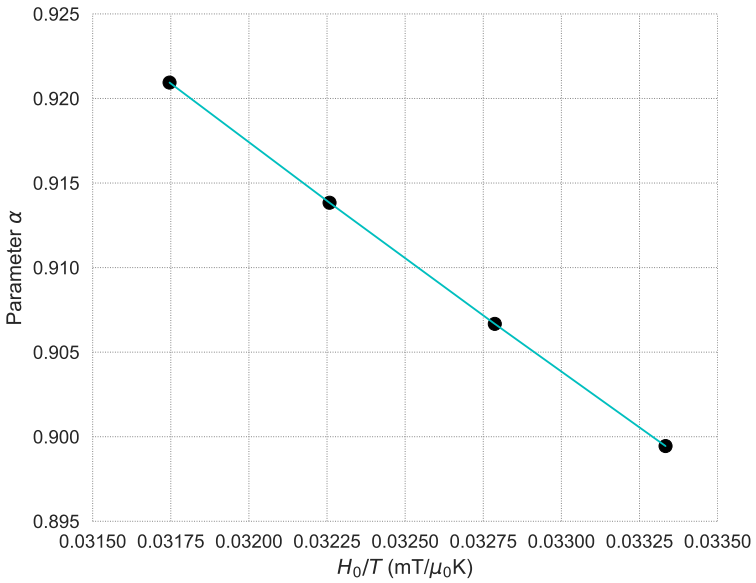

Figure 6.17: Best fit values of the function α, fitted to simulated data by $\alpha = A(H_0/T)^B$ using least-squares fitting. Best fit parameters were $A = 0.17$ and $B = -0.48$.

To estimate temperature, a calibration step is first required, where the parameters for the function $f(\tan\phi, H_0/T)$ are determined. Simulations were performed at a fixed temperature (300 K), for a range of field frequencies and amplitudes. Changing field frequency will influence the phase lag, and therefore $\tan\phi$, but will not affect $\alpha(H_0/T)$. This allows us to separately determine α and β. Frequencies were varied from 1 kHz to 24 kHz in 29 steps for three field amplitudes. Fitting results are shown in Fig. 6.16 and Fig. 6.17, where the ratio of the harmonics are normalized to the Langevin function harmonics (i.e. $\frac{M_5/M_3}{M_{5L}/M_{3L}}$). The best fit for parameter β was 2.6, and α was a function of H_0/T, as shown in Fig. 6.17, with best-fit values of $A = 0.17$ and $B = -0.48$.

Next, simulations were performed at a fixed field amplitude (10 mT/μ_0) for a range of frequencies and temperatures. When normalized, the harmonic ratios lie along the same curve when plotted against the phase lag for different values of temperature, shown in Fig. 6.18. This is a promising confirmation of our approach, as it indicates that varying temperature is interchangeable with varying the phase lag for a fixed amplitude, which was predicted by

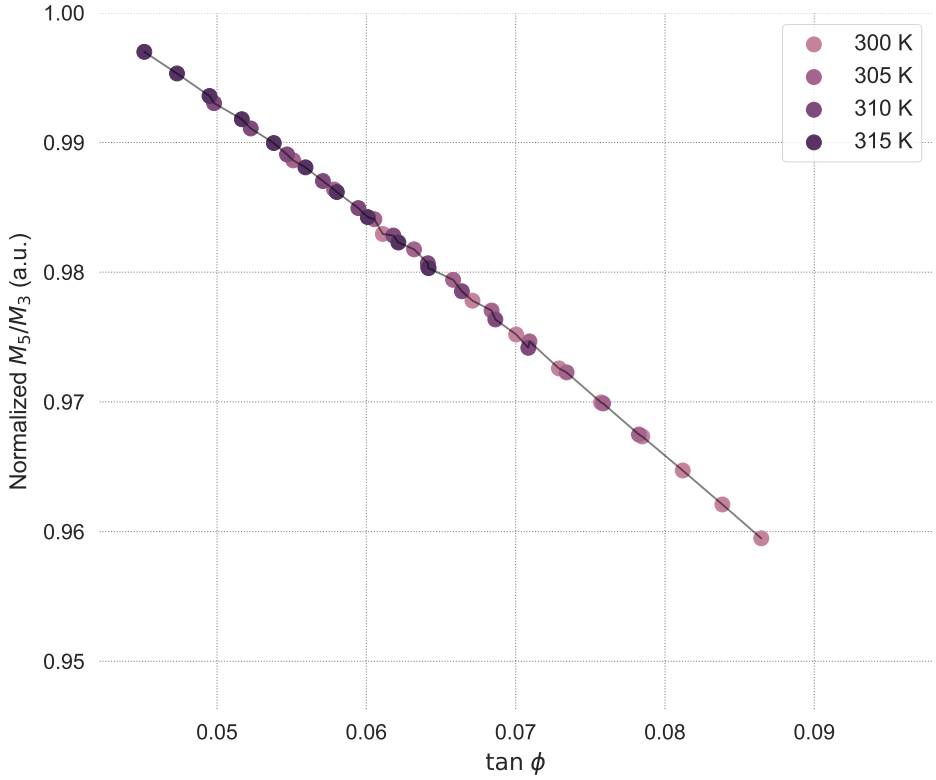

Figure 6.18: Simulated M_5/M_3 as a function of phase lag for a range of temperatures at a fixed amplitude. The solid line is a guide to the eye. All points lie along the same curve.

Eq. 6.54.

Finally, to predict the temperature from a given measurement, we can use the function $f(\tan\phi, H_0/T)$ with the determined parameters A, B, and β. For a given field frequency and amplitude, f will be a function of temperature alone, allowing us to calculate the predicted normalized harmonic ratio at a given temperature. Results are shown in Fig. 6.19, where the calculated value for M_5/M_3 from f is shown as a function of temperature. Simulated results of M_5/M_3 at different temperatures are shown as well. As the temperature deviates farther from 300 K, the point at which the calibration measurements were performed, the prediction generated by f is generally worse; however, overall the prediction and measurements are mostly in agreement.

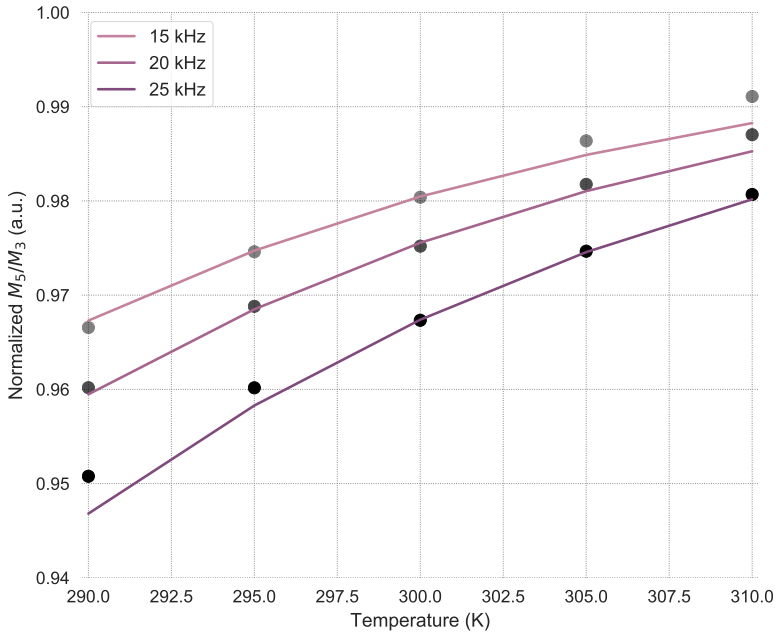

Figure 6.19: Calculations of f as a function of temperature (solid lines), and simulated M_5/M_3 (points) at a fixed 10 mT/μ_0 amplitude for different temperatures and frequencies.

This estimation process was then tested using AC measurements. Due to the high sensitivity requirements for measuring small temperature changes, a Quantum Design Physical Property Measurement System (PPMS) was used for measurements rather than the MPS system. For these measurements, the AC Measurement System (ACMS) option of the PPMS was used, which enables detection of up to 10 harmonics of the nanoparticle excitation response. A 25.3 nm nanoparticle sample was used for all measurements.

Calibration measurements were first performed at 300 K by varying the frequency in steps of 1 kHz and the amplitude in steps of 2 Oe (0.2 mT/μ_0). The ACMS can apply a maximum amplitude of 13 Oe (1.3 mT/μ_0), and a maximum frequency of 10 kHz. Least-squares fitting was performed on the calibration measurements to extract α and β. The resulting function f as a function of temperature with the best-fit results is shown in Fig. 6.20. Measurements were then performed at a fixed amplitude of 10 Oe (1 mT/μ_0) for a range of frequencies and temperatures. Measured results of M_5/M_3 are also shown in Fig. 6.20, and generally agree

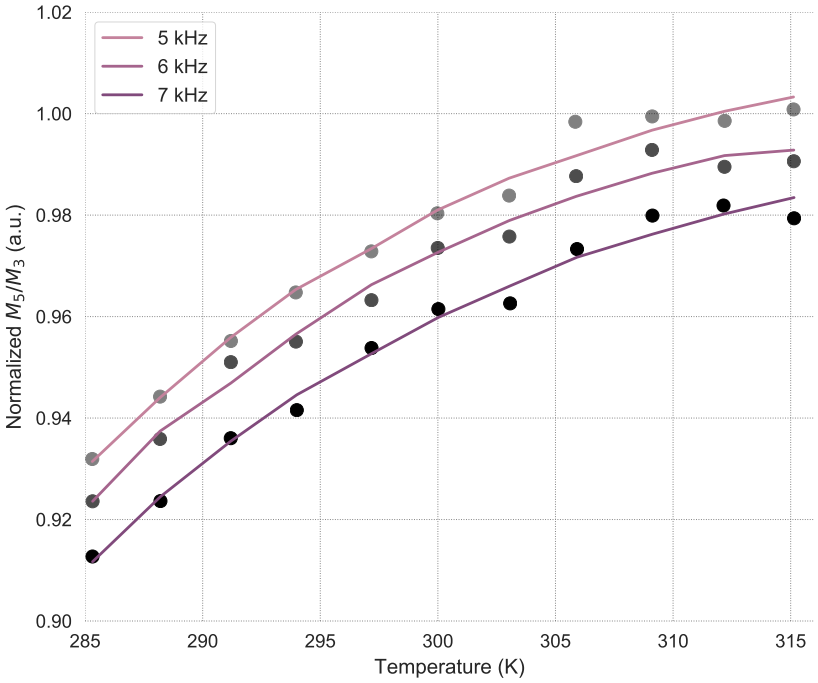

Figure 6.20: Calculations of f as a function of temperature (solid lines), and measured M_5/M_3 (points) at a fixed 1 mT/μ_0 amplitude for different temperatures and frequencies

with the calculated values of f from the calibration measurements.

By solving for temperature in Eq. 6.54 and inserting our fit parameters A, B, and β, we can directly calculate the predicted temperature from a given measurement of M_5/M_3 with fixed field conditions:

$$T = H_0 \left[\frac{\frac{M_3 M_{5L}}{M_5 M_{3L}} - 1}{A(\tan\phi)^\beta} \right]^{-\frac{1}{B}} \tag{6.56}$$

Calculations generated from the measured data at 6 kHz are shown in Fig. 6.21, where the predicted temperature, calculated from Eq. 6.56 is plotted against the actual temperature that was measured. The average prediction error for this frequency was 1.97 K, and the average prediction error for all frequencies measured was 1.52 K. These results are a promising indication that temperature quantification could be incorporated into MPI image scans, after an initial calibration measurement of the nanoparticle tracer. Using a multi-channel image reconstruction approach outlined in §6.2.3, temperature could be incorporated as a state variable during reconstruction, allowing for colorization of the final image based on temperature value. This was partially achieved in Ref. [147] with viscosity quantification, indicating that incorporating temperature quantification to MPI is possible. However, improvements to hardware and tracer design, such as some of those outlined in §5, may be required in order to improve sensitivity and achieve quantification of temperature to an accuracy of 1 K or less.

6.5 Conclusions and outlook

In this chapter, we outlined a procedure for multi-channel image reconstruction, both for continuous and discrete parameters, allowing for the generation of multicolor MPI images. The construction of multicolor MPI images based on core size discrimination and classification was achieved, and a procedure for quantifying temperature was proposed. The work outlined here points to a promising new direction for MPI, in which disease diagnostics and treatment can be combined with imaging.

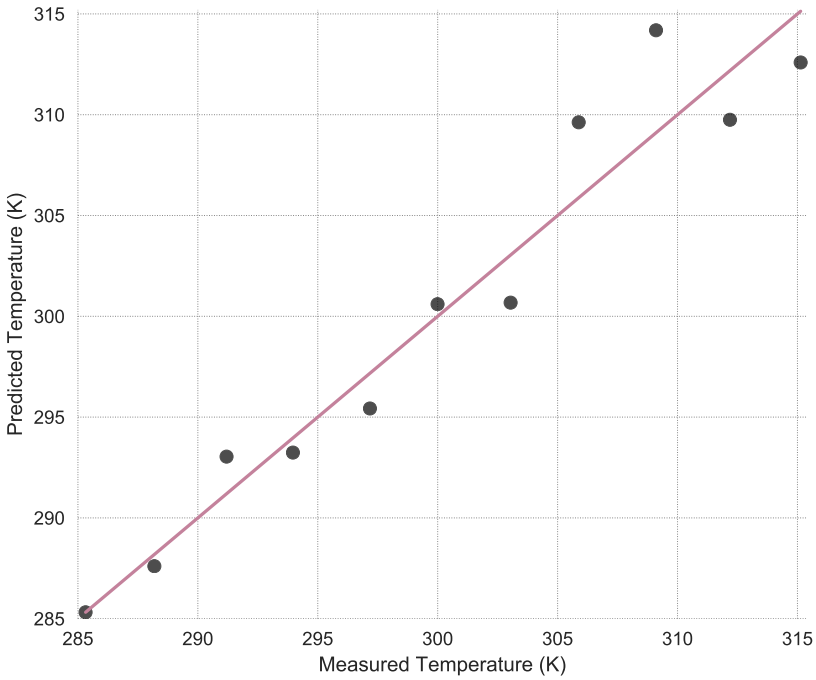

Figure 6.21: Predicted temperature, calculated from Eq. 6.56, versus measured temperature at 6 kHz (points). The solid line indicates a perfect prediction. The average prediction error is 1.97 K.

Chapter 7

CONCLUSIONS AND FUTURE WORK

Over the past decade and a half, MPI has evolved from a simple theoretical proposal to a full preclinical imaging system. Previous members of the Krishnan research group have worked extensively to experimentally develop nanoparticle synthesis, optimization, and functionalization for *in vivo* applications. My work has attempted to further this development and expand the scope of MPI, primarily by developing a deeper understanding of the underlying nanoparticle dynamics which comprise the physical principles behind MPI. In this dissertation, I have presented an overview of the current models of magnetic nanoparticle dynamics, and developed state-of-the-art computational models for modeling MNPs, using coupled stochastic Langevin equations as well as the coupled Fokker-Planck equation. Those computational models were used to explore the relaxation behavior of nanoparticles, and to develop a sophisticated understanding of the influence of internal and external state parameters on nanoparticle relaxation dynamics.

Those insights were then used to identify drive field conditions and nanoparticle core and hydrodynamic sizes for optimal MPI image quality, taking into account both practical considerations, like particle agglomeration, as well as underlying theoretical frameworks. A relationship between the drive field conditions, coating size, and optimal nanoparticle size was established, indicating that core size should be chosen based on hardware considerations, such as the drive field parameters, as well as on the intended functionalization of the nanoparticle surface. We developed and demonstrated a platform for multicolor MPI based on core size discrimination, showing simultaneous classification and spatial localization of nanoparticle tracers. A framework for general multi-channel image reconstruction was summarized, and finally, a procedure for temperature quantification with MPI was outlined.

To continue this work, there are still multiple possible avenues to pursue for multi-channel MPI, in particular. The incorporation of temperature quantification to MPI should be further investigated using MPI phantoms, and eventually with MPI *in vivo*. The possibility of quantifying or classifying several parameters simultaneously, such as viscosity and temperature, should also be investigated. Finally, enhancements to the simulation models should be made, such as enforcing approximations for performance speedup, or enabling the physical motion of nanoparticles in the simulation, allowing for modeling of particle agglomeration and interaction. More precise measurements of nanoparticle physical characteristics, such as the anisotropy and the damping parameter, for example with ferromagnetic resonance (FMR), should be made in order to obtain better values for the models. With an accurate, efficient model, a model-based approach to image reconstruction in f-space MPI could be taken, eliminating the need for an initial calibration system matrix measurement, allowing for significant speedup of image acquisition.

BIBLIOGRAPHY

[1] Kannan M Krishnan. Biomedical nanomagnetics: a spin through possibilities in imaging, diagnostics, and therapy. *Magnetics, IEEE Transactions on*, 46(7):2523–2558, 2010.

[2] Miriam Colombo, Susana Carregal-Romero, Maria F Casula, Lucía Gutiérrez, María P Morales, Ingrid B Böhm, Johannes T Heverhagen, Davide Prosperi, and Wolfgang J Parak. Biological applications of magnetic nanoparticles. *Chemical Society Reviews*, 41(11):4306–4334, 2012.

[3] Jon Dobson. Magnetic nanoparticles for drug delivery. *Drug development research*, 67(1):55–60, 2006.

[4] Kenneth J Widder, Andrew E Senyei, and David F Ranney. Magnetically responsive microspheres and other carriers for the biophysical targeting of antitumor agents. In *Advances in Pharmacology*, volume 16, pages 213–271. Elsevier, 1979.

[5] Sara Prijic and Gregor Sersa. Magnetic nanoparticles as targeted delivery systems in oncology. *Radiology and oncology*, 45(1):1–16, 2011.

[6] Stuart C McBain, Humphrey HP Yiu, and Jon Dobson. Magnetic nanoparticles for gene and drug delivery. *International journal of nanomedicine*, 3(2):169, 2008.

[7] Devika B Chithrani. Nanoparticles for improved therapeutics and imaging in cancer therapy. *Recent patents on nanotechnology*, 4(3):171–180, 2010.

[8] Dara L Kraitchman, Alan W Heldman, Ergin Atalar, Luciano C Amado, Bradley J Martin, Mark F Pittenger, Joshua M Hare, and Jeff WM Bulte. In vivo magnetic resonance imaging of mesenchymal stem cells in myocardial infarction. *Circulation*, 107(18):2290–2293, 2003.

[9] Takayasu Arai, Theo Kofidis, Jeff WM Bulte, Jorg De Bruin, Ross D Venook, Gerald J Berry, Michael V Mcconnell, Thomas Quertermous, Robert C Robbins, and Phillip C Yang. Dual in vivo magnetic resonance evaluation of magnetically labeled mouse embryonic stem cells and cardiac function at 1.5 t. *Magnetic Resonance in Medicine: An Official Journal of the International Society for Magnetic Resonance in Medicine*, 55(1):203–209, 2006.

[10] Luciano C Amado, Anastasios P Saliaris, Karl H Schuleri, Marcus St John, Jin-Sheng Xie, Stephen Cattaneo, Daniel J Durand, Torin Fitton, Jin Qiang Kuang, Garrick Stewart, et al. Cardiac repair with intramyocardial injection of allogeneic mesenchymal stem cells after myocardial infarction. *Proceedings of the National Academy of Sciences*, 102(32):11474–11479, 2005.

[11] Ka-Wing Au, Song-Yan Liao, Yee-Ki Lee, Wing-Hon Lai, Kwong-Man Ng, Yau-Chi Chan, Mei-Chu Yip, Chung-Yee Ho, Ed X Wu, Ronald A Li, et al. Effects of iron oxide nanoparticles on cardiac differentiation of embryonic stem cells. *Biochemical and biophysical research communications*, 379(4):898–903, 2009.

[12] Jaeyun Kim, Yuanzhe Piao, Nohyun Lee, Yong Il Park, In-Hwan Lee, Jung-Ho Lee, Seung R Paik, and Taeghwan Hyeon. Magnetic nanocomposite spheres decorated with nio nanoparticles for a magnetically recyclable protein separation system. *Advanced Materials*, 22(1):57–60, 2010.

[13] J Ugelstad, L Kilaas, P Stenstad, T Ellingsen, J Bjørgum, O Aune, T Nils Nilsen, R Schmid, and A Berge. Magnetic separation techniques applied to cellular and molecular biology. In *Preparation and Application of Monosized Composite Polymer Particles. Herausgegeben von JT Kemshead. Wordsmith's Conference Publications, Bristol, UK*, pages 235–254, 1991.

[14] Hakho Lee, Eric Sun, Donhee Ham, and Ralph Weissleder. Chip–nmr biosensor for detection and molecular analysis of cells. *Nature medicine*, 14(8):869, 2008.

[15] Laura Polito, Diego Monti, Enrico Caneva, Eleonora Delnevo, Giovanni Russo, and Davide Prosperi. One-step bioengineering of magnetic nanoparticles via a surface diazo transfer/azide–alkyne click reaction sequence. *Chemical communications*, (5):621–623, 2008.

[16] Miriam Colombo, Silvia Ronchi, Diego Monti, Fabio Corsi, Emilio Trabucchi, and Davide Prosperi. Femtomolar detection of autoantibodies by magnetic relaxation nanosensors. *Analytical biochemistry*, 392(1):96–102, 2009.

[17] Shaoyu Cai, Guohai Liang, Peng Zhang, Hui Chen, Song Zhang, Baohong Liu, and Jilie Kong. Rational strategy of magnetic relaxation switches for glycoprotein sensing. *Analyst*, 136(1):201–204, 2011.

[18] Conroy Sun, Jerry SH Lee, and Miqin Zhang. Magnetic nanoparticles in mr imaging and drug delivery. *Advanced drug delivery reviews*, 60(11):1252–1265, 2008.

[19] Marie-France Bellin. Mr contrast agents, the old and the new. *European journal of radiology*, 60(3):314–323, 2006.

[20] C Billotey, C Wilhelm, M Devaud, JC Bacri, J Bittoun, and F Gazeau. Cell internalization of anionic maghemite nanoparticles: quantitative effect on magnetic resonance imaging. *Magnetic Resonance in Medicine: An Official Journal of the International Society for Magnetic Resonance in Medicine*, 49(4):646–654, 2003.

[21] Rudolf Hergt, Silvio Dutz, Robert Müller, and Matthias Zeisberger. Magnetic particle hyperthermia: nanoparticle magnetism and materials development for cancer therapy. *Journal of Physics: Condensed Matter*, 18(38):S2919, 2006.

[22] Andreas Jordan, Regina Scholz, Peter Wust, Horst Fähling, and Roland Felix. Magnetic fluid hyperthermia (mfh): Cancer treatment with ac magnetic field induced excitation of biocompatible superparamagnetic nanoparticles. *Journal of Magnetism and Magnetic materials*, 201(1-3):413–419, 1999.

[23] Alison E Deatsch and Benjamin A Evans. Heating efficiency in magnetic nanoparticle hyperthermia. *Journal of Magnetism and Magnetic Materials*, 354:163–172, 2014.

[24] Ronald E Rosensweig. Heating magnetic fluid with alternating magnetic field. *Journal of magnetism and magnetic materials*, 252:370–374, 2002.

[25] R Hiergeist, W Andrä, N Buske, R Hergt, I Hilger, U Richter, and W Kaiser. Application of magnetite ferrofluids for hyperthermia. *Journal of Magnetism and Magnetic Materials*, 201(1):420–422, 1999.

[26] Bernhard Gleich and Jürgen Weizenecker. Tomographic imaging using the nonlinear response of magnetic particles. *Nature*, 435(7046):1214, 2005.

[27] Shuming Nie, Yun Xing, Gloria J Kim, and Jonathan W Simons. Nanotechnology applications in cancer. *Annu. Rev. Biomed. Eng.*, 9:257–288, 2007.

[28] Richard Mathew Ferguson, Amit P Khandhar, Hamed Arami, Loc Hua, Ondrej Hovorka, and Kannan M Krishnan. Tailoring the magnetic and pharmacokinetic properties of iron oxide magnetic particle imaging tracers. *Biomedizinische Technik/Biomedical Engineering*, 58(6):493–507, 2013.

[29] Scott J Kemp, R Matthew Ferguson, Amit P Khandhar, and Kannan M Krishnan. Monodisperse magnetite nanoparticles with nearly ideal saturation magnetization. *RSC Advances*, 6(81):77452–77464, 2016.

[30] Mamoru Hatakeyama, Hiroshi Kishi, Yoshinori Kita, Kensuke Imai, Kosuke Nishio, Satoki Karasawa, Yuka Masaike, Satoshi Sakamoto, Adarsh Sandhu, Akihiro Tanimoto, et al. A two-step ligand exchange reaction generates highly water-dispersed magnetic nanoparticles for biomedical applications. *Journal of Materials Chemistry*, 21(16):5959–5966, 2011.

[31] David Portet, Benoît Denizot, Elmar Rump, Jean-Jacques Lejeune, and Pierre Jallet. Nonpolymeric coatings of iron oxide colloids for biological use as magnetic resonance imaging contrast agents. *Journal of colloid and interface science*, 238(1):37–42, 2001.

[32] Iskandar I Yaacob, Anthony C Nunes, and Arijit Bose. Magnetic nanoparticles produced in spontaneous cationic-anionic vesicles: room temperature synthesis and characterization. *Journal of colloid and interface science*, 171(1):73–84, 1995.

[33] Carlos Tassa, Stanley Y Shaw, and Ralph Weissleder. Dextran-coated iron oxide nanoparticles: a versatile platform for targeted molecular imaging, molecular diagnostics, and therapy. *Accounts of chemical research*, 44(10):842–852, 2011.

[34] Jin Xie, Chenjie Xu, Nathan Kohler, Yanglong Hou, and Shouheng Sun. Controlled pegylation of monodisperse fe3o4 nanoparticles for reduced non-specific uptake by macrophage cells. *Advanced Materials*, 19(20):3163–3166, 2007.

[35] Tae-Jong Yoon, Kyeong Nam Yu, Eunha Kim, Jun Sung Kim, Byung Geol Kim, Sang-Hyun Yun, Byeong-Hyeok Sohn, Myung-Haing Cho, Jin-Kyu Lee, and Seung Bum Park. Specific targeting, cell sorting, and bioimaging with smart magnetic silica core–shell nanomaterials. *Small*, 2(2):209–215, 2006.

[36] Pedro Tartaj, Maria del Puerto Morales, Sabino Veintemillas-Verdaguer, Teresita González-Carreño, and Carlos J Serna. The preparation of magnetic nanoparticles for applications in biomedicine. *Journal of physics D: Applied physics*, 36(13):R182, 2003.

[37] Frank Caruso. Nanoengineering of particle surfaces. *Advanced materials*, 13(1):11–22, 2001.

[38] Angeles Villanueva, Magdalena Cañete, Alejandro G Roca, Macarena Calero, Sabino Veintemillas-Verdaguer, Carlos J Serna, María del Puerto Morales, and Rodolfo Miranda. The influence of surface functionalization on the enhanced internalization of magnetic nanoparticles in cancer cells. *Nanotechnology*, 20(11):115103, 2009.

[39] S Moein Moghimi, A Christy Hunter, and J Clifford Murray. Long-circulating and target-specific nanoparticles: theory to practice. *Pharmacological reviews*, 53(2):283–318, 2001.

[40] Theresa M Allen. Ligand-targeted therapeutics in anticancer therapy. *Nature Reviews Cancer*, 2(10):750, 2002.

[41] KJ Kirk. Nanomagnets for sensors and data storage. *Contemporary Physics*, 41(2):61–78, 2000.

[42] Behtash Behin-Aein, Sayeef Salahuddin, and Supriyo Datta. Switching energy of ferromagnetic logic bits. *IEEE Transactions on Nanotechnology*, 8(4):505–514, 2009.

[43] Andrew D Kent and Daniel C Worledge. A new spin on magnetic memories. *Nature nanotechnology*, 10(3):187, 2015.

[44] J Weizenecker, B Gleich, J Rahmer, H Dahnke, and J Borgert. Three-dimensional real-time in vivo magnetic particle imaging. *Physics in Medicine & Biology*, 54(5):L1, 2009.

[45] Yi-Xiang J Wang, Shahid M Hussain, and Gabriel P Krestin. Superparamagnetic iron oxide contrast agents: physicochemical characteristics and applications in mr imaging. *European radiology*, 11(11):2319–2331, 2001.

[46] R Matthew Ferguson, Kevin R Minard, and Kannan M Krishnan. Optimization of nanoparticle core size for magnetic particle imaging. *Journal of magnetism and magnetic materials*, 321(10):1548–1551, 2009.

[47] Chris Heyn, John A Ronald, Lisa T Mackenzie, Ian C MacDonald, Ann F Chambers, Brian K Rutt, and Paula J Foster. In vivo magnetic resonance imaging of single cells in mouse brain with optical validation. *Magnetic Resonance in Medicine*, 55(1):23–29, 2006.

[48] P Vogel, MA Rückert, P Klauer, WH Kullmann, PM Jakob, and VC Behr. First in vivo traveling wave magnetic particle imaging of a beating mouse heart. *Physics in Medicine & Biology*, 61(18):6620, 2016.

[49] Tarik F Massoud and Sanjiv S Gambhir. Molecular imaging in living subjects: seeing fundamental biological processes in a new light. *Genes & development*, 17(5):545–580, 2003.

[50] Kerstin Lüdtke-Buzug, Julian Haegele, Sven Biederer, Timo F Sattel, Marlitt Erbe, Robert L Duschka, Jörg Barkhausen, and Florian M Vogt. Comparison of commercial iron oxide-based mri contrast agents with synthesized high-performance mpi tracers. *Biomedizinische Technik/Biomedical Engineering*, 58(6):527–533, 2013.

[51] Ajay Singh, Tejas Patel, Joachim Hertel, Marializa Bernardo, Annamaria Kausz, and Louis Brenner. Safety of ferumoxytol in patients with anemia and ckd. *American Journal of Kidney Diseases*, 52(5):907–915, 2008.

[52] Patrick W Goodwill and Steven M Conolly. The x-space formulation of the magnetic particle imaging process: 1-d signal, resolution, bandwidth, snr, sar, and magnetostimulation. *IEEE transactions on medical imaging*, 29(11):1851–1859, 2010.

[53] Hendrik Paysen, James Wells, Olaf Kosch, Uwe Steinhoff, Jochen Franke, Lutz Trahms, Tobias Schaeffter, and Frank Wiekhorst. Improved sensitivity and limit-of-detection using a receive-only coil in magnetic particle imaging. *Physics in medicine and biology*, 2018.

[54] Laura R Croft, Patrick W Goodwill, Justin J Konkle, Hamed Arami, Daniel A Price, Ada X Li, Emine U Saritas, and Steven M Conolly. Low drive field amplitude for improved image resolution in magnetic particle imaging. *Medical physics*, 43(1):424–435, 2016.

[55] Kolja Them, Michael G Kaul, Caroline Jung, Martin Hofmann, Tobias Mummert, Franziska Werner, and Tobias Knopp. Sensitivity enhancement in magnetic particle imaging by background subtraction. *IEEE transactions on medical imaging*, 35(3):893–900, 2016.

[56] Kuan Lu, Patrick Goodwill, Bo Zheng, and Steven Conolly. Multi-channel acquisition for isotropic resolution in magnetic particle imaging. *IEEE transactions on medical imaging*, 37(9):1989–1998, 2018.

[57] Adam M Rauwerdink and John B Weaver. Viscous effects on nanoparticle magnetization harmonics. *Journal of Magnetism and Magnetic Materials*, 322(6):609–613, 2010.

[58] John B Weaver, Adam M Rauwerdink, and Eric W Hansen. Magnetic nanoparticle temperature estimation. *Medical physics*, 36(5):1822–1829, 2009.

[59] Jing Zhong, Meinhard Schilling, and Frank Ludwig. Magnetic nanoparticle temperature imaging with a scanning magnetic particle spectrometer. *Measurement Science and Technology*, 29(11):115903, 2018.

[60] Sonu Gandhi, Hamed Arami, and Kannan M Krishnan. Detection of cancer-specific proteases using magnetic relaxation of peptide-conjugated nanoparticles in biological environment. *Nano letters*, 16(6):3668–3674, 2016.

[61] Xiaojuan Zhang, Daniel B Reeves, Irina M Perreard, Warren C Kett, Karl E Griswold, Barjor Gimi, and John B Weaver. Molecular sensing with magnetic nanoparticles using magnetic spectroscopy of nanoparticle brownian motion. *Biosensors and Bioelectronics*, 50:441–446, 2013.

[62] Jan Dieckhoff, Aidin Lak, Meinhard Schilling, and Frank Ludwig. Protein detection with magnetic nanoparticles in a rotating magnetic field. *Journal of Applied Physics*, 115(2):024701, 2014.

[63] Ulrich M Engelmann, Carolyn Shasha, Eric Teeman, Ioana Slabu, and Kannan M Krishnan. Predicting size-dependent heating efficiency of magnetic nanoparticles from experiment and stochastic néel-brown langevin simulation. *Journal of Magnetism and Magnetic Materials*, 471:450–456, 2019.

[64] Marcela Gonzales-Weimuller, Matthias Zeisberger, and Kannan M Krishnan. Size-dependant heating rates of iron oxide nanoparticles for magnetic fluid hyperthermia. *Journal of magnetism and magnetic materials*, 321(13):1947–1950, 2009.

[65] Amit P Khandhar, R Matthew Ferguson, Julian A Simon, and Kannan M Krishnan. Enhancing cancer therapeutics using size-optimized magnetic fluid hyperthermia. *Journal of applied physics*, 111(7):07B306, 2012.

[66] Amit P Khandhar, R Matthew Ferguson, Julian A Simon, and Kannan M Krishnan. Tailored magnetic nanoparticles for optimizing magnetic fluid hyperthermia. *Journal of Biomedical Materials Research Part A*, 100(3):728–737, 2012.

[67] Victor F Puntes, Kannan M Krishnan, and A Paul Alivisatos. Colloidal nanocrystal shape and size control: the case of cobalt. *Science*, 291(5511):2115–2117, 2001.

[68] Yuping Bao. *Synthesis, self-assembly, and potential applications of cobalt-based nanoparti- cles with tailored magnetic properties.* PhD thesis, University of Washington, 2006.

[69] Marcela Gonzales-Weyhmiller. *Synthesis, modeling, and optimization of iron oxide nanoparticles for magnetic fluid hyperthermia.* PhD thesis, University of Washington, 2007.

[70] Richard Matthew Ferguson. *Tracer design for Magnetic Particle Imaging: modeling, synthesis, and experimental optimization of biocompatible iron oxide nanoparticles.* PhD thesis, University of Washington, 2011.

[71] Amit Khandhar. *Biomedical imaging and therapy with physically and physiologically tailored magnetic nanoparticles*. PhD thesis, University of Washington, 2014.

[72] Asahi Tomitaka, Hamed Arami, Sonu Gandhi, and Kannan M Krishnan. Lactoferrin conjugated iron oxide nanoparticles for targeting brain glioma cells in magnetic particle imaging. *Nanoscale*, 7(40):16890–16898, 2015.

[73] Hamed Arami. *Magnetic Particle Imaging (MPI) Tracers for In Vivo Applications*. PhD thesis, University of Washington, 2015.

[74] Eric Teeman, Carolyn Shasha, James E Evans, and Kannan M Krishnan. Intracellular dynamics of superparamagnetic iron oxide nanoparticles for magnetic particle imaging. *Nanoscale*, 2019.

[75] Kannan M Krishnan, Alexandre B Pakhomov, Yuping Bao, Peter Blomqvist, Yoonsoo Chun, Marcela Gonzales, Kelli Griffin, Xiaosong Ji, and Bradley K Roberts. Nanomagnetism and spin electronics: materials, microstructure and novel properties. *Journal of materials science*, 41(3):793–815, 2006.

[76] Edmund C Stoner and EP Wohlfarth. A mechanism of magnetic hysteresis in heterogeneous alloys. *Philosophical Transactions of the Royal Society of London A: Mathematical, Physical and Engineering Sciences*, 240(826):599–642, 1948.

[77] Michael A Martens, Robert J Deissler, Yong Wu, Lisa Bauer, Zhen Yao, Robert Brown, and Mark Griswold. Modeling the brownian relaxation of nanoparticle ferrofluids: Comparison with experiment. *Medical physics*, 40(2), 2013.

[78] Daniel B Reeves and John B Weaver. Simulations of magnetic nanoparticle brownian motion. *Journal of applied physics*, 112(12):124311, 2012.

[79] Robert J Deissler, Yong Wu, and Michael A Martens. Dependence of brownian and néel relaxation times on magnetic field strength. *Medical physics*, 41(1), 2014.

[80] William Fuller Brown Jr. Thermal fluctuations of a single-domain particle. *Physical Review*, 130(5):1677, 1963.

[81] William T Coffey and Yuri P Kalmykov. Thermal fluctuations of magnetic nanoparticles: Fifty years after brown. *Journal of Applied Physics*, 112(12):121301, 2012.

[82] Cindi L Dennis and Robert Ivkov. Physics of heat generation using magnetic nanoparticles for hyperthermia. *International Journal of Hyperthermia*, 29(8):715–729, 2013.

[83] Daniel B Reeves and John B Weaver. Combined néel and brown rotational langevin dynamics in magnetic particle imaging, sensing, and therapy. *Applied physics letters*, 107(22):223106, 2015.

[84] Daniel B Reeves and John B Weaver. Comparisons of characteristic timescales and approximate models for brownian magnetic nanoparticle rotations. *Journal of applied physics*, 117(23):233905, 2015.

[85] PC Fannin, BKP Scaife, and W Charles. New technique for measuring the complex susceptibility of ferrofluids. *Journal of Physics E: Scientific Instruments*, 19(3):238, 1986.

[86] Allan H Morrish. The physical principles of magnetism. *The Physical Principles of Magnetism, by Allan H. Morrish, pp. 696. ISBN 0-7803-6029-X. Wiley-VCH, January 2001.*, page 696, 2001.

[87] Peter Debye. Polar molecules. *New York, The Chemical Catalog Co., Inc.*, 1929.

[88] R Chantrell, J Popplewell, and S Charles. Measurements of particle size distribution parameters in ferrofluids. *IEEE Transactions on Magnetics*, 14(5):975–977, 1978.

[89] Jürgen Rahmer, Jürgen Weizenecker, Bernhard Gleich, and Jörn Borgert. Signal encoding in magnetic particle imaging: properties of the system function. *BMC medical imaging*, 9(1):4, 2009.

[90] Patrick W Goodwill and Steven M Conolly. Multidimensional x-space magnetic particle imaging. *IEEE transactions on medical imaging*, 30(9):1581–1590, 2011.

[91] William T Coffey and Yuri P Kalmykov. *The Langevin equation: with applications to stochastic problems in physics, chemistry and electrical engineering*. World Scientific, 2004.

[92] Saqlain A Shah, Daniel B Reeves, R Matthew Ferguson, John B Weaver, and Kannan M Krishnan. Mixed brownian alignment and néel rotations in superparamagnetic iron oxide nanoparticle suspensions driven by an ac field. *Physical Review B*, 92(9):094438, 2015.

[93] Jürgen Weizenecker. The fokker–planck equation for coupled brown–néel-rotation. *Physics in Medicine & Biology*, 63(3):035004, 2018.

[94] Yuriy L Raikher and Mark I Shliomis. The effective field method in the orientational kinetics of magnetic fluids. *Adv. Chem. Phys*, 87:595–751, 1994.

[95] R Matthew Ferguson, Amit P Khandhar, Christian Jonasson, Jakob Blomgren, Christer Johansson, and Kannan M Krishnan. Size-dependent relaxation properties of monodisperse magnetite nanoparticles measured over seven decades of frequency by ac susceptometry. *IEEE transactions on magnetics*, 49(7):3441–3444, 2013.

[96] Luis C Branquinho, Marcus S Carrião, Anderson S Costa, Nicholas Zufelato, Marcelo H Sousa, Ronei Miotto, Robert Ivkov, and Andris F Bakuzis. Effect of magnetic dipolar interactions on nanoparticle heating efficiency: Implications for cancer hyperthermia. *Scientific reports*, 3:2887, 2013.

[97] Matthieu Jamet, Wolfgang Wernsdorfer, Christophe Thirion, Veronique Dupuis, Patrice Mélinon, Alain Pérez, and Dominique Mailly. Magnetic anisotropy in single clusters. *Physical Review B*, 69(2):024401, 2004.

[98] WT Coffey. Ferromagnetic particles. 1993.

[99] Ning-Ning Song, Hai-Tao Yang, Hao-Liang Liu, Xiao Ren, Hao-Feng Ding, Xiang-Qun Zhang, and Zhao-Hua Cheng. Exceeding natural resonance frequency limit of monodisperse fe3o4 nanoparticles via superparamagnetic relaxation. *Scientific reports*, 3, 2013.

[100] José Luis García-Palacios and Francisco J Lázaro. Langevin-dynamics study of the dynamical properties of small magnetic particles. *Physical Review B*, 58(22):14937, 1998.

[101] DV Berkov and NL Gorn. Susceptibility of the disordered system of fine magnetic particles: a langevin-dynamics study. *Journal of Physics: Condensed Matter*, 13(41):9369, 2001.

[102] Paul Langevin. *On the theory of Brownian motion*. 1908.

[103] Eugene Wong and Moshe Zakai. On the convergence of ordinary integrals to stochastic integrals. *The Annals of Mathematical Statistics*, 36(5):1560–1564, 1965.

[104] AD Arelaro, Ana Lucia Brandl, E Lima, LF Gamarra, GES Brito, WM Pontuschka, and GF Goya. Interparticle interactions and surface contribution to the effective anisotropy in biocompatible iron oxide nanoparticles used for contrast agents. *Journal of applied physics*, 97(10):10J316, 2005.

[105] Hiroaki Mamiya and Balachandran Jeyadevan. Optimal design of nanomagnets for targeted hyperthermia. *Journal of Magnetism and Magnetic Materials*, 323(10):1417–1422, 2011.

[106] Jan Dieckhoff, Dietmar Eberbeck, Meinhard Schilling, and Frank Ludwig. Magnetic-field dependence of brownian and néel relaxation times. *Journal of Applied Physics*, 119(4):043903, 2016.

[107] S Havriliak and S Negami. A complex plane representation of dielectric and mechanical relaxation processes in some polymers. *Polymer*, 8:161–210, 1967.

[108] WT Coffey, DSF Crothers, JL Dormann, LJ Geoghegan, Yu P Kalmykov, JT Waldron, and AW Wickstead. Effect of an oblique magnetic field on the superparamagnetic relaxation time. *Physical Review B*, 52(22):15951, 1995.

[109] MA Martsenyuk, Yu L Raikher, and MI Shliomis. On the kinetics of magnetization of suspension of ferromagnetic particles. *Journal of Experimental and Theoretical Physics*, 38(2):413–416, 1974.

[110] Takashi Yoshida and Keiji Enpuku. Simulation and quantitative clarification of ac susceptibility of magnetic fluid in nonlinear brownian relaxation region. *Japanese Journal of Applied Physics*, 48(12R):127002, 2009.

[111] Saqlain A Shah, RM Ferguson, and KM Krishnan. Slew-rate dependence of tracer magnetization response in magnetic particle imaging. *Journal of applied physics*, 116(16):163910, 2014.

[112] PW Goodwill, A Tamrazian, LR Croft, CD Lu, EM Johnson, R Pidaparthi, RM Ferguson, AP Khandhar, KM Krishnan, and SM Conolly. Ferrohydrodynamic relaxometry for magnetic particle imaging. *Applied Physics Letters*, 98(26):262502, 2011.

[113] Hamed Arami, RM Ferguson, Amit P Khandhar, and Kannan M Krishnan. Size-dependent ferrohydrodynamic relaxometry of magnetic particle imaging tracers in different environments. *Medical physics*, 40(7), 2013.

[114] Klaas Bente, Matthias Weber, Matthias Graeser, Timo F Sattel, Marlitt Erbe, and Thorsten M Buzug. Electronic field free line rotation and relaxation deconvolution in magnetic particle imaging. *IEEE transactions on medical imaging*, 34(2):644–651, 2015.

[115] Laura R Croft, Patrick W Goodwill, and Steven M Conolly. Relaxation in x-space magnetic particle imaging. *Medical Imaging, IEEE Transactions on*, 31(12):2335–2342, 2012.

[116] Emine U Saritas, Patrick W Goodwill, Laura R Croft, Justin J Konkle, Kuan Lu, Bo Zheng, and Steven M Conolly. Magnetic particle imaging (mpi) for nmr and mri researchers. *Journal of Magnetic Resonance*, 229:116–126, 2013.

[117] Patrick William Goodwill, Emine Ulku Saritas, Laura Rose Croft, Tyson N Kim, Kannan M Krishnan, David V Schaffer, and Steven M Conolly. X-space mpi: magnetic nanoparticles for safe medical imaging. *Advanced Materials*, 24(28):3870–3877, 2012.

[118] R Matthew Ferguson, Kevin R Minard, Amit P Khandhar, and Kannan M Krishnan. Optimizing magnetite nanoparticles for mass sensitivity in magnetic particle imaging. *Medical physics*, 38(3):1619–1626, 2011.

[119] Tobias Knopp, Sven Biederer, Timo F Sattel, Marlitt Erbe, and Thorsten M Buzug. Prediction of the spatial resolution of magnetic particle imaging using the modulation transfer function of the imaging process. *IEEE transactions on medical imaging*, 30(6):1284–1292, 2011.

[120] William J Atkinson, Ivan A Brezovich, and Dev P Chakraborty. Usable frequencies in hyperthermia with thermal seeds. *IEEE Transactions on Biomedical Engineering*, (1):70–75, 1984.

[121] Richard Matthew Ferguson. *Tracer design for Magnetic Particle Imaging: modeling, synthesis, and experimental optimization of biocompatible iron oxide nanoparticles*. University of Washington, 2011.

[122] Ryan Hufschmid, Hamed Arami, R Matthew Ferguson, Marcela Gonzales, Eric Teeman, Lucien N Brush, Nigel D Browning, and Kannan M Krishnan. Synthesis of phase-pure and monodisperse iron oxide nanoparticles by thermal decomposition. *Nanoscale*, 7(25):11142–11154, 2015.

[123] J Rahmer, A Halkola, B Gleich, I Schmale, and J Borgert. First experimental evidence of the feasibility of multi-color magnetic particle imaging. *Physics in medicine and biology*, 60(5):1775, 2015.

[124] Michael J Hostetler, Stephen J Green, Jennifer J Stokes, and Royce W Murray. Monolayers in three dimensions: synthesis and electrochemistry of ω-functionalized alkanethiolate-stabilized gold cluster compounds. *Journal of the American Chemical Society*, 118(17):4212–4213, 1996.

[125] Roychelle S Ingram, Michael J Hostetler, and Royce W Murray. Poly-hetero-ω-functionalized alkanethiolate-stabilized gold cluster compounds. *Journal of the American Chemical Society*, 119(39):9175–9178, 1997.

[126] Marco Lattuada and T Alan Hatton. Functionalization of monodisperse magnetic nanoparticles. *Langmuir*, 23(4):2158–2168, 2007.

[127] Teresa Pellegrino, Liberato Manna, Stefan Kudera, Tim Liedl, Dmitry Koktysh, Andrey L Rogach, Simon Keller, Joachim Rädler, Giovanni Natile, and Wolfgang J Parak. Hydrophobic nanocrystals coated with an amphiphilic polymer shell: a general route to water soluble nanocrystals. *Nano letters*, 4(4):703–707, 2004.

[128] Carl D Walkey and Warren CW Chan. Understanding and controlling the interaction of nanomaterials with proteins in a physiological environment. *Chemical Society Reviews*, 41(7):2780–2799, 2012.

[129] Martin Lundqvist, Johannes Stigler, Giuliano Elia, Iseult Lynch, Tommy Cedervall, and Kenneth A Dawson. Nanoparticle size and surface properties determine the protein corona with possible implications for biological impacts. *Proceedings of the National Academy of Sciences*, 2008.

[130] Alexandra Hill and Christine K Payne. Impact of serum proteins on mri contrast agents: cellular binding and t 2 relaxation. *RSC advances*, 4(60):31735–31744, 2014.

[131] Mauro Ferrari. Cancer nanotechnology: opportunities and challenges. *Nature reviews cancer*, 5(3):161, 2005.

[132] Elaine Y Yu, Prashant Chandrasekharan, Ran Berzon, Zhi Wei Tay, Xinyi Y Zhou, Amit P Khandhar, R Matthew Ferguson, Scott J Kemp, Bo Zheng, Patrick W Goodwill, et al. Magnetic particle imaging for highly sensitive, quantitative, and safe in vivo gut bleed detection in a murine model. *ACS nano*, 11(12):12067–12076, 2017.

[133] Hamed Arami, Eric Teeman, Alyssa Troksa, Haydin Bradshaw, Katayoun Saatchi, Asahi Tomitaka, Sanjiv Sam Gambhir, Urs O Häfeli, Denny Liggitt, and Kannan M Krishnan. Tomographic magnetic particle imaging of cancer targeted nanoparticles. *Nanoscale*, 9(47):18723–18730, 2017.

[134] John D Hood, Mark Bednarski, Ricardo Frausto, Samira Guccione, Ralph A Reisfeld, Rong Xiang, and David A Cheresh. Tumor regression by targeted gene delivery to the neovasculature. *Science*, 296(5577):2404–2407, 2002.

[135] Dorit Goren, Aviva T. Horowitz, Dina Tzemach, Mark Tarshish, Samuel Zalipsky, and Alberto Gabizon. Nuclear delivery of doxorubicin via folate-targeted liposomes with bypass of multidrug-resistance efflux pump. *Clinical Cancer Research*, 6(5):1949–1957, 2000.

[136] Jennifer Sudimack and Robert J Lee. Targeted drug delivery via the folate receptor. *Advanced Drug Delivery Reviews*, 41(2):147–162, 2000.

[137] Alyssa Troksa. Superparamagnetic iron oxide nanoparticle coating enhanced visualization of vascular catheters. Master's thesis, University of Washington, 2016.

[138] Julian Haegele, Sven Biederer, Hanne Wojtczyk, Matthias Gräser, Tobias Knopp, Thorsten M Buzug, Jörg Barkhausen, and Florian M Vogt. Toward cardiovascular interventions guided by magnetic particle imaging: First instrument characterization. *Magnetic resonance in medicine*, 69(6):1761–1767, 2013.

[139] Julian Haegele, Sarah Vaalma, Nikolaos Panagiotopoulos, Jörg Barkhausen, Florian M Vogt, Jörn Borgert, and Jürgen Rahmer. Multi-color magnetic particle imaging for cardiovascular interventions. *Physics in medicine and biology*, 61(16):N415, 2016.

[140] Brendan J Barrett, Richard W Katzberg, Henrik S Thomsen, Nan Chen, Dushyant Sahani, Gilles Soulez, Jay P Heiken, Luigi Lepanto, Zhao-hui Ni, and Rendon Nelson. Contrast-induced nephropathy in patients with chronic kidney disease undergoing computed tomography: a double-blind comparison of iodixanol and iopamidol. *Investigative radiology*, 41(11):815–821, 2006.

[141] John B Weaver, Adam M Rauwerdink, Charles R Sullivan, and Ian Baker. Frequency distribution of the nanoparticle magnetization in the presence of a static as well as a harmonic magnetic field. *Medical physics*, 35(5):1988–1994, 2008.

[142] Adam M Rauwerdink, Eric W Hansen, and John B Weaver. Nanoparticle temperature estimation in combined ac and dc magnetic fields. *Physics in medicine and biology*, 54(19):L51, 2009.

[143] Adam M Rauwerdink, Andrew J Giustini, and John B Weaver. Simultaneous quantification of multiple magnetic nanoparticles. *Nanotechnology*, 21(45):455101, 2010.

[144] Daniel Hensley, Patrick Goodwill, Laura Croft, and Steven Conolly. Preliminary experimental x-space color mpi. In *Magnetic Particle Imaging (IWMPI), 2015 5th International Workshop on*, pages 1–1. IEEE, 2015.

[145] T Wawrzik, C Kuhlmann, F Ludwig, and M Schilling. Estimating particle mobility in mpi. In *Magnetic Particle Imaging (IWMPI), 2013 International Workshop on*, pages 1–1. IEEE, 2013.

[146] Mustafa Utkur, Yavuz Muslu, and Emine Ulku Saritas. Relaxation-based viscosity mapping for magnetic particle imaging. *Physics in Medicine & Biology*, 62(9):3422, 2017.

[147] Martin Möddel, Christian Meins, Jan Dieckhoff, and Tobias Knopp. Viscosity quantification using multi-contrast magnetic particle imaging. *New journal of physics*, 20(8):083001, 2018.

[148] Christian Stehning, Bernhard Gleich, and Jürgen Rahmer. Simultaneous magnetic particle imaging (mpi) and temperature mapping using multi-color mpi. *International Journal on Magnetic Particle Imaging*, 2(2), 2016.

[149] DH Lee, JM Jung, SY Kim, KT Kim, and YI Cho. Comparison tests for plasma viscosity measurements. *International Communications in Heat and Mass Transfer*, 39(10):1474–1477, 2012.

[150] KR Lee, AL Betz, S Kim, RF Keep, and JT Hoff. The role of the coagulation cascade in brain edema formation after intracerebral hemorrhage. *Acta neurochirurgica*, 138(4):396–401, 1996.

[151] U Rajendra Acharya, Eddie Yin-Kwee Ng, Jen-Hong Tan, and S Vinitha Sree. Thermography based breast cancer detection using texture features and support vector machine. *Journal of medical systems*, 36(3):1503–1510, 2012.

[152] Thomas D Vreugdenburg, Cameron D Willis, Linda Mundy, and Janet E Hiller. A systematic review of elastography, electrical impedance scanning, and digital infrared thermography for breast cancer screening and diagnosis. *Breast cancer research and treatment*, 137(3):665–676, 2013.

[153] Ralph J DeBerardinis, Julian J Lum, Georgia Hatzivassiliou, and Craig B Thompson. The biology of cancer: metabolic reprogramming fuels cell growth and proliferation. *Cell metabolism*, 7(1):11–20, 2008.

[154] Thomas A Mace, Lingwen Zhong, Casey Kilpatrick, Evan Zynda, Chen-Ting Lee, Maegan Capitano, Hans Minderman, and Elizabeth A Repasky. Differentiation of cd8+ t cells into effector cells is enhanced by physiological range hyperthermia. *Journal of leukocyte biology*, 90(5):951–962, 2011.

[155] Tobias Knopp and Thorsten M Buzug. *Magnetic particle imaging: an introduction to imaging principles and scanner instrumentation*. Springer Science & Business Media, 2012.

[156] Kai Wu, Yi Wang, Yinglong Feng, Lina Yu, and Jian-Ping Wang. Colorize magnetic nanoparticles using a search coil based testing method. *Journal of Magnetism and Magnetic Materials*, 380:251–254, 2015.

[157] AP Khandhar, P Keselman, SJ Kemp, RM Ferguson, PW Goodwill, SM Conolly, and KM Krishnan. Evaluation of peg-coated iron oxide nanoparticles as blood pool tracers for preclinical magnetic particle imaging. *Nanoscale*, 9(3):1299–1306, 2017.

[158] Nikolaos Panagiotopoulos, Sjef Cremer, Jürgen Rahmer, Jochen Franke, Robert Duschka, Sarah Vaalma, Michael Heidenreich, Jörn Borgert, Paul Borm, Jörg Barkhausen, et al. Spio-coating of devices for mpi-guided cardiovascular interventions: Proof of principle. In *Magnetic Particle Imaging (IWMPI), 2015 5th International Workshop on*, pages 1–1. IEEE, 2015.

[159] Johannes Salamon, Martin Hofmann, Caroline Jung, Michael Gerhard Kaul, Franziska Werner, Kolja Them, Rudolph Reimer, Peter Nielsen, Annika vom Scheidt, Gerhard Adam, et al. Magnetic particle/magnetic resonance imaging: in-vitro mpi-guided real time catheter tracking and 4d angioplasty using a road map and blood pool tracer approach. *PloS one*, 11(6):e0156899, 2016.

[160] R Matthew Ferguson, Amit P Khandhar, and Kannan M Krishnan. Tracer design for magnetic particle imaging. *Journal of applied physics*, 111(7):07B318, 2012.

[161] MRI Bruker Biospin. Gmbh ettlingen, germany,?mpi preclinical brochure.?, 2015.

[162] Denis Le Bihan, José Delannoy, and Ronald L Levin. Temperature mapping with mr imaging of molecular diffusion: application to hyperthermia. *Radiology*, 171(3):853–857, 1989.

[163] Thomas C Cetas. Will thermometric tomography become practical for hyperthermia treatment monitoring? *Cancer research*, 44(10 Supplement):4805s–4808s, 1984.

[164] Sinil Kim. Liposomes as carriers of cancer chemotherapy. *Drugs*, 46(4):618–638, 1993.

[165] JN Weinstein, RL Magin, MB Yatvin, and DS Zaharko. Liposomes and local hyperthermia: selective delivery of methotrexate to heated tumors. *Science*, 204(4389):188–191, 1979.

[166] Madeline Torres-Lugo and Carlos Rinaldi. Thermal potentiation of chemotherapy by magnetic nanoparticles. *Nanomedicine*, 8(10):1689–1707, 2013.

[167] Jean Himms-Hagen. Thyroid hormones and thermogenesis. In *Mammalian thermogenesis*, pages 141–177. Springer, 1983.

[168] Ana Paula Arruda, Wagner S Da-Silva, Denise P Carvalho, et al. Hyperthyroidism increases the uncoupled atpase activity and heat production by the sarcoplasmic reticulum ca2+-atpase. *Biochemical Journal*, 375(3):753–760, 2003.

[169] J Enrique Silva. Thyroid hormone control of thermogenesis and energy balance. *Thyroid*, 5(6):481–492, 1995.

[170] James F Gillooly, James H Brown, Geoffrey B West, Van M Savage, and Eric L Charnov. Effects of size and temperature on metabolic rate. *science*, 293(5538):2248–2251, 2001.

[171] Manfred Johannsen, Uwe Gneveckow, Burghard Thiesen, Kasra Taymoorian, Chie Hee Cho, Norbert Waldöfner, Regina Scholz, Andreas Jordan, Stefan A Loening, and Peter Wust. Thermotherapy of prostate cancer using magnetic nanoparticles: feasibility, imaging, and three-dimensional temperature distribution. *European urology*, 52(6):1653–1662, 2007.

[172] Burghard Thiesen and Andreas Jordan. Clinical applications of magnetic nanoparticles for hyperthermia. *International journal of hyperthermia*, 24(6):467–474, 2008.

[173] B Martinez, A Roig, X Obradors, E Molins, A Rouanet, and C Monty. Magnetic properties of γ-fe2o3 nanoparticles obtained by vaporization condensation in a solar furnace. *Journal of applied physics*, 79(5):2580–2586, 1996.

[174] H Vogel. The temperature dependence law of the viscosity of fluids. *Phys. Z*, 22:645–646, 1921.

[175] Jing Zhong, Meinhard Schilling, and Frank Ludwig. Magnetic nanoparticle thermometry independent of brownian relaxation. *Journal of Physics D: Applied Physics*, 51(1):015001, 2017.

Appendix A

FOKKER-PLANCK COEFFICIENTS

Below are the coefficients required to generate matrix **M** in Eq. 3.26. Each row and column of the matrix corresponds to an L and R value, as in $D_{L,R}$.

#	$D^{0,0}_{L-\Delta l,R-\Delta r}$	$f_{\Delta l,0}(L,0)g_{\Delta r,0}(R,0)$
# 1	$D^{0,0}_{L-2,R-2}$	$\frac{KV_c}{2Tk_B\tau_B\tau_N}\left[-\frac{3(L+1)(L+2)(R+1)(R+2)}{(2L+3)(2L+5)(2R+3)(2R+5)}\right][L\tau_N+R\tau_B]$
# 2	$D^{0,0}_{L-2,R}$	$\frac{KV_c}{2Tk_B\tau_B\tau_N}\left[\frac{3LR(L-1)(R+1)}{(2L-3)(2L-1)(2R-1)(2R+3)}\right]\left[\left(\frac{2L}{3}+\frac{2}{3}\right)\tau_N+\tau_B\right]$
# 3	$D^{0,0}_{L-2,R+2}$	$\frac{KV_c}{2Tk_B\tau_B\tau_N}\left[-\frac{3L(L-1)(R+1)(R+2)}{(2L-3)(2L-1)(2R+3)(2R+5)}\right][(-L-1)\tau_N+R\tau_B]$
#4	$D^{0,0}_{L,R-2}$	$\frac{KV_c}{2Tk_B\tau_B\tau_N}\left[\frac{LR(L+1)(R-1)}{(2L-1)(2L+3)(2R-3)(2R-1)}\right][3\tau_N+(2R+2)\tau_B]$
#5	$D^{0,0}_{L,R-1}$	$\frac{M_sV_c}{2Tk_B\tau_N}\left[\frac{B_3R(R+1)}{2R-1}\right]$
#6	$D^{0,0}_{L,R}$	$\frac{1}{2\tau_B}[-L(L+1)]+\frac{1}{2\tau_N}[-R(R+1)]+\frac{KV_c}{2Tk_B\tau_B\tau_N}\left[\frac{2LR(L+1)(R+11)}{(2L-1)(2L+3)(2R-1)(2R+3)}\right][\tau_N+\tau_B]$
#7	$D^{0,0}_{L,R+1}$	$\frac{M_sV_c}{2Tk_B\tau_N}\left[-\frac{B_3R(R+1)}{2R+3}\right]$
#8	$D^{0,0}_{L,R+2}$	$\frac{KV_c}{2Tk_B\tau_B\tau_N}\left[-\frac{L(L+1)(R+1)(R+2)}{(2L-1)(2L+3)(2R+3)(2R+5)}\right][-3\tau_N+2R\tau_B]$
#9	$D^{0,0}_{L+2,R-2}$	$\frac{KV_c}{2Tk_B\tau_B\tau_N}\left[\frac{3R(L+1)(L+2)(R-1)}{(2L+3)(2L+5)(2R-3)(2R-1)}\right][-L\tau_N+(R+1)\tau_B]$
#10	$D^{0,0}_{L+2,R}$	$\frac{KV_c}{2Tk_B\tau_B\tau_N}\left[\frac{R(L+1)(L+2)(R+1)}{(2L+3)(2L+5)(2R-1)(2R+3)}\right][-2L\tau_N+3\tau_B]$
#11	$D^{0,0}_{L+2,R+2}$	$\frac{KV_c}{2Tk_B\tau_B\tau_N}\left[-\frac{3(L+1)(L+2)(R+1)(R+2)}{(2L+3)(2L+5)(2R+3)(2R+5)}\right][L\tau_N+R\tau_B]$

Appendix B

PYTHON CODE FOR FOKKER-PLANCK SOLUTIONS

Below is the Python code used to generate solutions to the coupled Fokker-Planck equation. The output array MA contains each component of $D_{L,R}^{0,0}$ for each time step. The average particle moment in the z-direction is given by MA[:,0].

```
from numpy import genfromtxt
import numpy as np
import math
from scipy.integrate import odeint


T = 300.
k_B = 1.381e23
mu0 = 4*np.pi*1e7
eta = 8.9e4
gamma = 1.75e11
alpha = 1
M_s = 420000.
K = 5000.


def gen_coefs(L, R, dc, dh, b):


    V_c = (4/3.)*np.pi*(dc/2.)**3
    V_h = (4/3.)*np.pi*(dh/2.)**3
    tau_B = 3*eta*V_h/(k_B*T)
```

```
tau_N = V_c*M_s/(k_B*T*gamma)*(1 + alpha**2)/(2*alpha)
B_3 = b


coef = np.zeros(11)
coef[0] = K*V_c/(2*T*k_B*tau_B)*(3*L*R*(L  1)*(L + 1)*(R  1)/((2*L  3)*(2*L  1)
    ↪ *(2*R  3)*(2*R  1)))+K*V_c/(2*T*k_B*tau_N)*(3*L*R*(L  1)*(R  1)*(R +
    ↪ 1)/((2*L  3)*(2*L  1)*(2*R  3)*(2*R  1)))
coef[1] = K*V_c/(2*T*k_B*tau_B)*(2*L*R*(L  1)*(L + 1)*(R + 1)/((2*L  3)*(2*L
    ↪ 1)*(2*R  1)*(2*R + 3)))+K*V_c/(2*T*k_B*tau_N)*(3*L*R*(L  1)*(R + 1)
    ↪ /((2*L  3)*(2*L  1)*(2*R  1)*(2*R + 3)))
coef[2] = K*V_c/(2*T*k_B*tau_B)*(3*L*(L  1)*(L + 1)*(R + 1)*(R + 2)/((2*L  3)
    ↪ *(2*L  1)*(2*R + 3)*(2*R + 5)))+K*V_c/(2*T*k_B*tau_N)*(3*L*R*(L  1)*(
    ↪ R + 1)*(R + 2)/((2*L  3)*(2*L  1)*(2*R + 3)*(2*R + 5)))
coef[3] = K*V_c/(2*T*k_B*tau_B)*(3*L*R*(L + 1)*(R  1)/((2*L  1)*(2*L + 3)*(2*R
    ↪   3)*(2*R  1)))+K*V_c/(2*T*k_B*tau_N)*(2*L*R*(L + 1)*(R  1)*(R + 1)
    ↪ /((2*L  1)*(2*L + 3)*(2*R  3)*(2*R  1)))
coef[4] = M_s*V_c/(2*T*k_B*tau_N)*(B_3*R*(R + 1)/(2*R  1))
coef[5] = 1/(2*tau_B)*(L*(L + 1))+1/(2*tau_N)*(R*(R + 1))+K*V_c/(2*T*k_B*
    ↪ tau_B)*(2*L*R*(L + 1)*(R + 1)/((2*L  1)*(2*L + 3)*(2*R  1)*(2*R + 3)))+
    ↪ K*V_c/(2*T*k_B*tau_N)*(2*L*R*(L + 1)*(R + 1)/((2*L  1)*(2*L + 3)*(2*R
    ↪   1)*(2*R + 3)))
coef[6] = M_s*V_c/(2*T*k_B*tau_N)*(B_3*R*(R + 1)/(2*R + 3))
coef[7] = K*V_c/(2*T*k_B*tau_B)*(3*L*(L + 1)*(R + 1)*(R + 2)/((2*L  1)*(2*L +
    ↪ 3)*(2*R + 3)*(2*R + 5)))+K*V_c/(2*T*k_B*tau_N)*(2*L*R*(L + 1)*(R +
    ↪ 1)*(R + 2)/((2*L  1)*(2*L + 3)*(2*R + 3)*(2*R + 5)))
coef[8] = K*V_c/(2*T*k_B*tau_B)*(3*L*R*(L + 1)*(L + 2)*(R  1)/((2*L + 3)*(2*L
    ↪ + 5)*(2*R  3)*(2*R  1)))+K*V_c/(2*T*k_B*tau_N)*(3*R*(L + 1)*(L + 2)*(
```

```
        ↪ R  1)*(R + 1)/((2*L + 3)*(2*L + 5)*(2*R  3)*(2*R  1)))
    coef[9] = K*V_c/(2*T*k_B*tau_B)*(2*L*R*(L + 1)*(L + 2)*(R + 1)/((2*L + 3)*(2*
        ↪ L + 5)*(2*R  1)*(2*R + 3)))+K*V_c/(2*T*k_B*tau_N)*(3*R*(L + 1)*(L +
        ↪ 2)*(R + 1)/((2*L + 3)*(2*L + 5)*(2*R  1)*(2*R + 3)))
    coef[10] = K*V_c/(2*T*k_B*tau_B)*(3*L*(L + 1)*(L + 2)*(R + 1)*(R + 2)/((2*L +
        ↪  3)*(2*L + 5)*(2*R + 3)*(2*R + 5)))+K*V_c/(2*T*k_B*tau_N)*(3*R*(L +
        ↪ 1)*(L + 2)*(R + 1)*(R + 2)/((2*L + 3)*(2*L + 5)*(2*R + 3)*(2*R + 5)))

    return coef

def gen_matrix(dc, dh, Lmax, b):

    N = Lmax*Lmax
    matrix = np.zeros((N,N))
    for x in range(N):
        L = int(math.floor(x/Lmax))
        R = int(x % Lmax)
        coef = gen_coefs(L,R,dc,dh,b)

        if x+2*Lmax2 >= (L+2)*Lmax and x+2*Lmax2 < N: matrix[x,x+2*Lmax2] =
            ↪ coef[8]
        if x+2*Lmax < N: matrix[x,x+2*Lmax] = coef[9]
        if x+2*Lmax+2 < (L+3)*Lmax and x+2*Lmax+2 < N: matrix[x,x+2*Lmax+2]
            ↪ = coef[10]

        if x2 >= L*Lmax: matrix[x,x2] = coef[3]
        if x1 >= L*Lmax: matrix[x,x1] = coef[4]
```

```
            matrix[x,x] = coef[5]
            if x+1 < (L+1)*Lmax: matrix[x,x+1] = coef[6]
            if x+2 < (L+1)*Lmax: matrix[x,x+2] = coef[7]

            if x2*Lmax2 >= 0 and x2*Lmax2 < (L1)*Lmax: matrix[x,x2*Lmax2] = coef[0]
            if x2*Lmax >= 0 and x2*Lmax < (L1)*Lmax: matrix[x,x2*Lmax] = coef[1]
            if x2*Lmax+2 >= 0 and x2*Lmax+2 < (L1)*Lmax: matrix[x,x2*Lmax+2] =
                ↪ coef[2]



    M = matrix[1:]
    a = M[:,0]*(4*np.pi)**(2)
    M = M[:,1:]

    return M, a

Lmax = 25
B0=10e3
DiaCore=25e9
DiaHydro=50e9
f = 25000

m0 = np.zeros(Lmax**21)

time = np.linspace(0.0, 1e4, 1001)

field = B0*np.cos(2*np.pi*f*time)
```

```
def deriv(D, t):
    b = B0*np.cos(2*np.pi*f*t)
    M, a = gen_matrix(DiaCore,DiaHydro,Lmax,b)
    return np.dot(M, D) + a


MA = (4.*np.pi)**2/3.*odeint(deriv, m0, time)
```